Doctoral Thesis

The effects of heterogeneity and anisotropy on hydraulic fracture propagation

Nathaniel Dudfield Forbes Inskip

Submitted in fulfilment of the requirements for the degree of

Doctor of Philosophy in Earth Sciences of

Royal Holloway, University of London

November 2018

Declaration of Authorship

I, Nathaniel Dudfield Forbes Inskip, hereby declare that this thesis and the work presented in it is entirely my own. Where I have consulted the work of others, this is always clearly stated.

Signed:

Date:

Abstract

While considerable effort has been expended on the study of fracture propagation in rocks in recent years, our understanding of how fractures propagate through layered sequences with different mechanical properties remains poor. Yet, mechanical layering is a key parameter controlling the propagation of fractures across such sequences, along with any inherent mechanical anisotropy and heterogeneity within the individual layers. Organic-rich shales are a common target in unconventional hydrocarbon production, and are known to be highly anisotropic. Moreover, many hydrocarbon reservoirs contain large-scale heterogeneities such as layering. In this thesis I report measurements of the contrasting properties of rock strata within the Liassic sequence at Nash Point, South Wales, which is composed of interbedded shales and limestones, and how those properties influence fracture propagation.

Laboratory measurements including Young's modulus, tensile strength (σ_t) and mode-I fracture toughness (K_{Ic}), demonstrate that Nash Point shale is highly anisotropic whereas Nash Point limestone is essentially isotropic. It was found during testing that many of the fractures in the shale samples deflect from the intended direction, and as such it was not possible to fully characterise the fractures using σ_t or K_{Ic} alone. It was therefore necessary to adopt a fracture energy (G_c) based approach that allows analysis of fracture propagation conditions for both deflected and un-deflected fractures in all orientations. It was found that G_c increases as the angle from the bedding plane increases, but also that an elliptical function can be used to estimate values of G_c at angles between the normal and parallel to bedding orientations.

The numerical modelling section of this thesis demonstrates how a contrast in Young's modulus between layers in a sequence may affect fracture propagation across the sequence. When the layer hosting the fracture tip is the stiffer one, fracture arrest normally

occurs at the interface with the more compliant layer. When the layer above the interface is the stiffer one, fracture arrest may occur directly at the interface or within the host layer well below the interface.

It is clear from the results presented in thesis that both heterogeneity and anisotropy can have a significant effect on hydraulic fractures propagating in an unconventional reservoir, whereby there are several means by which a fracture may become arrested or deflected. Therefore both heterogeneity and anisotropy within a reservoir must be understood before any realistic forecast of fracture propagation can be made.

Acknowledgements

Although my name appears on the cover to this thesis, it would not have been possible for me to complete it without the help of many individuals along the way.

First and foremost I would like to thank my supervisors Phil Meredith and Agust Gudmundsson for their guidance throughout the project, and to Phil in particular for all his help with the experimental part of the project. His enthusiasm for experimental rock physics has definitely been contagious, where even carrying oversized blocks of rock in the pouring Welsh rain was not enough to dampen his spirits! I would also like to thank both Michael Chandler and John Browning for their input as co-authors, and John in particular for showing me the ropes in both COMSOL and using some of the lab equipment at UCL.

Financially this project would not have been possible without the support from the NERC CDT in Oil and Gas and Hannon Westwood.

None of the experimental work presented in this thesis would have been possible without the help from Jim Davy, Steve Boon, Neil Hughes and John Bowles from UCL, and I am eternally grateful for their help and guidance especially when things didn't always go to plan. I would also like to thank both Phil Benson and Stephan Gehne for their help in conducting UCS tests down in the rock mechanics labs at the University of Portsmouth.

At Royal Holloway I am very grateful to Mark Longbottom, Frank Lehane and Big Kev for putting up with my technical queries/support over the years, and Dan Parsonage for prolonging my rugby career, which has no doubt been one of the extra-curricular activities that has kept me sane throughout the PhD. I am also grateful to Margaret Collinson, Ian Watkinson and Nicola Scarselli, for their general guidance throughout the course of the PhD.

To everyone who has ever helped me in the field and in bringing samples back to the lab (Pete Burgess, John Webb, Emma Webb, Ieuan Jones, John Corr, Patricia Hughes) I thank you for donating your time, patience, strength of arms and in the case of John Webb his blood to the cause. At this point Stephan Gehne deserves a particular mention with help in the field, and to use his own words "shared with me the load of massive shale blocks to carry them to the car, which was parked way too far away". To Uncle Bob I thank you for lending me tools to use for field work (I'm sorry that they may not always have come back in the same condition I borrowed them in) and to Aunty Sally for making sure that I was well fed on the way back from my field excursions.

All of those in the Lamb clan who had to put up with my elusiveness over the last couple of years when I have been off on "field work" or at a "conference", but also for their support over the years (especially in being well fed and watered!).

Thanks also to Rhys Davies and Owen Hyner who gave up their time to read through my thesis. I certainly owe you both a pint for the time you will never get back.

To Anna Clark, Lorna Morrow and John Underhill (weeeh!) for everything they have done in setting up the CDT and organising some truly amazing courses. And to all the other members of the CDT who have made this last four years particularly memorable (What? Who? Light the beacons!). Even to Nick, Scott and Sean who have been of particular annoyance throughout the course, but I would not have it any other way.

Within the office I have several to thank for their help/distraction from the task in hand. Silvia whose command of the English language is unparalleled, however, despite her help I am still none the wiser with regards to using effect or affect. Camilla for her culinary advice on Italian food and constant supply of tea breaks, but also with the help of Paul managed to corrupt an entire summer of mine with Pokemon Go. Alex C for our interesting discussions on rock mechanics but also for his shared enthusiasm for all things

Welsh. Sandy for keeping me well fed and coffeeeeeed throughout the long days. Alex H, Kay, Brennan and Butler for rekindling my interest in Chess when I had no time to play it (i.e. in the final month of my write-up).

Apart from my parents, there are two individuals in particular whose teachings initially sparked my interest in earth science, physics and the crossover in between. These are my Geography teacher, Catrin Bellamy Jones, and Physics teacher, Ian Jones. Without their enthusiasm in their subjects I may not have started out on the path that has led me here.

The final three people deserve the biggest thanks of all. First to my parents, Roy and Jackie, who have supported me all the way through my life in whatever way they could. Without their help and guidance (and large food parcels) I would not be the person I am today and have been supportive of me in everything I have done.

Last but certainly not least I have to thank Kat, who has been my rock throughout the whole process, and especially during the harder times has pulled me through (usually with food), but has also put up with me when at times I have been intolerable. Caru ti!

‘Mae well da fi darllen y geiriadur na’r lwtsh yma, ond mae e’n edrych yn grêt.’

Owen Ceredig Hyner

Contents

1 Introduction

Hydraulic stimulation, or fracturing, of hydrocarbon reservoirs has been used to enhance reservoir permeability since the late 1940s (Clark 1949). However, despite this long use, and more recently its increased use in the development of unconventional hydrocarbon reservoirs, understanding of how mechanical anisotropy and heterogeneity (such as layering) within rock sequences affect fracture propagation remains poor. Although different, anisotropy and heterogeneity are sometimes used interchangeably. For example, a layered sequence, whereby the mechanical properties of each of the individual layers is different could be described as both anisotropic and/or heterogeneous. However, in the context of this thesis anisotropy will only refer to any anisotropy present within an individual layer in terms of mechanical properties, whereas heterogeneity will refer to the contrast in properties between individual layers in a sequence, or any non-directional dependent differences in properties within an individual layer (e.g. clasts within a layer).

This thesis considers the effects of anisotropy and heterogeneity on fracture propagation in three particular cases: shale sequences, limestone sequences and layered sequences.

1.1 Shale sequences

Shales, as a class, are the most abundant of sedimentary rock types, making up more than 50% of sedimentary material worldwide (Chandler *et al.* 2016). They are important not only as source rocks and seals in conventional hydrocarbon systems, but also as seals for potential carbon capture and storage (CCS) reservoirs (Levine *et al.* 2016), as well as being both source and reservoir rocks in unconventional gas plays (Boyer *et al.* 2011). Specifically, over the past decade or so, there has been an increased emphasis on producing hydrocarbons from unconventional resources such as gas shales. This involves

hydraulically fracturing these formations in order to increase the overall reservoir permeability.

Despite the importance and increased interest in shales, there remains a paucity of data describing their mechanical and physical properties, in particular when compared with the amount of available data on other sedimentary rocks, such as sandstones and limestones. The paucity of data on shales is especially noticeable regarding their fracture properties, such as tensile strength and fracture toughness. Part of the reason for this lack of data is that their mineralogy (usually a high clay content, and in particular when smectite is present, as it reacts with water used as a cooling fluid during sample preparation), microstructure, and inherent anisotropy mean that shales are difficult materials to work with (Islam & Skalle 2013; Chandler 2014).

1.2 Limestone sequences

A significant proportion of global hydrocarbon reserves exist within carbonate reservoirs, including limestones (Lamarche *et al.* 2012; Burberry & Peppers 2017; Li *et al.* 2018). Limestones are usually considered brittle and compared to other sedimentary rocks in a sedimentary basin are likely to have a high Young's modulus (Afşar *et al.* 2014). As such, following deposition and burial, limestones can often become fractured, thereby enhancing the porosity and permeability (Dashti *et al.* 2018; Li *et al.* 2018). In these instances it is important to know parameters such as fracture spacing, aperture, tortuosity etc. in order to calculate a more accurate reservoir porosity and permeability. Therefore it is important to know the fracture properties (tensile strength and fracture toughness) of the bulk rock so as to be able reduce the risk in determining such fracture parameters.

In instances where the permeability of a reservoir is particularly low (commonly < 1 mD for oil reservoirs and < 0.1 mD for gas reservoirs) hydraulic stimulation or hydraulic fracturing is required in order to allow the hydrocarbons to flow. Examples of limestone

reservoirs which are considered tight include the Taq Taq, Kirkuk, Jambur, Khabaz and Bai Hassan oil fields in the Zagros fold belt (Rashid *et al.* 2017) and the Dariyan formation in the central Persian Gulf (Hosseini *et al.* 2018). In these instances it is important to understand the fracture properties of the host rock so as to understand how fractures may propagate during stimulation.

1.3 Layered sequences

Although it is important to understand how the mechanical properties of individual rock types affect fracture propagation, most unconventional reservoirs contain more than one rock type, and are often layered, thus adding an extra complexity, heterogeneity. An example of a layered unconventional hydrocarbon reservoir requiring hydraulic stimulation is the Vaca Muerta formation in Argentina (Figure 1). The main target in the Vaca Muerta formation is an organic-rich shale but this is interbedded with other units such as sandstone, marl, calcareous beds, ash layers and sills (Fantín *et al.* 2014; Sosa *et al.* 2017). Each of the individual rock types are likely to have contrasting mechanical properties, which will likely affect how and if a fracture will propagate from one layer to the next.

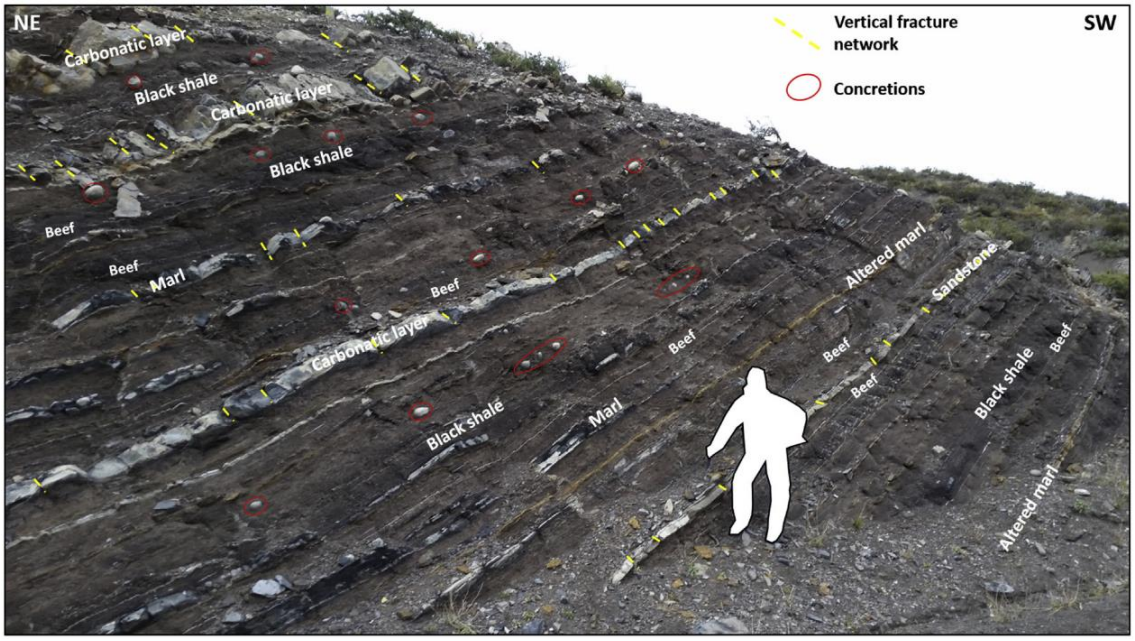

Figure 1: The Vaca Muerta formation at outcrop. The main target is the black shale. It is, however, interbedded with other units such as sandstone, marl and calcareous beds (indicated) and also ash layers and sills (not present at this outcrop). From Sosa *et al.* (2017) .

Not only is it important to understand how a fracture propagates through layered sequences in a petroleum geology sense, but it is also fundamental in other geological processes such as volcanology. Most volcanic eruptions occur only when a fluid-driven fracture, a dyke, is able to propagate through numerous crustal layers and interfaces, from its source magma chamber to the surface (Gudmundsson 2016). Thus, the mechanical conditions that allow a propagating dyke to successfully penetrate all the layers ahead of it rather than become arrested provide one of the main controls on whether an eruption occurs or not. Therefore, although the main focus of this thesis is on unconventional oil and gas reservoirs, many parts are relevant in other geological processes, and this is discussed in Chapters 5 and 6.

1.4 Fundamentals of Fracture Mechanics

In order to analyse fracture propagation in the cases above I have undertaken experimental and numerical modelling work, which is fundamentally underpinned by Griffith's

analysis (Griffith 1920) and the Linear Elastic Fracture Mechanics (LEFM) framework (Lawn 1993). Both of which are described below.

The theoretical (cohesive) strength of a rock can be expressed simply as the amount of energy or work required to break the atomic bonds within a material, and is expected to be approximately 10% of the Young's modulus of the material (Griffith 1920; Lawn 1993). However, the tensile strength of many brittle materials is known to be 0.1-1% of their Young's modulus. Realising this, Griffith (1920) postulated that the reason for this discrepancy was due to the existence of micro-cracks (so called Griffith flaws) within a material which act as stress concentrators, and it is the intensified stress at the tip of these Griffiths flaws that overcomes the local fracture resistance and allows cracks to nucleate and propagate. Griffith's work was based on that of Inglis (1913) who demonstrated that cavities or notches in a material can act to magnify stresses near their tips. He then extended the analysis using an energy based approach to explain the theoretical propagation of a pre-existing crack in a brittle material subjected to external loading (Griffith 1920; Lawn 1993), Figure 2A. Griffith's concept is based on the idea that the total energy of the system, U_T, is composed of mechanical energy of the system (which includes the elastic strain energy of the system but also the work associated with any displacement of the loading points), U_M, and the surface energy associated with the free surfaces of the pre-existing crack and that of any new surfaces created through crack extension, U_S. For a crack of length $2a$ U_M is defined as:

$$U_M = -\frac{\pi\sigma^2 a^2}{E} \tag{1}$$

Where σ is the remotely applied stress, a is the half crack length and E is the Young's modulus of the material. A decrease in U_M is associated with the extension of the crack, hence the negative sign in equation (1). For the same crack U_S is defined as:

$$U_S = 4a\gamma \tag{2}$$

Where γ is the free surface energy per unit area of the crack. Therefore, from the first law of thermodynamics, U_T is defined as:

$$U_T = -\frac{\pi\sigma^2 a^2}{E} + 4a\gamma \tag{3}$$

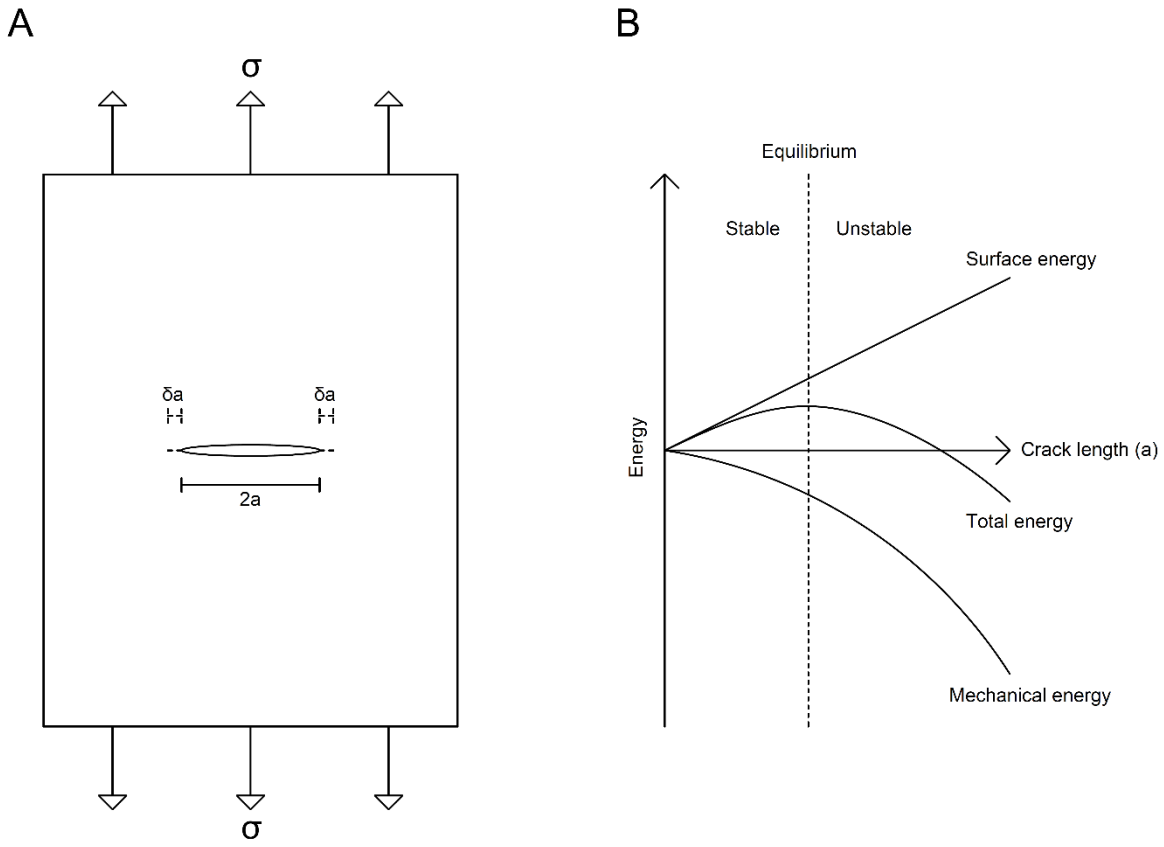

Figure 2: (A) Griffith static crack model for crack propagation where σ is the applied stress, *a* is the half crack length and *δa* is the length of crack extension. (B) Graphical representation of the Griffith energy balance.

Figure 2B is a graphical representation of equations (1) – (3) in terms of energy and crack length, *a*. As a crack extends initially there is an increase in the total energy of the system which relates to a period of stable crack growth i.e. energy needs to be put in to the system in order for the crack to grow. However, after a certain amount of crack extension there is a point at which there is no change in total energy and thereafter the decrease in mechanical energy overcomes the increase in surface energy, which leads to unstable crack growth i.e. no more energy input is required to extend the crack and so it is self-propagating. At this critical point, where the system is in equilibrium:

$$\frac{dU_T}{da} = 0 \tag{4}$$

And so:

$$-\frac{\pi\sigma^2 a}{E} + 4\gamma = 0 \tag{5}$$

This can then be re-written as:

$$\sigma_f = \sqrt{\frac{2E\gamma}{\pi a}} \tag{6}$$

Where σ_f is referred to as the fracture stress (i.e. the critical stress at which unstable fracture propagation occurs for a given fracture length a).

LEFM uses linear elastic theory to quantify the combination of an applied stress with a particular crack geometry that results in crack extension. Therefore it extends the Griffith analysis to be able to be able to provide a solution for general crack problems and different loading configurations. In analysing fracture propagation within the LEFM framework, there are three fundamental modes of crack tip displacement (Figure 3) (Atkinson 1987; Gudmundsson 2011). In mode-I, the fracture surfaces move directly apart, and it is therefore referred to as tensile or opening mode. In mode-II, the fracture surfaces shear over one another in a direction parallel to fracture propagation, so this is referred to as

sliding mode or in-plane shear. Finally, in mode-III, the fracture surfaces shear over one another in a direction perpendicular to fracture propagation, so this is referred to tearing mode or anti-plane shear.

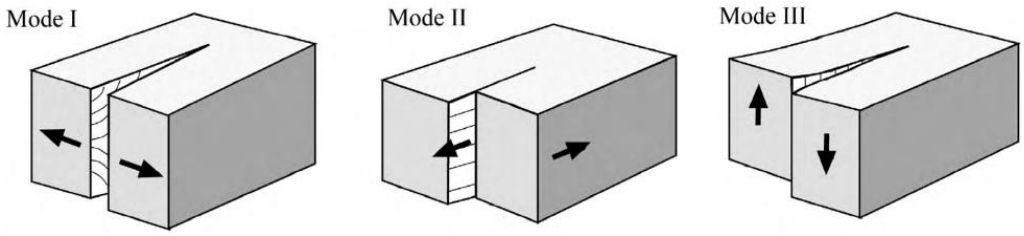

Figure 3: The ideal modes of displacement for fractures – mode-I, mode-II and mode-III. From Gudmundsson (2011)

Before taking these three modes into account it is necessary to rearrange equation (6) to:

$$\sigma\sqrt{\pi a} = \sqrt{2E\gamma} \tag{7}$$

Note how equation (7) does not include the fracture stress, but rather the remotely applied stress so that it applies to loading in a general sense rather than at the critical value. $\sigma\sqrt{\pi a}$ is called the stress intensity factor, K, and the critical value of K (i.e. $\sigma_f\sqrt{\pi a}$) is called the fracture toughness, K_c. Fracture toughness is a material property, and is a measure of a materials resistance to dynamic fracture propagation. K can be split into the three different modes of displacements, K_I, K_{II} and K_{III}, and therefore there are critical values of each of these stress intensities i.e. K_{Ic}, K_{IIc} and K_{IIIc}. Hydraulic fractures are predominately mode-I fractures and therefore my analysis mainly concerns K_{Ic}. However, as will be discussed in Chapter 3 and Chapter 6, if a fracture is mixed-mode its propagation will be controlled by some combination of K_I, K_{II} and K_{III}, none of which may reach their respective critical

value. Therefore, under these circumstances it is better to use a fracture energy based approach to analyse fracture propagation.

Fracture energy, G_c, is the critical value of the energy release rate, G, which again is based on the Griffith analysis and by manipulating equation (7) is defined as:

$$G = 2\gamma = \frac{\sigma^2 \pi a}{E} \tag{8}$$

Again, note that this considers the remotely applied stress rather than the fracture stress. For the critical case and by substituting K_c into equation (8) it becomes:

$$G_c = \frac{K_c^2}{E} \tag{9}$$

for plane stress conditions, or:

$$G_c = \frac{K_c^2 (1 - \upsilon^2)}{E} \tag{10}$$

for plane strain conditions, where v is Poisson's ratio. Fracture energy is a measure of how much energy is required to propagate a fracture dynamically, and is again a material property.

1.5 Study Area

In this study I measure and analyse physical and mechanical properties of a shale and limestone from the Porthkerry Formation outcropping at Nash Point, South Wales (Figure 4 and Figure 5). The Porthkerry formation is Hettangian-Sinermurian in age, and at Nash Point the sequence is comprised of interbedded shales and limestones, thus providing a good opportunity to study a layered sequence that may be analogous to other layered geological sequences generally. Based on vitrinite reflectance data the Porthkerry Formation is considered to have reached a maximum burial depth of 3.2 km during the Aptrian (Cornford 1986). A full description of the individual rock types are given in Chapters 3 and 4. However, for context, a brief description of both are given below.

Figure 4: Map of Wales, indicating the location of Nash Point but also Cardiff for reference.

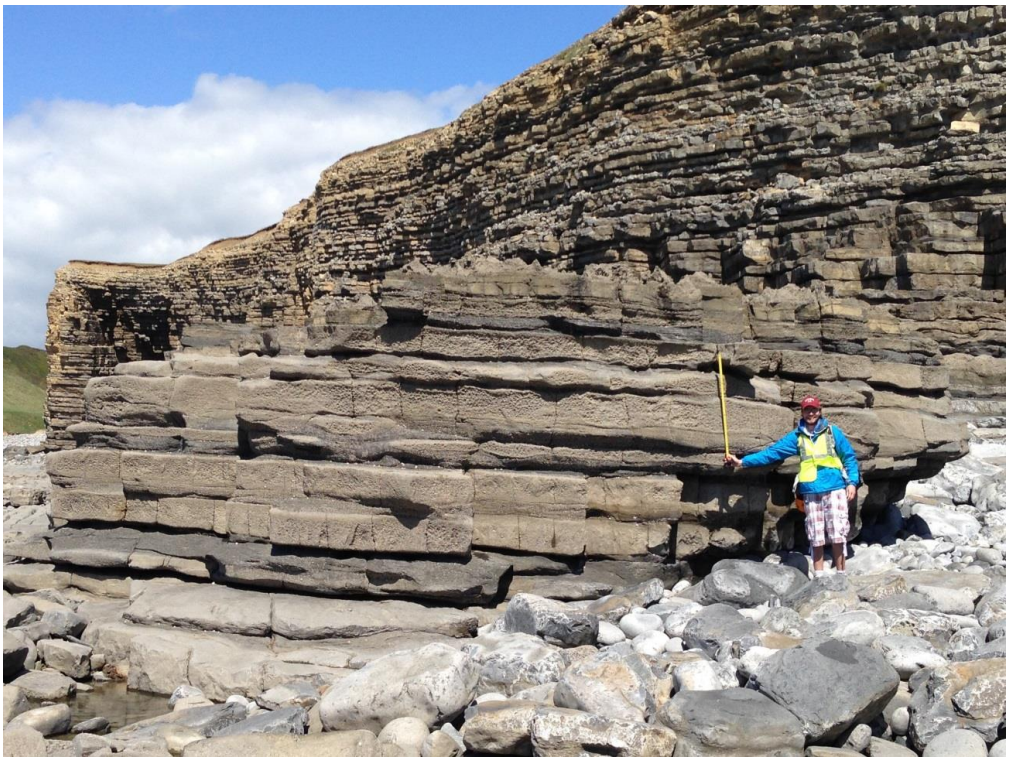

Figure 5: Outcrop at Nash Point demonstrating the interbedded shale and limestone sequence, whereby the light-coloured units are limestone and the darker units are shale. Note how there is a different weathering profile between the two units, the shales being more recessive.

Figure 6: Close up photograph showing the two rock units, again where the limestone is the lighter coloured of the two and the shale is the darker. Note how the limestone appears to be more massive in nature, while the shale is laminated. The limestone beds in this photograph are approximately 50 cm thick.

1.5.1 Nash Point shale

In terms of mineralogy Nash Point shale is somewhere in between a calcareous mudstone and a marly limestone, as it is composed predominately of calcite (50-70%) with lesser amounts of clay (20-30%) and quartz (10-20%). It has a porosity of ~6.5% and is composed mainly of shell fragments ranging from approximately 0.1 – 4 mm in length. It was found that Nash Point shale is highly anisotropic in terms of its mechanical properties, which is largely governed by the planar fabric of the material.

1.5.2 Nash Point limestone

Nash Point limestone is also composed predominately of calcite (>90%) with lesser amounts of quartz (5-7%), clay and other trace minerals (<3%). It has a porosity of ~1% and again is composed mainly of shell fragments ranging from approximately 0.1 – 3 mm in length. It was found that Nash Point limestone is essentially isotropic in terms of its mechanical properties, which is due to a lack of any preferential orientation of the grains within the material.

1.5.3 An analogue to other reservoirs?

1.5.3.1 Nash Point shale

Whilst Nash Point Shale is not a pure shale petrologically, it does share many of the features of other well-known gas-shales, which makes it a suitable analogue. In particular it's very similar to the Eagle Ford shale formation (Texas, USA), which is a major unconventional oil and gas play. The mineralogy of Eagle Ford shale has been studied by numerous authors (including, Chalmers & Bustin, 2017; Elston, 2014; Knorr, 2016; Milliken, Ergene, & Ozkan, 2016; Mokhtari, 2015; Mullen, Lowry, & Nwabuoku, 2010), and the same general mineralogy is observed, with Eagle Ford shale also being dominated by calcite with lesser amounts of clay, and quartz. For means of comparison, Chalmers and Bustin (2017) found that Eagle Ford shale contained 32-87% calcite (average of 57%), 2-38% clay (average of 17%), and 6-20% quartz (average of 14%). Porosities were

found to be between 3.5 – 10.3%, with an average value of 7.5%. In contrast, other oil and gas shales are more quartz rich, such as the Bowland shale, Posidonia shale, Barnett shale, Marcellus shale and Mancos shale (Table 1). However, in each of these cases there are still similarities with Nash Point shale in terms of porosity, permeability and TOC, and a comparison of Nash Point shale to other oil and gas shales in terms of mineralogy, porosity, permeability and TOC is given in Table 1.

Although the absolute values presented in Chapter 3 are likely directly relevant to mainly calcareous mudstones, most shales (and certainly the ones listed in Table 1) are known to be anisotropic which is due to the strong alignment of the grains within the material. As such, the method by which to characterise anisotropy in Chapter 3 and the general findings within are still considered valid for shales of different mineralogies.

Table 1: Compilation of petrological, petrophysical and geochemical data of oil and gas bearing shales from around the globe, and Nash Point shale. Data for Nash Point shale is from this study, apart from the permeability which is from Gehne (2018) and the TOC which Arzani (2004) measured from shales on the opposite side of the Bristol Channel of the same age and depositional environment. Data for the other shales are from the following sources: Klaver *et al.* (2012); BGS (2013); Gentzis (2013); Chandler (2014); Fantín *et al.* (2014); Heller *et al.* (2014); Lee (2015); Cuervo *et al.* (2016); Houben *et al.* (2016); Chalmers & Bustin (2017); Gehne (2018); Herrmann *et al.* (2018).

	Location	**Average clay content (%)**	**Average carbonate content (%)**	**Average quartz content (%)**	**Porosity (%)**	**Permeability (m^2)**	**TOC (%)**
Nash Point shale	UK	25	60	15	5 – 8	10^{-18} – 10^{-20}	1 – 6
Eagleford shale	USA	17	57	14	4 – 10	10^{-19} – 10^{-20}	1 – 7
Bowland shale	UK	6	21	74	5 – 10	NA	1 – 8
Posidonia shale	Europe (Whitby mudstone is the UK equivalent)	63	8	27	1 – 7	10^{-19} – 10^{-21}	1 – 15
Barnett shale	USA	39	14	45	1 – 12	10^{-20} – 10^{-22}	3 - 8
Marcellus shale	USA	52	1	38	0 – 18	10^{-20} – 10^{-21}	1 – 20
Mancos shale	USA	33	17	39	3 – 6	NA	1 - 3
Vaca Muerta	Argentina	23	34	22	7 – 13	NA	3 – 8

1.5.3.2 Nash Point limestone

A full comparison of Nash Point limestone to other limestones is presented in Chapter 4. However, for context, Nash Point is essentially isotropic in terms of its microstructure which is similar to many other limestones (Dibb *et al.* 1983; Gunsallus & Kulhawy 1984; Atkinson 1987; Nath Singh & Sun 1990; Guo *et al.* 1993; Khan & Al-Shayea 2000; Aliha *et al.* 2012; Cicero *et al.* 2014; Helmer *et al.* 2014). It also has a very low porosity (~1%) which is similar to some carbonate reservoirs, such as the hydrocarbon bearing section of the Bangestan Group in Iran which Dashti *et al.* (2018) measured to have ~3% porosity. Petrophysically, Nash Point limestone is more analogous to very low porosity carbonate reservoirs, however, as discussed in Chapter 4, its fracture properties (tensile strength and fracture toughness) are comparable to that of other limestones where data is available (Dibb *et al.* 1983; Gunsallus & Kulhawy 1984; Atkinson 1987; Nath Singh & Sun 1990; Guo *et al.* 1993; Khan & Al-Shayea 2000; Aliha *et al.* 2012; Cicero *et al.* 2014; Helmer *et al.* 2014). Although it is accepted that an increase in porosity generally relates to a decrease in strength and fracture toughness (Al-Harthi *et al.* 1999; Palchik & Hatzor 2004; Sabatakakis *et al.* 2008; Heap *et al.* 2009, 2014; Lian *et al.* 2011; Meille *et al.* 2012; Schaefer *et al.* 2015; Bubeck *et al.* 2016), the pore geometry is also important to consider (Bubeck *et al.* 2016). Carbonates are known to have a complex pore system (Tucker 2001; Tucker & Wright 2009; Haines *et al.* 2016; Rashid *et al.* 2017) and although the same general trend between porosity and strength is expected to exist, it is likely to be more complex than for other rocks containing comparatively simpler pore systems. Although it warrants further study, analysis of how porosity and pore networks in carbonates affect their fracture properties falls outside the scope of this thesis.

1.5.3.3 Nash Point as a layered sequence

Although the target in many unconventional reservoirs are organic rich shales, they are often interbedded with other lithologies, forming a layered sequence. Thus in stimulating

such reservoirs hydraulic fractures must cross the sequence as a whole, and therefore it is important to understand what affect the layering has on hydraulic fracture propagation. Examples of unconventional reservoirs include the Khazzan tight gas field in Oman (Sandstones interbedded with shales) (Shueili *et al.* 2016), the Woodfard shale in the USA (Shales interbedded with siltstones and chert beds) (Galvis *et al.* 2017), the Eagle Ford shale in the USA (Shales interbedded with limestones and chalk beds) (Mullen *et al.* 2010; Ferrill *et al.* 2014; Knorr 2016) and the Vaca Muerta formation in Argentina (Shales interbedded with sandstones, marls, calcareous beds, ash layers and sills) (Fantín *et al.* 2014; Sosa *et al.* 2017). Although each of these examples are different stratigraphically, it is the contrast in mechanical properties between the different lithologies (along with in-situ stress conditions) which control fracture propagation across the sequence (Teufel & Clark 1984; Cooke & Underwood 2001; Kavanagh *et al.* 2006; Gudmundsson 2011; Barnett & Gudmundsson 2014). As such, analysing how fractures may propagate across the sequence at Nash Point is analogous to how fractures propagate across a layered sequence (where the layers have contrasting mechanical properties) in a general case, and this is discussed extensively in Chapters 5 and 6. Furthermore, the sequence at Nash Point may be directly relevant to both the Eagle Ford and Vaca Muerta formation examples, as all three are sequences comprised of interbedded calcareous shales and carbonate facies. This would also be the case for other formations containing significant amounts of calcareous shales.

1.6 Experimental campaign

As hydraulic fractures are predominately mode-I fractures, in order for a hydraulic fracture to propagate at depth, both the tensile strength of the rock and the minimum principal compressive stress, σ_3 must be overcome (Gudmundsson 2011; Browning *et al.* 2015). However, it is also well-known that many rocks exhibit some form of mechanical

anisotropy and, in turn, this is expected to exert a significant influence on directional fracture propagation. Shales, for example, are known to be highly anisotropic, and usually transversely isotropic, where the axis of rotational symmetry is perpendicular to the bedding plane (Lee *et al.* 2015; Chandler *et al.* 2016; Forbes Inskip *et al.* 2018). Therefore, it is important to understand how this anisotropy may affect fracture propagation in reservoirs comprised largely of anisotropic rocks such as shales. When considering fracture propagation in a layered medium, we define three principal fracture orientations with respect to the bedding (anisotropy) plane – the Short-transverse, Arrester and Divider orientations (Figure 7):

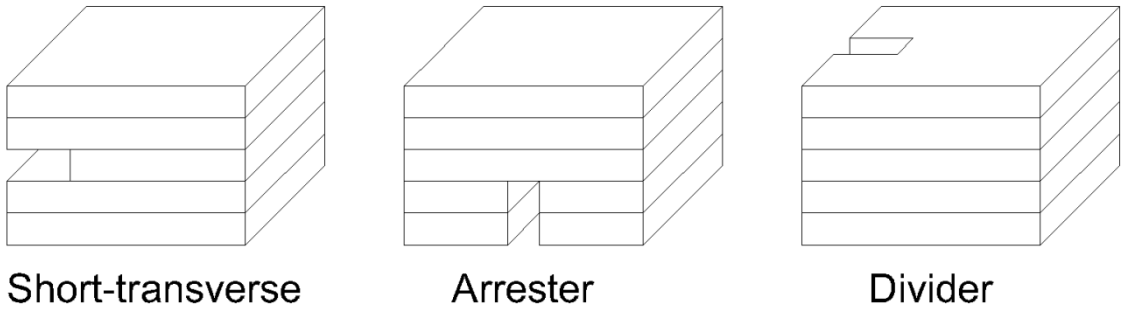

Figure 7: The three principal fracture orientations with regard to bedding planes: Short-transverse, Arrester and Divider. Modified after Chong *et al.* (1987)**.**

In the Short-transverse orientation both the fracture plane and the fracture propagation direction are parallel to bedding. Conversely, in the Arrester orientation both the fracture plane and the fracture propagation direction are normal to bedding. Finally, in the Divider orientation the fracture plane is normal to bedding while the fracture propagation direction is parallel to bedding.

In brittle materials such as rocks, and anisotropic rocks in particular, tensile strength measurements may not be very repeatable as they are dependent on the size and distribution of flaws within a sample, which is likely to vary due to the heterogeneous

nature of many rocks (Tavallali & Vervoort 2013; Perras & Diederichs 2014; Na *et al.* 2017; Forbes Inskip *et al.* 2018). As such, a more rigorous parameter to use to characterise a material's resistance to mode-I fracture propagation is the mode-I fracture toughness, K_{Ic}, (Lawn 1993). This is because K_{Ic} takes into consideration both the flaw size and the remotely applied stress. Although a few studies have tried to quantify anisotropy in terms of K_{Ic}, these have all been constrained to measuring K_{Ic} only in the three principal fracture orientations (Schmidt 1977; Chandler *et al.* 2016; Kabir *et al.* 2017) or, in the case of Lee *et al.* (2015) at one orientation between the principal fracture orientations. Therefore, one of the main aims of this project has been to conduct a systematic study of how K_{Ic} varies as a function of azimuth between the principal orientations in Nash Point shale. As far as I am aware of this is the first systematic study of how K_{Ic} varies between these principal orientations in shale, or indeed in any rock. This work is the focus of Chapter 3.

As such, where possible I have measured the mechanical properties of both rocks, Nash Point shale and Nash Point limestone, in each of the three principal orientations but also in the case of Nash Point shale at angles between the Short-transverse and the Arrester. Below is table summarising what experiments I have carried out and in what orientations they have been carried out in:

Table 2: Details of each of the mechanical properties measured as part of this study and the tests used to measure these properties. *Length in these cases refers to the thickness of the sample as described in Chapter 2. **It was not possible to obtain K_{Ic} values for Nash Point shale in the Arrester orientation using the Short-rod technique, and this is discussed in Chapter 6. Full details on how each of these tests are carried out are given in Chapter 2.

Mechanical property/properties being measured	**Type of test**	**Diameter of sample (mm)**	**Length of sample (mm)**	**Orientation tested**	
				Nash Point shale	**Nash Point limestone**
Ultrasonic wave velocities (Also used to calculate the dynamic Young's modulus)	Pulse transmission method	38	38	Radially every 10°	Radially every 10°
Static elastic properties (Young's modulus and Poisson's ratio)	Uniaxial Compressive Strength (UCS) test technique	25	62.5 – 75	Normal and parallel to bedding	Normal and parallel to bedding
Tensile strength	Brazil disk test technique	38	19*	Each of the three principal fracture orientations but also every 15° between the Short-transverse and the Arrester	Each of the three principal fracture orientations

Mode-I fracture toughness (K_{Ic})	Semi-circular Bend (SCB) technique	76	30*	Each of the three principal fracture orientations but also every 15° between the Short-transverse and the Arrester	Each of the three principal fracture orientations
Mode-I fracture toughness (K_{Ic})	Short-rod (SR) technique	60	89	Each of the three principal fracture orientations**	Each of the three principal fracture orientations

1.7 Aims

The aims of the overall thesis are to answer the following questions:

1. How does mechanical anisotropy within a rock unit affect fracture propagation?
2. How does large-scale heterogeneity, in particular mechanical layering, affect fracture propagation across a layered sequence?

1.8 Thesis outline

This thesis is submitted in the alternative format, and includes manuscripts which are at different stages in the publication process. Chapter 3 has already been published (Forbes Inskip *et al.* 2018) and Chapter 5 has been submitted to Scientific Reports. These chapters contain their own introduction, methodology, results, discussion and conclusions. Chapter 4 is also written in this format because it is my intention imminently to submit it to the Journal of Rock Mechanics and Rock Engineering. However the methodology in Chapter 4 does not stand alone, but rather references the Methodology chapter of this thesis (Chapter 2) in order to avoid repetition.

Below is an outline summary of the thesis organisation:

Chapter 2 – Methodology.

Chapter 3 – "Fracture properties of Nash Point shale as a function of orientation to bedding" (Journal of Geophysical Research: Solid Earth). The work here includes a systematic study of the mechanical anisotropy of Nash Point shale and how this may affect fracture propagation.

Chapter 4 – "Characterising the fracture properties of Nash Point limestone" (Manuscript to be submitted to the Journal of Rock Mechanics and Rock Engineering) –

The work here includes a systematic study of the mechanical anisotropy of Nash Point limestone and how this anisotropy may affect fracture propagation.

Chapter 5 – "Propagation and arrest of fractures in layered rock sequences" (Submitted to Scientific Reports). This is a numerical modelling study of how propagating fractures may be affected by mechanical layering in the crust using the Finite Element Method.

Chapter 6 – Critical Evaluation and Discussion. This chapter includes a critical evaluation of the methods used for this thesis, and brings together the results of Chapters 3-5 to better understand how fractures propagate through layered sequences.

Chapter 7 – Conclusions and further work

2 Methodology

2.1 Field data and sample collection

Blocks of shale and limestone were collected at Nash Point, South Wales (Figure 9) in the years 2015 and 2016. All sample blocks were taken from the same bed for each rock type (i.e. shale blocks from one shale bed and limestone blocks from one limestone bed).

The outcrop at Nash Point is heavily jointed, and so it was determined that the easiest way in which to collect samples would be to lever out blocks of material by use of a crowbar forced into the joints. It was relatively easy to lever out whole blocks of limestone as it is very competent. By contrast, collecting shale samples was much more problematic. As can be seen in Figure 6, Nash Point shale is laminated and consequently contains bedding plane fractures which are laterally extensive. In the field it is almost impossible to detect these fractures until a block has been levered out, at which point the block would sometimes fall apart along these planes of weakness. Hence, most material was collected from the more competent sections and may not always be fully representative of the shale sequence as a whole. This is a common occurrence, as is also reported in other studies (Chandler 2014; Lee 2015).

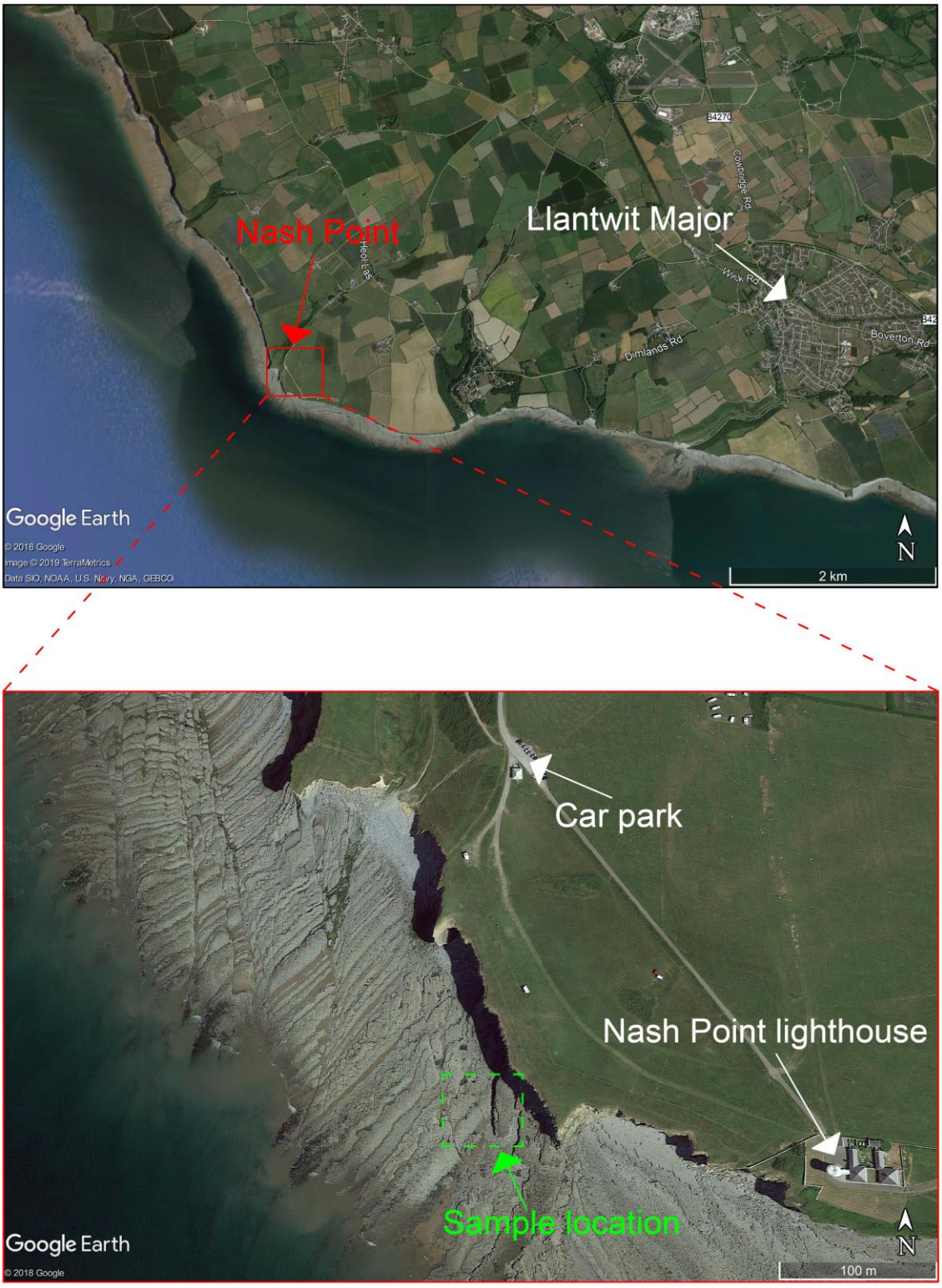

Figure 8: Location of where samples were taken from over the course of the project

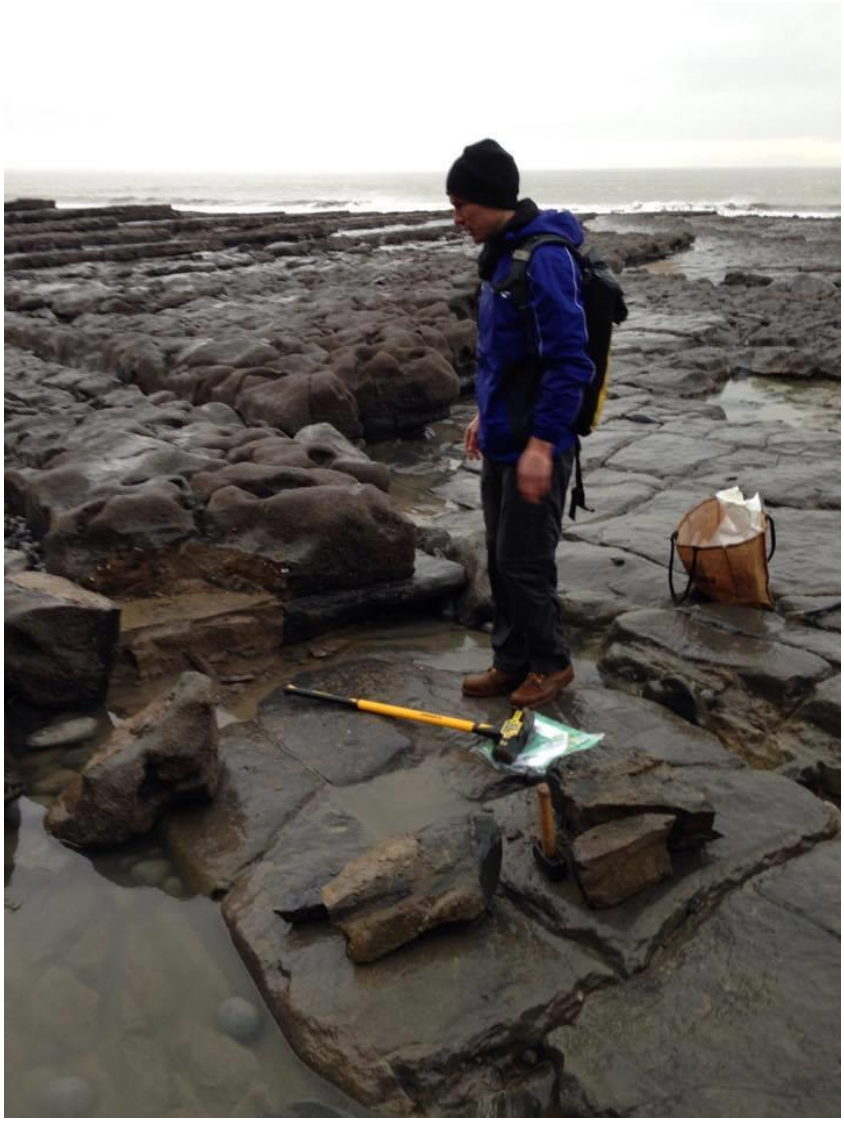

Figure 9: Collecting samples from shale and limestone beds at Nash Point, South Wales

2.1 Experimental methodology

2.1.1 Sample preparation

Samples were brought back to the Rock Preparation Laboratory at UCL, where samples were manufactured to the specific dimensions for the test methods described in the following sections As each of the different tests require a different sample size, the description given below is generic, and the specific dimensions are given in the descriptions of the relative test protocols.

The bedding planes were marked on all of the blocks prior to cutting and coring required to produce samples of suitable size for experimental measurements (Figure 10). For simplicity, the bedding planes were marked as continuous, parallel lines. However, it is noted that, in reality, there will be some slight variation from this. Different sized diamond coring drill bits were used to produce cores of the appropriate diameters for the specific experiments outlined below.

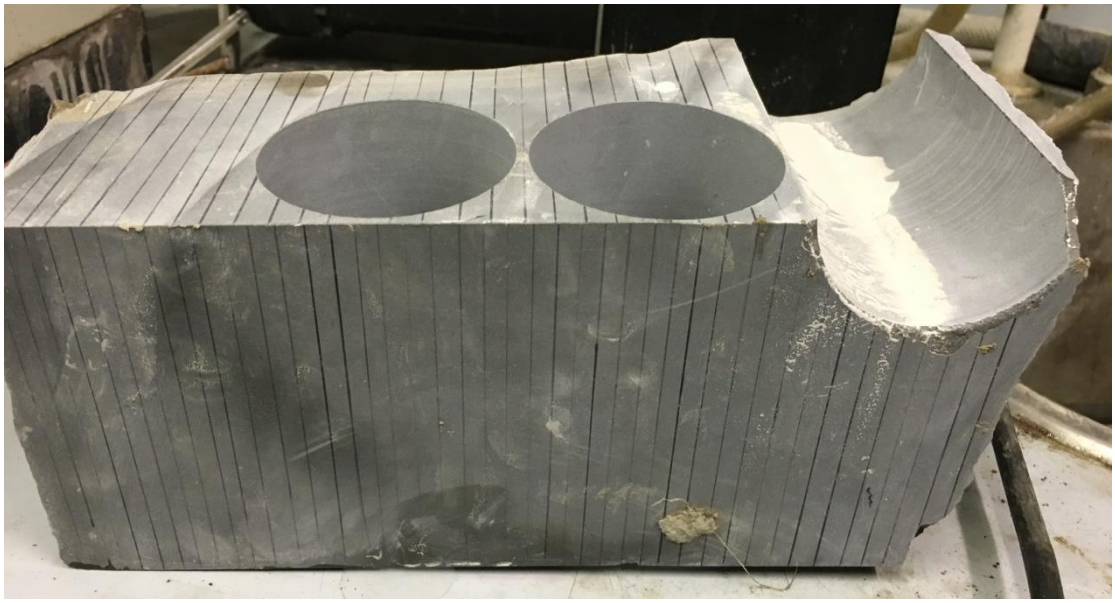

Figure 10: Limestone block collected from Nash Point. Here the bedding plane is marked by a series of black parallel lines prior to coring. The holes in the figure are approximately 64 mm in diameter, and produced core samples of 60 mm diameter.

Once a core had been drilled, the lines delineating the bedding planes were translated from the ends of the core to the sides. Cores were then cut to the desired length or using a rotary diamond saw, and ground flat and parallel to the desired thickness using a surface grinder with a diamond-impregnated grinding wheel. Again, the lines depicting the bedding plane were translated throughout sample preparation. Following this process, the samples are ready for testing (unless further preparations, such as cutting notches, were required for a particular test). As both rock types are fine grained, have low permeability

(Gehne 2018) and in the case of Nash Point limestone have very low porosity, it is reasonable to assume that the cooling fluid used during sample preparation is unlikely to permeate the samples, during the relatively short preparation time, enough to significantly affect any testing results. Therefore, no special drying of the samples was considered necessary.

Preparing samples of Nash Point limestone was relatively straightforward due to the limestone's competent nature. In contrast, preparing samples of Nash Point shale was problematic for the same reason that it was difficult to retrieve blocks of material from the field, namely that the samples would sometimes break apart along pre-existing weaknesses. In some instances, although the block was clamped securely, the vibrations caused by the coring process would open up any pre-existing fracture and this could lead to the block splitting into such small pieces that no useable samples could be made. I tried to minimise this by first making careful visual inspection of water dampened blocks prior to coring. Water dampening helps to reveal the pre-existing macro-fractures because water absorption into pre-existing fractures leads to a temporary colour change (darkening). Cores were then only taken from sections of blocks that had not revealed any pre-existing fractures, although sometimes this method still did not reveal all pre-existing fractures. Despite my best efforts many samples broke apart during preparation, and therefore samples were made from the more competent sections, and may not always be fully representative of the shale sequence as a whole. Furthermore, due to this issue several trips to the outcrop were required to obtain material, and consequently the experimental part of this PhD project took considerably more time than originally anticipated.

While I encountered problems with samples failing along pre-existing weaknesses, I did not experience some of the problems encountered by others (Chandler 2014; Lee 2015) in terms the shale samples expanding during coring as a result of the cooling fluid reacting

with swelling clays (such as smectite) within the material. Although I conducted XRD analysis to quantify the mineralogy of both Nash Point shale and Nash Point limestone (presented in Chapters 1, 3 and 4), I did not conduct clay separation analysis to determine the individual clay portions. However, based on this observation it is unlikely that smectite exists in any significant quantity in either Nash Point shale or Nash Point limestone.

2.1.2 Ultrasonic wave velocity measurements

Ultrasonic wave velocities were measured through shale and limestone cores of 38 mm x 38 mm (thickness x diameter), drilled both parallel and normal to bedding. This method was used to quantify the anisotropy of both lithologies. Measurements were initially taken both normal and parallel to bedding, and if the values were within 4% of each other the lithology was considered essentially isotropic. If the difference was greater than 4%, then circumferential measurements were taken in 10° angular increments between the bedding normal and bedding parallel orientations in order to quantify the amount of anisotropy. 4% was used as a threshold because the accuracy of picking the first arrival of ultrasonic waves using this set-up is considered to give errors between 1-4% (Vinciguerra *et al.* 2005). Measurements were taken on at least two cores in each orientation of each lithology.

Samples were mounted in a spring-loaded testing jig that ensured consistent contact of the measuring transducers with the sample (Figure 11). A JSR DPR300 35MHz Ultrasonic pulse generator was then used to excite a Panametrics V103 P-wave transmitting transducer (0.5 inch diameter piezoelectric element with 1 MHz resonant frequency) at one side of the sample. Waveforms passed through the sample and excited an identical receiving transducer at the opposite side of the sample. Received waveforms were captured and displayed on an Agilent Technologies 1.5 GHz 'Infiniium' digital oscilloscope (Figure 11).

Here the time difference between the initial pulse and the first arrival was measured as the P-wave travelled through the sample (Figure 11). This procedure was repeated again but with polarised S-wave transducers, in order to measure the travel time for a S-wave to cross the sample.

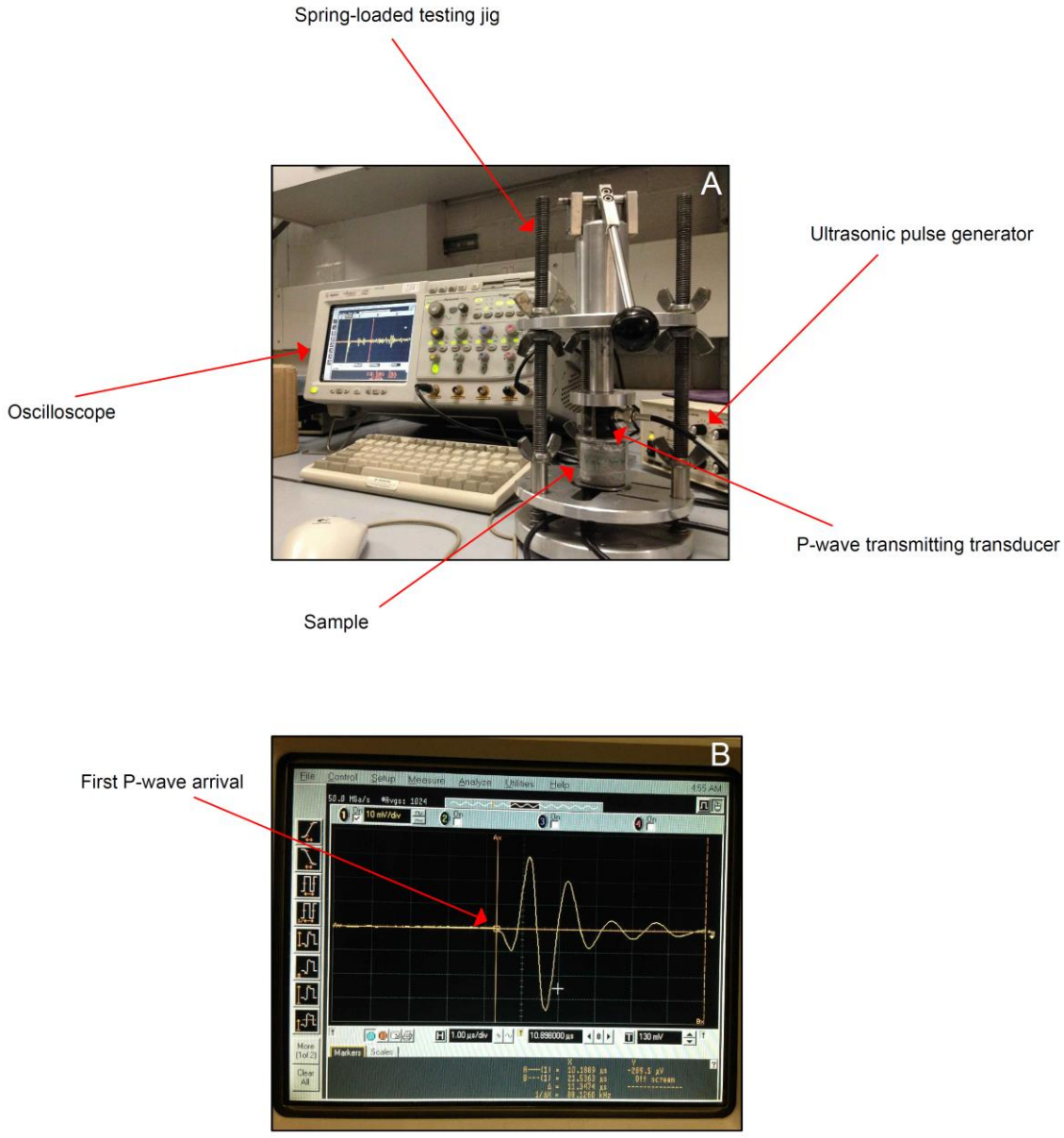

Figure 11: Set-up used for measuring ultrasonic velocities (A). Picking the first arrival to measure the travel time for a P-wave to cross the sample (B), where the x-axis is time (μs) and the y-axis is amplitude (mV).

Unfortunately, picking of the first arrival was considerably more difficult for the S-wave than for the P-wave. The main problem was that as the S-wave travels through the sample there is a mode conversion as it crosses the interfaces within the sample and a subsequent P-wave is created (Figure 12) (Modi *et al.,* 2016). As P-waves travel at a higher velocity than S-waves, they reach the receiving transducer first and so mask the onset of the first S-wave (Figure 12). However, as the amplitude of the S-wave arrival is expected to be significantly greater than that of the converted P-wave, it is usually possible to pick the S-waves peaks with confidence. Then as the sample is rotated to measure the anisotropy, the first S-wave peak can be measured as a function of azimuth. At some angles it may be clear as to when the first S-wave first arrives at the receiving transducer, and then this time should be noted down and the difference in time between the first peak and the onset measured. This difference in time is then subtracted from the travel time for the first peak for other angles of rotation of the sample so that the true S-wave velocity can be calculated. Another problem that was encountered was that shear wave splitting occurred when S-waves were transmitted through the sample at high angles to bedding (Radi *et al.,* 2015). This was more of a problem when measuring S-waves across the shale due to its greater anisotropy. Due to these problems there is a greater uncertainty when picking the arrival of the first S-wave across the sample measurements, however errors are still considered to be less than 4% (Vinciguerra *et al.* 2005).

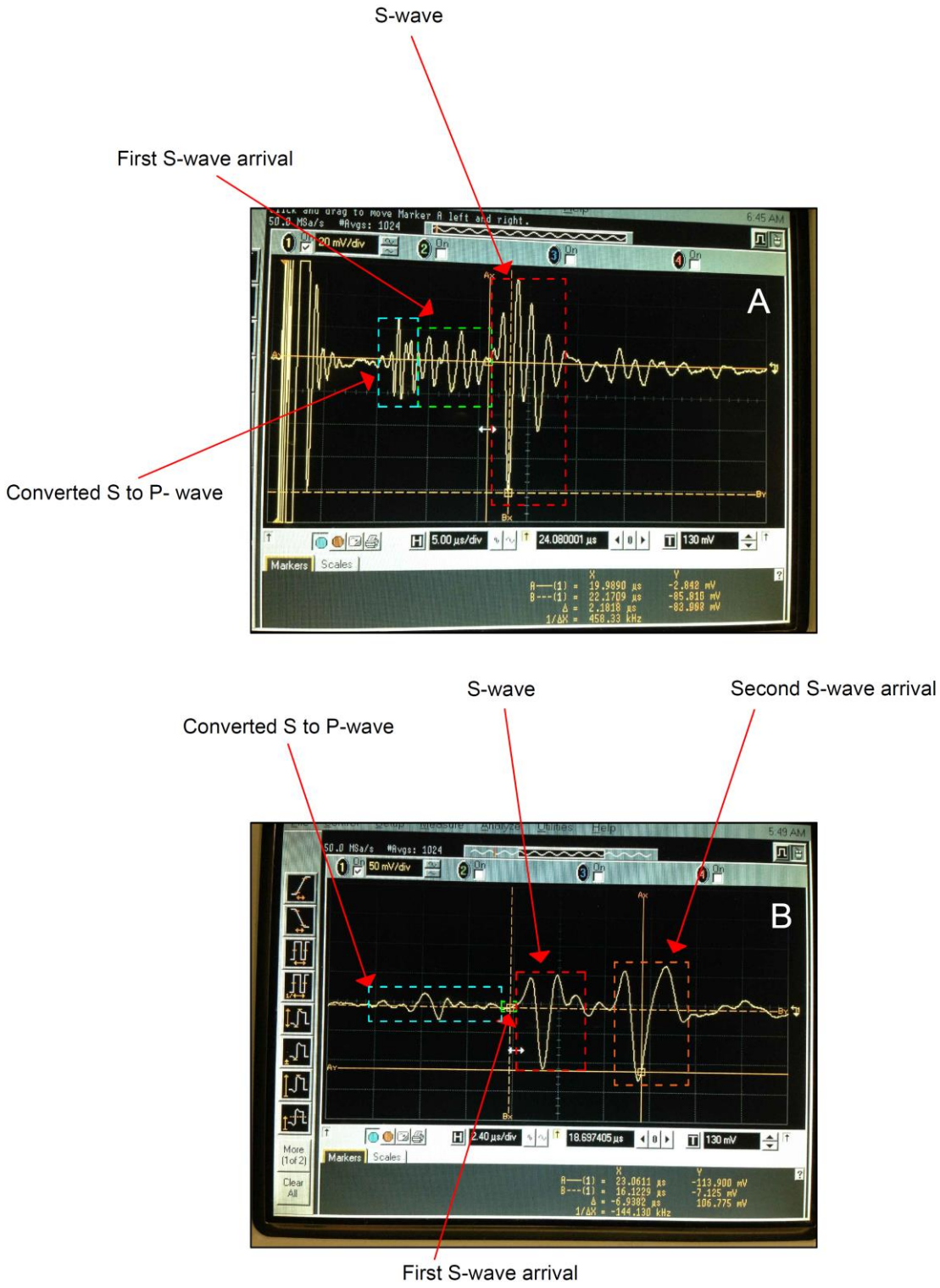

Figure 12: Picking the onset of the S-wave (A and B), where the x-axis is time (μs) and the y-axis is amplitude (mV). The blue boxes represent an area of a converted S to P-wave, the green boxes represent the area which could include the first onset of the S-wave and the red boxes represent an area of a S-wave. Example of possible shear wave splitting is shown in B, where the orange box is the second S-wave to arrive. Note how the area of possible onset of the first S-wave, the green box, is significantly smaller here, so that there is greater confidence in picking it. Furthermore, note how the peak of the second S-wave

arrival is larger than the first. At high angles (80°-100°) the first peak disappears and only the slower (second) S-wave is recorded.

Ultrasonic wave velocities are then calculated from the measured travel time for P and S-waves to cross the sample. Furthermore, I also measured the P-wave velocities of each sample prior to testing (i.e. tensile strength and fracture toughness samples) and compare these values to the values obtained from the baseline anisotropy measurements as described above. This was to check for any significant variability in the samples. Although these values are not presented in this thesis all the samples tested had P-wave velocities within 5% of the baseline measurements.

2.1.3 Uniaxial compressive strength test

The Uniaxial Compressive Strength (UCS) test is described by Bieniawski & Bernede (1979). For this study, it was used primarily to measure the static Young's modulus and Poisson's ratio.

Young's modulus is a measure of a material's stiffness, i.e. resistance to strain. If a material has a low Young's modulus it is considered compliant, whereas if it has a high Young's modulus it is considered stiff (Gudmundsson 2011). Poisson's ratio is the ratio of the lateral contraction or expansion to the axial expansion (elongation) or contraction of a material. Both of these are important elastic parameters or 'constants' when considering how fractures may propagate through a material.

Cylindrical samples with a diameter of 25 mm and of a length at least 2.5-3 times greater than the diameter (62.5-75 mm) were prepared in the same way as described previously. The UCS tests were carried out at the Rock Mechanics Laboratory at the University of Portsmouth, using an Instron 60 tonne uniaxial press. Samples were loaded uniaxially at a strain rate of 10^{-5} s^{-1} (Figure 13). This allowed for the sample to fail within 5-10 minutes

as recommended in the ISRM suggested method (Bieniawski & Bernede 1979). Corrections were applied before testing was conducted to account for deformations of the loading train and thus correct for its stiffness (This includes the machine but also the top and bottom end caps as demonstrated in Figure 13).

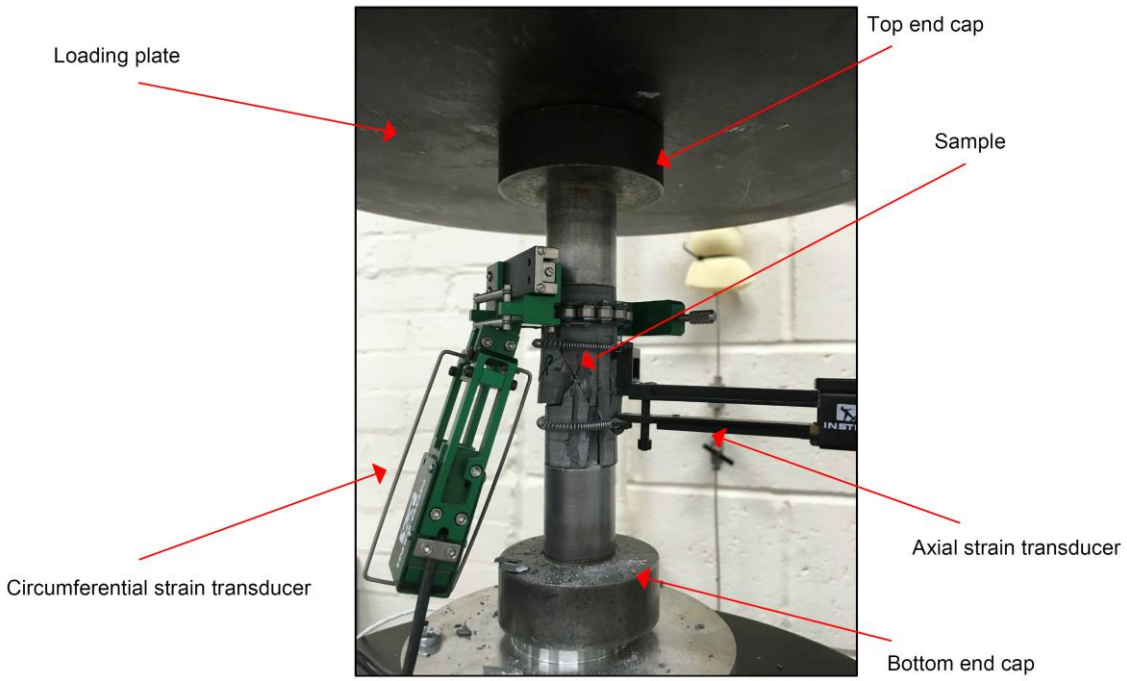

Figure 13: UCS test set up. Here the experiment has been run and the 75 mm long sample has failed. The green strain transducer on the left measures the circumferential displacement, while the black clip transducer on the right measures the axial displacement.

A load cell records the axially applied force, whereas axial strain is measured over a known gauge length by means of a clip transducer secured to the central section of the sample so as to obviate any end effects. Axial strain (ε_a) is calculated by:

$$\varepsilon_a = \frac{\Delta l}{l_0} \tag{11}$$

Where Δl is the change in gauge length and l_0 is the original gauge length. Circumferential strain is measured by means of a further clip transducer attached to a chain wrapped around the circumference of the sample. Since the axial strain transducer is located in the centre of the sample, the circumferential strain transducer has necessarily to be located somewhat off-centre. Circumferential strain (ε_c) is then calculated by:

$$\varepsilon_c = \frac{\Delta c}{c_0} \tag{12}$$

Where, Δc is change in circumference of the sample and c_0 is the original undeformed circumference.

From an UCS test, axial stress (calculated from the load measured by the load cell) and axial strain are used to calculate the Young's modulus. An example of axial and circumferential stress-strain curves from one of the UCS tests on Nash Point limestone is shown in Figure 14. Also plotted on Figure 14 is volumetric strain, which is calculated by:

$$\varepsilon_V = \frac{\Delta V}{V_0} \tag{13}$$

Where ΔV is change in volume of the sample and V_0 is the original undeformed volume. Plotting volumetric strain is a useful tool as the maximum volumetric strain marks the transition from compaction dominated deformation to dilatancy dominated deformation (Heap 2009).

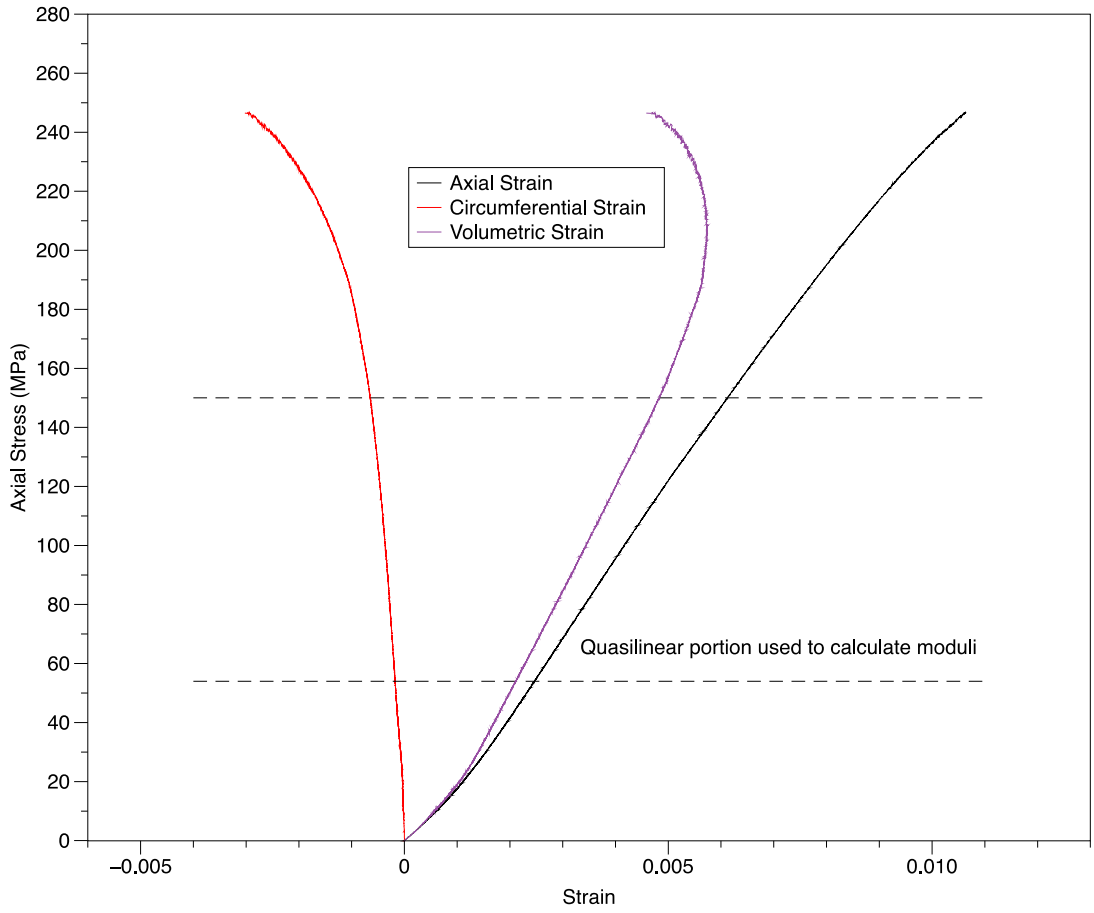

Figure 14: Example of axial and circumferential stress-strain graph obtained from a UCS test on Nash Point limestone.

Following the method of Heap & Faulkner (2008), static Young's moduli were calculated from the axial stress–strain curves after fitting with a third-order polynomial. After differentiation, the slopes of the stress–strain curves were determined over their entire lengths and the tangent static moduli calculated from the quasilinear regions of the curves (Figure 14).

Poisson's ratio is the negative ratio of the transverse strain to longitudinal strain. Normally this would be calculated from both the axial strain and the diametral strain, however unfortunately I did not have access to a diametral strain transducer but only a circumferential strain transducer. As such I calculated Poisson's ratio based on the ratio between axial strain and circumferential strain using:

$$\nu = -\frac{\text{Gradient of axial stress - strain curve}}{\text{Gradient of circumfere ntial stress - strain curve}} \quad (14)$$

Where ν is Poisson's ratio.

Using the circumferential strain to calculate Poisson's ratio in transversely isotropic material may have some limitations in that when loading normal to the axis of symmetry (which is parallel to bedding in the case of most sedimentary rocks) the circumferential strain will be an average of the strains at all angles between bedding parallel and bedding normal orientations. This point is discussed in detail in Chapters 3 and 6. The quasilinear portions of the stress-strain curves were used to calculate Young's modulus and Poisson's ratio, as indicated in Figure 14.

2.1.4 Tensile strength

The Brazil disk technique (ISRM 1978) was used to measure the indirect tensile strength of both Nash Point shale and limestone. This method is based on the fact that under uniaxial compression, tensile stress will accumulate in the centre of the rock sample. As tensile strength of a rock is lower than its compressive strength, the sample will fail in a tensile manner (Secor 1965). This is therefore a commonly used method to determine the tensile strength of rocks.

Disks of 19 mm x 38 mm (thickness x diameter) of both Nash Point shale and limestone are used for the Brazil disk tests in this case. The disks are cut from cores prepared as described above with their faces ground flat and parallel to each other.

This sample size is chosen as it is a requirement set out in the ISRM that the thickness of the sample is approximately the same size of the radius (ISRM 1978). Furthermore, Brazil disk tests for this size of sample are also carried out at the UCL labs on a regular basis.

Finally, the diameter of the sample must be related to the largest grain size of the rock by the ratio of at least 10:1, as set out in the ISRM suggested method (ISRM 1978). As both the shale and the limestone are very fine grained a diameter of 38 mm is acceptable. Unless stated otherwise this is the case for all experimental methods used in this thesis. The tests were conducted using the uniaxial loading frame in the UCL Rock and Ice Physics Laboratory. The apparatus is servo-controlled using LabView, based on force, actuator displacement or LVDT displacement control. The actuator piston is powered by a hydraulic ringmain, and can apply a maximum compressive load of 200 kN.

The circumferential surface of each test sample was wrapped with a double layer of masking tape and then mounted in the curved jaws of the loading jig (Figure 15) as per the ISRM suggested method. The test assembly was then placed in the load frame. Experiments were run under displacement control, using a constant displacement rate, and the load cell thereby applies a load on the sample, which is measured. In these experiments the displacement rate was set at 0.1 $mm.min^{-1}$, so as sample failure occurred within 1 – 2 minutes, commensurate with the ISRM recommendations. The failure load is then recorded and used to calculate the tensile strength of the rock (σ_t):

$$\sigma_t = 0.636 \frac{P}{Dt} \tag{15}$$

Where P is the failure load, D is the diameter of the sample, and t is the thickness of the sample.

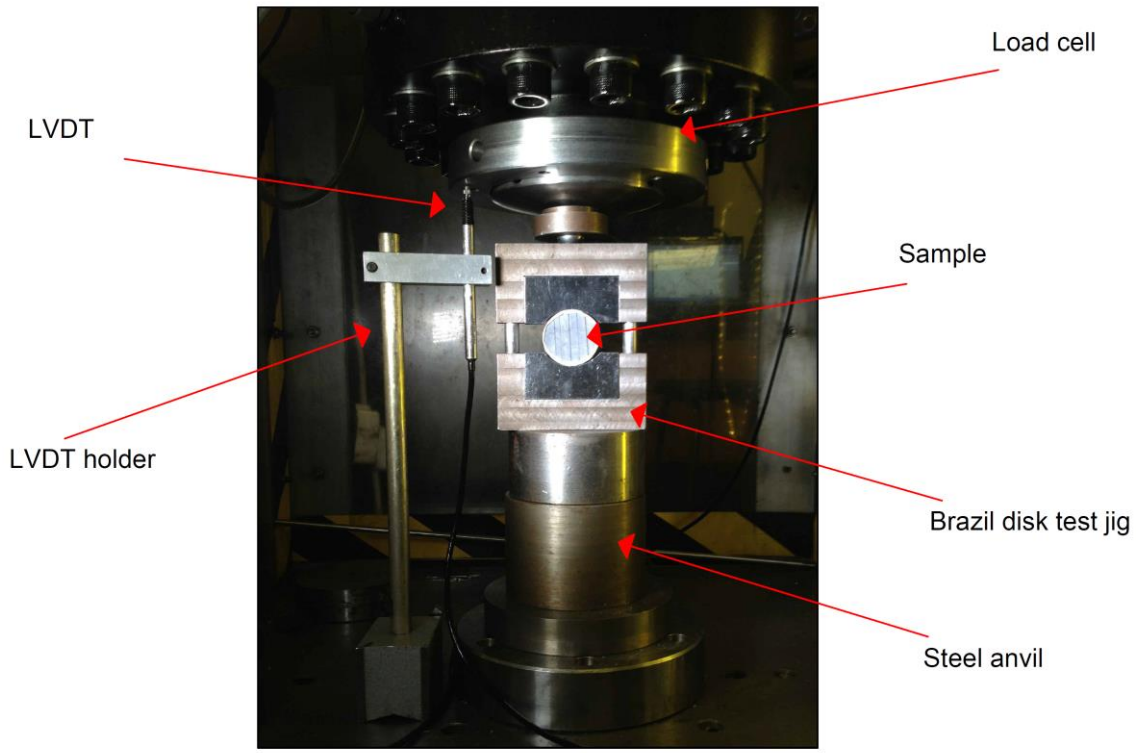

Figure 15: Brazil disk set up. Here the 38 mm diameter sample is mounted in the jaws and the uniaxial load is exerted vertically. The black lines on the sample indicate the bedding plane. The steel anvil here is used to bring the testing jig up to a height which is within the displacement range of the loading piston so that a load can be applied to the sample.

Sedimentary rocks are often considered transversely isotropic, where the axis of rotational symmetry coincides normal to the bedding plane. As such their mechanical properties may vary as a function of orientation. For fracture propagation there are considered three principal fracture orientations with respect to the bedding plane – the Short-transverse, Arrester and Divider – as discussed in Chapter 1.

Where possible (in the tensile strength and fracture toughness tests) the mechanical properties are measured in all three principal fracture orientations. Where this is not possible (UCS tests) the mechanical properties are measured both normal and parallel to bedding. Measurements are also taken in between these orientations where a significant difference exists between them (Figure 16). These results are discussed in Chapters 3 and

4, however for reference tensile strength was measured only in the three principal fracture orientations for Nash Point limestone, whereas it was also measured every 15° between the Short-transverse and Arrester for Nash Point shale.

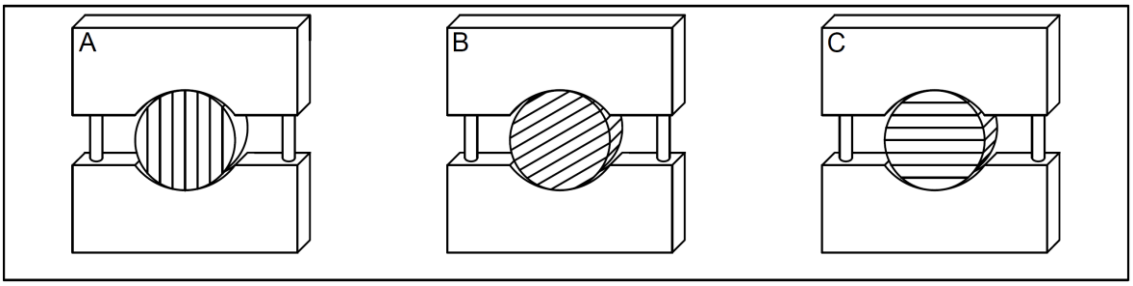

Figure 16: Schematic of Brazil disk test setup where samples are tested in the Short-transverse (A), 60° to bedding (B), and Arrester (C) orientations.

2.1.5 Fracture toughness

The fracture toughness of a material is a measure of its resistance to dynamic fracture propagation. As such it is believed to be a critical control of the propagation of hydraulic fractures (Yao 2012). Fracture toughness is a more fundamental parameter than tensile strength, as tensile strength measurements depend on the size of the most deleterious flaw within a sample, which cannot be easily measured. Fracture toughness tests are able to overcome this problem by introducing a large notch of known dimensions within the sample that is larger than any other pre-existing flaw (ISRM 1988). The tensile stress concentrates at the tip of this notch, and the fracture will therefore propagate from it. The condition for mode-I fracture propagation can be expressed as:

$$K_{Ic} \propto \sigma_R \sqrt{\pi a_c} \tag{16}$$

where K_{Ic} is the mode I fracture toughness, σ_R is the remotely applied stress and a_c is the critical fracture (or notch when referring to fracture toughness experiments, see Figure 17 and Figure 23) length.

There are four ISRM suggested methods to measure the fracture toughness of a rock, these are the Chevron Bend (CB), Cracked Chevron-notched Brazilian Disk (CCNBD) Semi-circular Bend (SCB) and the Short-rod (SR) (Ingraffea *et al.* 1984; ISRM 1988; Kuruppu *et al.* 2014; Ulusay 2014; Dai *et al.* 2015; Wei *et al.* 2018). As mentioned previously each of these use a notched sample, in the case of the CB, CCNBD and SR the notch is chevron shaped whereas in the SCB the notch is straight. The purpose of the chevron notch is to allow for a zone of stable fracture growth prior to the unstable growth where K_{Ic} is measured. A further advantage of chevron notched samples is that it can also be used to measure the effect of inelastic fracture growth on the measured value of K_{Ic}. Nevertheless, the SCB method was chosen because it is relatively easy to manufacture samples in orientations other than the three principal ones (Figure 19), and this allowed me to measure the variation of K_{Ic} with orientation. This would have been more problematic with chevron notched samples. However, I did test SR samples to compare results between the two methods, and hence ensure compatibility with previously published shale data (Schmidt 1977; Lee *et al.* 2015; Chandler *et al.* 2016).

Both of these methods are now described in detail below.

2.1.5.1 Semi Circular bend

Before describing how to manufacture the samples a schematic of a sample (to be used in conjunction with Table 3) and an example of a finished sample in the loading setup is presented in Figure 17. Unlike the other three methods to measure fracture toughness the SCB method uses a straight cut notched semi-circular sample loaded in three-point bending (Kuruppu *et al.* 2014).

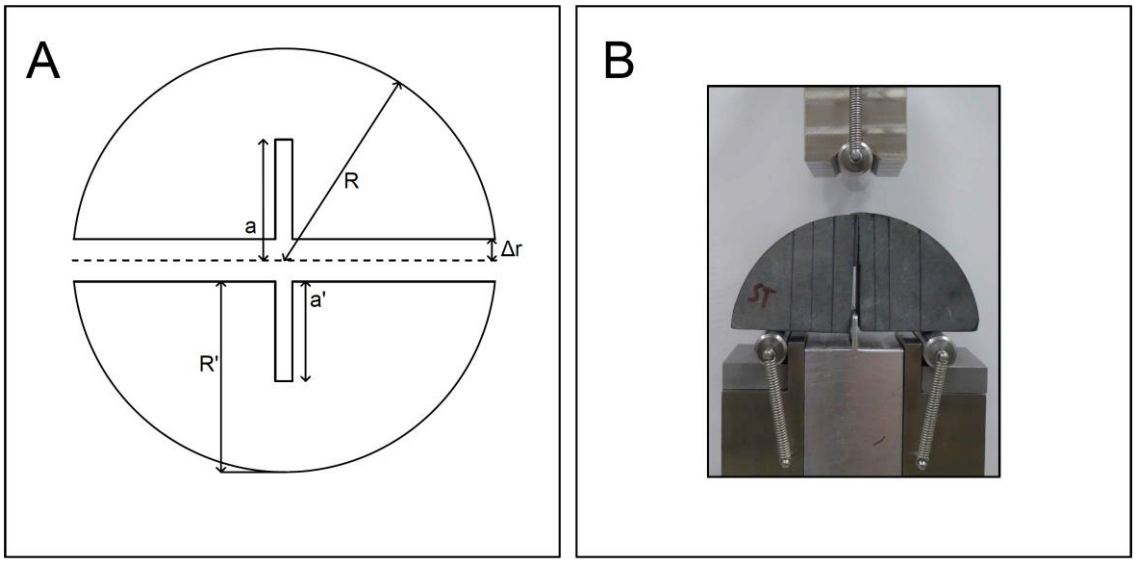

Figure 17: Schematic drawing of SCB sample with dimensions from Table 1 (left) SCB sample of Nash Point shale in the three point bending loading set up (right). The black lines depict the bedding plane, and therefore this sample has been tested in the Short-transverse orientation.

The finished sample is a semi-circular disk of 38 mm x 30 mm (notional radius x thickness), with a notch of notional length 19 mm cut into the middle of the flat part of the Semi-circular disk. The recommended geometrical dimensions of a SCB sample of diameter 76 mm are given below in Table 3.

Table 3: Recommended geometrical dimension for a SCB sample (Kuruppu *et al.* 2014)

Description	**Suggested value**	**Calculated value when D = 76 mm**
Diameter (D)	76 mm or at least 10x grain size	76 mm
Notional Radius (R)	36 mm	36 mm
Thickness (B)	0.4D	30 mm
Notional notch length (a)	$0.4 \leq a/R \leq 0.6$	$15.2 \text{ mm} \leq a \leq 22.8 \text{ mm}$
Notch thickness (t)	$t \leq 0.05D$	$t \leq 3.8$ mm
Span length (s)	$0.5 \leq s/(D) \leq 0.8$	$38 \text{ mm} \leq s \leq 60.8 \text{ mm}$

Cores of diameter 76 mm were drilled out of both shale and limestone blocks collected from the field. Each core is then cut into circular disks of approximately 32 mm thickness, thus allowing 2 mm for the disk to be ground flat on either side (Kuruppu *et al.* 2014; Ulusay 2014).

Three disks at a time can be ground flat using the grinding jig in Figure 18 and samples are ground to a thickness of 30 mm and so as the two sides are parallel.

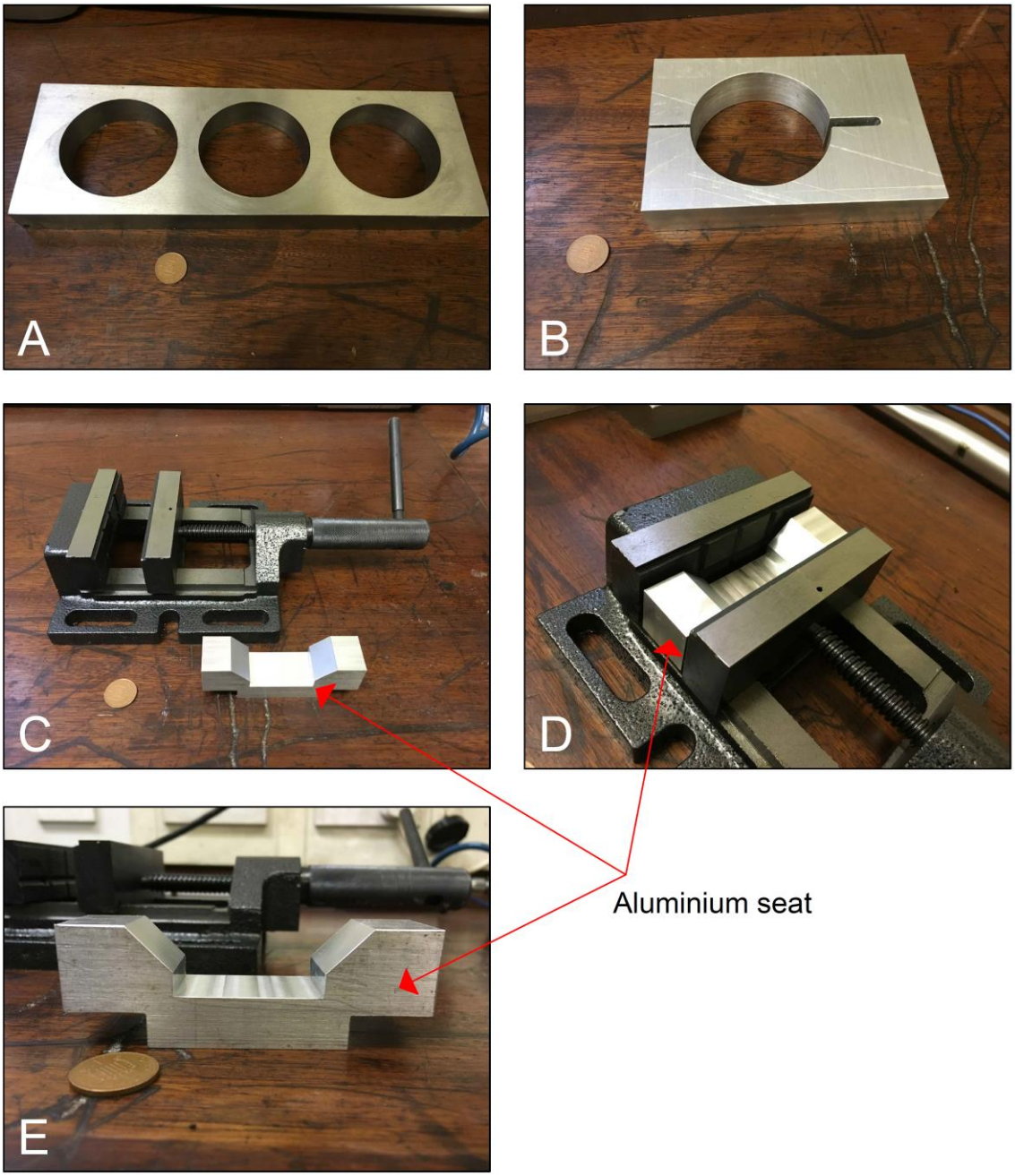

Figure 18: (A) Grinding jig for grinding three 76 mm diameter samples to 30mm thickness, (B) cutting jig for cutting 76 mm diameter disks in half, (C, D and E) machine vice and aluminium seat for semi-circular disk to sit on for grinding the bottom edge flat and grind out notch. Each one of these jigs and fixtures was designed and manufactured specifically for this project by Neil Hughes (UCL). One pence piece for scale.

Each disk is then cut in half using a cutting jig and rotary saw with a blade thickness of 2 mm. As the notch is ultimately made perpendicular to the diametral cut, it is important to orientate the samples properly before cutting the disks in half. When cutting the disks to

make samples to test in the Short-transverse orientation the cut needs to be made normal to bedding (so as then the notch is parallel to bedding). When cutting the disks to make samples to test in the Arrester orientation the cut needs to be made parallel to bedding (so as then the notch is normal to bedding). There is no need to orientate the samples being used to measure in the Divider orientation. If samples need to be made to test angles between the Arrester and Short-transverse then the angle to the bedding plane needs to be marked on the sample, and then it is cut accordingly (Figure 19). Although the method would ideally use a complete semi-circle, it would mean that almost half of the material would be wasted as the cut made by the rotary saw would mean that only one 'perfect' semi-circle could be manufactured from each disk. However, to minimise wastage a correction can be applied to the calculations made using this method to allow for both 'halves' of the cut disk to be tested, as set out in the ISRM suggested method (and described in detail in Chapter 3).

Once cut, the samples are placed in an aluminium alignment seat located in a machine vice. The samples are orientated so that the bottom edge can be ground flat, and so that the notch can be cut in the right orientation to the bedding plane. For example, a sample being used to measure in the Arrester orientation would need to have the bottom edge ground parallel to bedding. Then the notch will be cut perpendicular to the bottom edge, and therefore the bedding plane.

After each of the samples has had the bottom edge ground flat they are measured again to check if the radius, R, satisfies the following condition:

$$R_{final} \geq R - 0.025D \tag{16}$$

where R_{final} is the reduced radius (following cutting and grinding), R is the notional radius from Table 3 ($R = D/2$), and D is the sample diameter. If this is satisfied then the notch length, a, is as stated in Table 3, otherwise it is corrected by:

$$a' = a - \Delta r \tag{17}$$

where a' is the modified notch length, a is the notional notch length from Table 3, and Δr is the difference between the reduced radius and the notional radius. Through the cutting and grinding process not many samples satisfied equation (6) and therefore a modified notch length was used.

The samples are put back in the machine vice and the bottom edge made level using a spirit level. The notch is then ground in to the sample to the correct length by using a grinding wheel of thickness < 1.5 mm ± 0.2 mm. The grinding plate, which the machine vice is secured to magnetically, moves laterally during the grinding process so that the sample clears the grinding wheel on each pass. This is to make sure that the notch being ground is straight.

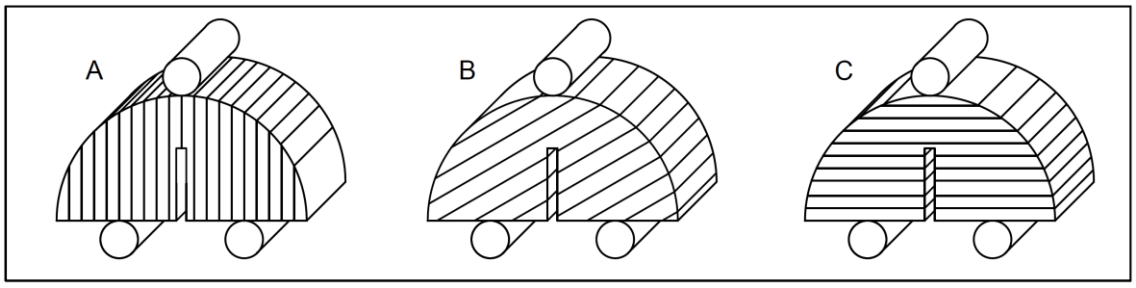

Figure 19: Schematic of SCB test set up where samples are tested in the Short- transverse (left), 60° to bedding (centre), and Arrester (right) orientations. In each case the solid black lines on the samples depict bedding plane orientation.

Again, testing is conducted in the uniaxial loading frame at the UCL Rock and Ice Physics Laboratory, in a conventional three-point bend set up (Figure 17). The SCB experiments require a much lower load than the Brazil disk tests and UCS tests, and a lower capacity 5kN load cell was therefore fitted and used to measure the load and maintain the same level of precision. Here the bottom of the sample is placed on two rollers which are set apart by a distance governed by the span length in Table 3. Although the rollers are in a fixed position they are able to rotate as the load is applied, therefore reducing any frictional resistance between the rollers and the sample to 0 (Kuruppu *et al.* 2014). The notch of the sample must be centred between the two rollers.

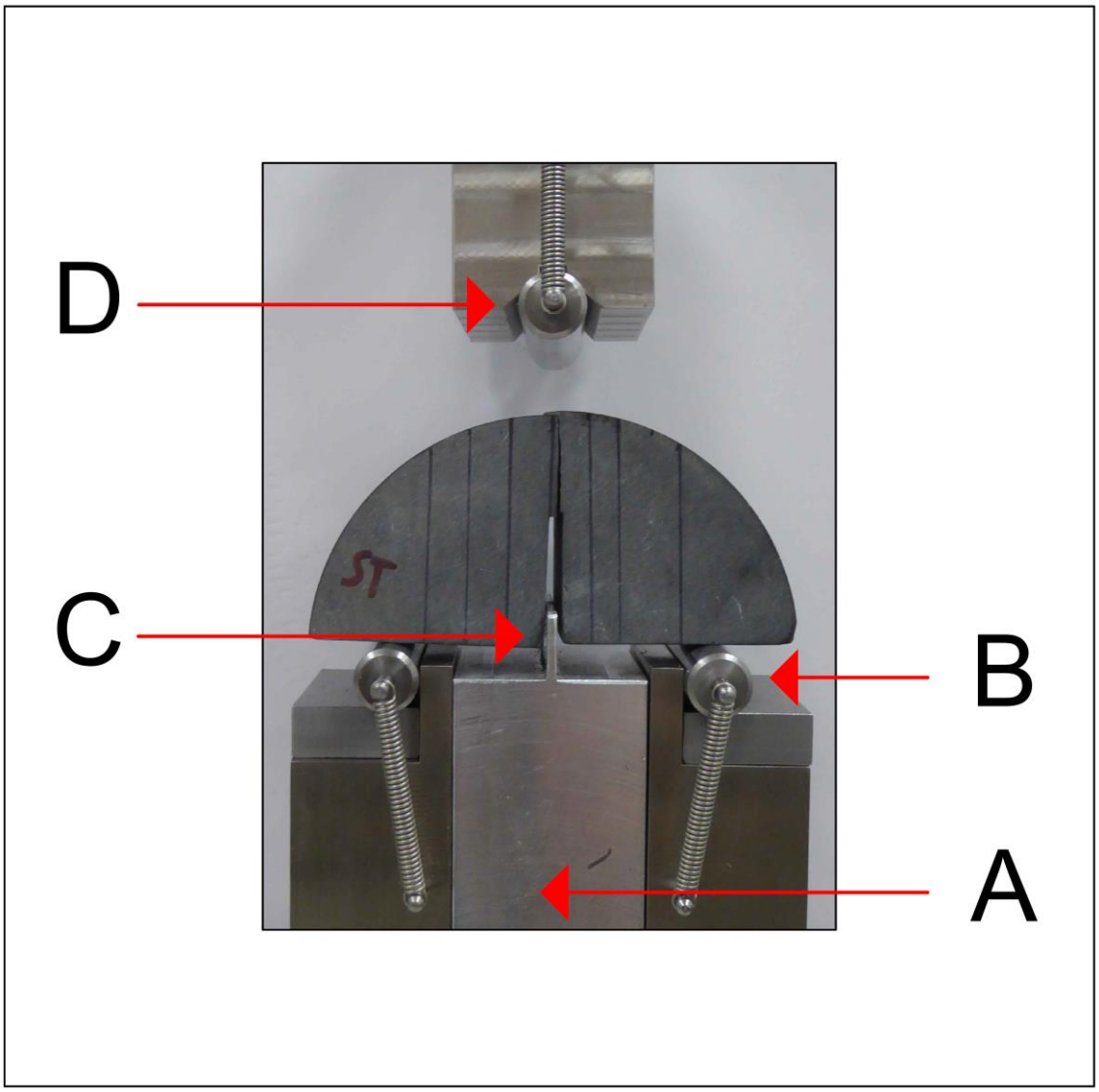

Figure 20: Photograph of finished sample in the loading jig; where A is the alignment block, B is one of the two bottom rollers, C is the central blade, and D is the moving top roller.

A third roller is attached to the moving loading ram and the sample set up is carefully aligned so that the notch is in line with the centre of the top roller. A specially designed alignment block assured both alignment of the notch with the loading roller above but also the centring of the notch between the two bottom rollers (A in Figure 20). The width of the alignment block controls the span between the two bottom rollers (B in Figure 20) which is set to a fixed value of 50 mm. A central blade on the alignment block (C in Figure 20) that fits into the sample notch controls the centralisation of the sample between the bottom rollers and also ensures that the sample is aligned at right angles to the rollers.

The alignment blade is sufficiently short so as not to interfere with the sample during testing.

Load is applied via the top roller at a constant displacement rate of 0.1 $mm.min^{-1}$, which is controlled via an LVDT.

The test may be paused momentarily once a small load has been applied in order to check the alignment of the rollers and to make sure that they are in contact with the sample along its entire thickness (Kuruppu *et al.* 2014). If this is the case then the test may then continue, otherwise the loading plate must be reversed and the necessary adjustments made to correct the alignment. This very small loading is not thought to affect the results. It was found that loading was not quite uniform across the top of some of the samples, therefore in order to minimise the effects of non-uniform loading, two layers of masking tape were applied to the top of these samples. This is similar to what is suggested when conducting Brazil disk tests, and it is not thought that this affected the results in any significant way. Once started, tests lasted between 60 and 140 seconds.

Only the peak load, P_{max}, is required from the test in order to calculate the fracture toughness. However, it is a recommended in the ISRM suggested method to plot displacement vs load throughout the test to verify that the load increased continuously with displacement until the point of failure (Kuruppu *et al.* 2014). The fracture toughness is then calculated by:

$$K_{Ic} = Y' \frac{P_{max} \sqrt{a' \pi}}{2R'B'} \tag{18}$$

where P_{max} is the peak load, a' is the modified notch length, R' is the reduced radius, B' is the sample thickness, and Y' is a non-dimensional stress intensity factor that accounts for the specific sample geometry and is as defined as:

$$Y' = -1.297 + 9.516\left(\frac{s}{2R'}\right) - \left[0.47 + 16.457\left(\frac{s}{2R'}\right)\right]\beta + \left[1.071 + 34.401\left(\frac{s}{2R'}\right)\beta^2\right] \tag{19}$$

where s is the span between the two bottom rollers and:

$$\beta = \frac{a'}{R'} \tag{20}$$

The fractured sample should be analysed and if the fracture plane deviates by more than 0.05D (3.8 mm for our samples) then the result should be disregarded and considered invalid. Figure 21 demonstrates examples of samples that would normally be considered valid (A) and invalid (B). However, through accounting for any mixed-mode component, even tests that produce fractures that deviate by more than 0.05D can be used. This is described thoroughly in Chapter 3.

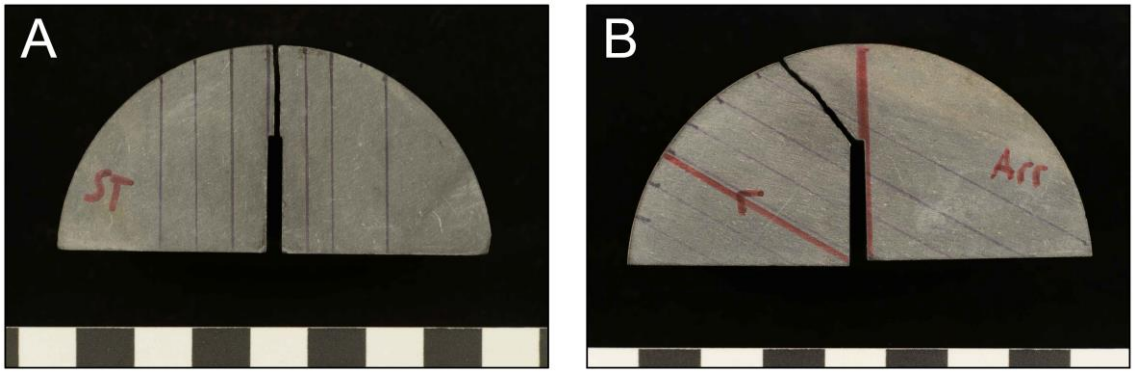

Figure 21: Examples of (A) a SCB test sample that would considered valid and (B) a SCB test sample that would normally be considered invalid due to the fracture deviation from the intended direction. In both cases the individual segments in the scale bar are 1 cm across. For reference (A) is a sample of Nash Point

shale tested in the Short-transverse orientation, while (B) is a sample of Nash Point shale tested at 60° to bedding.

2.1.5.2 Short-rod

Before describing how the samples were prepared, an illustration of a finished sample is provided in Figure 22 and Figure 23. Unfortunately it is rather difficult to manufacture SR samples at orientations between the Arrester and Short-transverse therefore I only tested samples in the three principal orientations using this method.

Figure 22: Short-rod sample of Nash Point Limestone with a one pence piece for scale. The black lines on the sample refer to the bedding plane.

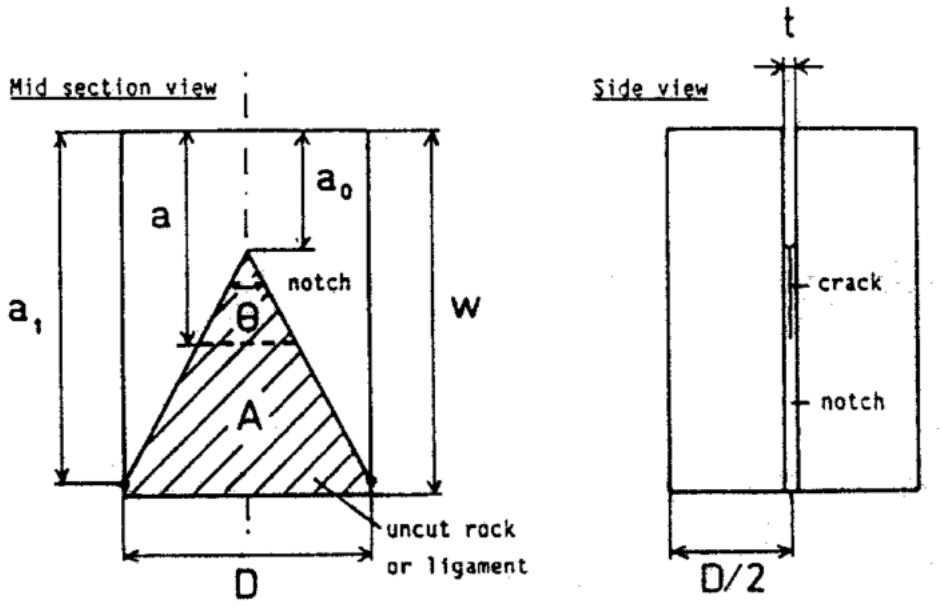

Basic notation:

D = diameter of short rod specimen
w = length of specimen, 1.45D
θ = chevron angle, 54.6°
a_0 = chevron tip distance from loaded end, 0.48·D
a = crack length
a_1 = maximum depth of chevron flanks
t = notch width
A = projected ligament area
F = load on specimen

Figure 23: Schematic diagram demonstrating the geometry of the ISRM suggested short-rod sample. From Ouchterlony (1988)

The samples are cores of length 89 mm and diameter 60 mm with a 25 mm wide groove ground out of the top of the sample. A chevron notch is then ground out, where the angle of the end of the notch is 54.6°±1°. Using the ISRM suggested method the specimen dimensions for a 60 mm diameter core are given below:

Table 4: Dimensions for a 60 mm diameter core as suggested by Ouchterlony (1988)

Dimension	Proportion	60mm sample
w	1.45D±0.02D	87±1.2 mm
a_0	0.48D±0.02D	28.8±1.2 mm
A_1-a_0	0.97D±0.02D	58.2±1.2 mm
2Θ	54.6°±1°	54.6°±1°
t	≤0.03D or 1 mm	1.8 mm

The main reason for using a 60 mm diameter sample is that Chandler (2014) used this dimension for his tests on a similar material, the Mancos shale, at UCL. Therefore all the apparatus and testing equipment used here is geared for this particular sample size.

Eight cores of both the shale and the limestone were drilled parallel to bedding and four cores were drilled of both the shale and the limestone normal to bedding. The cores drilled parallel to bedding were used to manufacture samples in the Short-transverse and Divider orientations, while those drilled normal to bedding were used to manufacture samples in the Arrester orientation. This therefore allowed for four tests in each of the three principal orientations. Next a groove of 25 mm is ground out from the top of each sample using a surface grinder. The edges of this groove are ultimately where a tensile load is applied during the test. Next the sample is mounted on a jig (Figure 24) so that a chevron notch can be ground out of the sample at the specified angle of 2Θ = 54.6°±1° (Figure 24 and Table 4). At the top of the jig there is a central lip which slots in to the 25mm groove so that the chevron notch can be ground out in the right orientation. The sample is mounted and fastened in the jig and one flank of the notch ground out. Following this the sample is rotated 180° and the second flank of the notch is ground out.

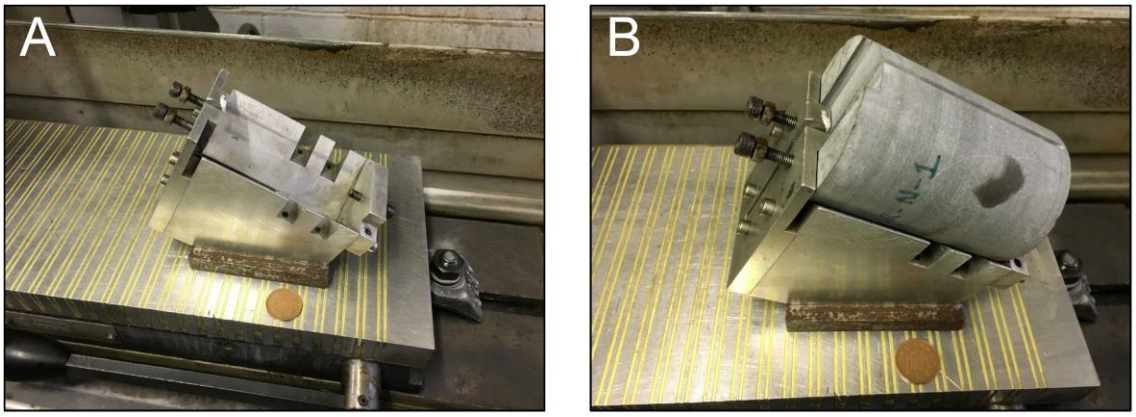

Figure 24: (A) Jig used for grinding in the chevron notch in the short rod sample (B) and with sample mounted. One pence piece for scale.

Sample preparation of the limestone was straightforward as it is highly competent and did not contain weak interfaces along which the sample might break apart during the preparation process. This was not always the case when preparing the shale samples, as was also the case when preparing the SCB samples. However, this is more of an issue when preparing SR samples as they are larger than SCB samples and therefore more bedding plane fractures are likely to be encountered during sample preparation. This is particularly problematic when coring normal to bedding. The thickness of the large blocks taken from the field ranged from 40 – 300 mm. Due to the length of the samples required (i.e. 89 mm – although cores of 100 mm were used to allow for cutting and grinding wastage) and the length of the core barrel only two samples can be made from one core, if the core was completely intact. Unfortunately this was often not the case when several bedding plane fractures existed across the thickness of the block, a whole core would become segmented into pieces that were too small to make samples out of. Furthermore, bedding plane fractures tended to extend across a whole sample block which meant that it was not possible to produce any cores normal to bedding from these particular blocks. Cores drilled parallel to bedding were slightly less problematic as the radius was only 60 mm compared to the 100 mm needed from the thickness of the block. However, there

were still a number of cores which either broke during sample preparation or were unusable.

The test itself is conducted in the uniaxial loading frame in the UCL Rock and Ice Physics Laboratory. Again, a 5kN load cell was used to measure and control the loading.

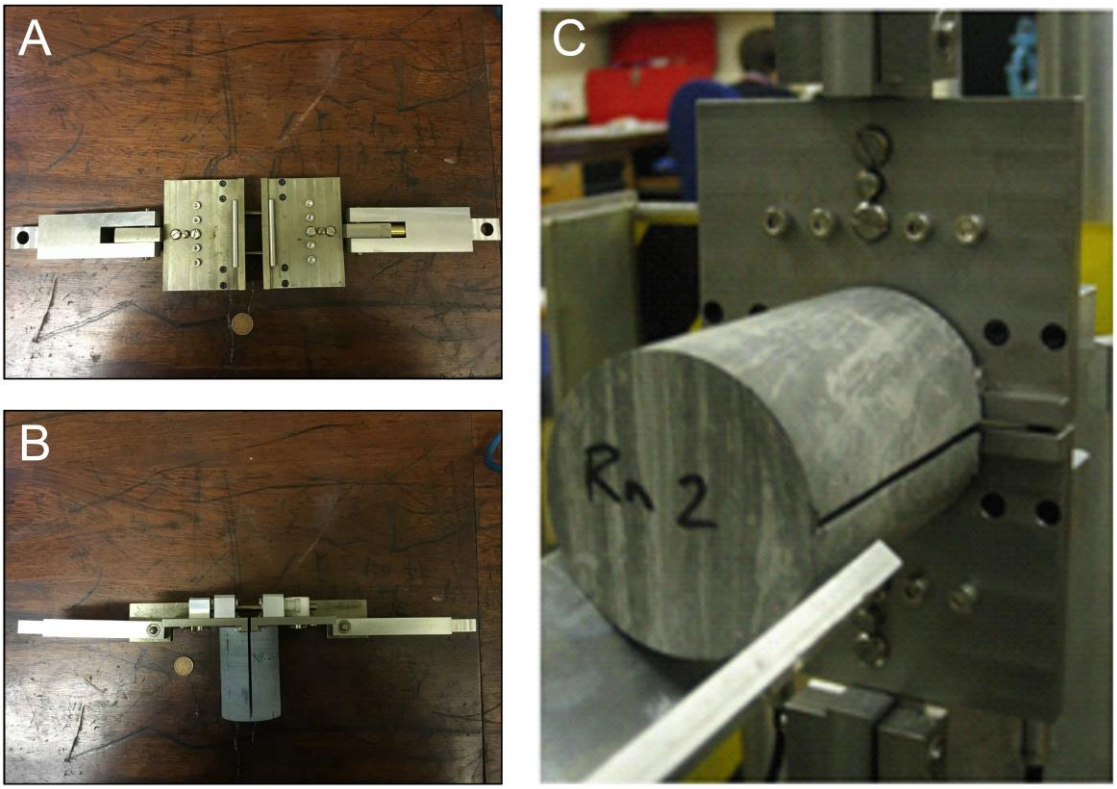

Figure 25: (A) Jaws used for the short-rod test, (B) jaws butted against groove in sample (bottom left). One pence piece for scale. (C) Mancos shale sample of diameter 60 mm in short-rod set up prior to testing (Chandler 2014)

A set of jaws is used to apply a tensile load on the sample (Figure 25) (ISRM 1988). The loading jaws are butted against the lips formed by the 25 mm groove that is ground out during sample preparation. Before any load is applied the sample is initially held in place using a V shaped support (Figure 25). During the experiment the upper jaw is attached to the actuator piston, while the lower jaw is fixed to the base. Two LVDTs are placed to measure the displacement between the jaws as a tensile load is applied. The experiment is run by displacement control using the average displacement of the two LVDTs. This displacement measures the displacement between the two jaws at the point of measuring.

However, the actual Crack Mouth Opening Displacement (CMOD), is calculated as follows:

$$CMOD = \delta_{LVDT} \times \frac{a_0}{L_{LVDT}} \tag{21}$$

where δ_{LVDT} is the displacement measured by the LVDTs, a_0 is the chevron tip to the load line, and L_{LVDT} is the distance from the LVDTs to the top of the chevron tip.

The CMOD displacement rate should also adhere to the following condition:

$$C\dot{MOD} > \frac{0.017 K_{Ic}}{E\sqrt{D}} \text{ m.s}^{-1} \tag{22}$$

Where $C\dot{MOD}$ is the displacement rate at the crack mouth, K_{Ic} is the fracture toughness, E is Young's modulus and D is the specimen diameter. By adhering to (22) the fracture propagation speed will be greater than 1 mm.s^{-1}. This is a condition set out in the ISRM suggested method to make sure that sub-critical crack growth processes do not affect the results (ISRM 1988; Chandler 2014). From (22) the appropriate $C\dot{MOD}$ can only be calculated by knowing the fracture toughness of the rock being tested. As this data was not available for Nash Point shale or limestone at the time, these rates were initially estimated using similar materials. The mean Arrester fracture toughness value of the Mancos shale from Chandler *et al.* (2016) was used to calculate the $C\dot{MOD}$ for Nash Point shale, and the fracture toughness of Welsh limestone quoted by Nath Singh & Sun (1990), was used to calculate the $C\dot{MOD}$ for Nash Point limestone. However, the static

Young's modulus, in the normal to bedding orientation, as calculated from the UCS tests was used for each rock type respectively. The table below demonstrates the minimum $CM\dot{O}D$ for Nash Point shale and limestone in each case, for a 60 mm diameter sample:

Table 5: Minimum $CM\dot{O}D$ values required for short-rod tests on Nash Point shale and limestone. *The values of K_{Ic} are not of Nash Point shale or limestone but for Mancos shale tested in the Arrester orientation (Chandler *et al.* 2016) and Welsh limestone (Nath Singh & Sun 1990)

	***K_{Ic} (MPa.m$^{1/2}$)**	***E* (GPa)**	**$CM\dot{O}D$ (mm.s^{-1})**
Nash Point shale	0.44	2.4	0.013
Nash Point limestone	0.85	28.5	0.002

From this analysis, the $CM\dot{O}D$ rates as listed in Table 5 were used for the initial testing before calculating a more appropriate $CM\dot{O}D$ based on the fracture toughness of Nash Point shale and limestone respectively. Following the initial testing I found that using Nash Point values for fracture toughness a minimum $CM\dot{O}D$ of 0.02 mm.s^{-1} for samples of Nash Point shale in the Arrester and Divider orientation, and 0.002 mm.s^{-1} for samples in the Short-transverse orientation are required. It was found that a $CM\dot{O}D$ of 0.002 mm.s^{-1} is sufficient for samples of Nash Point limestone in all orientations.

The tensile load is applied perpendicular to the chevron notch as the jaws are pulled apart, and this causes a fracture to propagate from the chevron tip (ISRM 1988; Chandler 2014). As the fracture propagates from the tip to the broader end of the chevron the width of the fracture front increases (as there is more material to fracture). The stress intensity of a fracture is proportional to the square root of the fracture length, and so as the fracture grows in length the stress intensity increases (Chandler 2014). As such, the load required to propagate the fracture decreases and this results in unstable fracture growth. By using

a chevron notch, fracture growth is initially stable, as the load required to continue to propagate the fracture increases as the width of the fracture front increases (ISRM 1988; Chandler 2014). However, eventually, the effect of the fracture length is greater than that of the widening fracture front width and so the fracture will propagate unstably and the sample fails (Chandler 2014). The fracture toughness is therefore calculated at this point, where the fracture propagation rate becomes unstable and critical (ISRM 1988; Chandler 2014).

The fracture toughness is calculated using (ISRM 1988):

$$K_{Ic} = \frac{24F_{\max}}{D^{1.5}} \tag{23}$$

where K_{Ic} is the fracture toughness, F_{max} is the failure load and D is the diameter of the sample. The result is considered invalid if the fracture deviates from the symmetry plane defined by the notch by more than 0.05D within 0.5D from the apex of the chevron V (ISRM 1988). However, Chandler *et al*. (2016) discovered that in many of the tests carried out in the Arrester and Divider orientations the fracture often exceeded this threshold. This was due to the significant mechanical anisotropy of the material and so it was decided to increase this threshold so that only if the fracture deviated by more than 5 mm (0.083D) it was considered invalid. As Nash Point shale exhibited a greater P-wave anisotropy (Chapter 3) than that of the Mancos shale in Chandler *et al.* (2016), it was also necessary to adopt this increased threshold. Figure 26 demonstrates samples from tests that would normally be considered valid (A) and invalid (B).

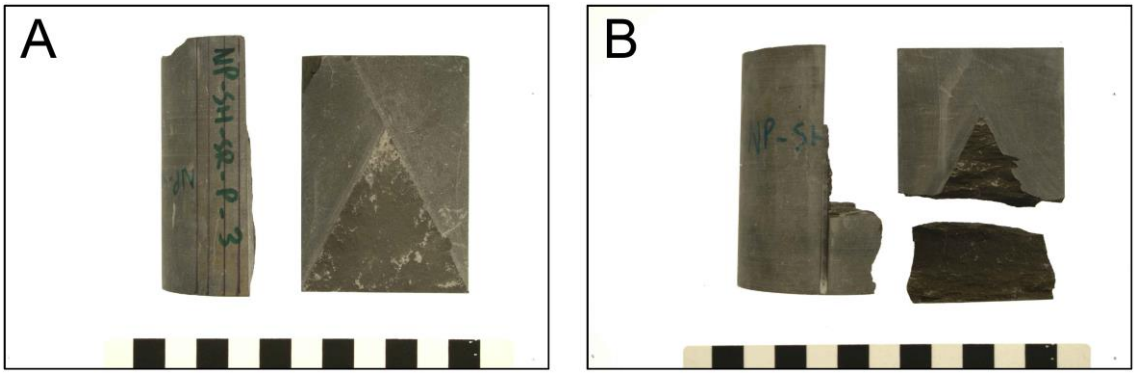

Figure 26: Examples of (A) a SR test sample that would considered valid and (B) a SR test sample that would normally be considered invalid due to the fracture deviation from the intended direction. In both cases the individual segments in the scale bar are 1 cm across. For reference (A) is a sample of Nash Point shale tested in the Short-transverse orientation, while (B) is a sample of Nash Point shale tested in the Arrester orientation.

2.2 Numerical modelling

Although analytical solutions can be used to calculate static stresses at the tip of a well-defined fracture in a homogeneous and isotropic model, it becomes too complex to do so when calculating changes of stress in a dynamic process in either a heterogeneous and/or anisotropic model. It is then necessary to use numerical models to approximate a solution. In this thesis I am interested as to how fractures may propagate in unconventional reservoirs which often contain large scale heterogeneities, such as layering. Furthermore, the target in many unconventional reservoirs is usually organic rich shales, which are known to be anisotropic. We therefore use the Finite Element Method (FEM) software COMSOL Multiphysics (versions 4.1 – 5.2a) (www.comsol.com) to model how both heterogeneity and anisotropy affect hydraulic fracture propagation. COMSOL Multiphysics is used extensively to model both geological and engineering processes (Gudmundsson & Lotveit 2012; Barnett & Gudmundsson 2014; Hickey & Gottsmann 2014; Browning & Gudmundsson 2015; Le Corvec *et al.* 2018), and therefore it is well tested and suited for using in this study.

2.2.1 Theory and model set up

FEM models work by taking a body or bodies and segmenting them into smaller, more manageable parts, called elements, in a process called meshing. All models assume linear elasticity through Hooke's law.

Therefore, assuming linear elasticity the deformation (strain) of a material is calculated from the stress applied to that material and the Young's modulus of that material. Or conversely the resultant stress is calculated from strain on a material with a known Young's modulus. The following descriptions of how a model is set up are generic, and details of the specific numerical models are described in the respective chapters (Chapters 5 and 6).

Our models are two-dimensional (2D) and are built using COMSOL's structural mechanics module. Crustal segments are built using 2D geometries such as rectangles and ellipses (Figure 27), which are based on geological measurements taken from the field. For example, hydraulic fractures such as dykes and sills, but also those associated with hydraulic fracturing, are commonly assumed to be ellipsoids or penny shaped. This assumption is based on field work, laboratory experiments and analogue models (Gudmundsson 2011; Brenne 2015; Kavanagh *et al.* 2015; Stoeckhert *et al.* 2015). A 2D slice through an ellipsoid shaped fracture, like that demonstrated in Figure 27, would be an ellipse, where the short axis is the aperture of the fracture and the long axis is the dip length or height.

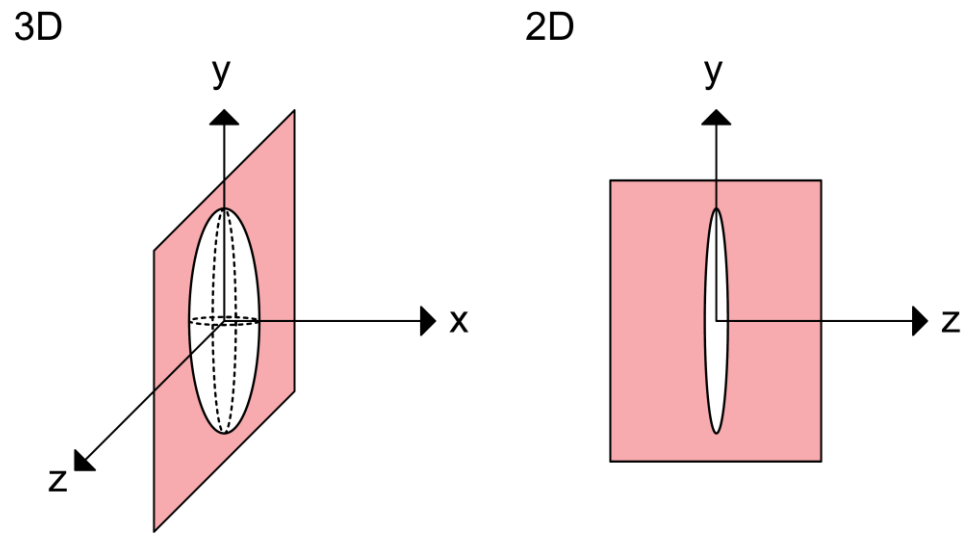

Figure 27: Schematic illustrations of a fracture in 3D drawn as an ellipsoid and a 2D slice of the fracture taken in the y-z plane. In the 2D slice the short axis is the aperture and the long axis is the fracture height (dip length).

Mechanical properties, such as Young's modulus, Poisson's ratio and density, are prescribed to the different geological units. These properties are taken directly from laboratory measurements or relevant field studies.

Hydraulic fractures in a rock propagate as a result of fluid pressure and the resultant stresses at the tip of the fracture overcoming the tensile strength of the rock and the minimum principal compressive stress (σ_3). At depth, σ_3 is commonly compressive, except in certain circumstances, such as in fast spreading rift zones, where it can be extensional. As such during the injection of fluid into a fracture, the effective stress at the fracture tip must first overcome σ_3, so that locally the regime becomes extensional. Finally, as fluid is continued to be injected into the fracture the tensile stress at the tip overcomes the tensile strength of the rock, and then the fracture propagates.

I here model fractures as a void, or cavity, with a prescribed overpressure acting within the fracture (Figure 28). For a mode-I fracture, such as a hydraulic fracture, overpressure

is defined as pressure above σ_3, and therefore takes into account the in-situ stresses. Other boundary conditions include fixing the corners of the model to avoid rigid body rotation or translation. It is also possible to model far-field stress conditions, such as extension, by prescribing either an overpressure or displacement on the model edges. However, all our models consider a relatively stable tectonic model.

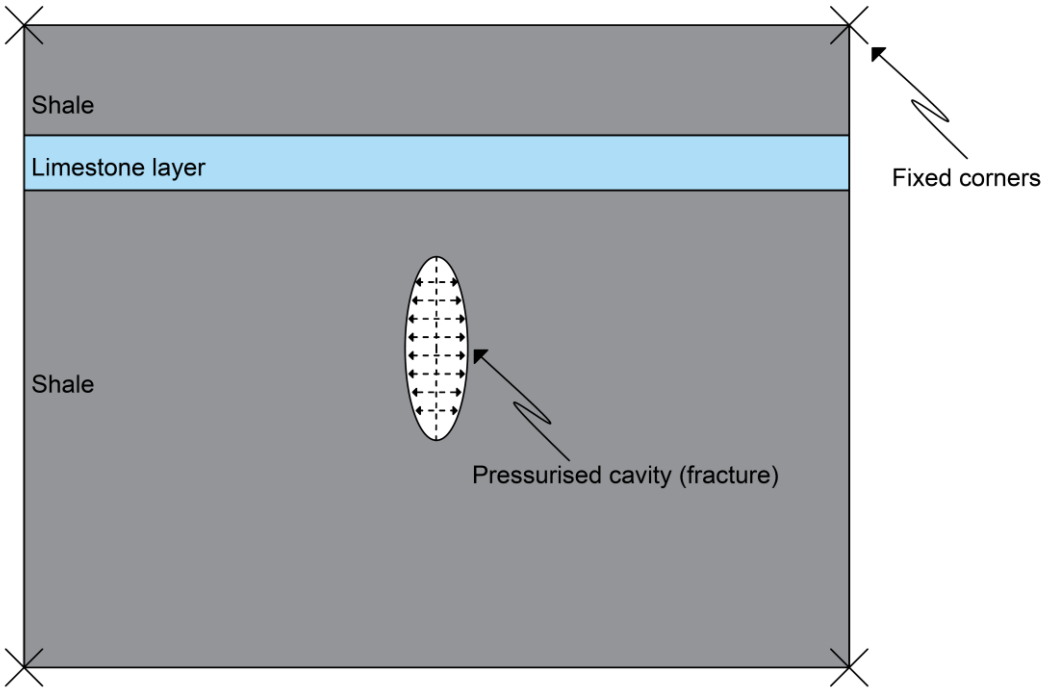

Figure 28: Example of a model set up with a pressurised cavity used to represent a hydraulic fracture. The crosses in the corners represent the fixing of the model. Here the fracture is fully enclosed in a shale unit. However above the fracture is a limestone layer. Note that the model here is not to scale, but is merely to demonstrate how a model is set up.

2.2.2 Meshing the model

Next the model is meshed so as to segment the model into smaller parts, called elements. It is on the joining nodes between elements which a series of simultaneous equations based on Hooke's law are solved for to produce a suitable solution of resultant stresses, strains and displacements, based on the model's loading conditions. A variety of different geometries can be used for the elements, although, conventionally triangular elements are

used. However, it is not expected that using different element geometries will affect the results significantly. In contrast, choosing a suitable element size is very important, and solutions can vary significantly based on the element size in the model. The element size for the models in this vary, being smallest near an area of interest (such as at a fracture tip or interface between different geological units) and largest in more homogeneous portions of the model. This is to provide better resolution of the numerical solutions in these areas of interest. The smallest element size used in this study is 0.006 m and the largest is 3 m (Figure 29).

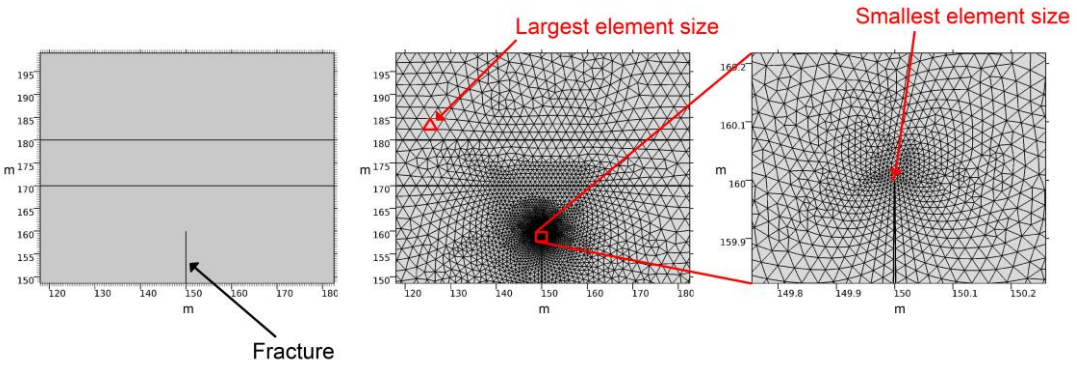

Figure 29: (Left) a basic model with a fracture modelled as a pressurised cavity situated below a layer. Please note that this extract is a zoomed in image and does not display the full extent of the model. (Middle) The same model as the previous image. Here, however, a triangular mesh has been applied to the model. Note how the largest elements are in the more homogeneous parts of the model and fine toward the fracture tip. (Right) A zoomed-in image of the fracture tip once the model has been meshed.

2.2.3 Model Outputs

Following a model run a series of model outputs can be displayed in COMSOL, in both 1D or 2D (or 3D if running a 3D model), such as tensile stress, shear stress, compressive stress and deformation. As hydraulic fractures are predominately mode-I it is common to plot the tensile stress as a contour map and both the maximum (σ_1) and intermediate (σ_2) principal compressive stresses as arrow surfaces (Figure 30) on the same 2D surface. The reason for this is that for a mode-I fracture to propagate the tensile stress at the tip of the fracture must overcome both the tensile strength of the rock and σ_3 (hence plotting tensile

stress as a contour map), but it will also propagate in the σ_1-σ_2 plane (hence the arrow surfaces). Arrow surfaces are displayed using a series of cone like geometries to demonstrate the orientation of the principal stresses. However, although the cone like geometry may give the impression of directionality, it is important to note this has no meaning and is only aesthetic. 1D graphs were also used to determine the tensile stress at the fracture tip.

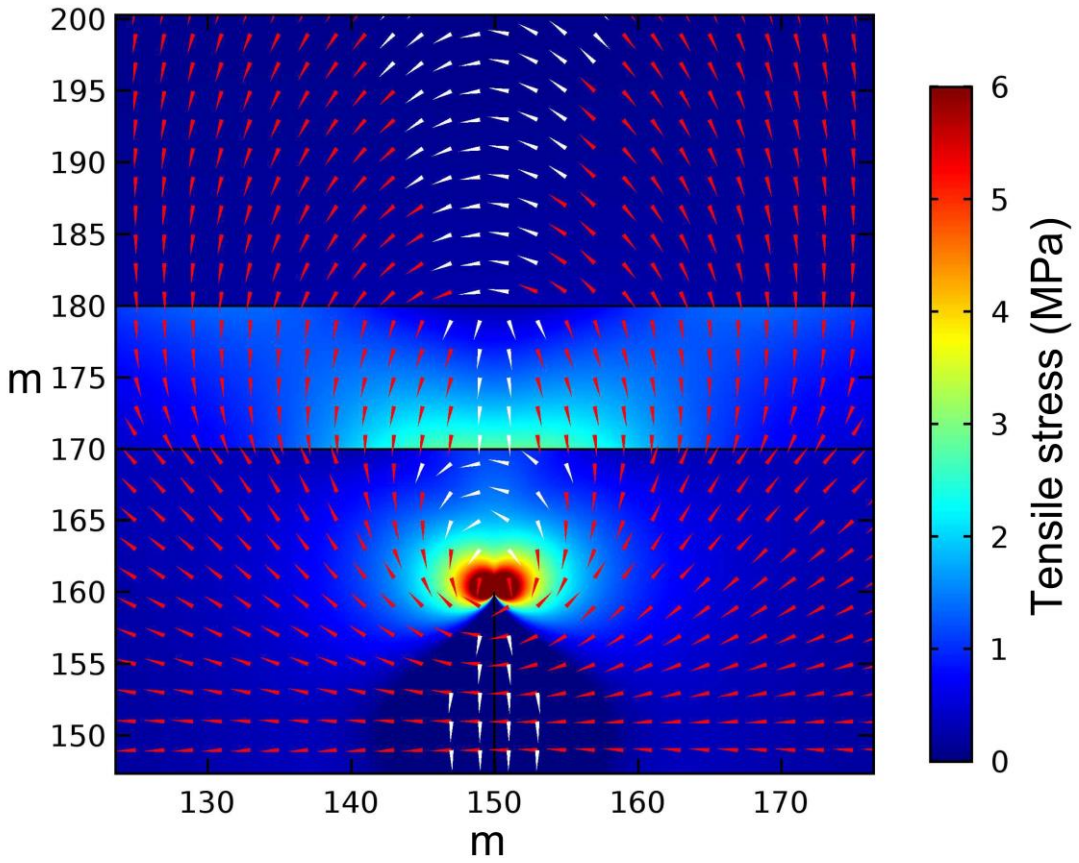

Figure 30: Output display from a model run using the set up in Figure 28. Here the contours are the magnitude of the tensile stress (MPa) where warmer colours represent a higher tensile stress. Note how the maximum tensile stress is at the fracture tip, but there are also concentrations in the layer above the fracture which has different mechanical properties to the layers above and below it. Two arrow surfaces are also plotted here. The red cones represent the σ_1 orientation, and the white cones the σ_2 orientation.

3 Fracture properties of Nash Point shale as a function of orientation to bedding

This chapter is written in a manuscript format and contains data gathered from Nash Point Shale. It was accepted by Journal of Geophysical Research: Solid Earth, and is therefore formatted in their specific journal style. As the publication is self-contained it includes its own methodology section which is identical to the relevant parts of the Methodology chapter in this thesis. As such the reader may want to skip over Section 3 if they have already read through the methodology chapter of this thesis. Supporting Information (B) was not included in the published article, but is included as part of this Chapter.

Author contribution – Nathaniel Forbes Inskip wrote the manuscript, conducted the field work and experimental work. Philip Meredith, Michael Chandler and Agust Gudmundsson contributed to data interpretation and made comments on the manuscript.

The full reference to the Journal article is:

Forbes Inskip, N. D., Meredith, P. G., Chandler, M. R., & Gudmundsson, A. (2018). Fracture properties of Nash Point shale as a function of orientation to bedding. *Journal of Geophysical Research: Solid Earth,* 123. https://doi. org/10.1029/2018JB015943

Journal of Geophysical Research: Solid Earth

RESEARCH ARTICLE
10.1029/2018JB015943

Fracture Properties of Nash Point Shale as a Function of Orientation to Bedding

Nathaniel D. Forbes Inskip[1,2], Philip G. Meredith[2], Michael R. Chandler[3], and Agust Gudmundsson[1]

[1]Department of Earth Science, Royal Holloway, University of London, Egham, UK, [2]Department of Earth Sciences, University College London, London, UK, [3]School of Earth and Environmental Sciences, University of Manchester, Manchester, UK

Key Points:
- Measurements of tensile strength and mode-I fracture toughness (K_{Ic}) show that Nash Point shale is mechanically highly anisotropic
- We find that a fracture energy (G_c) approach is more suitable than using K_{Ic} alone, because it allows analysis of mixed mode fracture propagation
- An elliptical function can be used to estimate G_c for fractures propagating at angles between the Short-transverse and Arrester directions

Supporting Information:
- Supporting Information S1

Correspondence to:
N. D. Forbes Inskip, nathaniel.forbesinskip.2014@live.rhul.ac.uk

Citation:
Forbes Inskip, N. D., Meredith, P. G., Chandler, M. R., & Gudmundsson, A. (2018). Fracture properties of Nash Point shale as a function of orientation to bedding. *Journal of Geophysical Research: Solid Earth*, *123*. https://doi.org/10.1029/2018JB015943

Received 13 APR 2018
Accepted 15 SEP 2018
Accepted article online 20 SEP 2018

Abstract Understanding how fracture networks develop in shale formations is important when exploiting unconventional hydrocarbon reservoirs and analyzing the integrity of the seals of conventional and carbon capture and storage reservoirs. Despite this importance, experimentally derived fracture data for shale remains sparse. Here we characterize shale from Nash Point in South Wales, United Kingdom, in terms of ultrasonic wave velocities, tensile strength, and fracture toughness (K_{Ic}). We measure these properties in multiple orientations, including angles oblique to the three principal fracture orientations—Short-transverse, Arrester, and Divider. We find that the Nash Point shale is mechanically highly anisotropic, with tensile strength and K_{Ic} values lowest in the Short-transverse orientation and highest in the Arrester and Divider orientations. Fractures that propagate in a direction oblique or normal to bedding commonly deflect toward the weaker Short-transverse orientation. Such deflected fractures can no longer be considered to propagate in pure mode-I. We therefore present a method to correct measured K_{Ic} values to account for deflection by calculating mode-I and mode-II *deflection* stress intensities (K_{Id} and K_{IId}, respectively). Because of the mixed-mode nature of deflected fractures, we adopt a fracture (G_c) energy-based approach that allows analysis of critical fracture propagation conditions for both deflected and undeflected fractures in all orientations. We find that G_c increases as the angle from the Short-transverse plane increases. We conclude that a modified elliptical function, previously applied to tensile strength and K_{Ic}, can be used to estimate values of G_c at angles between the Short-transverse and Arrester orientations.

1. Introduction

Shales, as a class, are the most abundant of sedimentary rock types, making up more than 50% of sedimentary material worldwide (Chandler et al., 2016). They are important not only as source rocks and seals in conventional hydrocarbon systems, but also as seals for potential carbon capture and storage reservoirs (Levine et al., 2016), as well as being both source and reservoir rocks in unconventional gas plays (Boyer et al., 2011). Specifically, over the past decade or so, there has been an increased emphasis on producing hydrocarbons from unconventional resources such as gas shales. This involves hydraulically fracturing these formations in order to increase the overall reservoir permeability.

Despite the importance and increased interest in shales, there remains a paucity of data describing their mechanical and physical properties, in particular, when compared with the amount of available data on other sedimentary rocks, such as sandstones and limestones. The paucity of data on shales is especially noticeable regarding their fracture mechanical properties (tensile strength, fracture toughness, and fracture energy). Part of the reason for this lack of data is that their mineralogy, microstructure, and inherent anisotropy mean that shales are difficult materials to work with (Chandler, 2014; Islam & Skalle, 2013).

Apart from environmental parameters such as the in situ stress field, pore fluid pressure, and the fracturing fluid pressure (Warpinski & Smith, 1990), the key material parameters involved in hydraulic fracturing are tensile strength, which controls fracture initiation, and tensile (mode-I) fracture toughness, which controls fracture propagation. Most sedimentary rocks exhibit some form of structural anisotropy, which is either the result of their depositional environment and the alignment of mineral grains, or is caused by the alignment of pores or microfractures. Such structural anisotropy commonly results in physical and mechanical anisotropy (Chandler et al., 2016; Chong et al., 1987; Kabir et al., 2017; Lee et al., 2015; Schmidt,

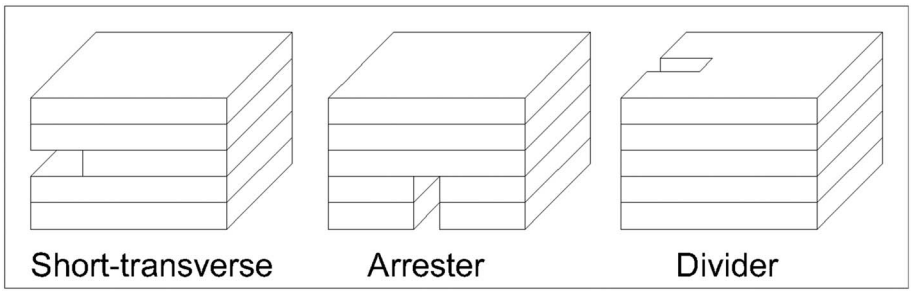

Figure 1. The three principal fracture orientations with regard to bedding planes: Short-transverse, Arrester, and Divider. Modified after Chong et al. (1987).

1977; Young et al., 1982). Therefore, many sedimentary rocks, including shales, exhibit transverse isotropy parallel to their bedding planes. We would thus expect their tensile strength and fracture toughness values also to be anisotropic. When considering the growth of essentially planar fractures in a material with a planar fabric, we can define three principal fracture orientations: Short-transverse, Arrester, and Divider (as illustrated in Figure 1; Chong et al., 1987). In the Short-transverse orientation both the fracture plane and fracture propagation direction are parallel to bedding. Conversely, in the Arrester orientation both the fracture plane and the fracture propagation direction are normal to bedding. Finally, in the Divider orientation the fracture plane is normal to bedding while the fracture propagation direction is parallel to bedding.

While there have been numerous reports of tensile strength anisotropy in layered rocks (e.g., Islam & Skalle, 2013; Li et al., 2017; Rybacki et al., 2015; Tavallali & Vervoort, 2013), there have been relatively few reported measurements of fracture toughness anisotropy in such rocks. This is particularly true for shales, for which only a handful of studies to date report data on the fracture toughness in more than one orientation (Chandler et al., 2016; Kabir et al., 2017; Lee et al., 2015; Schmidt, 1977). Schmidt (1977) measured the fracture toughness of Anvil Points shale in all three principal orientations using a three-point-bending methodology on samples which had previously been fatigue cracked. Schmidt (1977) also investigated the effect of kerogen content on the fracture toughness by testing specimens containing 80 ml/kg and 160 ml/kg of kerogen. It was found that specimens with a higher kerogen content had a significantly lower fracture toughness, in all three principal orientations. For specimens containing 80 ml/kg of kerogen the fracture toughness of samples tested in the Divider orientation was found to be the highest (1.08 MPa $m^{1/2}$) and samples tested in the Short-transverse orientation was found to be the lowest (0.75 MPa $m^{1/2}$). Samples tested in the Arrester orientation had a fracture toughness of 0.98 MPa.$m^{1/2}$, slightly lower than that for specimens tested in the Divider orientation. This trend was also observed when testing specimens containing 160 ml/kg of kerogen where the fracture toughness of samples tested in the Divider, Short-transverse, and Arrester orientations were 0.67 MPa $m^{1/2}$, 0.37 MPa $m^{1/2}$, and 0.60 MPa $m^{1/2}$, respectively.

Lee et al. (2015) measured the fracture toughness of samples of Marcellus shale in the Divider and Arrester orientations, and also in a direction 30° from the Arrester orientation, using the semicircular bend (SCB) methodology (Kuruppu et al., 2014). They found that the fracture toughness in the Arrester orientation (0.73 MPa $m^{1/2}$) was significantly higher than that in the Divider orientation (0.47 MPa $m^{1/2}$), but that the lowest value was obtained for fractures propagating at 30° to the Arrester orientation (0.18 MPa $m^{1/2}$). Chandler et al. (2016) reported fracture toughness data for Mancos shale in all three principal orientations, measured using the short rod (SR) methodology (International Society for Rock Mechanics, 1988). In contrast to Lee et al. (2015) they found the fracture toughness values in both the Arrester and Divider orientations to be the same at 0.44 MPa $m^{1/2}$, while the fracture toughness in the Short-transverse orientation was both significantly lower and also exhibited a bimodal distribution; 0.12 MPa $m^{1/2}$ and 0.31 MPa $m^{1/2}$. Optical and scanning electron microscopy of Mancos shale revealed layers of two distinctly different materials; fine-grained clay layers interwoven with coarser-grained silt layers. Chandler et al. (2016) postulated that in some of the Short-transverse samples tested the fracture propagated along a weaker clay layer, while in others, it propagated along a stronger silt layer and that this was the likely explanation for the bimodal fracture toughness distribution observed for this orientation.

Figure 2. (left) Map of Wales showing the location of Nash Point. (right) Cliff section at Nash Point demonstrating the interbedded shaly mudstones and limestone sequence. Cliff height in the background is approximately 30 m.

Kabir et al. (2017) report values of the fracture toughness of Niobrara shale from northeastern Colorado and Toarcian shale from the Paris basin, calculated indirectly using data from scratch and indentation tests. The calculated values for Niobrara shale range from 4.40 MPa $m^{1/2}$ in the Short-transverse orientation to 5.26 MPa $m^{1/2}$ in the Divider orientation. For Toarcian shale, they were only able to calculate fracture toughness in the Short-transverse orientation, and give a value of 4.06 MPa $m^{1/2}$. These calculated values are all close to an order of magnitude higher than those measured directly and reported by other workers.

To our knowledge, there has been no study to date that has systematically considered fracture nucleation and propagation in orientations other than the three principal ones. Here we report the results of a study in which we have measured both tensile strength and fracture toughness on samples of Nash Point shale in the three principal orientations and at intervals of 15° between the Short-transverse and Arrester orientations. We used the Brazil disk technique to measure tensile strength and the SCB methodology to measure fracture toughness. We also provide an analysis for calculating values of the fracture energy from measured fracture toughness values when fractures are observed to become deflected from their intended propagation direction.

2. Sample Material and Characterization

2.1. Mineralogy and Microstructure

In this study, we measure and analyze physical and mechanical properties of Nash Point shale, which is the shaly member of the Porthkerry Formation, outcropping at Nash Point on the Glamorganshire coast of Wales (Figure 2, left). The Porthkerry Formation is Hettangian-Sinermurian in age and is characterized by a sequence of interbedded shaly mudstones and limestones. Based on vitrinite reflectance data (Cornford, 1986), it is considered to have reached a maximum burial depth of 3.2 km during the Aptian.

The cliff section at Nash Point is approximately 30 m high and is laterally continuous for several kilometers (Figure 2, right). Mineral veins are common throughout, occurring over a range of scales from thicknesses of less than a millimeter and lengths (strike dimensions) of several centimeters to thicknesses in excess of several centimeters and lengths up to many meters. The latter primarily occur within the damage zones of faults and generally strike parallel or subparallel to the faults with which they are associated.

Thin section analysis demonstrates that Nash Point shale is moderately sorted, with grains that are predominately subangular and exhibit strong alignment within a clay matrix (Figure 3). The great majority of the grains are shell fragments, with a significant proportion of quartz grains also present. The shell fragments range in size from about 0.1 to 4 mm, with many appearing to originate from bivalves and some containing chert fragments. X-ray diffraction (XRD) analysis shows that Nash Point shale is composed predominately of calcite (50–70%), with lesser amounts of clay (20–30%) and quartz (10–20%).

The Nash Point shale used in this study had a porosity of ~6.5%, measured using helium pycnometry (Chalmers & Bustin, 2017; Chandler et al., 2016; Heap et al., 2009) and a bulk density of 2,430 kg/m^3.

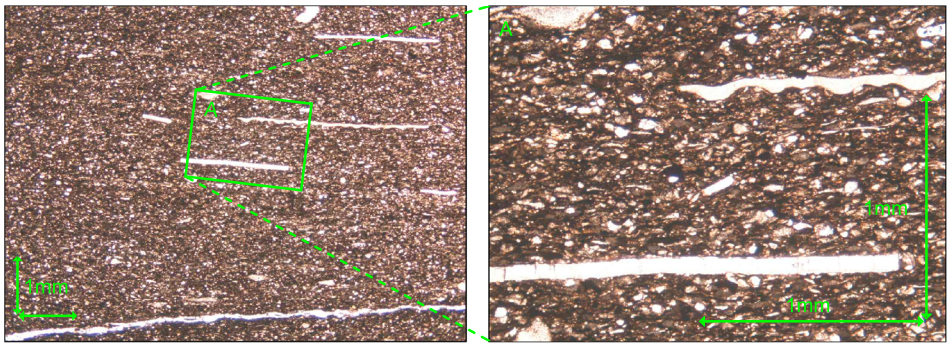

Figure 3. (left) Thin section of Nash Point shale with 1-mm bars for scale. (right) Inset area of thin section image on the left.

While Nash Point shale is not a pure *shale* petrologically, it does share many of the features of other well-known gas shales and, in particular, those of the Eagle Ford shale formation (Texas, USA), which is a major unconventional oil and gas play. The mineralogy of Eagle Ford shale has been studied by numerous authors (including Chalmers & Bustin, 2017; Elston, 2014; Knorr, 2016; Milliken et al., 2016; Mokhtari, 2015; Mullen et al., 2010), and the same general mineralogy is observed, with Eagle Ford shale also being dominated by calcite with lesser amounts of clay, and quartz. For means of comparison, Chalmers and Bustin (2017) found that Eagle Ford shale contained 32–87% calcite (average of 57%), 2–38% clay (average of 17%), and 6–20% quartz (average of 14%). Porosities were found to be between 3.5 and 10.3%, with an average value of 7.5%. These data were measured on core gathered from a depth of 4.1–4.2 km.

It is well known that shales often exhibit significantly greater mechanical anisotropy in outcrop samples than in subsurface (e.g., borehole) samples, particularly due to weathering effects and mineral alteration. However, we note that Knorr (2016) conducted XRD analysis on outcrop samples of Eagle Ford shale and found essentially the same mineralogical composition as that for the subsurface (borehole) samples reported above, suggesting that weathering had not altered the mineralogy in any significant way. No subsurface XRD data are available for Nash Point shale to make a similar comparison. However, the outcrop from which our Nash Point shale samples were taken occurs on a wave cut platform which is continuously eroded by the sea (both from wave action and the exceptionally high tidal range of the Bristol Channel). New rock surfaces are therefore unlikely to be exposed to weathering for any great length of time, so we consider any weathering effect on our samples to be minimal. Hence, based on this, and its similarity to Eagle Ford shale, we consider the mineralogy of the Nash Point shale outcrop material used in this study to be a reasonable approximation to the same material in the subsurface.

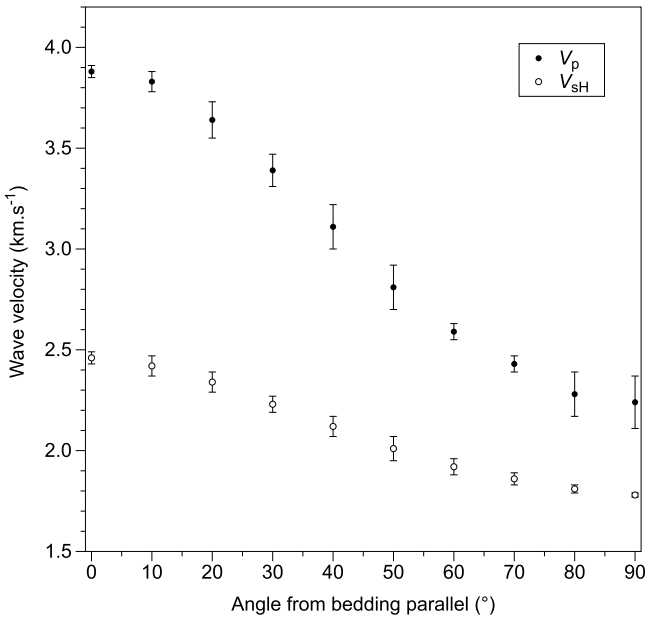

Figure 4. Ultrasonic *P* and *S* wave velocities of Nash point shale as a function of angle from bedding parallel.

2.2. Elastic Anisotropy

We characterized the anisotropy of Nash point shale by measuring the *P* wave and *S* wave velocities across the diameter of 38-mm cylindrical samples under dry, ambient pressure and ambient temperature conditions. Velocities were measured in 10° increments around the full 360° perimeter of two independent samples using the pulse transmission technique (Birch, 1960). Measurements were made using the same testing jig and ultrasonic transducers (with a resonant frequency of 1 MHz) as described by Vinciguerra et al. (2005). This results in a total of eight measurements for each orientation.

The results from all measurements are presented in Figure 4 (mean ± standard deviation), where the *P* wave velocity parallel to bedding (V_{p0}) is 3.88 ± 0.03 km/s and that normal to bedding (V_{p90}) is 2.24 ± 0.13 km/s. These values give a *P* wave velocity anisotropy of 54% calculated from:

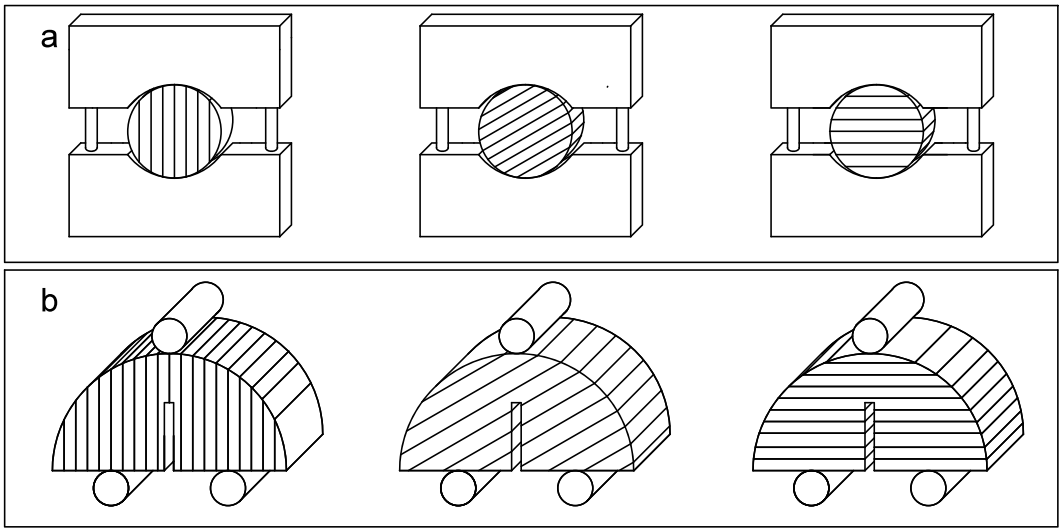

Figure 5. (a) Schematic of Brazil disk test setup where samples are tested in the Short-transverse (left), 60° to bedding (center), and Arrester (right) orientations. (b) Schematic of SCB test set up where samples are again tested in the Short-transverse (left), 60° to bedding (center), and Arrester (right) orientations. In each case the solid black lines on the samples depict bedding plane orientation.

$$\frac{V_{max} - V_{min}}{V_{mean}} \quad (1)$$

By comparison, the *S* wave velocity parallel to bedding (V_{sH0}) is 2.46 ± 0.03 km/s and that normal to bedding (V_{sH90}) is 1.78 ± 0.01 km/s. These values give an *S* wave velocity anisotropy of 32%. These values of anisotropy are high, even for shale. For example, Chandler (2014) found the Mancos shale to have a *P* wave velocity anisotropy of 22% and an *S* wave velocity anisotropy of 11%.

All our measurements were of phase velocities, but seismic dispersion should be negligible in a dry, low permeability rock such as Nash Point shale. Furthermore, it has been shown by Johnston and Christensen (1995) and Dewhurst and Siggins (2006) that the maximum difference between phase and group velocity under these conditions is less than 5%.

3. Sample Preparation and Experimental Methodology

3.1. Tensile Strength Measurements

The Brazil disk test methodology (International Society for Rock Mechanics, 1978) was used to measure the indirect tensile strength of samples of Nash Point shale measuring 38 mm in diameter by 19 mm in thickness. All samples were cored from a single block of material, and their surfaces ground flat and parallel to within 0.02 mm using a surface grinder. The bedding plane orientation was marked on all samples. Tensile strength measurements were then made in all three principal orientations and at intervals of 15° between the Short-transverse and Arrester orientations by simply rotating the sample disks between the loading platens (Figure 5a). It should be noted that in this study we quote values at orientations from bedding parallel, while in some studies values may be quoted at orientations from the axis of rotational symmetry, which in this case would be the bedding normal orientation. All samples were deformed by diametral loading at a constant displacement rate of 0.1 mm/min using a Brazil test jig mounted within a servo-controlled loading frame. This resulted in test durations from around 1 to 2 min, commensurate with International Society for Rock Mechanics (ISRM) recommendations. A minimum of four samples was tested in each orientation.

3.2. Fracture Toughness Measurements

The ISRM has published four suggested methods for measuring the mode I fracture toughness of rock; each of which has advantages and disadvantages. We elected to use the ISRM SCB methodology (Kuruppu et al., 2014) for our experiments, because it is efficient in terms of both material usage and in allowing for angles

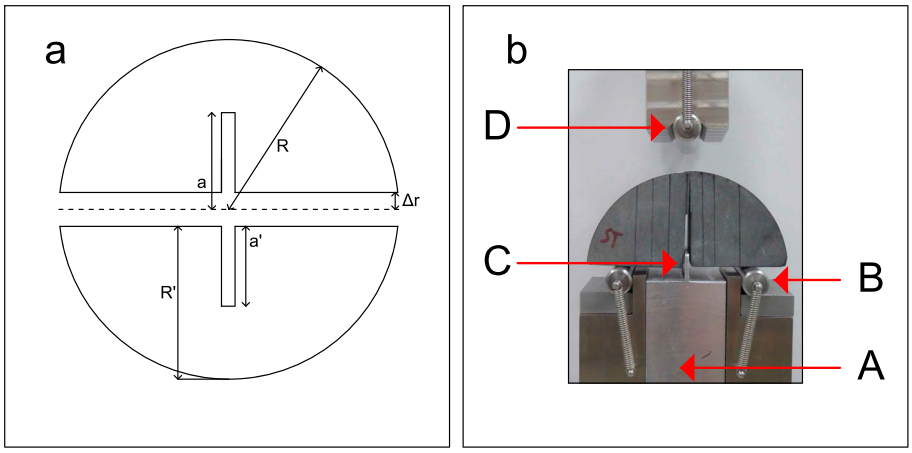

Figure 6. (a) Schematic of dimensions for a standard SCB sample after a circular disk has been cut in two. Here R is the notional radius, R' is the reduced radius, a is the notional notch length, a' is the modified notch length and $\Delta r = R - R'$. Modified after Kuruppu et al. (2014). (b) Photo of finished sample in the loading jig; where A is the alignment block, B is one of the two bottom rollers, C is the central blade, and D is the moving top roller.

between the Short-transverse and Arrester orientations to be measured relatively easily by simply cutting samples in different orientations (Figure 5b).

SCB samples were prepared in accordance with the geometry and dimensions suggested in Kuruppu et al. (2014). Samples were manufactured from 76-mm-diameter cores taken either normal or parallel to bedding. Each core was then cut into slices, which were ground flat and parallel to within 0.02 mm to produce disks of nominal thickness 30 mm.

Each 30-mm disk was subsequently cut in half using a diamond saw to create two quasi-semicircular samples, and the central saw-cut surfaces were ground flat using a surface grinder. This results in two samples that are less than fully semicircular due to the loss of material from the cutting and grinding processes. To complete each sample, a straight-cut notch was sawn into the center of the newly ground surface and perpendicular to it. The notional depth of the notch, a, must satisfy the following relation:

$$0.4 \leq \frac{a}{R} \leq 0.6 \tag{2}$$

where R is the notional sample radius. For this study, the notional radius was 38 mm and the notional notch depth was 22 mm so that $a/R = 0.58$. However, the loss of material from the cutting and grinding needs to be taken into account and the notch depth modified accordingly. This is achieved by measuring the reduced radius of the sample in the plane of the notch, R' and calculating the modified notch depth, a' where $a' = a - \Delta r$ and, $\Delta r = R - R'$. This results in a modified (actual) notch depth of 20 mm. Details of the geometry and dimensions of the SCB samples used in this study are given in Figure 6a. Use of these sample dimensions results in a fracture-front length of 30 mm and a total fracture area of 480 mm^2. Taking the geometric mean of the grain size range of Nash Point shale (0.6 mm), this means that the propagating fracture front spans an average of 50 grain diameters and that the fracture samples an average of some 1,300 grains during its propagation. We therefore suggest that the results of our experiments are fully representative of the fracture properties of the test material.

Figure 6b shows a Short-transverse-orientated SCB sample located within the testing jig. Sample positioning and alignment are controlled by a specially designed alignment block (A in Figure 6b). The width of the alignment block controls the span between the two bottom rollers (B in Figure 6b) which is set to a fixed value of 50 mm. A central blade on the alignment block (C in Figure 6b) that fits into the sample notch controls the centralization of the sample between the bottom rollers and also ensures that the sample is aligned at right angles to the rollers. The alignment blade is sufficiently short so as not to interfere with the sample during testing. All samples were loaded in three-point-bending via the moving top roller (D in Figure 6b) at a constant displacement rate of 0.1 mm/min, which resulted in test durations of between 60 and 140 s.

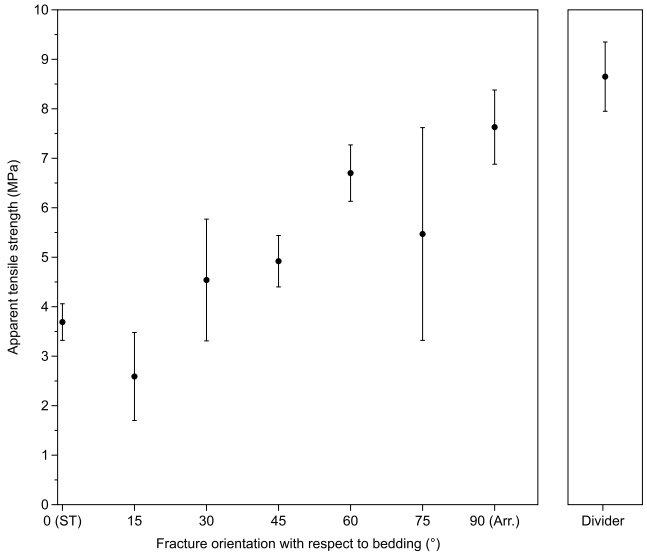

Figure 7. Mean apparent tensile strength (MPa) of Nash Point shale in the three principal orientations (where ST and Arr. refer to the Short-transverse and Arrester orientations, respectively), and at 15° intervals between the Short-transverse and Arrester orientations. Error bars show ±1 standard deviation.

The fracture toughness, K_{Ic}, is then calculated from (Kuruppu et al., 2014)

$$K_{Ic} = Y' \frac{P_{\max}\sqrt{a'\pi}}{2R'B'} \tag{3}$$

where P_{max} is the peak load, a' is the modified notch length, R' is the reduced radius, B' is the sample thickness, and Y' is a nondimensional stress intensity factor that accounts for the specific sample geometry and is as defined below:

$$Y' = -1.297 + 9.516\left(\frac{s}{2R'}\right) - \left[0.47 + 16.457\left(\frac{s}{2R'}\right)\right]\beta + \left[1.071 + 34.401\left(\frac{s}{2R'}\right)\beta^2\right] \tag{4}$$

where s is the span between the two bottom rollers and

$$\beta = \frac{a'}{R'} \tag{5}$$

Using the methodology described above, the fracture toughness of Nash Point shale was measured in the three principal orientations and at angles between the Short-transverse and Arrester orientations in 15° increments. A minimum of four samples was tested in each of the orientations.

4. Results

4.1. Tensile Strength

The tensile strengths of samples of Nash Point shale measured in the three principal orientations and at angles between the Short-transverse and Arrester orientations in 15° increments are given in Figure 7 (mean ± standard deviation)**.** The ISRM suggested method for measuring indirect tensile strength by the Brazil test inherently assumes that the maximum tensile stress occurs at the center of the sample and the tensile fracture therefore nucleates at this point. However, as we discuss later, the fracture in a significant number of our shale samples did not nucleate at or propagate through the center of the sample. Furthermore, a number of workers (e.g., Chen & Amadei, 1998; Claesson & Bohloli, 2002; Na et al., 2017) have proposed that the standard ISRM formulation is not appropriate for anisotropic materials and have suggested a number of alternatives. Since we have used the standard ISRM methodology in this study, we report our results as *apparent tensile strength* in Figure 7. In general, we observe a progressive increase in apparent tensile strength as the fracture angle changes from parallel to the Short-transverse orientation (3.69 MPa) to parallel to the Arrester orientation (7.63 MPa). There is some scatter in the data, with this being highest at angles oblique to the bedding orientation; specifically, at 15°, 30°, and 75°. The standard deviation for these angles as a percentage of the mean value is 34%, 27%, and 39%, respectively, compared with 11%, 10%, 8%, and 10% for angles of 0°, 45°, 60°, and 90° to bedding, respectively. It is perhaps not surprising that the scatter is highest at angles oblique to bedding, because these are the angles where we most commonly observe fractures that do not pass through the sample center, and deflections from the intended fracture orientation. As noted above, this issue is discussed in detail later. The propagation paths of fractures appear to be stable and repeatable at 0°, 45°, and 90°, but less so at these intermediate angles. The highest apparent tensile strength measured was in the Divider orientation (8.65 MPa), but it is somewhat similar to the Arrester orientation (7.63 MPa) and much higher than that measured in the Short-transverse orientation (3.69 MPa).

4.2. Fracture Toughness

Examples of load/displacement curves from tests on samples oriented in the Short-transverse, 45° to bedding and Arrester directions are given in Figure 8. All samples were loaded at the same displacement rate of 0.1 mm/min. For all tests, we observe an initial nonlinear phase due to bedding-in of the components of the loading train. This is followed by the main linear elastic loading phase, which continues until just prior

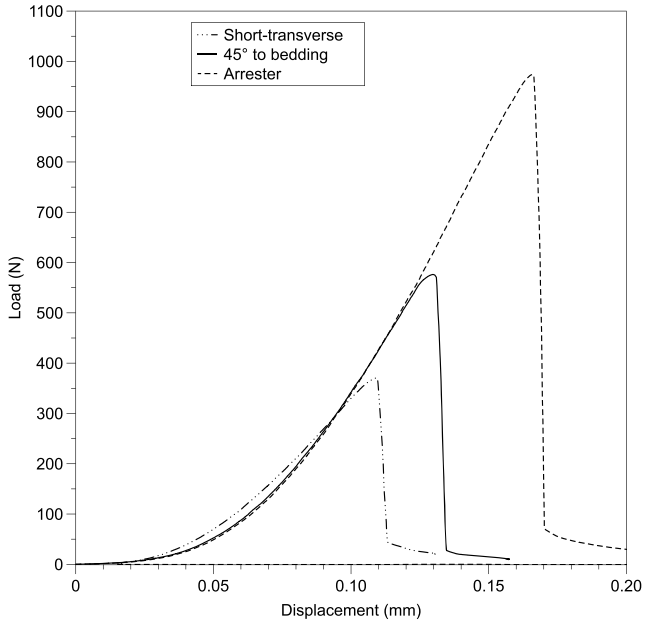

Figure 8. Examples of load-displacement curves for tests conducted on SCB samples oriented at 0° (Short-transverse), 45°, and 90° (Arrester) to bedding.

to failure, where we observe a very short roll-over phase. A key point is that the slopes of the load/displacement curves are very similar during the linear phase even though the samples fail at very different loads. The Arrester sample fails at a load that is close to 3 times higher than that for the Short-transverse sample, with the sample oriented at 45° to bedding failing at an intermediate value. The fracture toughness (K_{Ic}) of Nash Point shale samples measured in all three principal orientations and at angles between the Short-transverse and Arrester orientations in 15° increments are presented in Figure 9 (mean ± standard deviation). Similar to the tensile strength results, we observe a progressive increase in fracture toughness from parallel to the Short-transverse orientation (0.24 MPa $m^{1/2}$) to parallel to the Arrester orientation (0.74 MPa $m^{1/2}$). However, the fracture toughness values are better constrained and exhibit considerably less scatter. Again, the value of the fracture toughness in the Divider orientation (0.71 MPa $m^{1/2}$), is similar to that in the Arrester orientation (0.74 MPa $m^{1/2}$), with both being approximately 3 times higher than the value in the Short-transverse orientation (0.24 MPa $m^{1/2}$).

Of the 38 fracture toughness samples tested, five failed prematurely at anomalously low loads due to fractures propagating along thin calcite veins within the samples, which were generally orientated at high angles (60–90°) to bedding. These anomalous results have therefore been excluded from any further analysis.

For purposes of comparison, the fracture toughness of Nash Point shale was also measured in both the Short-transverse and Divider orientations using the same modified SR methodology described in Chandler et al. (2016) and using the same testing jigs and fixtures. The fracture toughness values from both methodologies are entirely consistent, and a synopsis of all the tensile strength and fracture toughness data measured in this study is presented in Table 1.

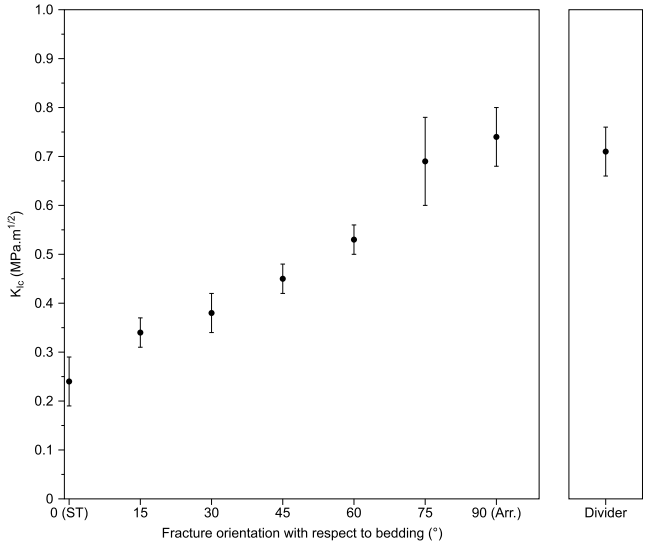

Figure 9. Mean fracture toughness, K_{Ic} (MPa $m^{1/2}$), of Nash Point shale in the three principal orientations (where ST and Arr. refer to the Short-transverse and Arrester orientations, respectively), and at 15° intervals between the Short-transverse and Arrester orientations. Error bars show ±1 standard deviation.

5. Discussion

5.1. Influence of Orientation on Fracture Properties

It is clear from Figure 7 that the apparent tensile strength of Nash Point increases progressively from samples tested in the Short-transverse orientation to those tested in the Arrester orientation. This is not surprising because the propagating fracture must traverse more interfaces (layers) as the angle to bedding is increased and all of the available interfaces when propagating in the Arrester orientation. By contrast, the fracture will ideally propagate along only a single layer in the Short-transverse orientation. In reality, however, the bedding layers are rarely perfectly parallel, and Short-transverse fractures may therefore need to traverse a small number of interfaces as they propagate. At some of the intermediate angles there is a significant degree of scatter in the data, particularly at 30° and 75° to bedding. Postmortem inspection of the fractures in these samples reveals that (i) they commonly do not pass through the center of the sample, and (ii) they commonly deflect away from the intended (load-parallel) direction toward the weaker Short-transverse (bedding-parallel) direction for at least part of the propagation pathway. An example of both occurrences is given in Figure 10. We suggest that this competition between propagation in the direction of the applied stress and propagation along the weak bedding plane may well be responsible for the higher degree of scatter observed at these intermediate angles.

Table 1
Summary of the Mean Apparent Tensile Strength and Fracture Toughness of Nash Point Shale in the Three Principal Fracture Orientations and at 15° Intervals Between the Short-Transverse and Arrester

Orientation with respect to bedding plane	Apparent tensile strength (MPa)	K_{Ic}, [SCB] (MPa $m^{1/2}$)	K_{Ic}, [SR] (MPa $m^{1/2}$)
0° (Short-transverse)	3.69 ± 0.37	0.24 ± 0.05	0.30 ± 0.09
15°	2.59 ± 0.89	0.34 ± 0.03	—
30°	4.54 ± 1.23	0.38 ± 0.05	—
45°	4.92 ± 0.52	0.45 ± 0.03	—
60°	6.70 ± 0.57	0.53 ± 0.03	—
75°	5.47 ± 2.15	0.69 ± 0.09	—
90° (Arrester)	7.63 ± 0.75	0.74 ± 0.06	—
Divider	8.65 ± 0.70	0.71 ± 0.05	0.73 ± 0.06

Note. It was only possible to measure the fracture toughness in the Short-transverse and Divider orientations using the short-rod (SR) methodology. However, the measured values in these orientations are in good agreement with the corresponding values using the semicircular bend (SCB) methodology.

The fracture toughness data presented in Figure 9 exhibit similar characteristics to those of the tensile strength data (Figure 8), but with significantly less scatter. Again, there is a progressive increase in values from samples tested in the Short-transverse orientation to those tested in the Arrester orientation; with the Arrester orientation values being some 3 times higher than the Short-transverse value. However, values for the Arrester and Divider orientations are essentially the same. This is entirely as expected, because the fracture necessarily traverses all of the available interfaces in both of these orientations. In the Arrester orientation all of the interfaces are sampled sequentially, while in the Divider orientation they are all sampled simultaneously.

5.2. Comparison of the Fracture Properties of Nash Point Shale With Those of Other Shales

Fracture toughness values for a range of shales are presented in Table 2; taken from the literature, where values were directly measured in more than one principal orientation. The K_{Ic} values measured in this study for Nash Point shale all lie within the range of values for other shales listed in Table 2. Furthermore, the data from all of the studies where K_{Ic} was measured in all three principal orientations (Schmidt, 1977; Chandler et al., 2016; this study) demonstrate a very similar relationship; with K_{Ic} values for the Arrester and Divider orientations being generally very similar, but much higher than values for the Short-transverse orientation.

From the Griffith criterion (Paterson & Wong, 2005), we can write the following relationship between tensile strength and mode-I fracture toughness:

$$\sigma_t = C\frac{K_{Ic}}{\sqrt{a}} \tag{6}$$

where σ_t is tensile strength, C is a dimensionless geometric factor, and a is a characteristic flaw size. Previous compilations have shown that a broadly linear relationship exists between K_{Ic} and the tensile strength of numerous rock types (e.g., Bhagat, 1985; Chandler et al., 2016; Gunsallus & Kulhawy, 1984; Zhang, 2002). We illustrate this relationship for shales in Figure 11, where both K_{Ic} and tensile strength data were available for the same rock in the same study (Chandler et al., 2016; Chong et al., 1987; Schmidt, 1977). Note that data from Chong et al. (1987) are included in Figure 11, but were not included in Table 2 as values were only measured in a single orientation. The data of Figure 11 include values from tests in the three principal fracture orientations, together with values from this study measured at angles between the Short-transverse and Arrester orientations. A linear least squares fit to the data of Figure 11 is found to have a gradient of 13.7 $m^{-1/2}$ with an associated R^2 value of 0.71. As previously discussed by Chandler et al. (2016), where the K_{Ic} versus σ_t relationship is essentially linear, this implies that the characteristic flaw size controlling fracture nucleation is essentially the same between the different shale formations and the different fracture orientations.

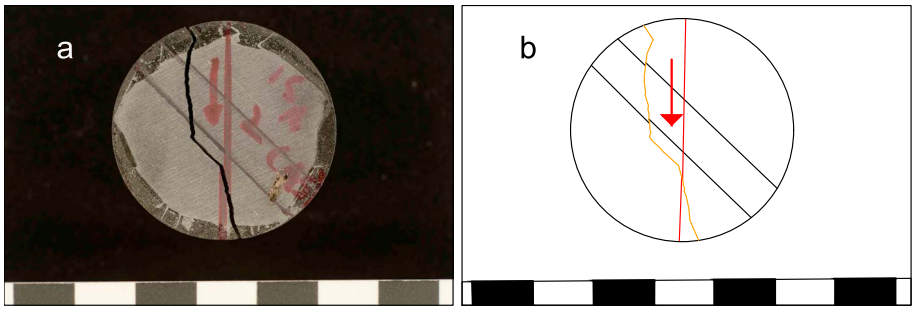

Figure 10. (a) Photo and (b) corresponding schematic sketch of a tested Brazil disk sample demonstrating how the induced fracture (orange) steps between the bedding plane (solid black lines across the sample) and the loading direction (red arrow).

Table 2
Summary of K_{Ic} Values From This Study and Others in Which K_{Ic} was Directly Measured in More Than One of the Principal Fracture Orientations

Material	K_{Ic}, Short-transverse (MPa m$^{1/2}$)	K_{Ic}, Arrester (MPa m$^{1/2}$)	K_{Ic}, Divider (MPa m$^{1/2}$)	Methodology	Reference
Nash Point shale	0.24	0.74	0.71	SCB	This study
Nash Point shale	0.3	—	0.73	Short-rod	This study
Mancos shale[a]	0.12 (ST_{low}); 0.31 (ST_{high})	0.44	0.44	Short-rod	Chandler et al. (2016)
Marcellus shale	-	0.73	0.47	SCB	Lee et al. (2015)
Anvil Points shale (80 ml/kg kerogen content)	0.75	0.98	1.08	Three-point bending	Schmidt, (1977)
Anvil Points shale (160 ml/kg kerogen content)	0.37	0.60	0.67	Three-point bending	Schmidt (1977)

Note. SCB = semicircular bend.
[a]Chandler et al. (2016) found that the K_{Ic} measured in the Short-transverse orientation had a bimodal distribution, and so both values are given in this table.

5.3. Fracture Orientation and Tortuosity

Postmortem examination of samples from both fracture toughness and tensile strength tests shows that fractures propagating in the Short-transverse and Divider orientations are relatively straight in comparison with those propagating in other orientations (Figures 12 and 13). Deflection of the induced fractures away from the loading direction and toward the Short-transverse orientation is common both in samples tested at intermediate angles (Figure 12) and in those tested in the Arrester orientation (Figure 13). In comparison with undeflected fractures, we observe that deflected fractures are more tortuous, and we suggest that this tortuosity is again due to competition between the orientation of the applied load and the orientation of the weak Short-transverse orientation throughout the propagation of the fracture.

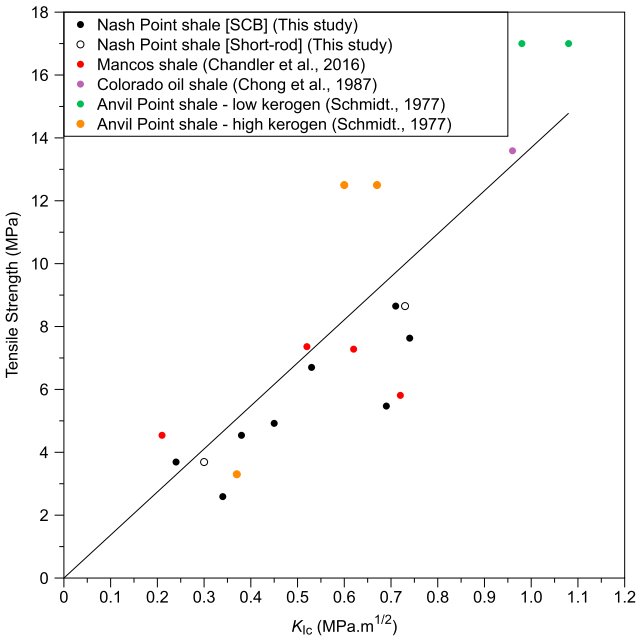

Figure 11. The relationship between tensile strength and fracture toughness of different shale formations (Chandler et al., 2016; Chong et al., 1987; Schmidt, 1977). The solid line is a linear least squares fit to the data, with a forced intercept of zero, a gradient of 13.7 m$^{-1/2}$, and an R^2 value of 0.71.

This phenomenon has also been reported by Tavallali and Vervoort (2013), from a study in which they analyzed the fracture patterns produced from Brazil disk tensile tests on a transversely isotropic layered sandstone from Modave (southern Belgium). Tavallali and Vervoort (2013) conducted tests over a range of angles between bedding parallel and bedding normal and report that different modes of fracture occurred at the different angles. They therefore report their values as *Failure strengths* rather than *Tensile strengths*. Furthermore, we have noted earlier that a significant number of the fractures in our Brazil disk tensile strength tests did not pass through the center of the sample. This was also reported by Tavallali & Vervoort, 2013) and Na et al. (2017). Consequently, we conclude that we cannot be confident that the failure loads in these tests correspond to the true tensile strength, and we have therefore reported the results as *apparent tensile strength*. At the time of writing we know of no method that can be used to correct such tensile strength values to account for fracture deflections. However, we have developed a method that can be used to correct fracture toughness values when the fracture is deflected from its intended propagation direction; and we present this analysis below. Overall, we therefore consider fracture toughness to be a more fundamental and rigorous measure of the resistance to tensile fracture propagation, especially in anisotropic materials such as shales.

5.4. Determination of the Point at Which Fracture Toughness Is Evaluated

In Figure 14, we plot the dimensionless stress intensity factor for the SCB specimen (from equation (4)), Y', as a function of the dimensionless

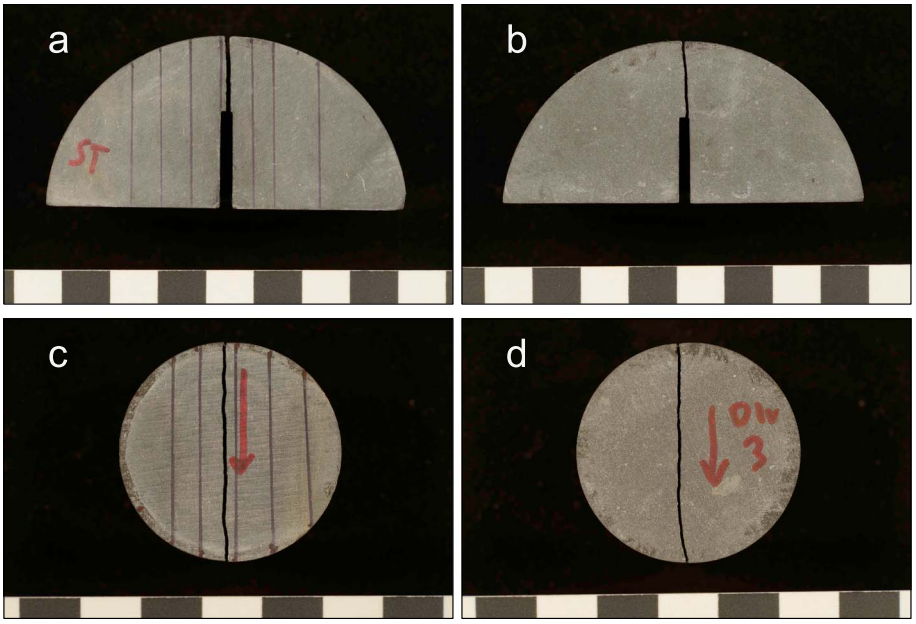

Figure 12. SCB and Brazil disk samples tested in the Short-transverse (12a, 12c) and Divider (12b, 12d) orientations. Solid black lines show the orientation of the bedding plane and a scale bar lies below each sample where each division is 1 cm. Fractures in these orientations are straight and propagate both parallel to the loading orientation and bedding plane.

fracture length, β, for a sample with the dimensions used in this study. The red circle shows the values of Y' and β for our sample dimensions with a notional notch depth of 22 mm. In the region where the dimensionless stress intensity is decreasing as a function of increasing fracture length (left of the vertical dashed line), the fracture propagation is inherently stable. By contrast, in the region where the dimensionless stress intensity is increasing as a function of increasing fracture length (right of the vertical

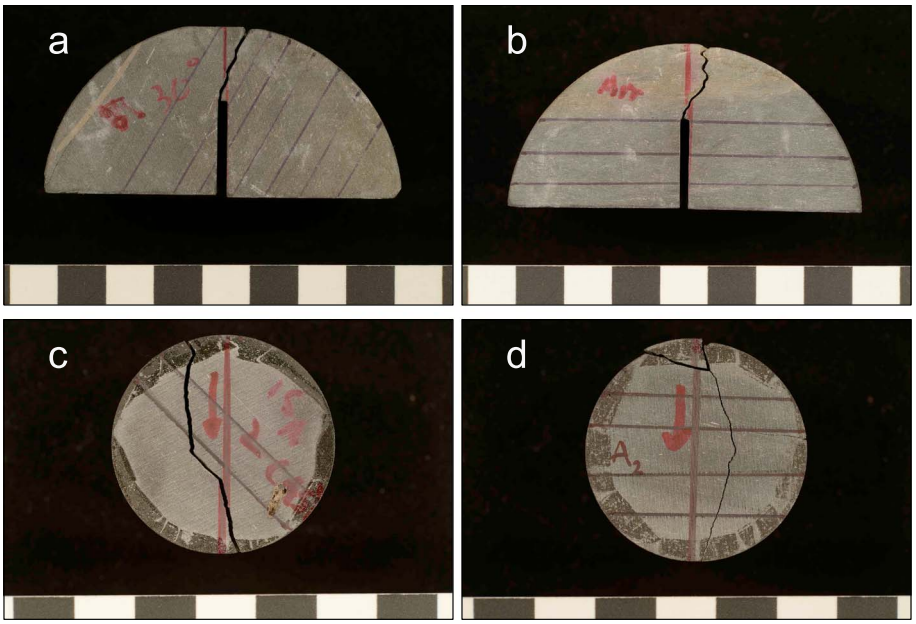

Figure 13. SCB and Brazil disk samples tested oblique to bedding (13a, 13c) and in Arrester orientation (13b, 13d). Solid black lines show the orientation of the bedding plane, and a scale bar lies below each sample where each division is 1 cm. Fractures in these orientations are tortuous and often deflect toward the Short-transverse orientation.

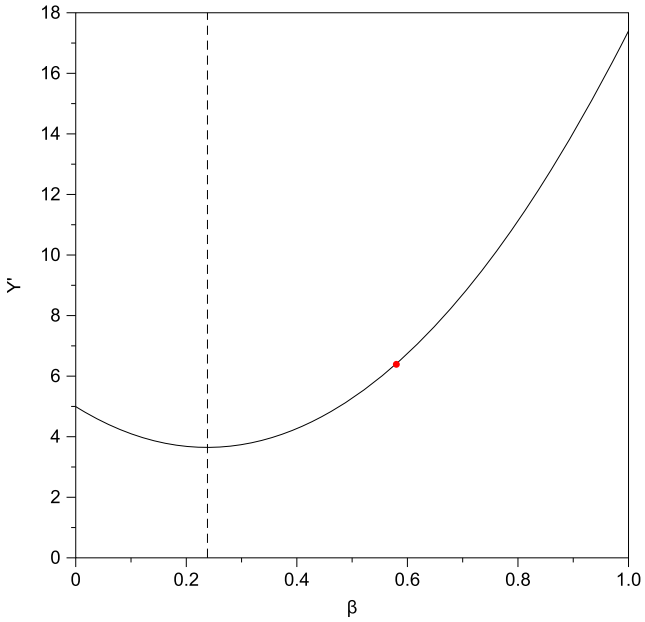

Figure 14. Dimensionless stress intensity factor, Y', as a function of dimensionless fracture length, β, for the semicircular bend (SCB) specimen geometry, calculated from equation (5). The red point shows Y' and β for our chosen notch depth. The vertical dashed line marks the minimum in Y' which separates the region where fracture growth is inherently stable (left of dashed line) from the region where it is inherently unstable (right of dashed line).

dashed line), the fracture propagation is inherently unstable. For this study, we specifically chose sample dimensions so that the values of Y' and β were comfortably within the region of the $Y'(\beta)$ curve where the fracture would always propagate in an unstable (critical) manner (red circle to the right of the vertical dashed line in Figure 14). Under these circumstances, the peak load is recorded at the onset of fracture propagation, and K_{Ic} is therefore also evaluated at this point. Hence, if the fracture deflects after some increment of growth in the correct orientation (e.g., Figure 15a), the fracture toughness evaluation remains valid. Only if the fracture deflection occurs from the initiation point (e.g., Figure 15b) does the calculation become invalid, and the fracture deflection then needs to be accounted for in the evaluation of the fracture toughness.

5.5. Effect of Deflection on Fracture Toughness

When propagating fractures deviate from the intended orientation, they most commonly deflect toward the weaker Short-transverse orientation. An example is shown in Figure 15b. Here the notch is cut at 60° to bedding but the fracture deflects immediately from its initiation point through an angle of approximately 33°, so that it propagates at an angle of 27° to bedding. Under these conditions, the fracture propagates in mixed mode, rather than as a pure mode-I fracture, and we can no longer assume that K_{II} is zero. Furthermore, it is important to recall that, for a sample with a starter notch oriented at angle of ϕ to the Arrester orientation (i.e., 90° − ϕ to bedding), the measured fracture toughness is only valid for that angle if the fracture continues to propagate at angle ϕ at least to the point where the peak load is recorded. If the fracture becomes deflected before this point and propagates at some other angle, ζ, then the apparent fracture toughness evaluated from the peak load K_{Ic} (ζ) needs to be corrected by some geometric factor that takes account of the deflection. The relevant angles for such an analysis are illustrated and defined in Figure 16.

We have therefore developed a method of correcting the measured apparent K_{Ic} for deflections from the initiation path. This allows determination of a deflected-corrected mode-I stress intensity factor, K_{Id}. However, since the deflected fracture propagates in mixed mode, critical crack growth is likely controlled by some combination of K_I and K_{II}, and hence K_{Id} alone cannot be considered a critical value. The two-dimensional symmetry of the SCB specimen, together with direct postmortem measurement of the deflection angle from the sample surface, allows us to use the known stress intensities at the tip of the starter notch and the measured deflection angle to determine the forms of the deflection-corrected mode-I and mode-II stress intensities, K_{Id} and K_{IId}, as set out below.

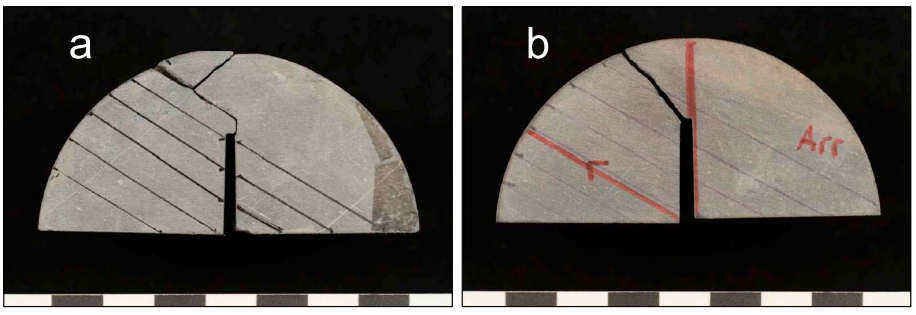

Figure 15. (a) A sample manufactured at 60° to bedding where the fracture has deviated during loading, but not immediately. (b) A fractured sample manufactured at 60° to bedding, in which the fracture immediately deviates to 27° to bedding. Black lines depict the bedding plane, and a scale bar lies below each sample where each division is 1 cm.

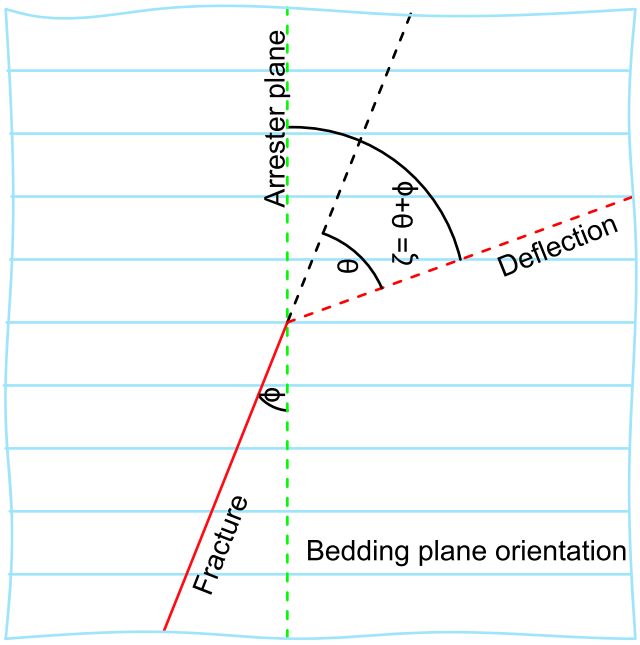

Figure 16. Definitions of the angles used in the analysis here. ϕ is the angle between the initial notch and the Arrester orientation. θ is the angle between the deflected fracture and the initial notch. ζ is the angle between the deflected fracture and the Arrester orientation ($\zeta = \theta + \phi$). Modified after Chandler et al. (2016).

5.6. Stress Intensity at the Tip of a Deflected Fracture

Cotterell and Rice (1980) solved for the mode-I and mode-II stress intensity factors, K_I and K_{II}, at the tip of an infinitesimal deflection of a two-dimensional fracture in an elastically isotropic material from the stress intensities and surface tractions of the initiating deflection. The deflection stress intensity factors, K_{Id} and K_{IId}, are given by

$$K_{Id} = C_{11}K_I + C_{12}K_{II} \tag{7}$$

$$K_{IId} = C_{21}K_I + C_{22}K_{II} \tag{8}$$

where

$$C_{11} = \frac{1}{4}\left[3\cos\left(\frac{\theta}{2}\right) + \cos\left(\frac{3\theta}{2}\right)\right] \tag{9}$$

$$C_{12} = \frac{3}{4}\left[\sin\left(\frac{\theta}{2}\right) + \sin\left(\frac{3\theta}{2}\right)\right] \tag{10}$$

$$C_{21} = \frac{1}{4}\left[\sin\left(\frac{\theta}{2}\right) + \sin\left(\frac{3\theta}{2}\right)\right] \tag{11}$$

$$C_{22} = \frac{1}{4}\left[\cos\left(\frac{\theta}{2}\right) + 3\cos\left(\frac{3\theta}{2}\right)\right] \tag{12}$$

and K_I and K_{II} are the stress intensity factors in the intended fracture orientation and θ is the angle from that orientation at which the deflection initiates. In using equations (7) and (8), which were derived for an elastically isotropic material, we inherently assume that the effect of the fracture toughness anisotropy significantly outweighs any effect of elastic anisotropy. Cotterell and Rice (1980) showed that, for the cases of pure mode-I and mode-II loading of the main fracture, these functions agree with the computations of Bilby et al. (1978) to within 5% and 10%, respectively, for values of θ from 0° to 90°.

Since, for our sample geometry, the peak load is recorded at the onset of fracture growth (as shown in section 5.4), the mode-I stress intensity factor of the main fracture, K_I, can be determined from equation (3) with a' set equal to the modified (actual) notch length, and K_{II} set equal to zero. If θ is set equal to the measured initial deflection angle on the sample surface, then equations (7) and (8) can be used to find the stress intensities at the tip of an infinitesimal deflection in this θ direction. We can therefore use the value of K_{Ic} determined from equation (3), in combination with the measured deflection angle, to determine the deflection-corrected stress intensity values, K_{Id} and K_{IId}, measured at the deflection point, simply from $K_{Id} = C_{11} \times K_{Ic}$, and $K_{IId} = C_{21} \times K_{Ic}$.

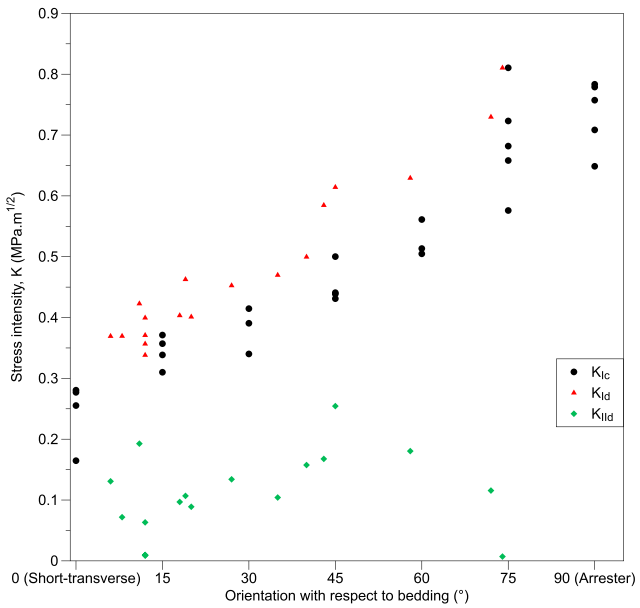

Figure 17. K_{Ic}, K_{Id}, and K_{IId} as a function of orientation from bedding.

Figure 17 shows values of K_{Ic} plotted as a function of orientation to bedding for un-deflected fractures, together with K_{Id} and K_{IId} for deflected fractures, also plotted as functions of orientation to bedding. The magnitude of the correction to K_{Ic} required to obtain the values of K_{Id} for the deflected fractures is seen to be small but systematic, with values of K_{Id} always being slightly higher than K_{Ic} for the same orientation. The calculated values of K_{IId} appear to show no systematic change with orientation across the whole data range and exhibit a mean of 0.11 ± 0.07 MPa $m^{1/2}$. However, since K_{IId} is not negligible with respect to K_{Id}, especially at low angles to bedding, we suggest that a fracture energy-based approach may be more appropriate than a stress intensity-based approach in analyzing the full spectrum of fracture propagation in this material.

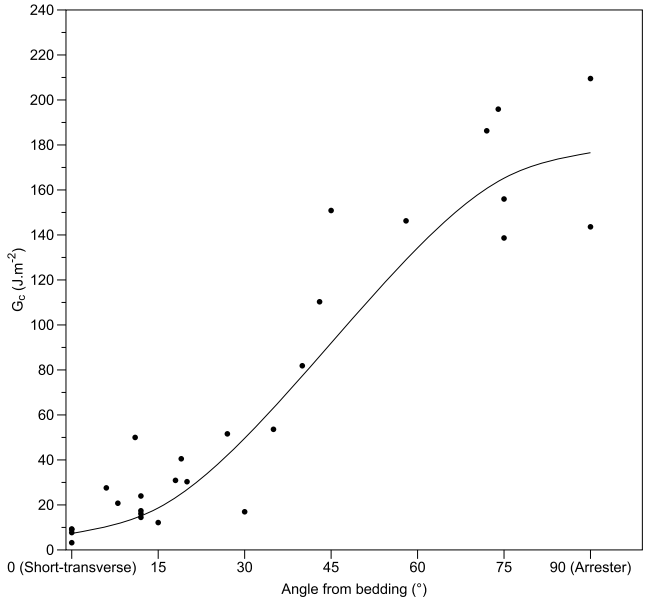

Figure 18. G_c as a function of angle from bedding. The solid curve is derived from equation (17) where $G_{c,Arrester}$ and $G_{c,Short\text{-}transverse}$ are found to be 176.56 J/m^2 and 7.32 J/m^2, respectively.

5.7. Fracture Energy at the Tip of Deflected and Undeflected Fractures

The fracture energy, G, can be determined directly from the stress intensities via

$$G = \frac{1-\nu^2}{E}\left(K_I^2 + K_{II}^2\right) \tag{13}$$

where ν is Poisson's ratio and E is Young's modulus. For the case of a critical undeflected fracture, $K_I = K_{Ic}$ and $K_{II} = 0$. Therefore,

$$G_c = \frac{1-\nu^2}{E}K_{Ic}^2 \tag{14}$$

However, for deflected fractures, $K_I = K_{Id}$ and $K_{II} = K_{IId}$. So we can write

$$G_c = \frac{1-\nu^2}{E}\left({K_{Id}}^2 + {K_{IId}}^2\right) \tag{15}$$

However, for an anisotropic material like shale, the values of Young's modulus and Poisson's ratio will also vary as a function of orientation, as has previously been discussed by Ong et al. (2016) and Meléndez-Martínez and Schmitt (2016). We have therefore measured the static Young's modulus and Poisson's ratio on cylindrical samples of Nash Point shale in both the bedding-normal and bedding-parallel orientations. We have also calculated the dynamic Young's modulus for each orientation using the elastic wave velocity data of Figure 4 and standard relationships (Eissa & Kazi, 1988; King, 1983). Finally, we calculated the static Young's moduli for each orientation by normalizing the end-member dynamic values to the static values measured parallel and normal to bedding, with the assumption that the same relation applies across the whole range of angles. A complete description of the methodology, together with plots of the dynamic and static moduli and a table of all the values used in our calculations of G_c from equations (14) and (15) is presented in the Supporting Information S1. Our measured values of static Poisson's ratio vary by more than a factor of 4 between the bedding-normal and bedding-parallel orientations. However, the expression for Poisson's ratio used in the calculation of G_c is $(1 - \nu^2)$. Substituting our end-member measured values into this expression gives a value of 0.92 ± 0.07, a variation of less than 8%. We have therefore used this mean value in all our calculations of G_c. Again, a full description is provided in the supporting information.

We plot the resulting fracture energies as a function of orientation from bedding in Figure 18. We observe that G_c increases as the angle from bedding increases, but in a nonlinear manner.

Sesetty and Ghassemi (2016) suggested that the fracture toughness of anisotropic materials should vary elliptically with respect to fracture orientation from bedding and that the fracture toughness at any angle (β) between the Short-transverse and Arrester orientations could therefore be approximated by the following relation:

$$K_{Ic,\beta} = K_{Ic,Arrester}\sin^2(\beta) + K_{Ic,Short=transverse}\cos^2(\beta) \tag{16}$$

where β is the angle measured from the Short-transverse orientation. Their suggestion is based on the work of Buczek and Herakovich (1985) who reasoned that the tensile strength of anisotropic rocks varied elliptically between the Short-transverse and Arrester values, and the linear relationship between tensile strength and fracture toughness (equation (6)). However, we find that neither our tensile strength nor our fracture toughness data are well described by such an elliptical approximation. By contrast, we find that an elliptical approximation provides a good fit to the fracture energy data according to

$$G_{c,\beta} = G_{c,Arrester}\sin^2(\beta) + G_{c,Short\text{-}transverse}\cos^2(\beta) \tag{17}$$

We have therefore plotted this function on Figure 18, constrained by our end-member Short-transverse and Arrester values of G_c. While there is clearly some scatter, we find the function fits well, with an R^2 value of 0.90.

We suggest that the reason why fracture energy appears to vary elliptically between the Short-transverse and Arrester orientations, while tensile strength and fracture toughness do not, may well be because fracture energy is able to take account of any fracture propagation with a mixed mode element, while the other parameters are not.

6. Conclusions

We report a study in which we have measured ultrasonic wave velocities, tensile strength, and fracture toughness on samples of Nash Point shale in multiple orientations, including the three principal fracture orientations (Short-transverse, Arrester, and Divider). We used the Brazil disk technique to measure apparent tensile strength and the SCB methodology to measure fracture toughness. It was found that both the apparent tensile strength and the fracture toughness of Nash Point shale were much lower in samples tested in the Short-transverse than in the Arrester orientations. Samples tested in the Divider orientation, produced values that were very similar to samples tested in the Arrester orientation. Both the apparent tensile strength and fracture toughness increased progressively between the Short-transverse and the Arrester orientations.

Fracture deflection was commonly observed in both apparent tensile strength and fracture toughness samples, with fractures deviating from the intended direction toward the weaker Short-transverse orientation. We therefore propose a method of correcting the measured apparent K_{Ic} for fractures that are deflected from the initiation point. This allows the determination of a deflection-corrected mode-I stress intensity factor, K_{Id}. However, since deflected fractures propagate in mixed mode, critical crack growth is likely controlled by some combination of K_I and K_{II}, and hence K_{Id} alone cannot be considered a critical value. We therefore adopted a fracture energy (G_c) based approach to analyze fracture propagation at orientations between the Short-transverse and Arrester orientations and determined the angular variation of G_c.

We observe that G_c increases with increasing angle to bedding, but in a nonlinear manner. Further, we find that the orientation-dependent G_c values are well fit by an elliptical relation with an R^2 value of 0.90. As such we propose that it is possible to calculate a good approximation of G_c values at angles between the Short-transverse and Arrester orientation of an anisotropic material using the approach presenent here and the Short-transverse and Arrester values.

Hydraulic fractures in unconventional oil and gas reservoirs are often modeled as having straight geometries with little or no correction for roughness, tortuosity, or deflection (Li et al., 2017; Wangen, 2017; Zhao et al., 2017). Furthermore, many models also consider reservoirs to be mechanically isotropic (Feng & Gray, 2018; Li et al., 2017; Wangen, 2017; Zhao et al., 2017). Our results demonstrate that neither assumption is likely to be valid either for shale units or reservoirs composed largely of shale. However, the results presented should be useful in the analysis of how fractures may propagate in highly anisotropic rocks, such as shales, especially where the propagation path is oblique to the three principal directions (Short-transverse, Arrester, and Divider). Such analysis may enhance development and management of unconventional oil and gas reservoirs and understanding the integrity of seals in conventional and carbon capture and storage reservoirs.

Acknowledgments
We thank the NERC CDT in Oil and Gas (grant NE/M00578X/1), and Hannon Westwood for supporting N. F. I. through his research, while M. C. acknowledges support from the UK Natural Environment Research Council (grant NE/M001458/1). We also thank Neil Hughes, Steve Boon, Jim Davy, and John Bowles for help with the experimental work, and Nicolas Brantut for his help in analyzing the fracture deflections in the SCB samples. Finally, we thank Stephan Gehne, John Webb, Kathryn Lamb, Emma Davies, John Corr, Jackie Forbes Inskip, Roy Forbes Inskip, Robert Inskip, and Sally Inskip for their help in collecting samples from Nash Point and for their general support. We thank Julia Gale and Douglas Schmitt for thoughtful and detailed comments on an earlier version of this manuscript, which have helped improve the text and clarify the arguments. All data used for this study can be accessed via the data repository Hydroshare: http://www.hydroshare.org/resource/2491340819 3b41caa1896a6e60327946

References

Bhagat, R. (1985). Mode I fracture toughness of coal. *International Journal of Mining Engineering*, *3*(3), 229–236. https://doi.org/10.1007/BF00880769

Bilby, B. A., Cardew, G. E., & Howard, I. C. (1978). Stress intensity factors at the tips of kinked and forked cracks. In D. M. R. Taplin (Ed.), *Advances in research on the strength and fracture of materials* (pp. 197–200). New York: Pergamon. https://doi.org/10.1016/B978-0-08-022142-7.50039-9

Birch, F. (1960). The velocity of compressional waves in rocks to 10 kilobars, Part 1. *Journal of Geophysical Research*, *65*, 1083–1102. https://doi.org/10.1029/JZ065i004p01083

Boyer, C., Lewis, R., Miller, C. K., & Clark, B. (2011). Shale gas: A global resource. Oilfield Review.

Buczek, M. B., & Herakovich, C. T. (1985). A normal stress criterion for crack extension direction in orthotropic composite materials. *Journal of Composite Materials*, *19*(6), 544–553. https://doi.org/10.1177/002199838501900606

Chalmers, G. R. L., & Bustin, R. M. (2017). A multidisciplinary approach in determining the maceral (kerogen type) and mineralogical composition of Upper Cretaceous Eagle Ford Formation: Impact on pore development and pore size distribution. *International Journal of Coal Geology*, *171*, 93–110. https://doi.org/10.1016/j.coal.2017.01.004

Chandler, M. R. (2014). A fracture mechanics study of an anisotropic shale. Univeristy College London.

Chandler, M. R., Meredith, P. G., Brantut, N., & Crawford, B. R. (2016). Fracture toughness anisotropy in shale. *Journal of Geophysical Research: Solid Earth*, *121*, 1706–1729. https://doi.org/10.1002/2015JB012756

Chen, C., & Amadei, B. (1998). Determination of deformability and tensile strength of anisotropic rock using Brazilian tests. *International Journal of Rock Mechanics and Mining Sciences*, *35*(1), 43–61. https://doi.org/10.1016/S0148-9062(97)00329-X

Chong, K. P., Kuruppu, M. D., & Kuszmaul, J. S. (1987). Fracture toughness determination of layered materials. *Engineering Fracture Mechanics*, *28*(1), 43–54. https://doi.org/10.1016/0013-7944(87)90118-4

Claesson, J., & Bohloli, B. (2002). Brazilian test: Stress field and tensile strength of anisotropic rocks using an analytical solution. *International Journal of Rock Mechanics and Mining Sciences*, *39*(8), 991–1004. https://doi.org/10.1016/S1365-1609(02)00099-0

Cornford, C. (1986). The Bristol Channel graben: Organic geochemical limits on subsidence and speculation on the origin of inversion. *Geoscience in South-West England*, *6*(3), 360–367.

Cotterell, B., & Rice, J. R. (1980). Slightly curved or kinked cracks. *International Journal of Fracture*, *16*(2), 155–169. https://doi.org/10.1007/BF00012619

Dewhurst, D. N., & Siggins, A. F. (2006). Impact of fabric, microcracks and stress field on shale anisotropy. *Geophysical Journal International*, *165*, 135–148.

Eissa, E. A., & Kazi, A. (1988). Relation between static and dynamic Young's moduli of rocks. *International Journal of Rock Mechanics and Mining Sciences And*, *25*(6), 479–482. https://doi.org/10.1016/0148-9062(88)90987-4

Elston, H. W. (2014). Mineralogical and geochemical assessment of the Eagle Ford shale. Ohio State University.

Feng, Y., & Gray, K. E. (2018). Modeling of curving hydraulic fracture propagation from a wellbore in a poroelastic medium. *Journal of Natural Gas Science and Engineering*, *53*, 83–93. https://doi.org/10.1016/j.jngse.2018.02.020

Gunsallus, K. L., & Kulhawy, F. H. (1984). A comparative evaluation of rock strength measures. *International Journal of Rock Mechanics and Mining Sciences and Geomechanics*, *21*(5), 233–248. https://doi.org/10.1016/0148-9062(84)92680-9

Heap, M. J., Vinciguerra, S., & Meredith, P. G. (2009). The evolution of elastic moduli with increasing crack damage during cyclic stressing of a basalt from Mt. Etna volcano. *Tectonophysics*, *471*(1–2), 153–160. https://doi.org/10.1016/j.tecto.2008.10.004

International Society for Rock Mechanics (1978). Suggested methods for determining tensile strength of rock materials. *International Journal of Rock Mechanics and Mining Sciences and Geomechanics*, *15*(3), 99–103. https://doi.org/10.1016/0148-9062(78)90003-7

International Society for Rock Mechanics (1988). Suggested methods for determining the fracture toughness of rock. *International Journal of Rock Mechanics and Mining Science and Geomechanics Abstracts*, *33*(8), 803–847. https://doi.org/10.1016/S0148-9062(96)00015-0

Islam, M. A., & Skalle, P. (2013). An experimental investigation of shale mechanical properties through drained and undrained test mechanisms. *Rock Mechanics and Rock Engineering*, *46*(6), 1391–1413. https://doi.org/10.1007/s00603-013-0377-8

Johnston, J. E., & Christensen, N. I. (1995). Seismic anisotropy of shales. *Journal of Geophysical Research*, *100*(B4), 5991–6003.

Kabir, P., Ulm, F.-J., & Akono, A.-T. (2017). Rate-independent fracture toughness of gray and black kerogen-rich shales. *Acta Geotechnica*. https://doi.org/10.1007/s11440-017-0562-0

King, M. S. (1983). Static and dynamic elastic properties of rocks from the Canadian shield. *International Journal of Rock Mechanics and Mining Science and Geomechanics Abstracts*, *20*(5), 237–241. https://doi.org/10.1016/0148-9062(83)90004-9

Knorr, A. F. (2016). The effect of rock properties on fracture conductivity in the Eagle Ford. SPE Asia Pacific Hydraulic Fracturing Conference. Texas A&M University. https://doi.org/10.2118/181867-MS

Kuruppu, M. D., Obara, Y., Ayatollahi, M. R., Chong, K. P., & Funatsu, T. (2014). ISRM-suggested method for determining the Mode I static fracture toughness using semi-circular bend specimen. In R. Ulusay (Ed.), *The ISRM suggested methods for rock characterization, testing and monitoring 2007–2014* (pp. 107–114). Wien: Springer.

Lee, H. P., Olson, J. E., Holder, J., Gale, J. F. W., & Myers, R. D. (2015). The interaction of propagating opening mode fractures with preexisting discontinuities in shale. *Journal of Geophysical Research: Solid Earth*, *120*, 169–181. https://doi.org/10.1002/2014JB011358

Levine, J. S., Fukai, I., Soeder, D. J., Bromhal, G., Dilmore, R. M., Guthrie, G. D., et al. (2016). U.S. DOE NETL methodology for estimating the prospective CO_2 storage resource of shales at the national and regional scale. *International Journal of Greenhouse Gas Control*, *51*, 81–94. https://doi.org/10.1016/j.ijggc.2016.04.028

Li, W., Rezakhani, R., Jin, C., Zhou, X., & Cusatis, G. (2017). A multiscale framework for the simulation of the anisotropic mechanical behavior of shale. *International Journal for Numerical and Analytical Methods in Geomechanics*, *41*(14), 1494–1522. https://doi.org/10.1002/nag.2684

Meléndez-Martínez, J., & Schmitt, D. R. (2016). A comparative study of the anisotropic dynamic and static elastic moduli of unconventional reservoir shales: Implication for geomechanical investigations. *Geophysics*, *81*(3), D245–D261. https://doi.org/10.1190/geo2015-0427.1

Milliken, K. L., Ergene, S. M., & Ozkan, A. (2016). Quartz types, authigenic and detrital, in the upper cretaceous eagle ford formation, South Texas, USA. *Sedimentary Geology*, *339*, 273–288. https://doi.org/10.1016/j.sedgeo.2016.03.012

Mokhtari, M. (2015). Characterization of anisotropy in organic-rich shales: Shear and tensile failure, wave velocity, matrix and fracture permeability. Colorado School of Mines.

Mullen, J., Lowry, J. C., & Nwabuoku, K. C. (2010). Lessons learned developing the Eagle Ford shale. In *SPE Tight Gas Completions Conference* (pp. 2–3). https://doi.org/10.2118/138446-MS

Na, S. H., Sun, W. C., Ingraham, M. D., & Yoon, H. (2017). Effects of spatial heterogeneity and material anisotropy on the fracture pattern and macroscopic effective toughness of Mancos shale in Brazilian tests. *Journal of Geophysical Research: Solid Earth*, *122*, 6202–6230. https://doi.org/10.1002/2016JB013374

Ong, O. N., Schmitt, D. R., Kofman, R. S., & Haug, K. (2016). Static and dynamic pressure sensitivity anisotropy of a calcareous shale. *Geophysical Prospecting*, *64*(4), 875–897. https://doi.org/10.1111/1365-2478.12403

Paterson, M. S., & Wong, T. (2005). *experimental rock deformation—The brittle field*. Berlin: Springer.

Rybacki, E., Reinicke, A., Meier, T., Makasi, M., & Dresen, G. (2015). What controls the mechanical properties of shale rocks?—Part I: Strength and Young's modulus. *Journal of Petroleum Science and Engineering*, *135*, 702–722. https://doi.org/10.1016/j.petrol.2015.10.028

Schmidt, R. A. (1977). Fracture mechanics of oil shale—Unconfined fracture toughness, stress corrosion cracking, and tension test results. In *The 18th U.S. Symposium on Rock Mechanics (USRMS)*. American Rock Mechanics Association.

Sesetty, V., & Ghassemi, A. (2016). Numerical modeling of hydraulic fracture propagation from horizontal wells in anisotropic shale. 50th US Rock Mechanics/Geomechanics Symposium.

Tavallali, A., & Vervoort, A. (2013). Behaviour of layered sandstone under Brazilian test conditions: Layer orientation and shape effects. *Journal of Rock Mechanics and Geotechnical Engineering*, *5*(5), 366–377. https://doi.org/10.1016/j.jrmge.2013.01.004

Vinciguerra, S., Trovato, C., Meredith, P. G., & Benson, P. M. (2005). Relating seismic velocities, thermal cracking and permeability in Mt. Etna and Iceland basalts. *International Journal of Rock Mechanics and Mining Sciences*, *42*(7-8), 900–910. https://doi.org/10.1016/j.ijrmms.2005.05.022

Wangen, M. (2017). A 2D volume conservative numerical model of hydraulic fracturing. *Computers and Structures*, *182*, 448–458. https://doi.org/10.1016/j.compstruc.2017.01.003

Warpinski, N., & Smith, M. B. (1990). Rock mechanics and fracture geometry. In J. L. Gidley, S. A. Holditch, D. E. Nierode, & R. W. Veatch, Jr. (Eds.), *Recent advances in Hydraulic Fracturing* (pp. 57–80). Richardson, TX: Society of Petroleum Engineers.

Young, C., Patti, N. C., & Trent, B. C. (1982). *Stratigraphic variations in oil shale fracture properties*. Larime, Wyoming: USA Department of Energy.

Zhang, Z. X. (2002). An empirical relation between mode I fracture toughness and the tensile strength of rock. *International Journal of Rock Mechanics and Mining Sciences*, *39*(3), 401–406. https://doi.org/10.1016/S1365-1609(02)00032-1

Zhao, J., Chen, X., Li, Y., Fu, B., & Xu, W. (2017). Numerical simulation of multi-stage fracturing and optimization of perforation in a horizontal well. *Petroleum Exploration and Development*, *44*(1), 119–126. https://doi.org/10.1016/S1876-3804(17)30015-0

Journal of Geophysical Research

Supporting Information for

Fracture properties of Nash Point shale as a function of orientation to bedding

Nathaniel D. Forbes Inskip[1,2], Philip G. Meredith[2], Michael R. Chandler[3] and Agust Gudmundsson[1]

[1] Department of Earth Science, Royal Holloway, University of London, Egham, United Kingdom

[2] Department of Earth Science, University College London, London, United Kingdom

[3] School of Earth, and Environmental Sciences, University of Manchester, Manchester, United Kingdom

Contents of this file

Introduction

In order to calculate G_c using equations (14) and (15) in section 5.7. both the Young's modulus and Poisson's ratio need to be known. For an anisotropic material like shale, the values of Young's modulus and Poisson's ratio will vary as a function of orientation. We have therefore calculated the relevant dynamic elastic moduli for each orientation using the elastic wave velocity data of Figure 4 and the standard relationships (Eissa & Kazi, 1988; King, 1983). We then calculated the static moduli by normalizing the end-member dynamic values to the static values measured parallel and normal to bedding, with the assumption that the same relation applied across the whole range of angles. These angular dependent values are presented in Figures S1 and S2 and were then used to calculate values of G_c for all fracture orientations from equations (14) and (15).

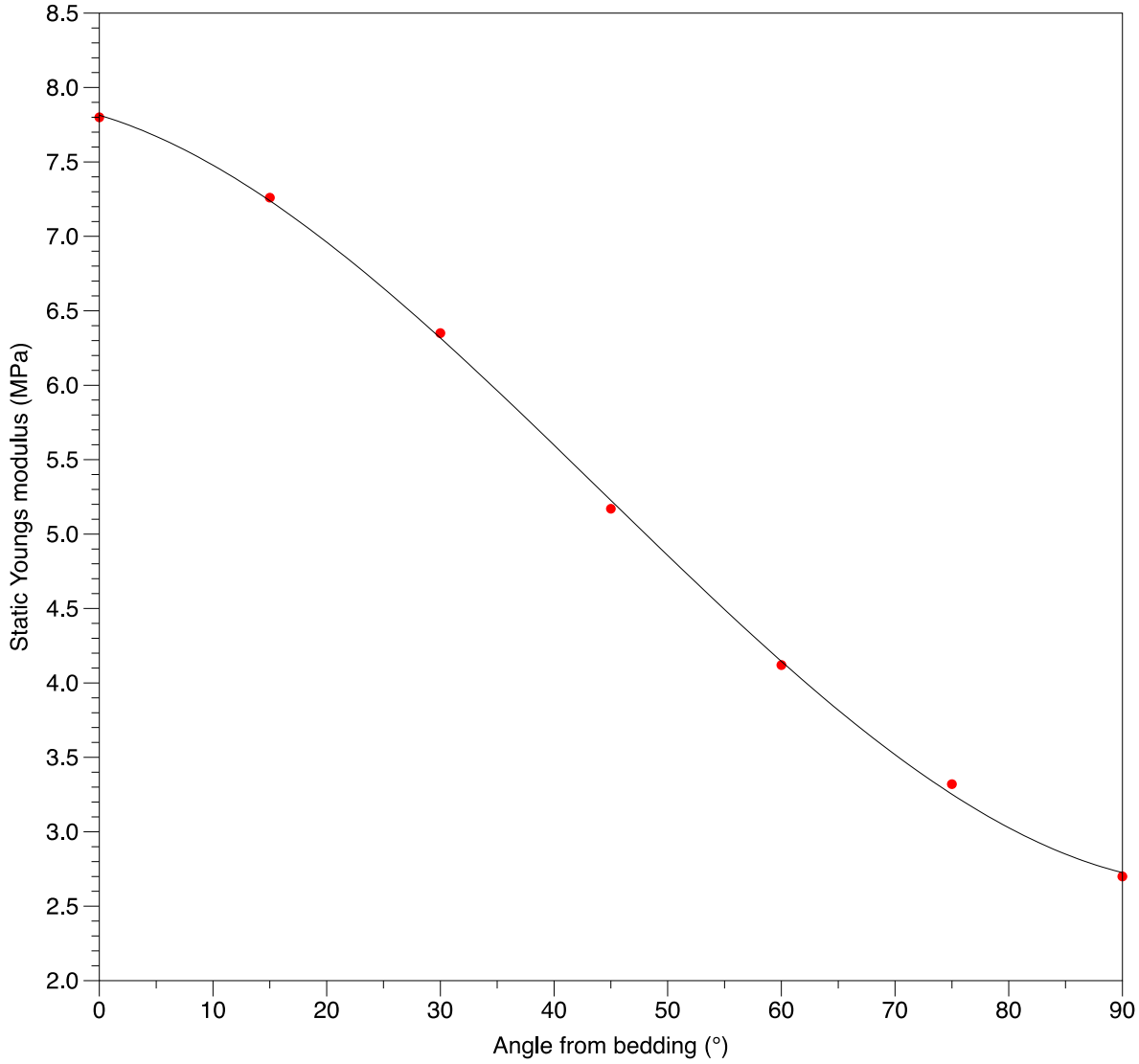

Figure S1: Static Young's modulus of Nash Point shale as a function of angle from bedding parallel, derived using the method described in the discussion section.

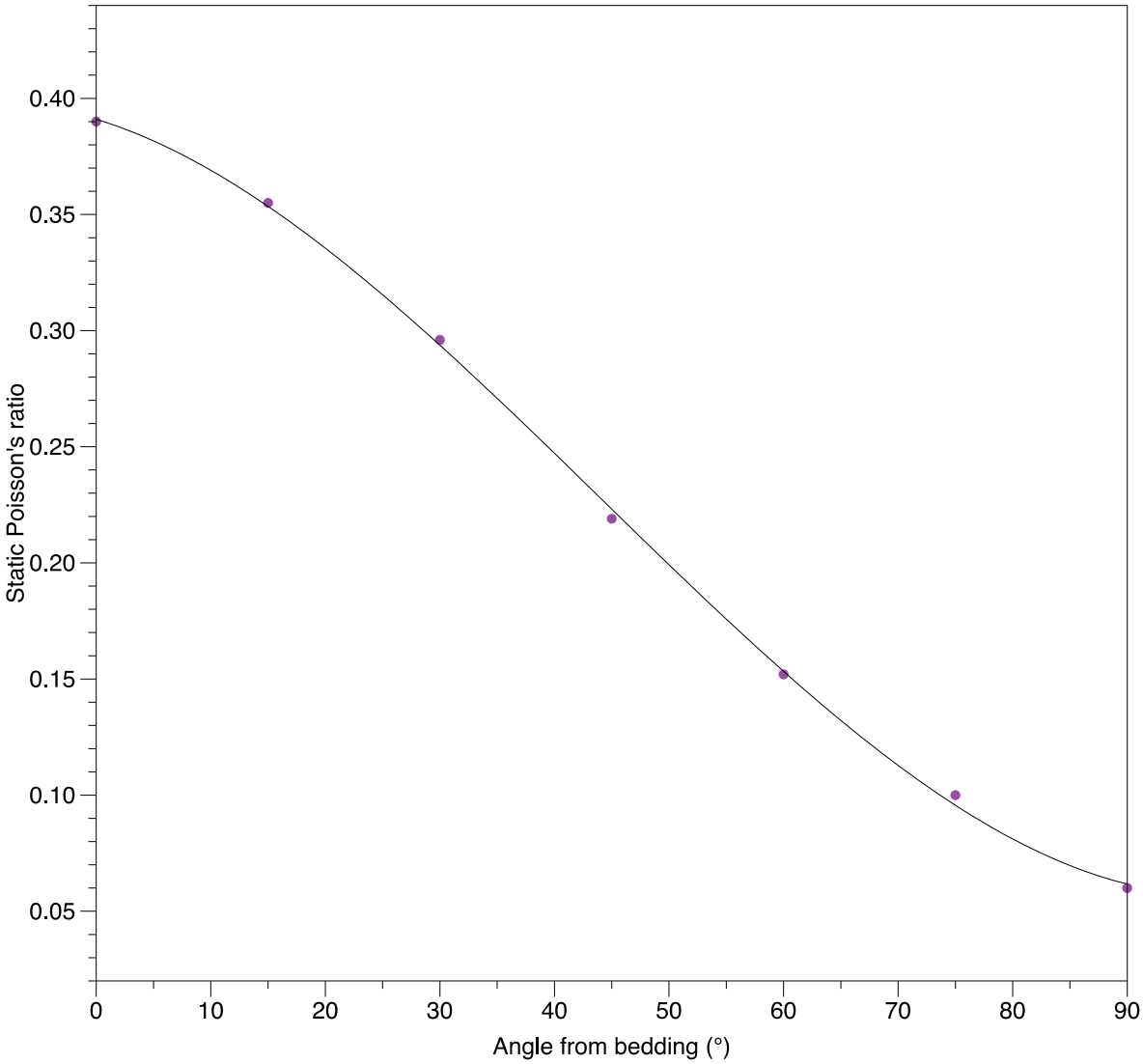

Figure S2: Static Poisson's ratio of Nash Point shale as a function of angle from bedding parallel, derived using the method described in the discussion section.

Supporting information (B)

Representative stress-strain graphs (from which the static moduli in the Supporting Information (A) are calculated from) from tests loading cores in each orientation (normal and parallel to bedding) are presented in Figures S1 and S2.

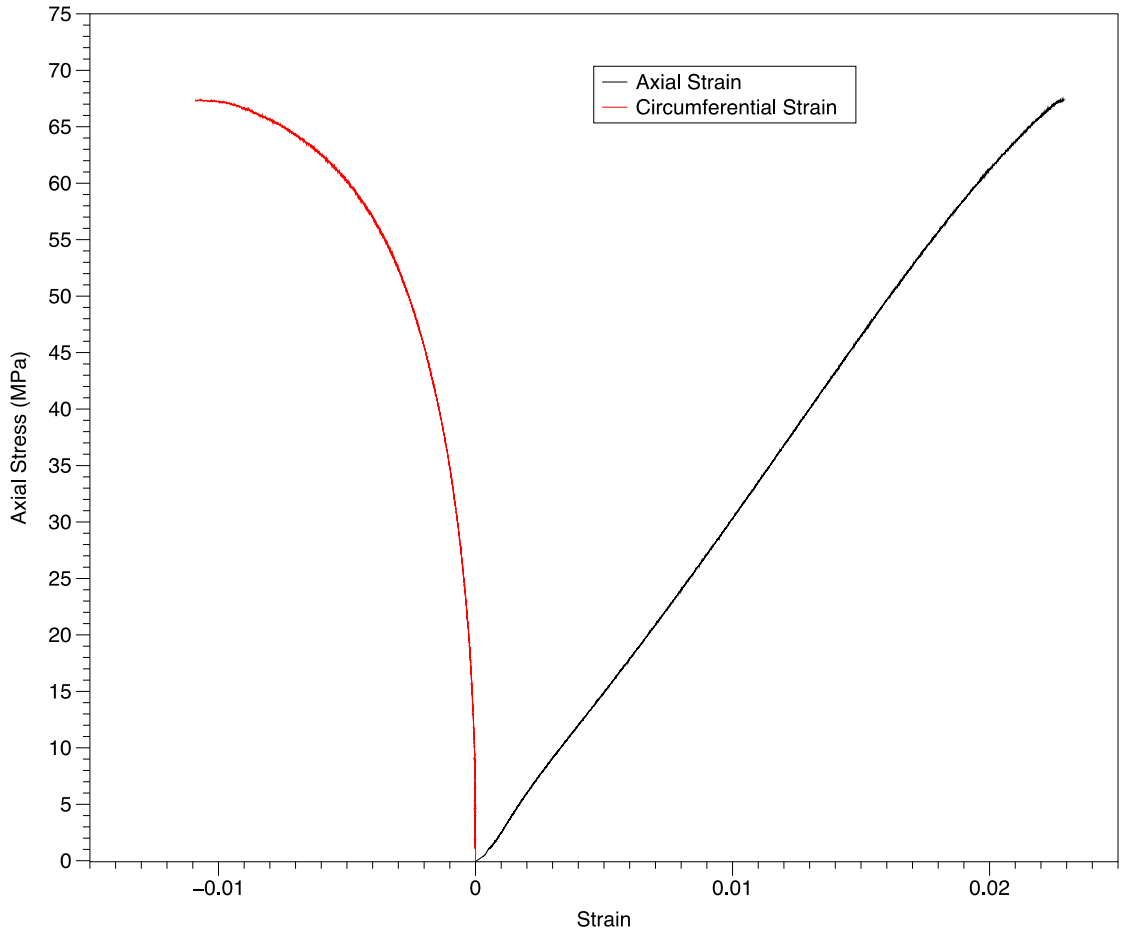

Figure S1: Axial and Circumferential strain plotted as a function of stress for a Nash Point shale core loaded normal to bedding.

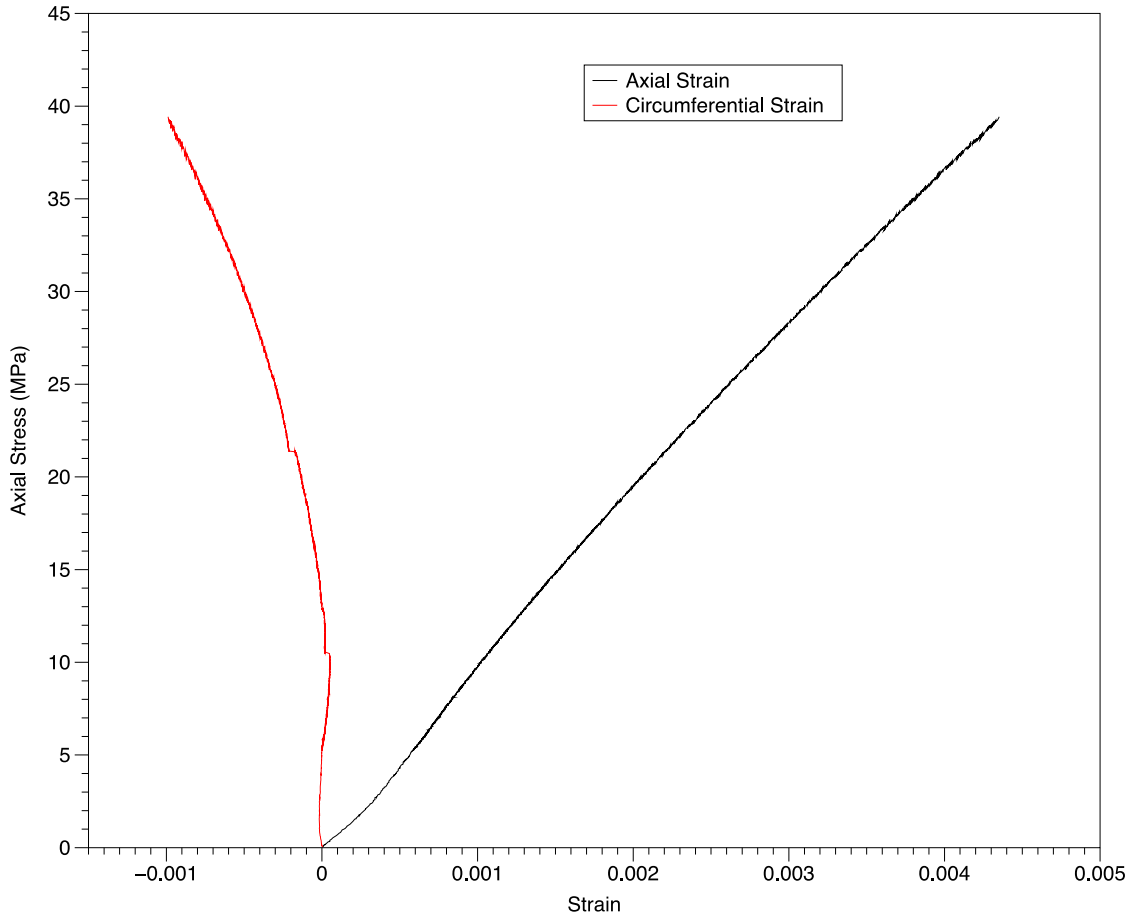

Figure S2: Axial and Circumferential strain plotted as a function of stress for a Nash Point shale core loaded parallel to bedding.

4 Characterising the fracture properties of Nash Point limestone

This chapter is written in a manuscript format and contains data gathered from Nash Point limestone. This manuscript will be submitted to Journal of Rock Mechanics and Rock Engineering. As it has not been submitted yet I have not included a detailed methodology section but instead refer the reader back to the methodology chapter of this thesis.

The manuscript is written with the aim of improving the understanding of how fractures may propagate in limestones which make up a significant proportion of carbonate reservoirs. However, this data is also important in the context of how fractures may propagate across the layered sequence at Nash Point, and its comparison to Nash Point shale. This is highlighted in sections of the manuscript but addressed in detail in Chapter 6.

Author contribution – Nathaniel Forbes Inskip wrote the manuscript, conducted the field work and experimental work. Philip Meredith contributed to data interpretation and made comments on the manuscript.

Characterising the fracture properties of Nash Point limestone

Abstract

Carbonate reservoirs contain a significant proportion of the global hydrocarbon reserves. However they are often tight and therefore permeability is usually dependent on either fluid flow through existing fractures or those produced from hydraulically stimulating the reservoir. As such understanding how fracture networks develop in carbonate reservoirs is key in understanding how best to produce from such reservoirs. Despite its prolificacy as a reservoir, there is a paucity in studies that have measured key fracture properties such as tensile strength and fracture toughness, particularly in more than one orientation, in carbonates. As such, we measure both the tensile strength and fracture toughness of Nash Point limestone in the three principal fracture orientations to determine what affect mechanical anisotropy may have on fracture propagation. We find Nash Point limestone to be essentially isotropic in terms of grain alignment within the rock matrix but then also in terms of its fracture properties. As such fracture propagation will be governed largely by external factors such as the in-situ stress. We also compare the fracture toughness of Nash Point limestone to that of others limestones in the literature, to investigate how porosity may affect fracture toughness. Although it is generally accepted that the fracture toughness will be lower for porous rocks, it was found that, for the data available, this relationship was not as strong in limestones. This is likely due to their complex pore geometry.

Introduction

A significant proportion of global hydrocarbon reserves exist within carbonate reservoirs, including limestones (Lamarche *et al.* 2012; Burberry & Peppers 2017; Li *et al.* 2018). Limestones are usually considered brittle and compared to other sedimentary rocks in a

sedimentary basin are likely to have a high Young's modulus (Afşar *et al.* 2014). As such following deposition and burial, limestones can often become fractured, thereby enhancing the porosity and permeability (Dashti *et al.* 2018; Li *et al.* 2018). In these instances it is important to know parameters such as fracture spacing, aperture, tortuosity etc. in order to calculate a more accurate reservoir porosity and permeability. Therefore it is important to know the fracture properties (tensile strength and fracture toughness) of the bulk rock so as to be able reduce the risk in determining such fracture parameters.

In instances where the permeability of a reservoir is particularly low (commonly < 1 mD for oil reservoirs and < 0.1 mD for gas reservoirs) hydraulic stimulation or hydraulic fracturing is required in order to allow the hydrocarbons to flow. Examples of limestone reservoirs which are considered tight include the Taq Taq, Kirkuk, Jambur, Khabaz and Bai Hassan oil fields in the Zagros fold belt (Rashid *et al.* 2017) and the Dariyan formation in the central Persian Gulf (Hosseini *et al.* 2018). In these instances it is important to know the fracture properties of the host rock so as to understand how fractures may propagate during stimulation.

Despite its prolificacy as a reservoir rock, not many studies have been conducted on limestones whereby the tensile strength and the fracture toughness have been measured, especially in more than one orientation. Moreover, the data presented in many of these studies is sparse, particularly in terms of testing orientation, but sometimes even basic descriptions of the rock are omitted. For example, Nath Singh & Sun (1990) measured the tensile strength and mode-I fracture toughness (K_{Ic}) of 'Welsh limestone', but any further description of the rock was limited to it being homogenous on a macroscopic scale. Nevertheless values of 8.49 MPa and 0.85 MPa.m$^{1/2}$ were obtained for tensile strength and K_{Ic}, respectively. Nath Singh & Sun (1990) used the Semi-cricular Bend test (SCB) to measure K_{Ic}, however, they do not state at which orientation the samples were tested. Similarly, Guo *et al.* (1993) measured K_{Ic} for 'white limestone' and 'grey limestone' but

give no further description of either rock. They found 'white limestone' to have a K_{Ic} of 1.65 MPa.m$^{1/2}$ and 'grey limestone' to have a K_{Ic} of 1.42 MPa.m$^{1/2}$, both measured using the Chevron Bend test (CB). Unfortunately, given the circumstances these results by themselves are only useful in providing a range of K_{Ic} values for limestone as a generic lithology.

Dibb *et al.* (1983) has also measured K_{Ic} for two different limestones, 'Carboniferous limestone' and 'Jurassic limestone', but again gives no further detail about the two rocks, or what orientation they were tested in. Using the Straight Cut Notch in three-point bending (SCN-3) they found K_{Ic} to be 1.25 MPa.m$^{1/2}$ and 1.04 MPa.m$^{1/2}$ for Carboniferous and Jurassic limestones, respectively.

Others have provided more detail with regards to the description of the rock being tested such as Stoeckhert *et al.* (2016) who measured both the tensile strength and K_{Ic} of a limestone from Southern Germany, called the Treuchtlinger Marmor, which is Jurassic in age. The tensile strength was measured to be 8.2 ± 2.2 MPa, where K_{Ic} was only plotted in a graph and from reading the value from the graph is approximately 1.3 MPa.m$^{1/2}$ (using the CB test). However, no further description, including orientation of the sample during testing, is provided. Therefore, although the geographic location and age are loosely constrained, these values are again mainly useful for determining a broad range of values for limestone as a generic lithology. It should be noted that the main focus of these studies was not to analyse any orientation dependence on fracture properties and therefore further descriptive analysis may not have been needed for them to complete their work.

Cicero *et al.* (2014) also measured the tensile strength and K_{Ic} of a limestone, but from the South East of Spain. It is described as being oolitic, homogenous and isotropic. Using a Straight Cut Notched sample in four-point bending (SCN-4) the K_{Ic} was measured to be 0.72 MPa.m$^{1/2}$ and the tensile strength to be 7.8 ± 1.1 MPa. Again, the orientation of the

78 samples during testing is not stated. The use of isotropic in this study appears to be
79 exclusively a visual description of the rock rather than a quantitative measure of any
80 mechanical anisotropy. However, as mechanical anisotropy and structural anisotropy are
81 inevitably linked, it could be assumed that the rock may not contain any significant
82 mechanical anisotropy. It may be for this reason that no orientation of the sample during
83 testing is provided.
84 Both the tensile strength and K_{Ic} of a limestone from the central province of Saudi Arabia
85 are presented by Khan & Al-Shayea (2000). Here the limestone is described as being a
86 homogenous, muddy limestone with a porosity of 5.4 %. Tensile strength was found to
87 vary between 2.13 – 2.39 MPa, with a mean value of 2.31 MPa. The main focus of the
88 study was to analyse the effect of specimen geometry on measuring K_{Ic} using different
89 suggested methods - The Straight Edge Cracked Round Bar Bend (SECRBB), SCB,
90 Cracked Chevron Notched Brazil Disk (CCNBD) and Centre-cracked Circular Disk
91 (CCCD). They concluded that while the results from some of these methods were
92 comparable there was a difference between samples which had a straight cut notch and
93 those which had a chevron cut notch. Using the CCCD method K_{Ic} was measured to be
94 0.42 MPa.m$^{1/2}$. By comparison K_{Ic} measured using the CCNBD (i.e. a chevron cut
95 notched sample) was 0.61 MPa.m$^{1/2}$. Again, no orientation of the sample being tested is
96 given.
97 Like Khan & Al-Shayea (2000), Aliha *et al*. (2012) also compares the results from the
98 SCB and CCCD methods, but using samples of Guiting limestone. Guiting limestone is
99 described as homogenous, porous, and predominately consisting of calcite. However, this
100 is not supported by any quantitative work in this study and although it is stated that
101 Guiting limestone is widely available in the UK, the origin of the samples are not
102 constrained any further. Aliha *et al.* (2012) find that K_{Ic} measurements obtained from the

two methods are different, with the SCB method producing a higher K_{Ic} (0.35 MPa.m$^{1/2}$) than the CCCD (0.24 MPa.m$^{1/2}$). Again, no orientation of the sample being tested is given. Helmer *et al.* (2014) measured the K_{Ic} of a limestone from the South of France called 'Pierre de Lens', which is Necomian in age. The limestone is described as ooilitic, homogenous and isotropic. Again the term isotropic here appears to be referring to any visual structural anisotropy rather than any quantitative measure of mechanical anisotropy. Porosity was measured to be 13% and the limestone is composed of 99.9% calcite. Young's modulus and Poisson's ratio were also measured and found to be 10 GPa and 0.3, respectively, however the orientation with respect to bedding for these measurements is not known. K_{Ic} was measured using three methods, SCB (0.64 MPa.m$^{1/2}$), CCCD (0.62 MPa.m$^{1/2}$) and the CCNDB (0.68 MPa.m$^{1/2}$). All three methods produced comparable results, however no orientation of the samples being tested is given. Of the studies considered here only three provide details on the orientation with respect to bedding of their samples, Gunsallus & Kulhawy (1984), Schmidt (1976) and Atkinson (1987). Gunsallus & Kulhawy (1984) measured both the tensile strength and K_{Ic} of two limestones, Irondequoit and Reynales limestones, from the Rochester area of New York. Samples were taken from exploratory borings for a tunnel project. The Irondequoit limestone has an approximate thickness of 5.5 m and comprises varying amounts of limestone, dolomite and calcareous shale. The limestone is described as crinoidal and has a porosity of 3%. Tensile strength was measured to be 11.9 MPa, with a range of 10.4 - 13.2 MPa. K_{Ic} was measured using the Short-rod test (SR), producing a mean value of 1.36 MPa.m$^{1/2}$ and a range of 0.93 – 1.82 MPa.m$^{1/2}$. It was stated that the failure was perpendicular to the bedding plane, which could mean that failure was either in the Arrester or Divider orientation. Reynales limestones had a similar thickness, 5.2 m, and also contained varying amounts of limestone, dolomite and calcareous shale but also traces of chert. The porosity was lower, being 0.7 %. A mean K_{Ic} value of 2.06 MPa.m$^{1/2}$

129 with a range of 1.76 – 2.17 MPa.m$^{1/2}$ was measured using the SR test. Again, failure was
130 reported to be perpendicular to the bedding plane.
131 Schmidt (1976) measured both tensile strength and K_{Ic} of Indiana limestone in a variety
132 of orientations. Indiana limestone is described as fossiliferous, composed mainly of
133 calcium carbonate, homogenous on a macroscopic scale with a slight preference for grain
134 orientation parallel to bedding. The porosity was measured to be 10-15%. Tensile strength
135 was measured using the direct pull tensile-test on samples cored parallel to bedding. In
136 such a set up fractures are most likely to propagate perpendicular to bedding, and as such
137 may be in the Arrester or Divider orientation. From these tests the tensile strength was
138 measured to be 5.38 MPa. K_{Ic} was measured in each of the three principal fracture
139 orientations from one sample block and only in the Divider orientation from a second
140 sample block. They measured K_{Ic} using the SCN-3 method. From the sample block where
141 samples in all three orientations were taken, values in the Arrester and Divider orientation
142 were the same (0.85 MPa.m$^{1/2}$) and slightly higher than those in the Short-transverse
143 orientation (0.71 MPa.m$^{1/2}$). Samples tested from the second sample block in the Divider
144 orientation were slightly higher than those from the first sample block (0.94 MPa.m$^{1/2}$).
145 A mean Divider value, taken across both sample blocks, was therefore 0.87 MPa.m$^{1/2}$.
146 Finally, Atkinson (1987) has collated some further K_{Ic} data from limestones, these include
147 data from the Balmholtz limestone (1.77 MPa.m$^{1/2}$), Hällekis limestone (1.25 MPa.m$^{1/2}$),
148 Klinthagen limestone (1.31 MPa.m$^{1/2}$), 'Shelly' limestone (1.44 MPa.m$^{1/2}$) and Solnhofen
149 limestone (1.01 MPa.m$^{1/2}$ normal to bedding and 0.87 MPa.m$^{1/2}$ parallel to bedding).
150 Even though the level of detail of the results presented in these studies is variable they
151 provide us with a broad range of tensile strength and K_{Ic} for different limestones, with
152 tensile strength ranging from 2.31 – 15 MPa and K_{Ic} ranging from 0.24 – 2.06 MPa.m$^{1/2}$.
153 These broad ranges demonstrate how variable the mechanical properties of limestone can
154 be and are presented in Table 2.

155 In this manuscript we report the results of a study where we have measured a suite of
156 mechanical properties, including both the tensile strength and K_{Ic} of Nash Point limestone
157 in order to improve our understanding of how its mechanical properties may influence
158 fracture propagation. Furthermore, this data is then compared to the data from the studies
159 discussed above.

160 **Sample material and characterisation**

161 **Mineralogy and microstructure**

162 In this section, we measure and analyse physical and mechanical properties of Nash Point
163 limestone, which is the limestone member of the Porthkerry Formation, outcropping at
164 Nash Point.

165 Thin section analysis demonstrates that Nash Point limestone is poorly sorted, with grains
166 that are angular to sub-angular with no significant alignment of the grains apparent
167 (Figure 1). The great majority of the grains are shell fragments, such as bivalve,
168 gastropod, echinoderm and sponge spicules. The nature of the grain angularity and the
169 amount of shell fragments present suggest that the environment of deposition was low
170 energy and likely shallow marine. The shell fragments range in size from about 0.1 mm
171 to 3 mm. XRD analysis shows that Nash Point limestone is comprised predominately of
172 calcite (>90%), with lesser amounts of quartz (5-7%), clays and other trace minerals
173 (<3%).

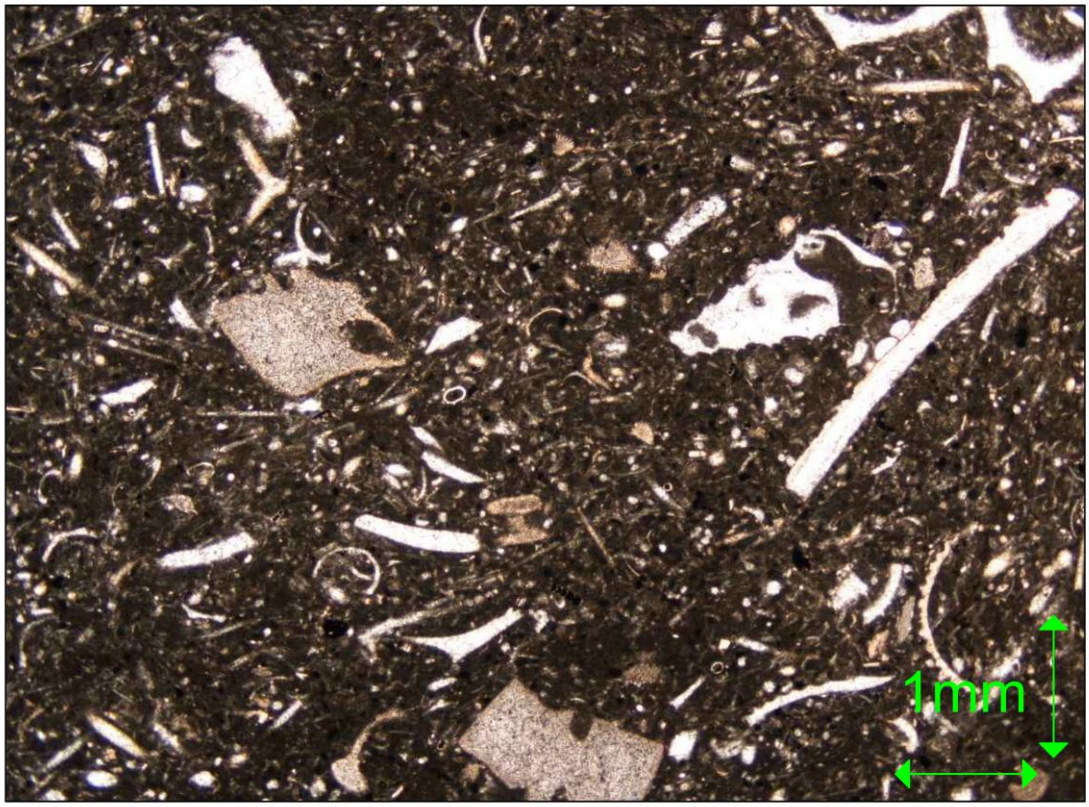

Figure 1: Thin section of Nash Point limestone with 1 mm bars for scale.

The Nash Point limestone samples used in this study had a porosity of ~1%, measured using Helium pycnometry (Heap *et al.* 2009; Chandler *et al.* 2016; Chalmers & Bustin 2017), and a bulk density of 2671 kg.m^{-3}. This density is very close to that of pure calcite (2710 kg.m^{-3}), which is unsurprising given the XRD results and the very low porosity. Our porosity value compares well to the results presented in Afşar *et al.* (2014) where the effective porosity of limestone samples taken from the Bristol Channel ranged from 0.82 – 1.52%.

Elastic anisotropy and moduli

We characterised the anisotropy of Nash point limestone by measuring the P-wave and S-wave velocities of 38 mm cylindrical samples under dry, ambient pressure and ambient temperature conditions as is described in the methodology chapter. Velocities were measured both parallel and normal to bedding of at least two independent samples where

189 the P-wave velocity parallel to bedding (V_{p0}) was measured to be 5.88±0.03 km.s^{-1} and
190 normal to bedding (V_{p90}) to be 5.79±0.02 km.s^{-1}. These values give a P-wave velocity
191 anisotropy of <2% calculated from:
192
193 $$\frac{V_{max} - V_{min}}{V_{mean}} \quad (1)$$
194
195 By comparison, the S-wave velocity parallel to bedding (V_{sH0}) is 3.50±0.03 km.s^{-1} and
196 that normal to bedding (V_{sH90}) is 3.48±0.02 km.s^{-1}. These values give a S-wave velocity
197 anisotropy of <1%. As such, and given that these values of anisotropy are within the error
198 considered of picking first arrivals for both P and S waves (Vinciguerra *et al.* 2005), Nash
199 Point limestone can be considered essentially isotropic.
200 Static (tangent) Young's modulus and Poisson's ratio were measured from conventional
201 uniaxial compression tests, as described in the methodology chapter, on cores loaded
202 parallel and normal to bedding. The Young's modulus parallel to bedding was 26.3 GPa
203 and normal to bedding was 28.5 GPa. Poisson's ratio was found to be 0.14 when cores
204 were loaded in each of the two orientations. Examples of representative stress-strain
205 curves are provided in the Supporting Information. Our Young's modulus values are
206 lower than those measured by Afşar *et al.* (2014), who found the static Young's modulus
207 of limestone samples from the Bristol Channel to range from 38 – 48 GPa. Afşar *et al.*
208 (2014) conducted field-work in three areas along the Bristol Channel - Nash Point,
209 Lilstock and Kilve but they do not indicate where the samples used to measure the
210 Young's modulus are from, or if they are average values from samples taken from more
211 than one site. Therefore, it is not known if the difference may just be due to the natural
212 variability of the Young's modulus of limestone in the Liasic portion of the Bristol
213 Channel, or if there are differences between the three areas.

Table 1: Elastic characterisation of Nash Point limestone.

	Normal to bedding	**Parallel to bedding**
V_p (km.s^{-1})	5.79±0.02	5.88±0.03
V_s (km.s^{-1})	3.48±0.02	3.50±0.03
Static Young's modulus (GPa)	28.5	26.3
Poisson's ratio	0.14	0.14

Methods

In this manuscript we present both tensile strength and mode-I fracture toughness (K_{Ic}) results obtained from using the Brazil disk test (Tensile strength), Semi-circular Bend and Short-rod tests (K_{Ic}). As ultrasonic wave velocity measurements on Nash Point limestone demonstrate no significant anisotropy, all further testing was completed in the three principal fracture orientations (Short-transverse, Arrester and Divider) only. All three of the methods used in this manuscript have already been described in detail in the Methodology chapter of this thesis; therefore I refer the reader back to that chapter for a description of these methods.

Results

Tensile strength

The tensile strength (mean ± one standard deviation) of samples of Nash Point limestone measured in the three principal orientations are given in Figure 2 and Table 2. All of the tests produced fractures that were straight and passed through the centre of the sample and are therefore considered valid (see Figure 4).

The strength values ± one standard deviation in all orientations overlap which supports the findings from the ultrasonic wave velocity measurements that Nash Point limestone is essentially isotropic.

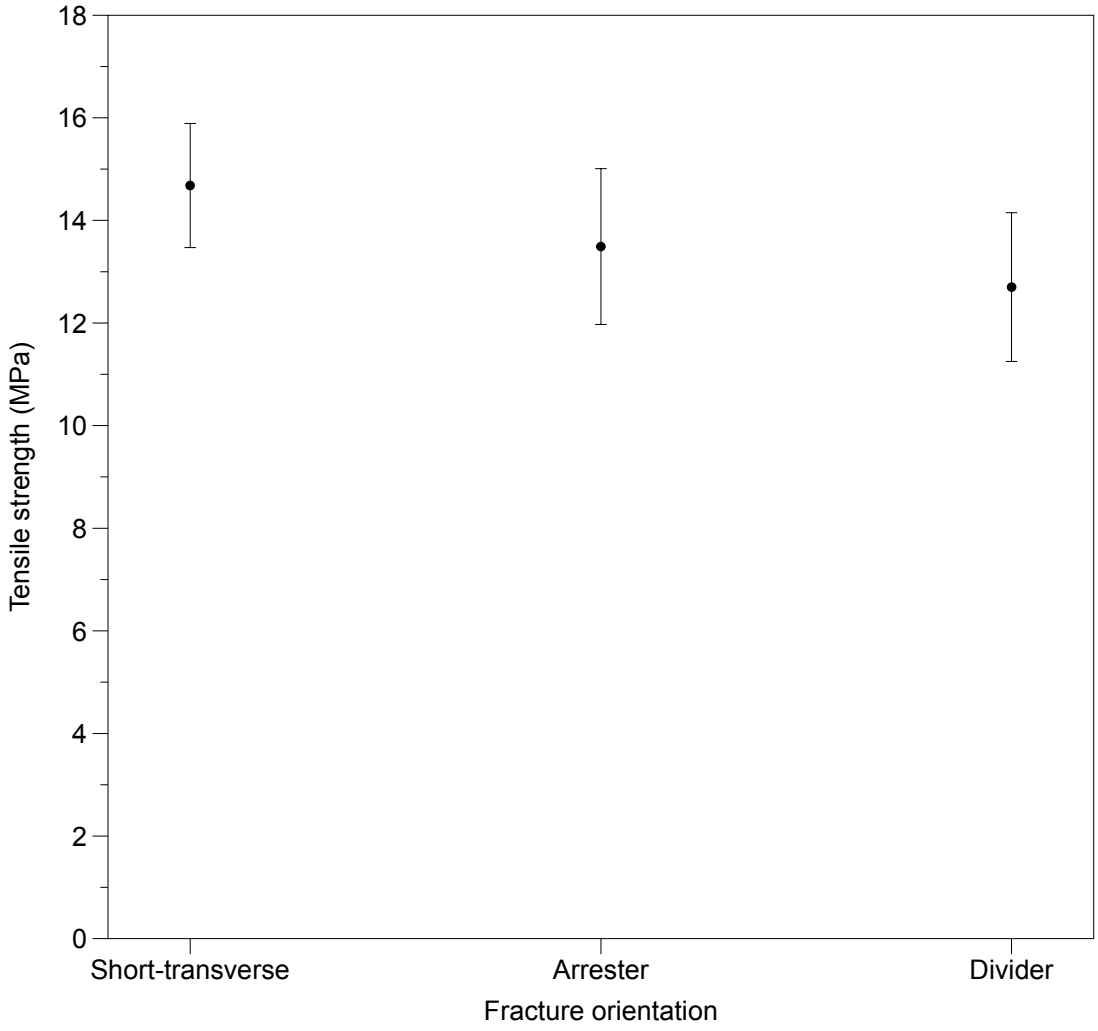

Figure 2: Mean tensile strength (MPa) of Nash Point limestone in the three principal fracture orientations. Error bars show ± one standard deviation.

Fracture toughness

Results from both the SCB and Short-rod tests are given in Figure 3 and Table 2, where the mean ± one standard deviation are plotted for each of the three principal orientations. All tests are considered valid as they met the necessary criteria of not deviating by more than 5% of the sample diameter from the intended direction in each method (Ingraffea *et al.* 1984; Kuruppu *et al.* 2014) (See Figure 4).

243 K_{Ic} measurements in all three orientations using the SCB method overlap when taking
244 into account ± one standard deviation. This is also the case for measurements using the
245 SR method, although, measurements made using the SR method are slightly higher than
246 those from using the SCB method. However, there is overlap between the two set of
247 results in the Arrester and Divider orientation. Again these results support the findings
248 from the ultrasonic wave velocity measurements that Nash Point limestone is essentially
249 isotropic.

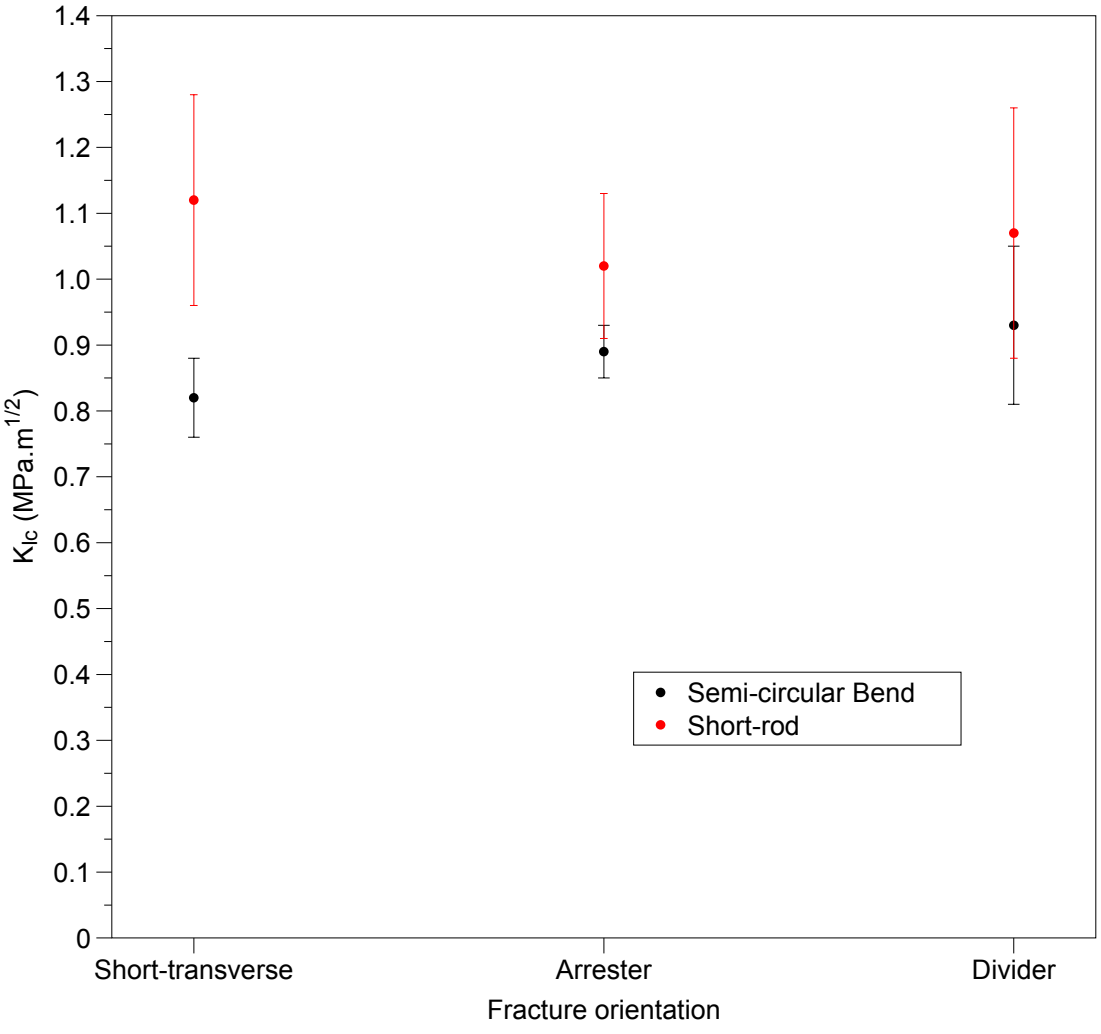

250

251 Figure 3: Mean mode-I fracture toughness [K_{Ic}] (MPa.m$^{1/2}$) of Nash Point limestone in the three principal
252 fracture orientations using both the Semi-circular Bend [SCB] and Short-rod [SR] methods. Error bars show
253 ± one standard deviation.

254

255 Table 2: Fracture properties of a variety of limestones. *Here it is not known if the fracture orientation was either Arrester or Divider. Abbreviations for the different methods are:
256 Semi-circular Bend [SCB], Chevron Bend [CB], Straight Cut Notched sample in four point bending [SCN-4], Centre Cracked Circular Disk [CCCD], CCNBD [Cracked Chevron
257 Notched Brazilian Disk [CCNBD], Short-Rod [SR], Double Torsion [DT] and Straight Cut Notched sample in three point bending [SCN-3]. In terms of grain size many authors only
258 give a qualitative description of the grain size, based on the Wentworth classification, whereas some give a more quantitative value. As such we use the Wentworth classification to
259 provide a quantitative range of grain sizes where only a description was given and a descriptive analysis where a quantitative grain size is given. The original data from the respective
260 study is given in **bold.**

Type of limestone	**Orientation**	**Tensile strength (MPa)**	**K_{Ic} [method] (MPa.m$^{1/2}$)**	**Porosity**	**Grain size**	**Study**
Nash Point limestone	Short-transverse	14.68 ± 1.38	0.82 ± 0.05 [SCB] 1.12 ± 0.16 [SR]	1%	**Fine to medium sand, with some larger shell fragments (0.1 – 3 mm)**	This study
Nash Point limestone	Arrester	13.49 ± 1.10	0.89 ± 0.03 [SCB] 1.02 ± 0.11 [SR]	1%	**Fine to medium sand, with some larger shell fragments (0.1 – 3 mm)**	This study
Nash Point limestone	Divider	12.7 ± 1.25	0.93 ± 0.10 [SCB] 1.07 ± 0.19 [SR]	1%	**Fine to medium sand, with some larger shell fragments (0.1 – 3 mm)**	This study
Indiana limestone	Short-transverse	-	0.71 [SCN-3]	10-15%	**Medium sand** (0.25 – 0.5 mm)	Schmidt (1976)

Indiana limestone	Arrester	5.38*	0.85 [SCN-3]	10-15%	**Medium sand** (0.25 – 0.5 mm)	Schmidt (1976)
Indiana limestone	Divider	5.38*	0.89 [SCN-3]	10-15%	**Medium sand** (0.25 – 0.5 mm)	Schmidt (1976)
Irondequoit limestone	Perpendicular to bedding	11.9	1.36 [SR]	3	**Fine to medium sand** (0.125 – 0.5 mm)	Gunsallus & Kulhawy (1984)
Reynales limestones	Perpendicular to bedding	15	2.06 [SR]	0.7	**Fine to medium sand** (0.125 – 0.5 mm)	Gunsallus & Kulhawy (1984)
Solnhofen limestone	Normal to bedding	-	1.01 [DT]	-	Very Fine silt **(0.005 mm)**	Atkinson (1984)
Solnhofen limestone	Parallel to bedding	-	0.87 [DT]	-	Very Fine silt **(0.005 mm)**	Atkinson (1984)
Pierre de Lens	?	-	0.62 [CCCD] 0.64 [SCB] 0.68 [CCNBD]	13%	Medium sand **(0.3 mm)**	Helmer *et al.* (2014)
Guiting limestone	?	-	0.24 [CCCD] 0.35 [SCB]	Porous	-	Aliha *et al.* (2012)

Limestone (Saudi Arabia)	?	2.31	0.35 - 0.42 [CCCD] 0.61 [CCNBD]	5.4%	-	Khan & Al-Shayea (2000)
Oolitic limestone (SE Spain)	?	7.8 ± 1.1	0.72 [SCN-4]	-	Coarse sand **(0.8 mm)**	Cicero *et al.* (2014)
Treuchtlinger Marmor	?	8.2 ± 2.2	~1.3 [CB]	-	-	Stoeckhert *et al.* (2016)
Jurassic limestone	?	-	1.04 [SCN-3]	-	-	Dibb *et al.* (1983)
Carboniferous limestone	?	-	1.25 [SCN-3]	-	-	Dibb *et al.* (1983)
White limestone	?	-	1.65 [CB]	-	-	Guo *et al.* (1993)
Grey limestone	?	-	1.42 [CB]	-	-	Guo *et al.* (1993)
Welsh limestone	?	8.49 ± 0.86	0.85 [SCB]	-	Medium sand (0.125 – 0.5 mm)	Nath Singh & Sun (1990)

Balmholtz limestone	?	-	1.77 [CB]	-	-	Bergkvist & Fornerod (1979)
Hällekis limestone	?	-	1.25 [SCN-4]	-	-	Lundborg & Almgren (1972)
Shelly limestone	?	-	1.44 [SR]	-	Medium sand, with some larger shell fragments(0.25 – 3 mm)	Meredith (1989)
Klinthagen limestone	?	-	1.31 [CB]	-	-	Ouchterlony & Sun (1983)

261

Discussion

Influence of orientation on fracture properties

Looking at all the data, Nash Point limestone is essentially isotropic. This is entirely consistent with the ultrasonic wave velocity measurments and any lack of grain alignment within the rock matrix.

Although the outcrop at Nash Point is bedded there is uncertainty as to whether the limestone beds are primary depositional origin or secondary diagenetical origin. The latter has been hypothesised by Sheppard *et al.* (2006), and the nodular nature of some of the beds may support this hypothesis. If so these beds are likely to have grown outwards in all directions from a nucleation point to form nodules, and therefore would not necessarily be expected to contain structural alignment. Consequently, we would not expect there to be any significant mechanical anisotropy.

However, the majority of the rock is made up of shell fragments that are depositional in nature, and therefore their lack of alignment may not be entirely explainable from a diagenetic model which is based on the dissolution and re-precipitation of calcareous minerals. As such, the question still remains open as to whether or not these limestone beds are primary or secondary in nature. However our measurements demonstrate that there is no significant mechanical anisotropy with respect to the bedding orientation. Furthermore, in terms of fracture paths, fractures in each of the three principal fracture orientations were essentially straight and exhibited very little or no tortuosity (Figure 4). This is entirely as expected given the isotropic nature of Nash Point limestone. This is also important in terms of the fluid flow potential of fractures, where the transport properties of the straight fractures in Nash Point limestone are likely to be very different to those of tortuous fractures in other rock formations, such as Nash Point shale (Forbes Inskip *et al.* 2018) [This point is discussed further in Chapter 7].

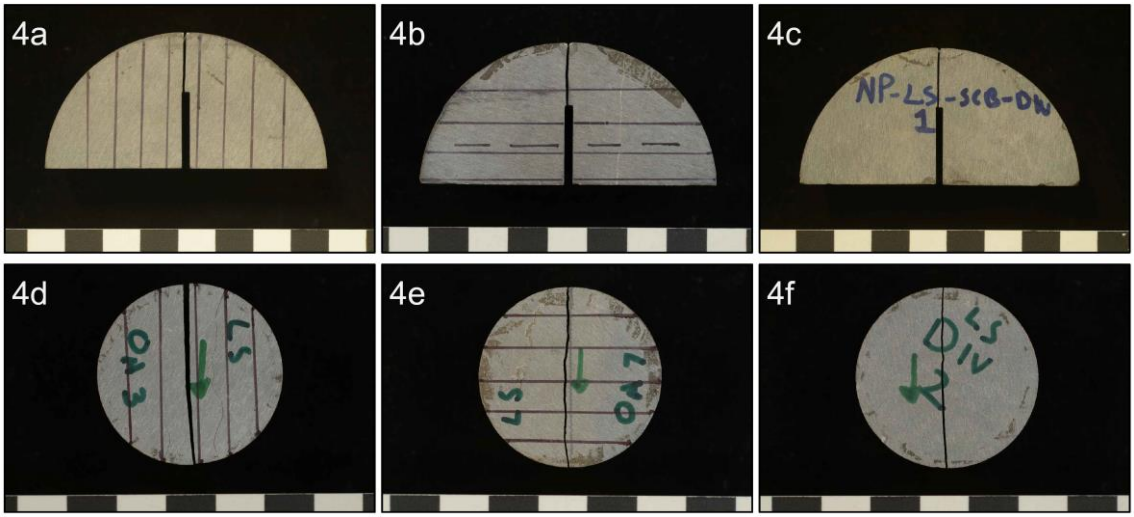

Figure 4: SCB and Brazil disk samples tested in the Short-transverse (a and d), Arrester (b and e) and Divider (c and f) orientations. Solid black lines show the orientation of the bedding plane and a scale bar lies below each sample where each division is 1 cm. The green arrows depict the loading orientation in the Brazil disk samples. Fractures in each of the orientations are straight and parallel with the loading orientation.

Comparison of the different methods to measure K_{Ic}

Since K_{Ic} is defined as a material property, the results from the different methods of measuring it should be the same. Although there is significant overlap between the two methods used here in the Arrester and Divider orientations, there is no such overlap in the Short-transverse orientation (when considering one standard deviation). Furthermore, the mean in each of the three orientations is consistently higher when using the Short-rod. However, there is internal consistency with results obtained from each method (i.e. that K_{Ic} is essentially the same in all three orientations). Interestingly, Khan & Al-Shayea (2000) found that there was a difference between K_{Ic} measured using samples with a straight cut notch, and those using a chevron cut notch. They found that K_{Ic} was on average 45% greater when using the CCNDB (0.61 MPa.m$^{1/2}$) compared to the CCCD (0.42 MPa.m$^{1/2}$), where all sample geometries except the type of notch were the same in both sets of tests. In our results the SR, which contains a chevron cut notch, produces K_{Ic}

values which are higher than those of a method which uses a straight cut notch, the SCB. We found SR results to be 35% greater than those obtained from the SCB in the Short-transverse orientation, and 15% grater in the Arrester and Divider orientations. Therefore, although we also find that the chevron cut notched samples produced a higher K_{Ic} value, the difference is not as great as what is quoted by Khan & Al-Shayea (2000). Aliha *et al.* (2012) also found discrepancies between results using different methods of measuring K_{Ic}. They used both the CCCD and the SCB methods to measure K_{Ic} of Guiting limestone, and found that CCCD produced a lower K_{Ic} value (0.24 MPa.m$^{1/2}$) than the SCB method (0.35 MPa.m$^{1/2}$). Aliha *et al*. (2012) suggests that this discrepancy is a function of the different sample geometries, and suggest that a modified form of the maximum tangential stress can be used to predict the results of K_{Ic} using different methods.

Others found very little variation between testing methods such as Helmer *et al.* (2014), who found that K_{Ic} of the Pierre de Lens limestone measured using the CCCD, SCB and CCNBD was 0.62, 0.64 and 0.68 MPa.m$^{1/2}$, respectively. Ultimately, all methods used for measuring K_{Ic} require a complicated sample geometry which includes a notch. This is to create stress concentrations at the tip of the notch and as such stress throughout the sample is non-uniform. Therefore it is unsurprising that in some instances there are discrepancies between results obtained using different methods, and so we would suggest that caution is taken when comparing results using different methods.

Comparison of the fracture properties of Nash Point limestone with those of other limestones

Porosity

It is accepted that an increase in porosity generally relates to a decrease in strength and fracture toughness (Al-Harthi *et al.* 1999; Palchik & Hatzor 2004; Sabatakakis *et al.* 2008; Heap *et al.* 2009, 2014; Lian *et al.* 2011; Meille *et al.* 2012; Schaefer *et al.* 2015; Bubeck

et al. 2016). When plotting K_{Ic} against porosity for the data in Table 2 it is found that a weak relationship exists between the two ($R^2 = 0.20$) (Figure 5)

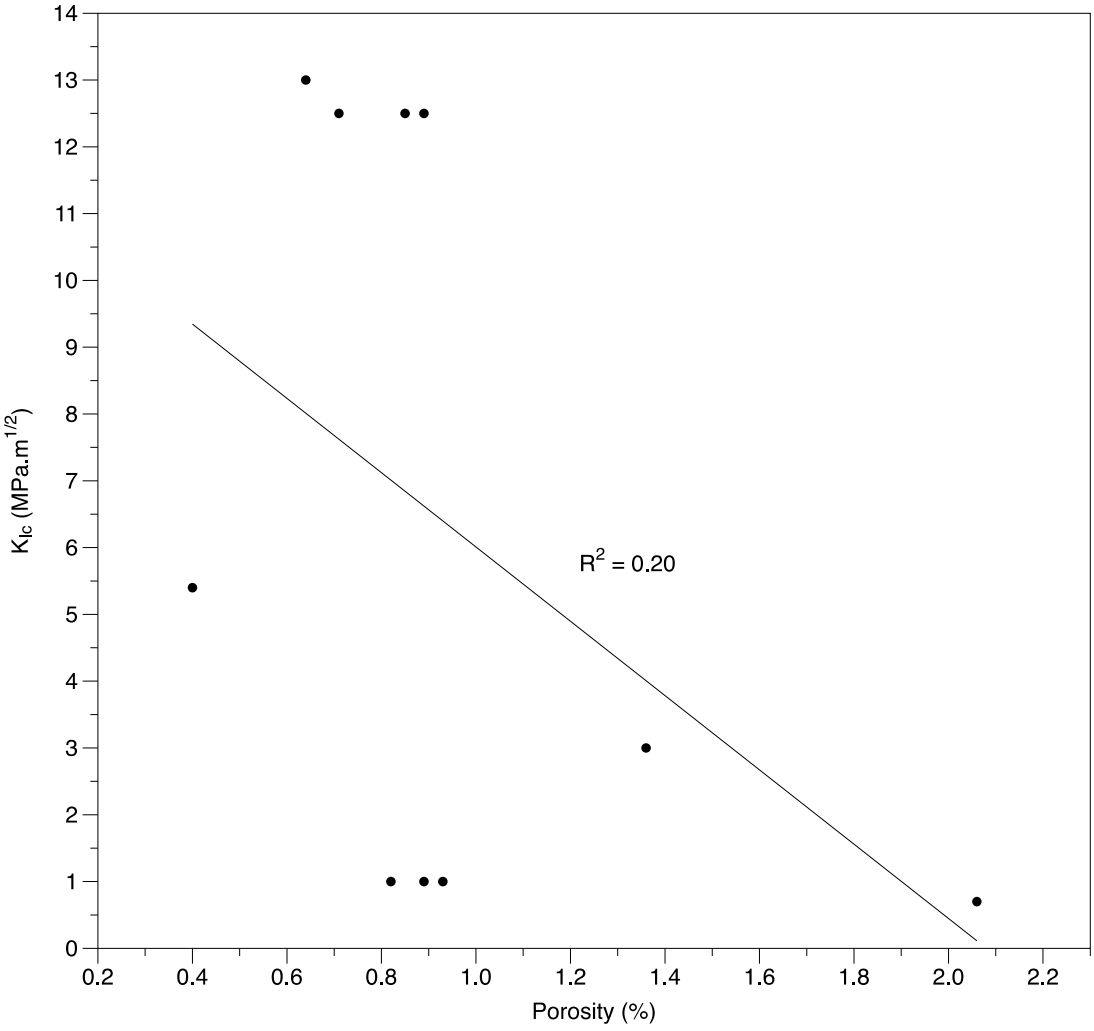

Figure 5: Variation of K1c with Porosity of limestone data in Table 2.

In addition to the total porosity, it is also important to consider the pore geometry and pore network within (Bubeck *et al.* 2016). Carbonates are known to have a complex pore system (Tucker 2001; Tucker & Wright 2009; Haines *et al.* 2016; Rashid *et al.* 2017) and although the same general trend between porosity and strength is expected to exist, it is likely to be more complex than for other rocks containing comparatively simpler pore systems. This may explain the low R^2 in Figure 5.

343 **Grain size**

344 The grain size of a material is also known to affect the fracture properties of a material,
345 where generally the fracture toughness of a material is expected to increases with
346 increasing grain size (Li & Li 1989; Meredith 1989). This is normally associated with a
347 change from predominantly intergranular fracture in fine grained materials to
348 predominantly transgranular fracture in coarser grained materials (Meredith 1989).
349 Unfortunately for the studies considered here (those in Table 2), data on the grain size of
350 the respective rocks is vague, with most only giving a qualitative description of the grain
351 size based on the Wentworth scale (Wentworth 1922). However, some do provide a more
352 quantitative value for grain size. As such we use the Wentworth classification to provide
353 a quantitative range of grain sizes where only a description was given and a descriptive
354 analysis where a quantitative grain size is given (Table 2). We then use the geometric
355 mean of the end members of the grain size range and plot this against K_{Ic} in Figure 6.

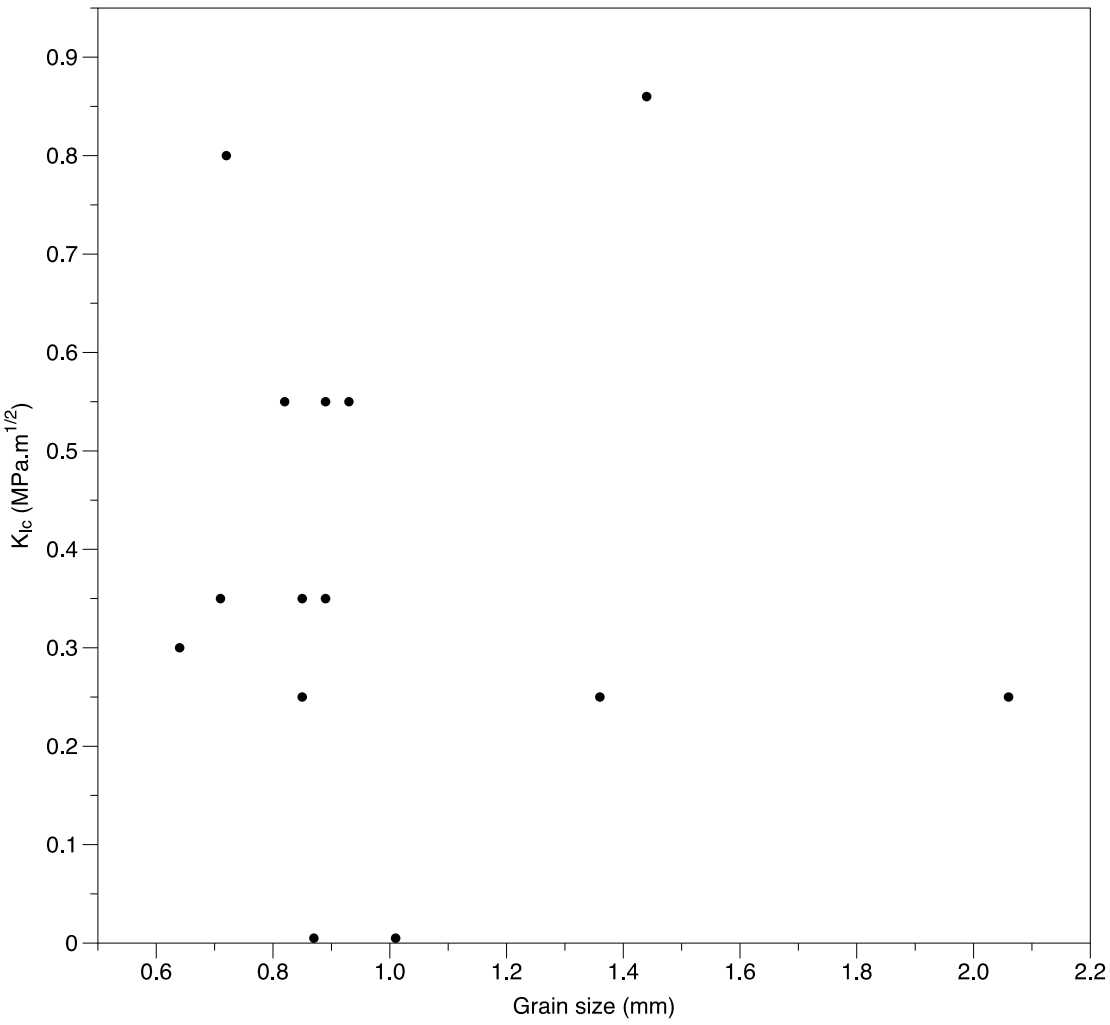

Figure 6: Variation of K1c with grain size of limestone data in Table 2.

Clearly, from Figure 6, no strong relationship exists for the data available (the calculated R^2 was less than 0.01). However, this is likely due to the fact that we have had to make a significant assumption with regards to grain size when no quantitative value is given.

Orientation to bedding

Unlike most of the studies presented in Table 2, we have measured both the tensile strength and K_{Ic} in all three principal fracture orientations and found Nash Point limestone to be essentially isotropic in terms of its fracture properties. Many of the aforementioned studies considered their respective limestone(s) to be homogenous and isotropic in terms

of their structure, and if so it is likely that their fracture properties would not be significantly different in the three principal orientations. Only Schmidt (1976) measured K_{Ic} in all three principal orientations (on Indiana limestone) and found that values in the Short-transverse were lower than the other two orientations which were almost the same. They described Indiana limestone to contain some mild alignment of the grains with the bedding plane. Although not a limestone, some authors have measured the fracture toughness of shales in different orientations with respect to bedding (Schmidt 1977; Lee *et al.* 2015; Chandler *et al.* 2016; Forbes Inskip *et al.* 2018). In each of these cases there was a strong alignment of the grains within the respective rocks, and it was also found that K_{Ic} was lower in the Short-transverse orientation compared to the Arrester and Divider orientations. As such, it is likely that the alignment of grains in the samples of Indiana limestone is the cause of anisotropy.

In a broader sense our mean values of tensile strength (12.70 – 14.68 MPa) and K_{Ic} (0.82 – 0.93 MPa.m$^{1/2}$ using the SCB method and 1.02 – 1.12 MPa.m$^{1/2}$ using the SR method) fall well within the range of values presented in Table 2 i.e. Tensile strength of 2.31 – 15 MPa and K_{Ic} of 0.24 – 2.06 MPa.m$^{1/2}$. Furthermore, our tensile strength values compare reasonably well with those of Afşar *et al*. (2014) who also measured the tensile strength of limestone samples from the Bristol Channel, and found their tensile strength to be between 9-11 MPa.

Impact on preferential fracture orientation

Given that there does not appear to be any significant trend or indeed difference in the fracture properties with regards to orientation to bedding, we consider Nash Point limestone to be essentially isotropic in terms of its mechanical properties.

Consequently fracture orientation in this material will be affected only by other external factors and primarily the in-situ stress field.

As hydraulic fractures are by definition predominately mode-I they will propagate parallel to the maximum principal compressive stress (σ_1) and in the plane perpendicular to the minimum principal compressive stress (σ_3). In both extensional and relatively static tectonic regimes σ_1 tends towards the vertical stress with depth due to the increased load of the overburden, where σ_3 is then horizontal. As such where there is little or no mechanical anisotropy, as is the case with Nash Point limestone, fractures will generally grow vertically at all depths

Conclusions

The focus of this study has been on understanding what may affect fracture propagation in limestone sequences, by measuring the fracture properties of Nash Point limestone in the three principal fracture orientations. It was found that there was no significant difference of either the tensile strength or the mode-I fracture toughness (K_{Ic}) between the different orientations tested. As such we consider Nash Point limestone to be essentially isotropic. Following thin section analysis it was found that no significant alignment of the grains exists, and as such it is likely that this lack of structural anisotropy is carried through to the lack of mechanical anisotropy. Other studies that measured tensile strength and/or K_{Ic} of different limestones often described their samples as being homogenous and isotropic based on visual analysis. However, in none of these studies was a full characterisation of the fracture properties with orientation carried out.

Schmidt (1976) was the only study which we found to carry out an extensive characterisation of K_{Ic} with orientation, measuring it in all three principal fracture orientations. Interestingly it was found that K_{Ic} was lower in samples tested the Short-transverse orientation compared to those tested in the Arrester and Divider orientations (which were almost the same). However, unlike the other studies considered here they described their samples as displaying a slight structural anisotropy whereby there was some alignment of the grains with the bedding plane.

We also found fractures produced from both the Brazil disk and Semi-circular Bend (SCB) tests were very straight, with little to no tortuosity present. As such we would consider fractures propagating in a rock like Nash Point limestone (a limestone with no significant structural anisotropy) to be straight, and their orientation to be governed mainly by the in-situ stress at the time of fracture formation.

Finally, we also tried to relate K_{Ic} to porosity using data from other studies on different limestones. However, we found no strong relationship existed, for the data available. We reason that the complex pore geometry and pore network that exists in limestones is likely complicate any relationship between porosity and K_{Ic}.

References

Afşar, F., Westphal, H. & Philipp, S.L. 2014. How facies and diagenesis affect fracturing of limestone beds and reservoir permeability in limestone-marl alternations. *Marine and Petroleum Geology*, **57**, 418–432, https://doi.org/10.1016/j.marpetgeo.2014.05.024.

Al-Harthi, A.A., Al-Amri, R.M. & Shehata, W.M. 1999. The porosity and engineering properties of vesicular basalt in Saudi Arabia. *Engineering Geology*, **54**, 313–320, https://doi.org/10.1016/S0013-7952(99)00050-2.

Aliha, M.R.M., Sistaninia, M., Smith, D.J., Pavier, M.J. & Ayatollahi, M.R. 2012. Geometry effects and statistical analysis of mode I fracture in guiting limestone. *International Journal of Rock Mechanics and Mining Sciences*, **51**, 128–135, https://doi.org/10.1016/j.ijrmms.2012.01.017.

Atkinson, B.K. 1984. Subcritical Crack Growth in Geological Materials. *Journal of Geophysical Research*, 4077–4114.

Atkinson, B.K. 1987. *Fracture Mechanics of Rock*. London, https://doi.org/10.1007/978-94-007-2595-9.

445 Bergkvist, H. & Fornerod, M. 1979. Fracture Toughness Measurements on Core Samples.

446 Bubeck, A., Healy, D., Walker, R.J., Holwell, D.A. & Dobbs, M. 2016. Pore geometry as
447 a control on rock strength. *Earth and Planetary Science Letters*, **457**, 38–48,
448 https://doi.org/10.1016/j.epsl.2016.09.050.

449 Burberry, C.M. & Peppers, M.H. 2017. Fracture characterization in tight carbonates: An
450 example from the Ozark Plateau, Arkansas. *AAPG Bulletin*, **101**, 1675–1696,
451 https://doi.org/10.1306/01251715242.

452 Chalmers, G.R.L. & Bustin, R.M. 2017. A multidisciplinary approach in determining the
453 maceral (kerogen type) and mineralogical composition of Upper Cretaceous Eagle
454 Ford Formation: Impact on pore development and pore size distribution.
455 *International Journal of Coal Geology*, **171**, 93–110,
456 https://doi.org/10.1016/j.coal.2017.01.004.

457 Chandler, M.R., Meredith, P.G., Brantut, N. & Crawford, B.R. 2016. Fracture toughness
458 anisotropy in shale. *Journal of Geophysical Research : Solid Earth*, **121**, 1–24,
459 https://doi.org/10.1002/2015JB012756.

460 Cicero, S., García, T., Castro, J., Madrazo, V. & Andrés, D. 2014. Analysis of notch effect
461 on the fracture behaviour of granite and limestone: An approach from the Theory of
462 Critical Distances. *Engineering Geology*, **177**, 1–9,
463 https://doi.org/10.1016/j.enggeo.2014.05.004.

464 Dashti, R., Rahimpour-Bonab, H. & Zeinali, M. 2018. Fracture and mechanical
465 stratigraphy in naturally fractured carbonate reservoirs-A case study from Zagros
466 region. *Marine and Petroleum Geology*, **97**, 466–479,
467 https://doi.org/10.1016/j.marpetgeo.2018.06.027.

468 Dibb, T.E., Hughes, D.W. & Poole, A.B. 1983. The identification of critical factors
469 affecting rock durability in marine environments. *Quarterly Journal of Engineering*

Geology and Hydrogeology, **16**, 149–161, https://doi.org/10.1144/gsl.qjeg.1983.016.02.08.

F. Stoeckhert, Brenne, S., Molenda, M. & Alber, M. 2016. Mode I fracture toughness of rock under confining pressure. *Eurock2016*.

Forbes Inskip, N.D., Meredith, P.G., Chandler, M.R. & Gudmundsson, A. 2018. Fracture properties of Nash Point shale as a function of orientation to bedding. *Journal of Geophysical Research: Solid Earth*, 1–17, https://doi.org/10.1029/2018JB015943.

Gunsallus, K.L. & Kulhawy, F.H. 1984. A comparative evaluation of rock strength measures. *International Journal of Rock Mechanics and Mining Sciences and Geomechanics*, **21**, 233–248, https://doi.org/10.1016/0148-9062(84)92680-9.

Guo, H., Aziz, N.I. & Schmidt, L.C. 1993. Rock fracture-toughness determination by the Brazilian test. *Engineering Geology*, **33**, 177–188, https://doi.org/10.1016/0013-7952(93)90056-I.

Haines, T.J., Michie, E.A.H., Neilson, J.E. & Healy, D. 2016. Permeability evolution across carbonate hosted normal fault zones. *Marine and Petroleum Geology*, **72**, 62–82, https://doi.org/10.1016/j.marpetgeo.2016.01.008.

Heap, M.J., Vinciguerra, S. & Meredith, P.G. 2009. The evolution of elastic moduli with increasing crack damage during cyclic stressing of a basalt from Mt. Etna volcano. *Tectonophysics*, **471**, 153–160, https://doi.org/10.1016/j.tecto.2008.10.004.

Heap, M.J., Xu, T. & Chen, C. feng. 2014. The influence of porosity and vesicle size on the brittle strength of volcanic rocks and magma. *Bulletin of Volcanology*, **76**, 1–15, https://doi.org/10.1007/s00445-014-0856-0.

Helmer, G., Sulem, J., Ghabezloo, S., Rohmer, J. & Hild, F. 2014. Experimental evaluation of the fracture toughness on a limestone. *Rock Engineering and Rock*

494 *Mechanics: Structures in and on Rock Masses*, 217–221,
495 https://doi.org/10.1201/b16955-34.

496 Hosseini, M., Tavakoli, V. & Nazemi, M. 2018. The effect of heterogeneity on NMR
497 derived capillary pressure curves, case study of Dariyan tight carbonate reservoir in
498 the central Persian Gulf. *Journal of Petroleum Science and Engineering*, **171**, 1113–
499 1122, https://doi.org/10.1016/j.petrol.2018.08.054.

500 Ingraffea, A., Gunsallus, K., Beech, J. & Nelson, P. 1984. A Short-rod based system for
501 fracture toughness testing of rock. *In*: Underwood, J. H., Freiman, S. W. & Baratta,
502 F. I. (eds) *Chevron-Notched Specimens - Testing and Stress Analysis*. Philadelphia,
503 ASTM, 152–166.

504 Khan, K. & Al-Shayea, N.A. 2000. Effect of specimen geometry and testing method on
505 mixed Mode I-II fracture toughness of a limestone rock from Saudi Arabia. *Rock*
506 *Mechanics and Rock Engineering*, **33**, 179–206,
507 https://doi.org/10.1007/s006030070006.

508 Kuruppu, M.D., Obara, Y., Ayatollahi, M.R., Chong, K.P. & Funatsu, T. 2014. ISRM-
509 Suggested method for Determining the Mode I static fracture toughness using Semi-
510 circular Bend specimen. *In*: Ulusay, R. (ed.) *The ISRM Suggested Methods for Rock*
511 *Characterization, Testing and Monitoring 2007-2014*. Springer, 107–114.

512 Lamarche, J., Lavenu, A.P.C., Gauthier, B.D.M., Guglielmi, Y. & Jayet, O. 2012.
513 Relationships between fracture patterns, geodynamics and mechanical stratigraphy
514 in Carbonates (South-East Basin, France). *Tectonophysics*, **581**, 231–245,
515 https://doi.org/10.1016/j.tecto.2012.06.042.

516 Lee, H.P., Olson, J.E., Holder, J., Gale, J.F.W. & Myers, R.D. 2015. The interaction of
517 propagating opening mode fractures with preexisting discontinuities in shale.
518 *Journal of Geophysical Research : Solid Earth*, **120**, 169–181,

https://doi.org/10.1002/2014JB011358.

Li, B., Shen, H., Qu, S., Wang, D. & Liu, C. 2018. Tight carbonate reservoir characterization based on the modified rock physics model. *Journal of Applied Geophysics*, **159**, 374–385, https://doi.org/10.1016/j.jappgeo.2018.09.012.

Li, W.-L. & Li, J.C.M. 1989. The effect of grain size on fracture toughness. *Philosophical Magazine A*, **59**, 1245–1261, https://doi.org/10.1080/01418618908221173.

Lian, C., Zhuge, Y. & Beecham, S. 2011. The relationship between porosity and strength for porous concrete. *Construction and Building Materials*, **25**, 4294–4298, https://doi.org/10.1016/j.conbuildmat.2011.05.005.

Lundborg, N. & Almgren, L.A. 1972. Bestamning av brottseghet hos bergmaterial.

Meille, S., Lombardi, M., Chevalier, J. & Montanaro, L. 2012. Mechanical properties of porous ceramics in compression: On the transition between elastic, brittle, and cellular behavior. *Journal of the European Ceramic Society*, **32**, 3959–3967, https://doi.org/10.1016/j.jeurceramsoc.2012.05.006.

Meredith, P.G. 1989. Comparative fracture toughness testing of rocks. *In*: Mihashi, H., Takahashi, H. & Wittman, F. H. (eds) *Fracture Toughness and Fracture Energy: Test Methods for Concrete and Rock*. Rotterdam, Brookfield, 265–278.

Nath Singh, R. & Sun, G. 1990. A numerical and experimental investigation for determining fracture toughness of Welsh limestone. *Mining Science and Technology*, **10**, 61–70, https://doi.org/10.1016/0167-9031(90)90850-R.

Ouchterlony, F. & Sun, Z. 1983. New Methods of Measuring Fracture Toughness on Rock Cores.

Palchik, V. & Hatzor, Y.H. 2004. The Influence of Porosity on Tensile and Compressive Strength of Porous Chalks. *Rock Mechanics and Rock Engineering*, **37**, 331–341,

https://doi.org/10.1007/s00603-003-0020-1.

Rashid, F., Glover, P.W.J., Lorinczi, P., Hussein, D. & Lawrence, J.A. 2017. Microstructural controls on reservoir quality in tight oil carbonate reservoir rocks. *Journal of Petroleum Science and Engineering*, **156**, 814–826, https://doi.org/10.1016/j.petrol.2017.06.056.

Sabatakakis, N., Koukis, G., Tsiambaos, G. & Papanakli, S. 2008. Index properties and strength variation controlled by microstructure for sedimentary rocks. *Engineering Geology*, **97**, 80–90, https://doi.org/10.1016/j.enggeo.2007.12.004.

Schaefer, L.N., Kendrick, J.E., Oommen, T., Lavallee, Y. & Chigna, G. 2015. Geomechanical rock properties of a basaltic volcano. *Frontiers in Earth Science*, **3**, 1–15, https://doi.org/10.3389/feart.2015.00029.

Schmidt, R.A. 1976. Fracture-toughness testing of limestone. *Experimental Mechanics*, **16**, 161–167, https://doi.org/10.1007/BF02327993.

Schmidt, R.A. 1977. Fracture Mechanics Of Oil Shale - Unconfined Fracture Toughness, Stress Corrosion Cracking, And Tension Test Results. *In*: *The 18th U.S. Symposium on Rock Mechanics (USRMS)*. American Rock Mechanics Association.

Sheppard, T.H., Houghton, R.D. & Swan, A.R.H. 2006. Bedding and pseudo-bedding in the Early Jurassic of Glamorgan: Deposition and diagenesis of the Blue Lias in South Wales. *Proceedings of the Geologists' Association*, **117**, 249–264, https://doi.org/10.1016/S0016-7878(06)80033-7.

Tucker, M. & Wright, V. 2009. *Carbonate Sedimentology*, https://doi.org/10.1002/9781444314175.

Tucker, M.E. 2001. Sedimentary Petrology: An introduction to the Origin of Sedimnetary Rocks.

567 Vinciguerra, S., Trovato, C., Meredith, P.G. & Benson, P.M. 2005. Relating seismic
568 velocities, thermal cracking and permeability in Mt. Etna and Iceland basalts.
569 *International Journal of Rock Mechanics and Mining Sciences*, **42**, 900–910,
570 https://doi.org/10.1016/j.ijrmms.2005.05.022.

571 Wentworth, C.K. 1922. A Scale of Grade and Class Terms for Clastic Sediments. *The*
572 *Journal of Geology*, **30**, 377–392.

573

574

Supporting information

The static elastic moduli presented in Table 1 were measured from conventional uniaxial compression tests following the method of Heap & Faulkner (2008), and as described in the methodology Chapter of this thesis. Representative stress-strain graphs from tests loading cores in each orientation are presented in Figures S1 and S2.

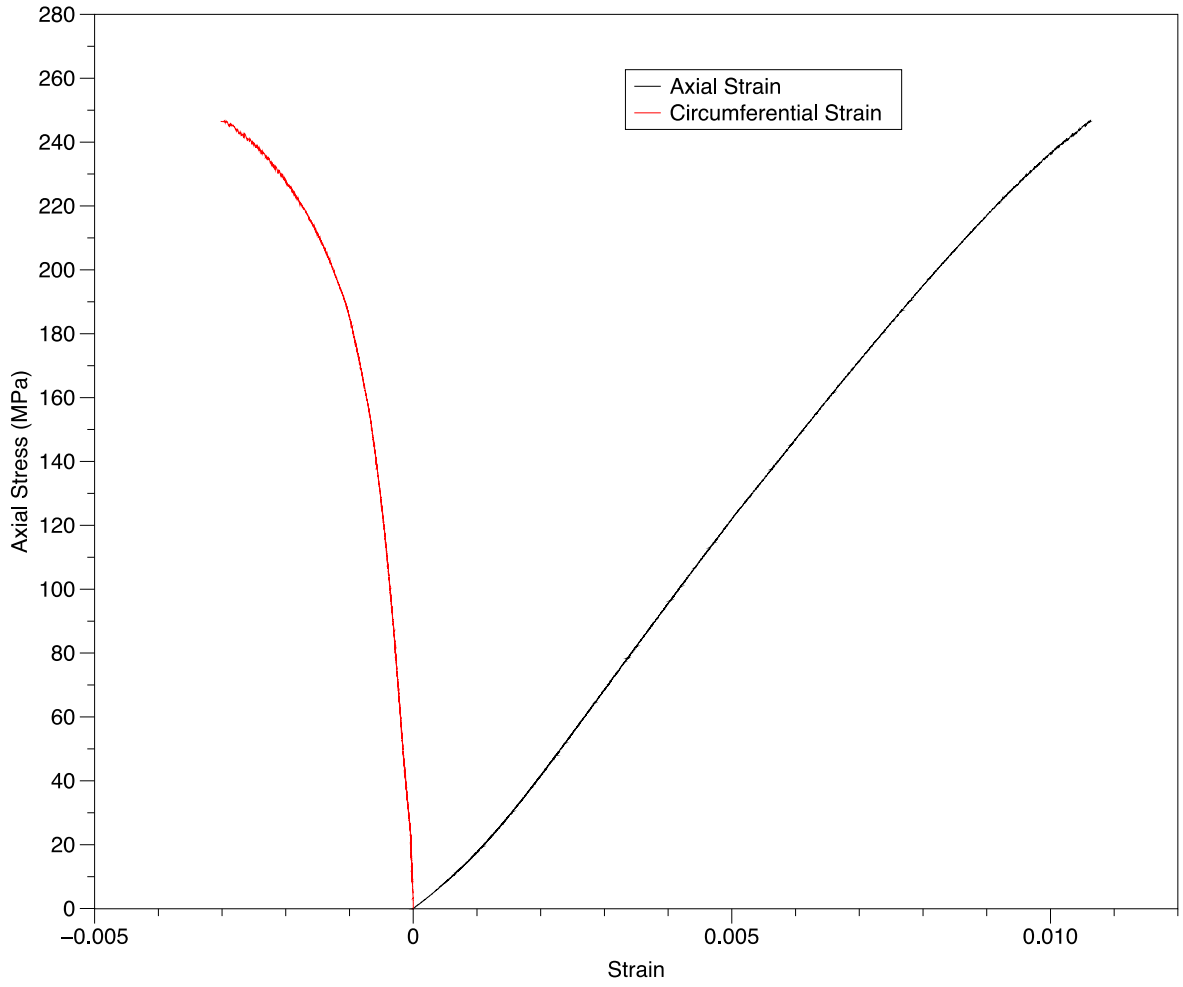

Figure S1: Axial and Circumferential strain plotted as a function of stress for a Nash Point limestone core loaded normal to bedding.

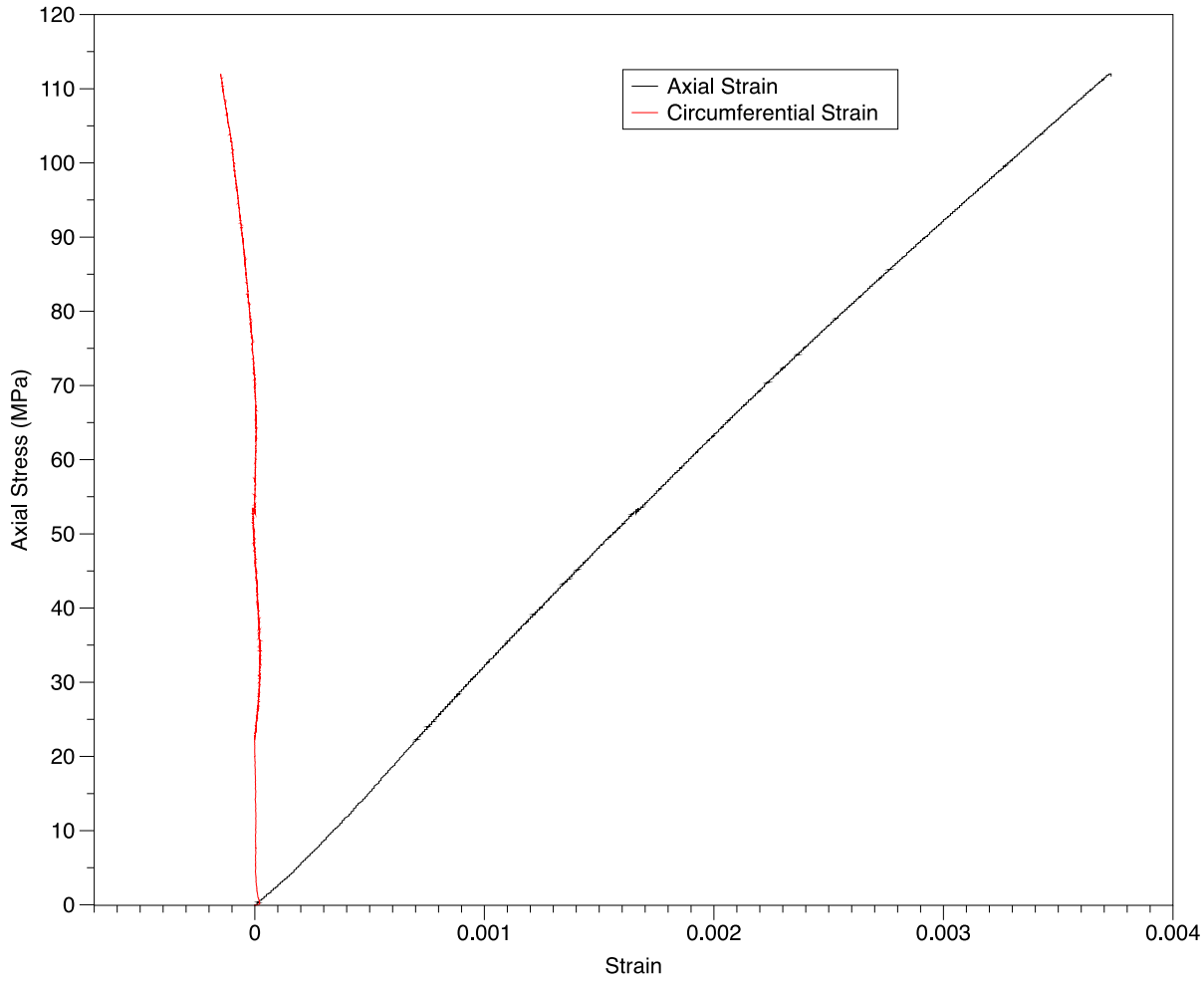

588

589 Figure S2: Axial and Circumferential strain plotted as a function of stress for a Nash Point limestone core
590 loaded parallel to bedding.

591

592 It should be noted that in these examples the sample loaded parallel to bedding failed at
593 a lower load than the sample loaded normal to bedding. This was due to the sample failing
594 along a thin calcite vein present within the sample. However, this was not found to affect
595 the moduli, and is discussed in detail in Chapter 6.

5 Propagation and arrest of fractures in layered rock sequences

This chapter is written in a manuscript format and contains the results of numerical models used to analyse fluid-driven vertical fractures in layered rock sequences with two contrasting layers; exploring the stress-field effects of variations in layer stiffness, proximity of fracture tip to layer interface, and layer thickness. It has been submitted to Scientific Reports and is therefore written and formatted using their specific guidelines.

Author contribution – Nathaniel Forbes Inskip wrote the manuscript and ran the numerical modelling. John Browning, Philip Meredith, and Agust Gudmundsson contributed to data interpretation and made comments on the manuscript.

Propagation and arrest of fractures in layered rock sequences

Nathaniel Forbes Inskip[1,2,3], John Browning[4], Philip G Meredith[3], Agust Gudmundsson[2]

[1] The Lyell Centre, Heriot-Watt University, Edinburgh, United Kingdom

[2] Department of Earth Sciences, Royal Holloway University of London, Egham, United Kingdom

[3] Department of Earth Sciences, University College London, London, United Kingdom

[4] Department of Mining Engineering and Department of Structural and Geotechnical Engineering, Pontificia Universidad Católica de Chile, Santiago, Chile

Abstract

Fracture propagation in layered rock sequences controls many of the dynamic processes on the planet, such as dyke-fed volcanic eruptions, earthquake ruptures, landslides, and the evolution of plate boundaries. Yet it remains poorly understood. For example, we do not know the conditions for dyke arrest (preventing potential eruptions) or hydraulic-fracture arrest in gas shales (preventing a potential pollution of aquifers). Here we present new numerical results on fluid-driven (mode-I) vertical fractures in layered rock sequences with two contrasting layers; exploring the stress-field effects of variations in layer stiffness, proximity of fracture tip to layer interface, and layer thickness. When the layer hosting the fracture tip is the stiffer one, fracture arrest normally occurs at the interface with the more compliant layer. When the layer above the interface is the stiffer one, fracture arrest may occur directly at the interface or within the host layer well below the interface. The conclusions are supported by field observations of arrested joints and dykes.

Understanding and forecasting the conditions leading to propagation or arrest of fractures in crustal segments composed of different layers is a fundamental and unsolved problem in Earth Sciences. This is important because fractures largely control key processes in fields such as volcanology, seismology, engineering geology, hydrogeology, and petroleum geology. Most rock fracture propagation models assume that the crustal segment hosting the fracture is either isotropic and homogeneous (i.e. non-layered), or, at most, composed of only a few layers or units [1]. Most volcanic eruptions occur only when a fluid-driven fracture, a dyke, is able to propagate through numerous crustal layers and interfaces, from its source magma chamber to the surface [2]. Thus, the mechanical conditions that allow a propagating dyke to successfully penetrate all the layers ahead of it rather than become arrested provide one of the main controls on whether an eruption occurs or not. Similarly, the size of an earthquake is primarily governed by the ability of faults and fractures to propagate. Most faults propagate for very short distances before they become arrested, whereas some propagate for great distances and hence generate large earthquakes, resulting in the well-known power-law size-frequency distribution of earthquakes [3,4]. Similarly, the generation and evolution of large calderas, which are responsible for some of the most voluminous past volcanic eruptions, are also governed by the ability of faults to connect a sub-surface magma chamber to the surface [2,5]. Also, man-made hydraulic (fluid-driven) fractures, commonly used to increase the permeability of fluid-filled reservoirs of various types, propagate in a manner that is mechanically analogous to that of dykes, particularly vertically oriented hydraulic fractures which are commonly generated to increase permeability in unconventional reservoirs [6]. As such, improved understanding of fracture propagation in volcanoes and faults zones is necessary to increase the reliability of eruption forecasting, to estimate the likely sizes of earthquakes and, in doing so, to reduce the potential associated hazards. Understanding man-made fracture propagation in unconventional reservoirs is important to maximise

resource production, but also to reduce the likelihood of induced seismicity and aquifer contamination.

Fluid-driven fractures (which includes dykes and hydraulic fractures) are predominately extension fractures and hence modelled as mode-I cracks [7], while faults are formed from a combination of extension fractures and shear fractures and hence are modelled as a mixture of mode-I, mode-II and mode-III cracks. Despite the different modes of fracture propagation, certain conditions must be met for any fracture to propagate. Generally, both the minimum principal stress (σ_3) and the tensile strength of the material need to be overcome for a mode-I fracture to propagate, whereas for a mode-II or mode-III fracture the shear strength of the material must be overcome. As such it is important to understand the magnitude and distribution of tensile stress (for mode-I fractures) and/or shear stress (for mode-II or mode-III fractures) at the tip of fractures in geological sequences.

Whilst there have been many studies on hydraulic fracture propagation [8,9,18,10–17], both using analytical [14,19] and numerical modelling techniques [12,20], none of these studies fully represent the heterogeneous (i.e. layered) nature of the crust. However, many crustal segments are heterogeneous, particularly crustal segments hosting oil and gas reservoirs, for example the Vaca Muerta formation in Argentina. Here the target reservoir is the shale units within the Vaca Muerta formation, but the shale is interbedded with limestone beds/nodules, ash layers and sills, all of which are likely to have different mechanical properties [21,22]. Similarly, crustal segments hosting volcanoes are also often heterogeneous and composed of many different layers each with contrasting mechanical properties [23]. It has been shown that the layering in volcanic edifices can inhibit fluid-driven fracture propagation, in this case dykes, and hence influence the frequency of volcanic eruptions [24]. In fact, field evidence suggests that most dykes either become arrested in the crust or deflected to form sills [17].

Previous work that takes data from field observations, and analytical and numerical models [14,17,19,25–30] suggests that mechanical stratigraphy can have significant effects on fracture propagation in layered sequences. This study focuses on the effects of three parameters on the tensile stress concentration at the tip of a mode I (extension) fracture, and in particular fluid-driven fractures (hydraulic fractures). These three parameters are (1) Young's modulus contrast across the interface between two layers; that is, difference in Young's modulus between the layer hosting the fracture tip and the layer ahead of the fracture tip (above the interface); (2) distance from the fracture tip to the interface (tip proximity to the interface); and (3) thickness of the layer ahead of the interface. We show that all these parameters affect the local tensile stress at the fracture tip, and hence the probability of fracture arrest at or, alternatively fracture propagation through, the interface. The results have wide implications for the propagation of rock fractures and fracture-related processes such as volcanic eruptions, hydraulic fracturing, and earthquakes. Here, however, the modelling is confined to extension fractures (mode-I cracks).

Results

Field observations

In Figure 1 we present field examples which highlight the influence of contrasting rock mechanical properties on fracture propagation.

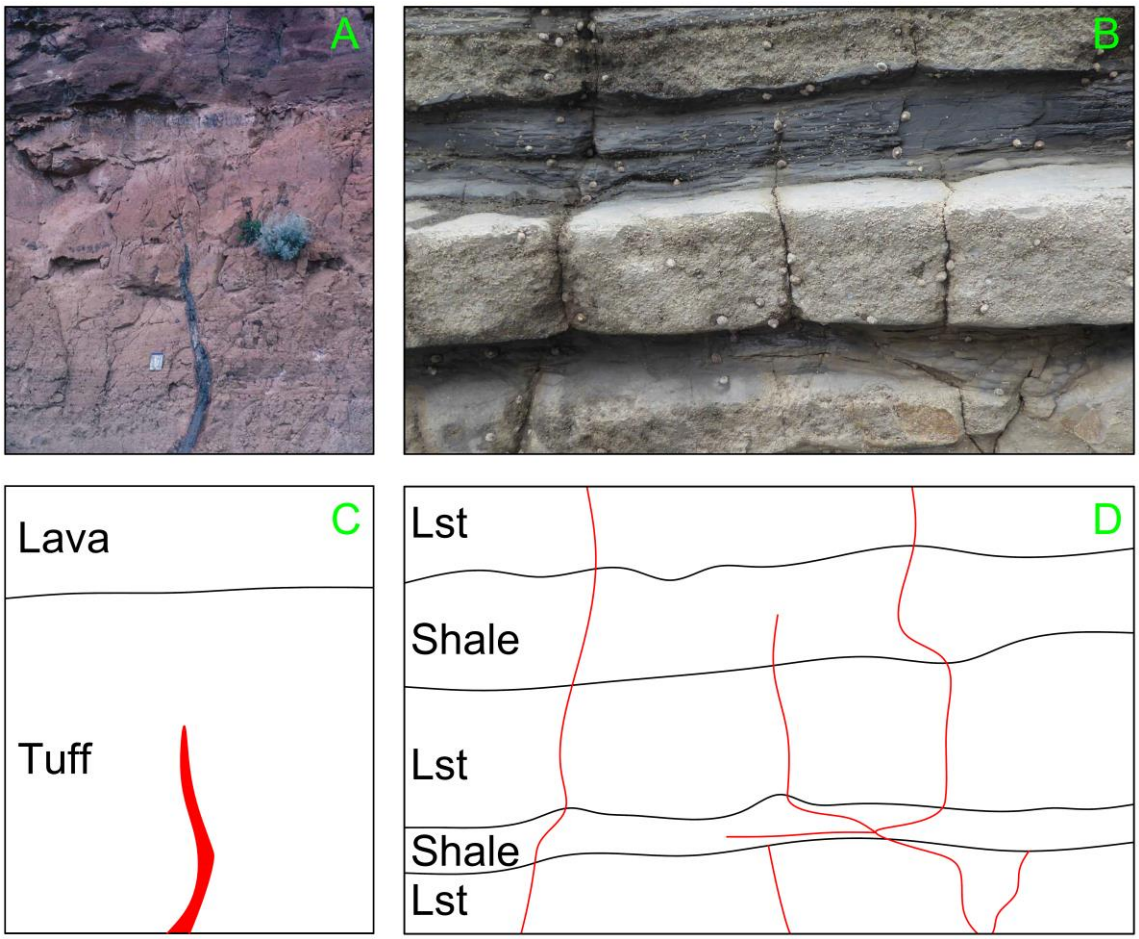

Figure 1: (A) Dyke in Tenerife, Canary Islands, propagating through a compliant (low Young's modulus) tuff (pyroclastic) layer towards a stiffer (higher Young's modulus) lava flow. Here the thickness (palaeo-aperture) of the dyke is 0.25 m at the bottom of the exposure, and it thins towards the tip, where the dyke was arrested before reaching the interface with the stiff lava. (B) Series of joints in a interbedded limestone (stiff) and shale (compliant) sequence at Nash Point, South Wales, UK. The thickest shale bed in this figure is approximately 0.3 m. Within the centre of this shale bed one of the joints is arrested before reaching the stiffer limestone above, whereas other joints have propagated through the whole sequence or become arrested at the interface between the two layers. (C) and (D) are schematics of (A) and (B), respectively, where black lines depict interfaces between different rock units and red lines depict the outline of the dyke in (C) and the joints in (D).

The example in Figure 1A is a basaltic dyke on the volcanic island of Tenerife, Canary Islands, whose palaeo-aperture (thickness) is approximately 0.25 m at its base and thins towards the tip. The stiffness (Young's modulus) of the tuff layer hosting the dyke is much lower than that of the lava flow on top of the tuff. In this section, the dyke became arrested prior to reaching the interface between the tuff and the lava flow. It is more common for fractures to become arrested or deflected at the interface between two units

112 or layers, and so the fact that the observed dyke becomes arrested within a unit, rather
113 than at the interface between units, needs explaining. By contrast, the arrest of a dyke (or
114 any mode-I fracture) at an interface between two layers is well understood and explained
115 in terms of three main mechanisms, namely: Cook-Gordon delamination, stress barriers,
116 and elastic mismatch (which are described in the Supplementary Material) [7,17,23]. Our
117 observations suggest that the mechanism governing fractures arrested within units/layers
118 and not at their interfaces, such as that shown in Figure 1A, may be subtly different.

119 The fractures in Figure 1B occur in an interbedded limestone and shale sequence at Nash
120 Point, South Wales. The fracture pattern is ubiquitous through the entire sequence and
121 along the several km of coastal exposure, and consists primarily of joints (which may or
122 may not be fluid driven) and mineral veins which are both predominantly mode-I in
123 nature. In this example, the limestone layers are much stiffer (higher Young's modulus)
124 than the shale layers. In Figure 1B three fractures propagate across the sequence. Two of
125 the fractures cross quasi-vertically through the entire sequence, while one becomes
126 arrested within a shale bed, and does not reach the interface with the limestone layer
127 above. We seek to understand how fractures can become arrested prior to meeting an
128 interface.

129 To date, the effect of layering on tensile stress distributions at the fracture tip prior to
130 meeting an interface between layers has received little attention. Müller (1986) concluded
131 that the stress intensity factor at a fracture tip decreased when a fracture propagated
132 towards a stiffer layer, but increased when the fracture propagated towards a more
133 compliant layer. However, this work did not consider the effect of layer thickness, and
134 some important model parameters are omitted (such as fracture aspect ratio, internal fluid
135 pressure, and the model dimension). Here we present a systematic study of the effects that
136 mechanical layering has on the tensile stresses at the tip of a hydraulic fracture, using the
137 Finite Element Method (FEM). In our models, we consider three variables, namely: (1) a

138 contrast in Young's modulus between the layers, (2) the proximity of the fracture tip to
139 the layer ahead of the fracture tip, and (3) the thickness of that layer.

140 In addition to the three variables being considered here, the tensile stress at the tip of the
141 fracture depends also on the dimensions of the fracture. In nature, many mode-I hydraulic
142 fractures have a length to aperture aspect ratio of approximately 1000 : 1 [7,26]. We
143 therefore use this aspect ratio for the fractures in our models where length refers to the
144 dip dimension of a fracture rather than the strike dimension. Aperture is the amount of
145 fracture opening which, for 'frozen' or filled fractures such as dykes and mineral veins,
146 is approximately equal to the measured thickness.

147 **Numerical models**

148 Here we present results from 529 model runs where we investigated the three variables,
149 namely; Young's modulus contrast, layer thickness, and distance from fracture tip to
150 interface; first individually, and then all together. In all models, the crustal segment
151 measured 300 x 300 m in vertical cross-section with fixed corners to avoid rigid body
152 translation or rotation of the model. The initial conditions for each model prescribe a 10
153 m long fracture (dip dimension) with a maximum aperture of 0.01 m contained within a
154 host layer (Figure 2). Internal fluid pressure within the fracture, more specifically an
155 overpressure of 0.5 MPa, was the only loading.

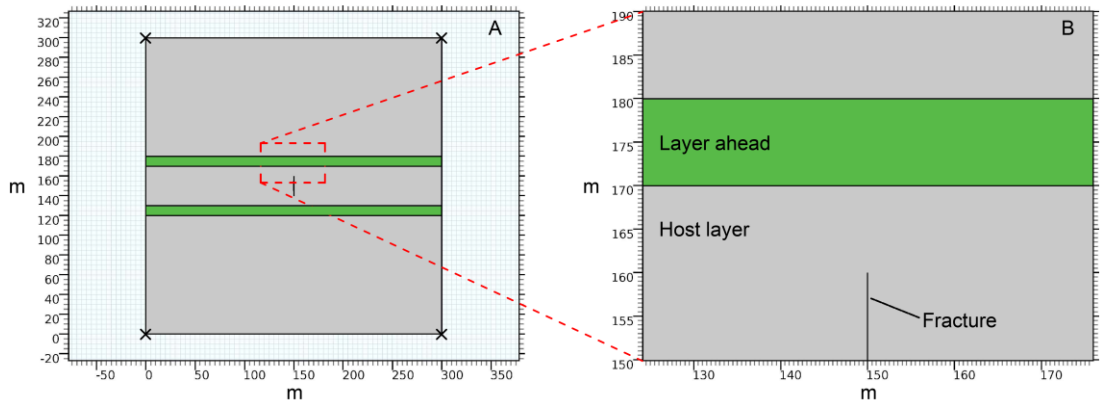

Figure 2: (A) Model setup. The model is 300 × 300 m in vertical cross-section to avoid any edge effects. The 10 m tall (dip dimension) fracture is fully contained within the middle layer (host layer) which has the same properties as the top and bottom layers. The properties of the two layers in green vary throughout this study. (B) Zoomed-in image with annotations demonstrating which is the layer hosting the fracture and which is the layer ahead (green).

Effect of Young's modulus contrasts

We model how the tensile stress at the tip of a hydraulic fracture is affected by a succeeding layer (referred to as layer ahead) with a Young's modulus that is different from or contrasting to the layer hosting the fracture (referred to as the host layer). The properties of the host layer remained constant throughout the analysis, namely a Young's modulus of 10 GPa, a Poisson's ratio of 0.25, and a density of 2600 $kg.m^{-3}$. In all the models, the layer ahead of the fracture tip was 10 m thick and its lower interface 10 m ahead of the crack tip.

Figure 3 shows the variation in fracture-tip tensile stress as a function of Young's modulus ratio between the host layer and the layer ahead (A), along with model extracts showing the tensile stress distribution when the Young's modulus of the layer ahead was 1.25 GPa (a ratio of 0.125) (B) and 80 GPa (a ratio of 8) (C). Clearly, the contrast in Young's modulus between the host layer and the layer ahead affects the tensile-stress field at the tip of the hydraulic fracture. When the Young's modulus of the layer ahead and the host layer are the same, i.e. the model is homogeneous, the tensile stress at the

fracture tip is 3.84 MPa. When the Young's modulus of the layer ahead is lower than in the host layer, producing a Young's modulus ratio of < 1, the tensile stress at the fracture tip is higher. This is as expected because more compliant material with a lower Young's modulus is less able to concentrate stress. Therefore for lower Young's modulus ratios the tensile stress at the fracture tip is higher. Conversely, when the Young's modulus of the layer ahead is higher than in the host layer, producing a Young's modulus ratio of > 1, the tensile stress at the fracture tip is lower. This is due to the fact that stress is dissipated into the stiffer layer ahead (see Figure 3C – where stress concentrates across the interface). In both Figures 3B and 3C the tensile stress drops significantly within a few tens of centimetres from the fracture tip (i.e. from approximately 4 MPa to less than 0.1 MPa).

When plotted, the variation of tensile stress at the fracture tip with respect to a variation in Young's modulus ratio fits a power law distribution. For the highest Young's modulus ratio modelled (i.e. 8) the tensile stress at the fracture tip is 13% lower than the model with the lowest Young's modulus ratio (i.e. 0.125).

This suggests that, for any given value of host-rock tensile strength, a larger fluid overpressure is required to propagate a fracture when the layer ahead is stiffer than the host layer. This is in excellent agreement with analytical studies which indicate that many extension fractures become arrested at interfaces where the layer ahead of the interface is stiffer than the layer below the interface that hosts the propagating fracture[6, 15, 16]. This mechanism of fracture arrest is referred to as *elastic mismatch*.

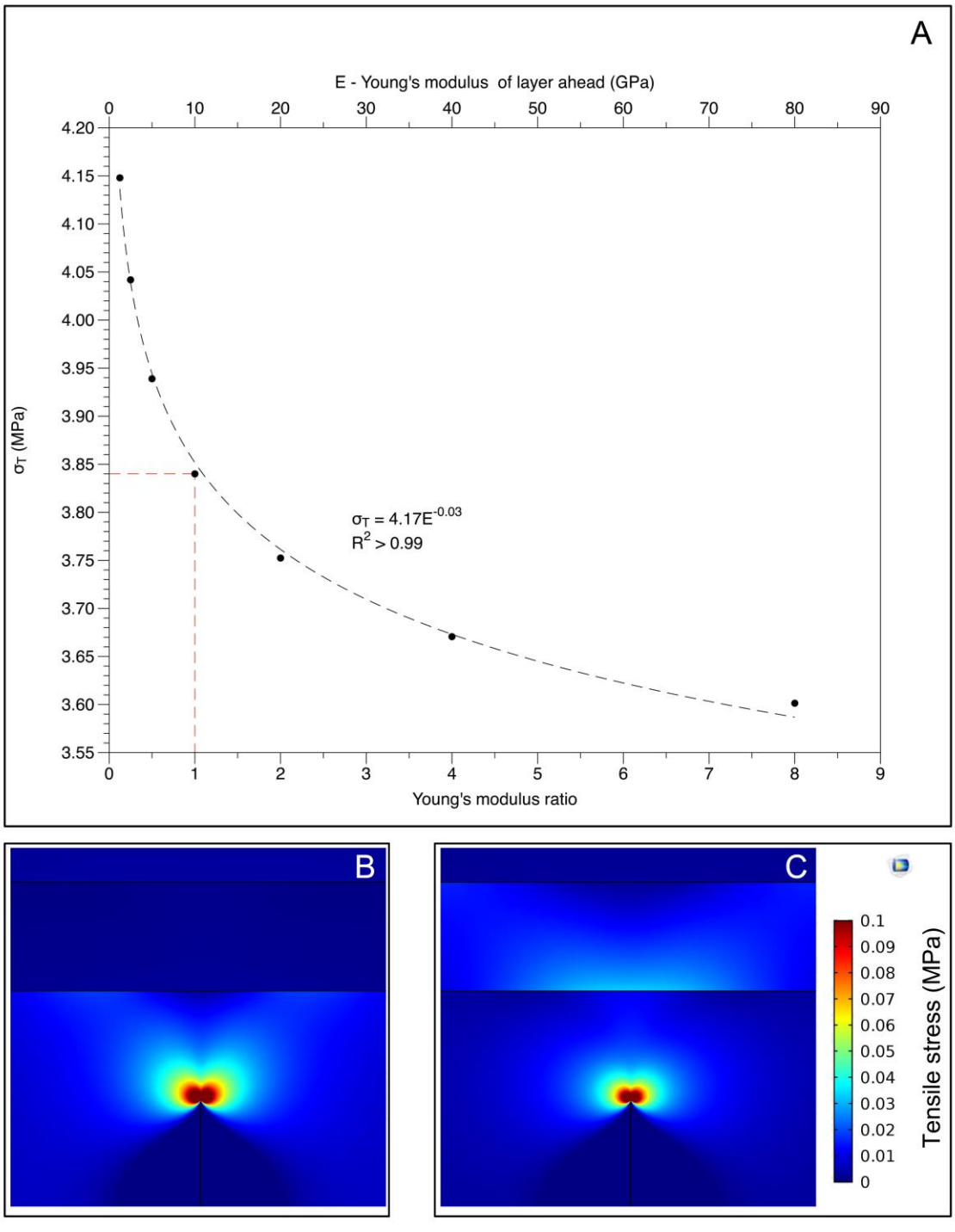

198

199 Figure 3: (A) Variation in the tensile stress, σ_T, at the fracture tip with Young's modulus of the layer ahead. The red
200 line depicts the homogeneous case. (B) Tensile stress within the model. Warmer colours signify higher tensile stress.
201 In this model the layer ahead had a Young's modulus of 1.25 GPa (a Young's modulus ratio of 0.125), which was the
202 lowest value of Young's modulus used in our models. In this case the tensile stress at the fracture tip is 4.15 MPa. (C)
203 Is the same as (B) but here the layer ahead has a Young's modulus of 80 GPa (a Young's modulus ratio of 8), which
204 was the highest value of Young's modulus used in our models. In this case the tensile stress at the fracture tip is 3.6
205 MPa. Both (B) and (C) are approximately 30 x 30 m insets from the model.

Changes in thickness of the layer ahead

To extend our analysis, we also consider how changes in Young's modulus ratio and in the thickness of the layer ahead affect tensile stress at the fracture tip, by running two sets of models: (1) a model with a Young's modulus ratio of 0.5, and (2) a model with a Young's modulus ratio of 2. With these modulus ratios, the layer ahead has a Young's modulus contrast of 2 in both cases. As in the previous model runs, the distance between the fracture tip and the interface (between the host layer and the layer ahead) remains at 10 m or 1 fracture length (as the fracture in all models is 10 m long) while the thickness of the layer ahead is varied from 2 m to 80 m.

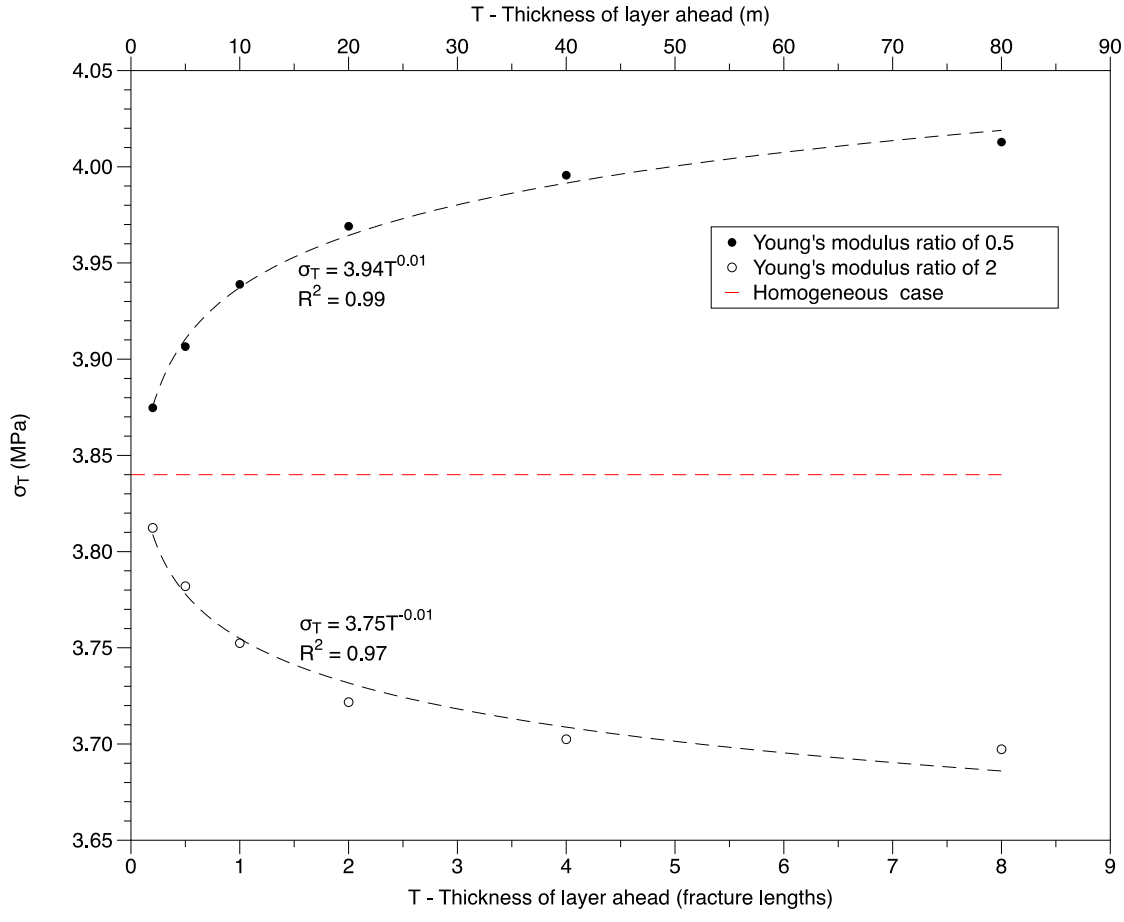

Figure 4: Variation in the maximum tensile stress σ_T at the fracture tip with changes in thickness of the layer ahead, for Young's modulus ratios of 0.5 and 2. A power-law function has been fitted to both datasets, and the tensile stress for the homogeneous case (i.e. where the Young's modulus of the hosting layer and the layer ahead are the same) is plotted as a dashed red line.

Young's modulus ratio of 0.5

When Young's modulus of the layer ahead is lower than that of the host layer, the concentration of tensile stress at the fracture tip is higher. This effect is greater when the thickness of the more compliant layer ahead is larger. Thus, the maximum tensile stress at the fracture tip increases as a (positive) power-law function of the increase in thickness of the layer ahead (Figure 4).

Young's modulus ratio of 2

When the Young's modulus of the layer ahead is higher than that of the host layer, the concentration of tensile stress at the fracture tip is lower. This is because much of the stress is dissipated into the stiffer layer ahead (Figure 4). Consequently the tensile stress at the fracture tip is lower when the comparatively stiff layer ahead is thicker. The maximum tensile stress at the fracture tip decreases as a (negative) power-law function of the increase in the thickness of the layer ahead (Figure 4).

In both implementations of the model (ratios of 0.5 and 2) the tensile stress at the fracture tip approaches the homogeneous value of 3.84 MPa as the thickness of the layer ahead approaches zero (Figure 4). Thus, as the thickness of the layer ahead is decreased, its effect on the tensile stress at the fracture tip also decreases. When the layer ahead has the maximum modelled thickness of 80 m, the peak tensile stress is ~4% higher than the homogeneous value of 3.84 MPa for a modulus ratio of 0.5, and ~4% lower for a modulus ratio of 2.

Change in distance between the fracture tip and the interface

Here we consider how changes in distance to the layer ahead, for the modulus ratios of 0.5 and 2, affect the tensile stress concentration at the fracture tip. In these manifestations of the model, the thickness of the layer ahead is kept constant at one fracture length, or 10 m.

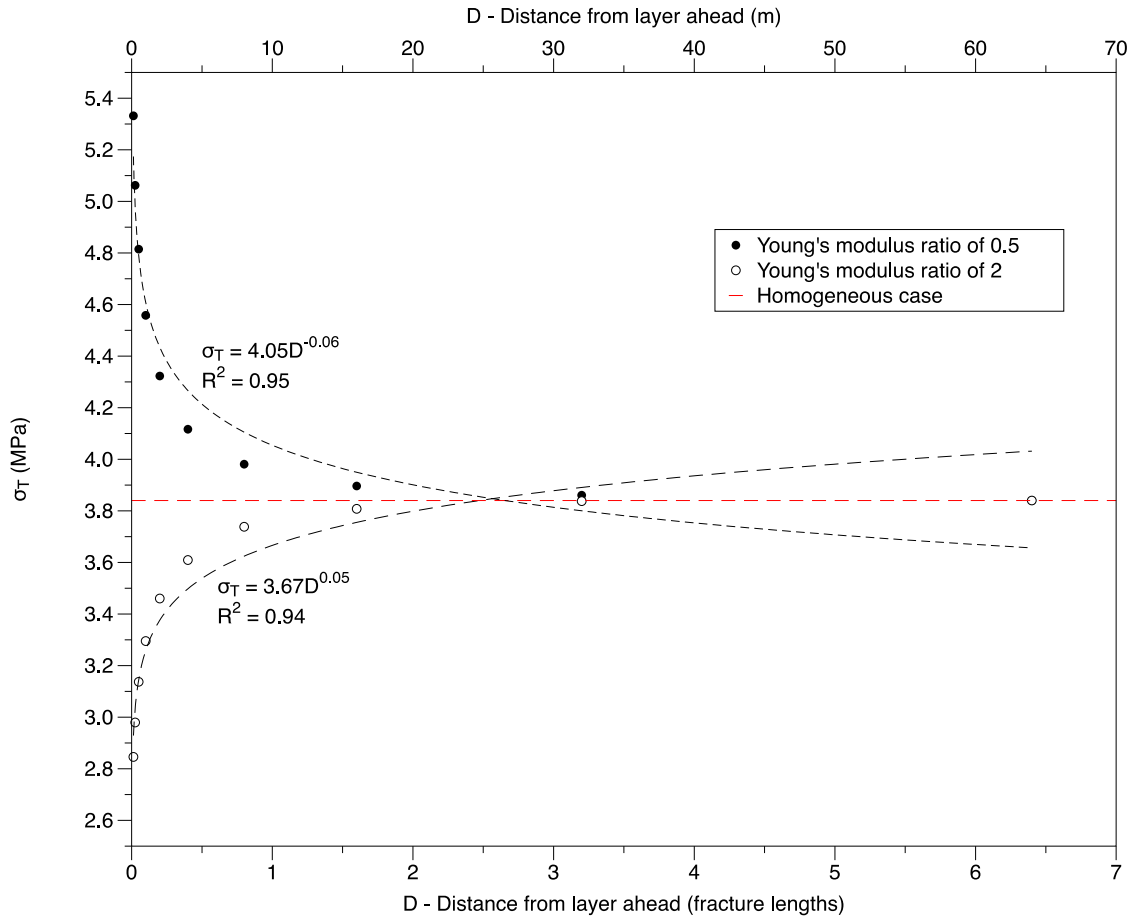

245

246 Figure 5: Variation of the maximum tensile stress σ_T at the fracture tip with distance from the interface ahead, for
247 Young's modulus ratios of 0.5 and 2. A power law function has been fitted to both sets of model output data, and the
248 tensile stress for the homogeneous case is plotted as a dashed red line.

249 Young's modulus ratio of 0.5

250 Here the tensile stress at the fracture tip is significantly larger when the fracture tip is
251 closer to an interface with a more compliant layer (modulus ratio of 0.5) ahead (Figure
252 5). When the fracture tip is close to the interface, there is less host-layer material between
253 the fracture tip and the interface available to dissipate the stress, and this results in a
254 greater tensile stress concentration at the fracture tip. Again, the increase in tensile stress
255 with decreasing distance to the interface is well fit with a power law.

256 Young's modulus ratio of 2

257 Under these conditions, the tensile stress at the fracture tip is significantly lower when
258 the fracture tip is closer to the interface with the stiffer layer ahead (modulus ratio of 2)

(Figure 5). When the fracture tip is closer to the interface with the stiffer layer, it concentrates more of the stress, thereby reducing the stress at the fracture tip. Again, the increase in tensile stress with decreasing distance to the interface is generally well fit with a power law.

For both conditions, the model demonstrates that the tensile stress at the fracture tip is highly dependent on the fracture's proximity to the layer ahead. However, this dependence decreases significantly as the distance between the fracture tip and the layer ahead is increased. Our data are generally well fit by a power law up to the distance where they both have the same value as the homogeneous case. At greater distances it is a poor fit as our values for both ratios are the same as the homogeneous case. The results show that there is essentially no effect on fracture-tip tensile stress in the far-field, where the distance to the interface exceeds approximately 30 m, or 3 fracture lengths

Furthermore, the sign of the change in fracture-tip stress depends on the modulus contrast. For a fracture approaching close (0.125 m) to an interface with a more compliant layer, where the modulus ratio is 0.5, the fracture-tip tensile stress is 37% higher than in the far-field. By contrast, for a fracture approaching close to an interface with a stiffer layer, with a modulus ratio of 2, the fracture-tip tensile stress is 26% lower than in the far-field.

In a geological context, these results suggest that, for any given loading condition, when the tip of a fluid-pressure driven fracture approaches a layer interface, the tensile stress at the fracture tip will gradually increase if the layer being approached is more compliant than the host layer, but will gradually decrease if the layer being approached is stiffer than the host layer. Hence, such fractures (for example, dykes) propagating through a comparatively compliant layer but approaching the interface with a comparatively stiff layer may become arrested well before they reach the interface; a phenomenon well-known from field observations [7,17] (Figure 1). By contrast, a fracture propagating through a comparatively stiff layer but approaching the interface with a comparatively compliant

layer is likely to become arrested, if at all, only at the interface itself. Again, this interpretation is well supported by field observations which show, for example, that most fractures in stiff limestone layers propagate right up to the interfaces with adjacent and more compliant. shale layers [7].

Varying all three parameters simultaneously

Of the three parameters discussed here that influence the fracture-tip tensile stress, the proximity to the interface between mechanically dissimilar layers appears to have the largest affect, while the thickness of the layer being approached appears to have the least affect. Nevertheless, it is important to understand how the tensile stress may vary with combined changes in all three parameters

In order to combine changes in all three parameters simultaneously, we ran a series of multi-parametric model runs with (1) Young's modulus ratios between 0.0125 and 8, (2) fracture tip to interface proximities between 0.125 m and 40 m (0.0125 to 4 fracture lengths), and (3) layer thicknesses of 1 m and 80 m (0.1 and 8 fracture lengths). The outputs from all model runs are provided in the Supporting Information. A representative selection of the outputs is displayed in Figure 6.

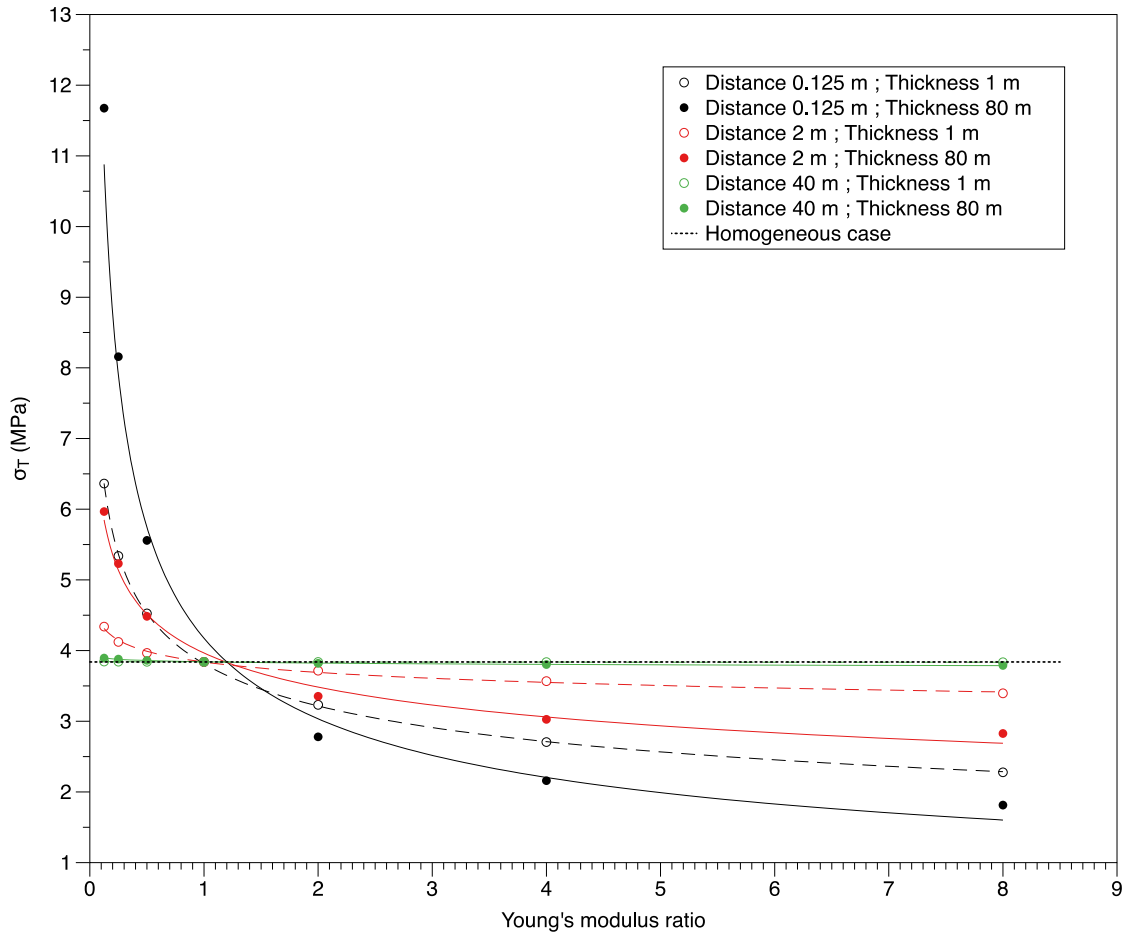

Figure 6: Tensile stress at the fracture tip as a function of variations in all three parameters: (1) Young's modulus ratios between 0.0125 to 8), (2) interface proximities from 0.125 m to 40 m, and (3) succeeding layer thicknesses of 1 m and 80 m. The tensile stress for the homogeneous case is plotted as a horizontal dotted black line. All other lines plotted are power law fits for their respective data set.

When combining the variations in all three parameters, we find that the tensile stress at the fracture tip can range from a minimum of 1.81 MPa to a maximum of 11.67 MPa (Figure 6). Importantly, this range of values is significantly higher than when each of the variables was changed independently. Both the maximum value (204% higher than for the homogeneous case) and the minimum value (53% lower than for the homogeneous case) occur when the fracture tip is closest to the interface and when the thickness of the layer ahead is greatest (80 m or 8 fracture lengths).

Although the highest and lowest tensile stresses occur at the model parameter extremes, these reflect rock properties and boundary conditions that are commonly found in

315 fractured sedimentary basins and volcanic provinces. Furthermore, significant variations
316 in tensile stress ahead of the fracture tip are predicted even in the model runs with less
317 severe variations in Young's modulus, thickness, and interface proximity. For example,
318 when the thickness of the layer ahead is only 1 m, and the fracture tip is 0.125 m from the
319 interface, we still observe maximum and minimum tensile stresses that are 66% higher
320 (6.36 MPa) and 41% lower (2.28 MPa) than the homogeneous value, and thus still
321 important. For example, in the Vaca Muerta formation, individual layer thicknesses vary
322 from a few centimetres to a few metres [21]. Therefore, if a fluid-pressure driven fracture
323 of length <10 m were modelled assuming a homogeneous formation with no mechanical
324 contrast between layers, the resulting stress magnitudes would likely contain significant
325 errors when compared with a more realistic, heterogeneous layered model.

326 The same is true for crustal segments hosting volcanoes where individual (commonly
327 compliant) pyroclastic layers can range in thickness from a few tens of centimetres to tens
328 or even hundreds of metres, whereas (significantly stiffer) sills and lava flows may be as
329 thick as tens or (particularly sills) hundreds of metres. The tensile stress at the tip of a
330 dyke with a height (dip dimension) of <1 km may be very different depending on whether
331 the hosting crustal segment is modelled as being homogeneous or heterogeneous (i.e.
332 containing layering). Stratovolcanoes normally contain many compliant pyroclastic (tuff)
333 layers alternating with much stiffer lava flows (and some sills) through which dykes must
334 propagate in order to reach the surface to erupt [23]. Most dykes, however, do not reach the
335 surface but rather become arrested at some depth in the volcano [7,17,24,26]. Based on the
336 model presented here, dyke arrest when the layer ahead (above the interface) is more
337 compliant than the layer hosting the dyke tip is most likely to occur directly at the
338 interface. This follows because the tensile stress at the fracture tip increases as it
339 approaches the interface, encouraging further propagation. This comparatively high
340 tensile stress may also help to open the interface, resulting in a Cook-Gordon

delamination [7,17]. By contrast, dyke arrest when the layer ahead is stiffer than the host layer can occur either at the interface itself, or at some distance before the interface is reached. This occurs because the tensile stress at the dyke tip decreases as it approaches the interface. Thus, the arrest location is not confined to the interface itself, but actually becomes increasingly more likely as the dyke tip approaches the interface. This is, indeed, what is commonly observed in the field (Figure 1). Furthermore, the reduction in the fracture (dyke) tip tensile stress as the tip comes into closer proximity with the interface with a stiffer layer is one of the primary reasons why elastic mismatch commonly leads to fracture arrest. Thus, the present numerical model provides strong support for the elastic mismatch mechanism of fracture arrest[6,16], which is based on analytical considerations. More specifically, our results indicate that when mode I (extension) fractures (such as a dykes) approach an interface, arrest of the fracture tip is most likely when the layer ahead of the interface is stiffer than the layer hosting the fracture tip (Figure 7).

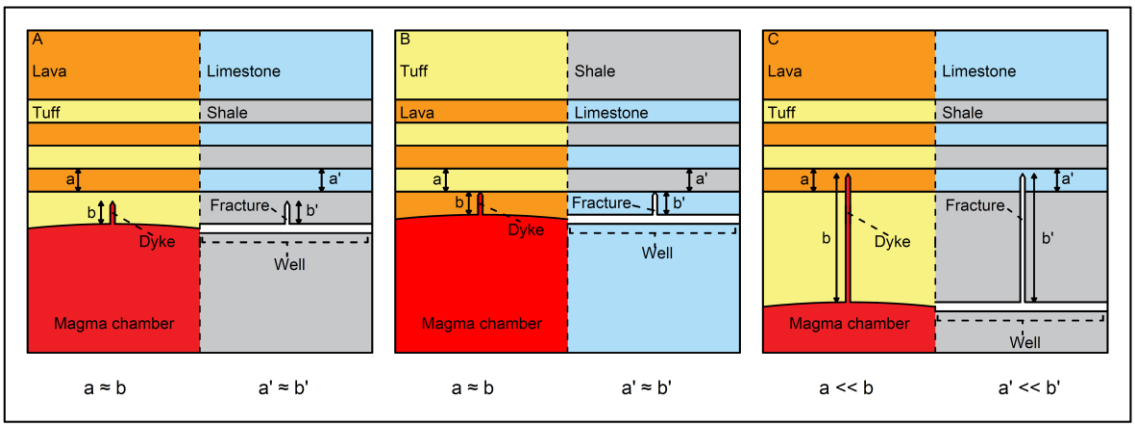

Figure 7: Examples of how a fracture may become arrested based on mechanical layering and fracture length for a dyke in a stratovolcano and a hydraulic fracture propagating from a horizontal well in a sedimentary basin. (A) Fracture is propagating from a relatively compliant layer (tuff in a volcano and shale in a sedimentary basin) towards a comparatively stiff layer (lava flow in the volcano and limestone in the sedimentary basin), where the fracture length is approximately the same as the thickness of the layer ahead. Here the fracture may become arrested before reaching the interface between the two layers. (B) Fracture is propagating from a relatively stiff layer towards a comparatively compliant layer, where the fracture length is approximately the same as the thickness of the layer ahead. Here the

fracture is more likely to reach, and be arrested at, the interface between the two layers. (C) Fracture has originated from a relatively compliant layer compared to the comparatively stiff layer above, but where the fracture length is much greater than the thickness of the layer ahead. Here the effects of the stiffer layer ahead in reducing the tensile stress at the fracture tip are overcome by the length of the fracture being much greater than the thickness of the layer ahead and, as such, the fracture is more likely to propagate from the compliant layer into the stiff layer.

Conclusions

This study presents outputs from a numerical model which highlight how crustal layering affects fracture propagation. Our model simulates fluid-pressure driven mode-I fractures which are analogous to volcanic intrusions such as dykes and man-made hydraulic fractures which are often generated to stimulate oil and gas reservoirs. The results, however, may be applicable to other modes of fracture propagation, with some modifications.

In our model, we altered the thickness of the layer ahead of a propagating fracture, the proximity of the fracture tip to the interface with the layer ahead, and the Young's modulus contrast between the layer hosting the fracture and the layer ahead. The results show that all three parameters affect the tensile stress concentration at the fracture tip, and therefore also influence the potential for fracture propagation or, alternatively, arrest. Overall, the model results show that:

- Tensile stress at fracture tips increase as the tip approaches an interface if the layer ahead (above the interface) is more compliant than the layer hosting the fracture tip, but decrease when the layer ahead is stiffer than the hosting layer.
- The contrast in Young's modulus between the layers (elastic mismatch) has a larger effect on the fracture-tip tensile stress as the layer ahead of the propagating fracture increases in thickness and as the proximity of the fracture tip to the interface decreases.

- Fracture arrest is most likely to occur exactly at the interface when the layer ahead is more compliant than the host layer. By contrast, when the layer ahead is stiffer than the host layer fracture arrest can occur either at the interface, or at some distance within the host layer before the interface is reached. These results are in agreement with field observations of fracture arrest in dykes and other extension fractures.

Methods

We used finite element method software, COMSOL Multiphysics, to investigate how layering affects the fracture propagation of fluid driven fractures such as volcanic intrusions and hydraulic fractures in oil and gas reservoirs. In our models we model the fracture as a void with an internal overpressure of 0.05 MPa. We used this value for overpressure as it produced tensile stress values at the tip that were in the range of the tensile strengths of many rocks, i.e. 0.5 – 9 MPa [7,32]. The fracture dimensions were kept constant throughout the study with a fracture length of 10 m and aperture of 0.01 m. These values were chosen as they represent an aspect ratio common for many fluid driven fractures [7,26]. The overall model size in vertical cross-section is 300 x 300 m so as to avoid any edge effects, with fixed corners to stop rigid body translation or rotation of the model (Figure 2). We used a mesh with a maximum element size of 3 m and minimum element size of 0.006 m.

The fracture was fully confined to what we refer to the 'host layer', which had the following properties: Young's modulus of 10 GPa, Poisson's ratio of 0.25 and density of 2600 $kg.m^{-3}$. These values were chosen as they fall within a realistic range for many sedimentary and igneous rocks [7] and they also allowed for a realistic and large range of Young's modulus values for the layer ahead to be modelled (i.e. 1.25 – 80 GPa or a ratio

414 of 0.125 – 8). It has been suggested that a contrast or change in either Poisson's ratio or
415 density over any realistic range is likely to have a negligible effect on stress magnitudes
416 in comparison to a contrast or a change in Young's modulus [33,34]. Our preliminary
417 numerical modelling results also supported this, and as such we did not conduct an
418 extensive study into the effects of Poisson's ratio or density contrast on tensile stress at
419 the fracture tip.

420 Unless stated otherwise, the layer ahead is 10 m thick, and the distance between the
421 fracture tip and the interface with the layer ahead is also 10 m. As the fracture length is
422 10 m, both this distance and the thickness of the layer ahead are equal to 1 fracture length.
423 We consider that the results from this study are likely scale dependent. For this reason,
424 we also quote thicknesses and distances in terms of fracture length. The results can then
425 more easily be applied to hydraulic fractures over a wide range of sizes.

426 When modelling how the thickness of the layer ahead may affect the tensile stress at the
427 fracture tip we considered a range of thicknesses for that layer between 1 and 80 m, as
428 this adequately covers the range of unit thicknesses found in many sedimentary and
429 volcanic sequences. This also represents a range of 0.1 – 8 fracture lengths. In terms of
430 hydraulic fractures associated with oil and gas reservoirs, this scale is likely to be a good
431 representation. However, for volcanic intrusions, which can be orders of magnitude
432 larger, a smaller lower bound limit may be more representative to simulate, for example,
433 fine ash layers. Unfortunately, due to computational constraints, we were unable to model
434 such a thin layer ahead as it would have required a much smaller element size. However,
435 the results presented in this study show expected trends assuming the layer ahead is
436 thinner than 0.1 fracture lengths, in that the tensile stress at the fracture tip should
437 converge towards the homogeneous case (i.e. the case without layers or where the layers
438 have the same mechanical/elastic properties).

A range of 0.125 - 64 m was used when considering how a change in proximity to the interface ahead may affect the tensile stress at the fracture tip. This represents a range of 0.0125 – 6.4 fracture lengths. Again, this represents a realistic range for hydraulic fractures propagating in oil and gas reservoirs. But for volcanic intrusion emplacement, a range including a lower limit might be more representative since these are typically much larger. For reasons already discussed, it was not possible to model the fracture tip at such close proximities to the layer ahead due to the same computational constraints. However, the trends are likely to remain the same, in that, as the proximity increases, the effect on the tensile stress at the fracture tip will increase, depending on the Young's modulus ratio between the host layer and the layer ahead.

In the case where the Young's modulus ratio was 1 (i.e. the Young's modulus of the host layer and the layer ahead were the same), the model can be considered homogeneous, and as such any change in the layer ahead (position or thickness) should not affect the tensile stress at the fracture tip. However, we found that when modelling the effect of changing all three parameters simultaneously, there were small differences (mean of <0.1% difference across all model runs) in the tensile stress in this homogeneous case. These small differences are caused by an automatic fining of the mesh when the fracture tip is closer to the layer ahead, and as the thickness of the layer ahead is reduced. As such we normalised the results so that, for the homogeneous case, the tensile stress was always 3.84 MPa. This therefore allowed for direct comparisons between model runs.

The absolute values in this study are only valid for an example which matches the model parameters. For this reason, we compare the results using a scale related to the length of the fracture, but also report percentage changes in the tensile stress at the fracture tip.

References

1. Segall, P. *Earthquake and Volcano Deformation*. *Princeton University Press*

(2010). doi:10.1002/0471743984.vse7429

2. Gudmundsson, A. The mechanics of large volcanic eruptions. *Earth-Science Rev.* **163,** 72–93 (2016).

3. Scholz, C. H. *The Mechanics of Earthquakes and Faulting*. (Cambridge University Press, 2002).

4. Main, I. & Naylor, M. Extreme events and predictability of catastrophic failure in composite materials and in the Earth. *Eur. Phys. J. Spec. Top.* **205,** 183–197 (2012).

5. Browning, J. & Gudmundsson, A. Caldera faults capture and deflect inclined sheets: an alternative mechanism of ring dike formation. *Bull. Volcanol.* **77,** (2015).

6. Forbes Inskip, N. D., Meredith, P. G., Chandler, M. R. & Gudmundsson, A. Fracture properties of Nash Point shale as a function of orientation to bedding. *J. Geophys. Res. Solid Earth* 1–17 (2018). doi:10.1029/2018JB015943

7. Gudmundsson, A. *Rock Fractures in Geological Processes*. (Cambridge University Press, 2011).

8. Chandler, M. R. A Fracture Mechanics Study of an Anisotropic Shale. (PhD, Univeristy College London, 2014).

9. Lee, H. P., Olson, J. E., Holder, J., Gale, J. F. W. & Myers, R. D. The interaction of propagating opening mode fractures with preexisting discontinuities in shale. *J. Geophys. Res. Solid Earth* **120,** 169–181 (2015).

10. Montgomery, C. T. *et al.* Hydraulic fracturing, history of an enduring technology. *J. Pet. Technol.* 26–41 (2010).

11. Yao, Y. Linear elastic and cohesive fracture analysis to model hydraulic fracture

in brittle and ductile rocks. *Rock Mech. Rock Eng.* **45,** 375–387 (2012).

12. Virgo, S., Abe, S. & Urai, J. L. Journal of Geophysical Research : Solid Earth Models of fracture sealing. 8708–8727 (2014). doi:10.1002/2014JB011520

13. Fisher, K. & Warpinski, N. Hydraulic-fracture-height growth : Real data. *Soc. Pet. Eng.* (2012). doi:10.2118/145949-PA

14. Kavanagh, J. L., Boutelier, D. & Cruden, A. R. The mechanics of sill inception , propagation and growth : Experimental evidence for rapid reduction in magmatic overpressure. *Earth Planet. Sci. Lett.* **1,** 1–12 (2015).

15. Tang, H., Li, S. & Zhang, D. The effect of heterogeneity on hydraulic fracturing in shale. *J. Pet. Sci. Eng.* **162,** 292–308 (2018).

16. Gudmundsson, A., Simmenes, T. H., Larsen, B. & Philipp, S. L. Effects of internal structure and local stresses on fracture propagation, deflection, and arrest in fault zones. *J. Struct. Geol.* **32,** 1643–1655 (2010).

17. Barnett, Z. A. & Gudmundsson, A. Numerical modelling of dykes deflected into sills to form a magma chamber. *J. Volcanol. Geotherm. Res.* **281,** 1–11 (2014).

18. Chandler, M. R., Meredith, P. G., Brantut, N. & Crawford, B. R. Fracture toughness anisotropy in shale. *J. Geophys. Res. Solid Earth* **121,** 1–24 (2016).

19. Kavanagh, J. L., Menand, T. & Daniels, K. A. Gelatine as a crustal analogue: Determining elastic properties for modelling magmatic intrusions. *Tectonophysics* **582,** 101–111 (2013).

20. Zhao, J., Chen, X., Li, Y., Fu, B. & Xu, W. Numerical simulation of multi-stage fracturing and optimization of perforation in a horizontal well. *Pet. Explor. Dev.* **44,** 119–126 (2017).

21. Sosa, A., Espinoza, D. N., Frydman, M., Barredo, S. & Cuervo, S. Analyzing a

suitable elastic geomechanical model for Vaca Muerta Formation. *J. South Am. Earth Sci.* **79,** 472–488 (2017).

22. Fantín, M. A. *et al.* Vaca Muerta stratigraphy in central neuqúen basin: Impact on unconventional project development. *Soc. Pet. Eng.* 11 (2014). doi:10.15530/urtec-2014-1923793

23. Gudmundsson, A. Toughness and failure of volcanic edifices. *Tectonophysics* **471,** 27–35 (2009).

24. Gudmundsson, A. & Philipp, S. L. How local stress fields prevent volcanic eruptions. *J. Volcanol. Geotherm. Res.* **158,** 257–268 (2006).

25. Gudmundsson, A., Fjeldskaar, I. & Brenner, S. L. Propagation pathways and fluid transport of hydrofractures in jointed and layered rocks in geothermal fields. *J. Volcanol. Geotherm. Res.* **116,** 257–278 (2002).

26. Geshi, N., Kusumoto, S. & Gudmundsson, A. Effects of mechanical layering of host rocks on dike growth and arrest. *J. Volcanol. Geotherm. Res.* **223–224,** 74–82 (2012).

27. Brenner, S. L. & Gudmundsson, A. Arrest and aperture variation of hydrofractures in layered reservoirs. *Geol. Soc. London, Spec. Publ.* **231,** 117–128 (2004).

28. Larsen, B. & Gudmundsson, A. Linking of fractures in layered rocks: Implications for permeability. *Tectonophysics* **492,** 108–120 (2010).

29. McGinnis, R. N., Ferrill, D. A., Morris, A. P., Smart, K. J. & Lehrmann, D. Mechanical stratigraphic controls on natural fracture spacing and penetration. *J. Struct. Geol.* **95,** 160–170 (2017).

30. Smart, K. J., Ofoegbu, G. I., Morris, A. P., McGinnis, R. N. & Ferrill, D. A. Geomechanical modeling of hydraulic fracturing: Why mechanical stratigraphy,

stress state, and pre-existing structure matter. *Am. Assoc. Pet. Geol. Bull.* **98,** 2237–2261 (2014).

31. Müller, W. Brittle crack growth in rocks. *Pure Appl. Geophys.* **124,** 693–709 (1986).

32. Amadei, B. & Stephansson, O. *Rock Stress and Its Measurement*. (Springer, Berlin, 1997).

33. Le Corvec, N., Muirhead, J. D. & White, J. D. L. Shallow magma diversions during explosive diatreme-forming eruptions. *Nat. Commun.* **9,** 1459 (2018).

34. Gudmundsson, A., De Guidi, G. & Scudero, S. Length–displacement scaling and fault growth. *Tectonophysics* **608,** 1298–1309 (2013).

Supplementary Material for

Propagation and arrest of fractures in layered rock sequences

Nathaniel Forbes Inskip[1,2,3], John Browning[4], Philip G Meredith[3], Agust Gudmundsson[2]

[1] The Lyell Centre, Heriot-Watt University, Edinburgh, United Kingdom

[2] Department of Earth Sciences, Royal Holloway University of London, Egham, United Kingdom

[3] Department of Earth Sciences, University College London, London, United Kingdom

[4] Department of Mining Engineering and Department of Structural and Geotechnical Engineering, Pontificia Universidad Católica de Chile, Santiago, Chile

Supplementary text 1

Below is a description of the three interface or contact mechanisms for fracture arrest – Cook-Gordon delamination, stress barrier and elastic mismatch – as referenced to in the main text. For a more detailed discussion of these mechanism we refer the reader to the references [1–4].

Cook-Gordon delamination

For a propagating hydraulic fracture the maximum tensile stress occurs at the its tip and should the magnitude of tensile stress overcome both the tensile strength of the rock and the minimum principal compressive stress, σ_3, the fracture will propagate. It is known that the magnitude of tensile stress decreases with an increase in distance from the fracture tip [1]. However, as a propagating fracture approaches an interface between layers, the magnitude of tensile stress ahead of the fracture may be sufficient to open up (delaminate) the interface. Whether opening occurs depends on the strength of the interface, but also on magnitude of normal stress acting on the interface, which for a horizontal interface at depth would likely be the vertical stress which, for zones of extension, is commonly maximum principal compressive stress, σ_1. Upon meeting this now delaminated interface the fracture may become arrested, or if the fluid pressure within the fracture is sufficient to overcome the strength of the interface but also the normal stress, the fracture may deflect into the interface. This mechanism is more prevalent at shallow depths as the magnitude of the normal stress is expected to be lower [2].

Stress barrier

A stress barrier is a mechanism whereby fracture arrest occurs due to the local stress field being unfavourable for continued fracture propagation. For a hydraulic fracture, which propagates perpendicular to σ_3, it usually involves the abrupt rotation of the σ_3

plane at an interface between rock layers of contrasting mechanical properties, such as Young's modulus. This abrupt rotation of the σ_3 plane may occur either from residual stress from previous tectonics activity [2], or through differential bending of the individual rock layers. Differential bending of the individual layers will induce compressive stresses at the bottom but tensional stresses at the top of the individual layers [5,6]. It is this abrupt change from a tensional stress state from the top of one layer to a compressional stress state in the bottom of a subsequent layer which can cause the rotation of the σ_3 plane. This rotation of the σ_3 plane may cause a hydraulic fracture to arrest, or deflect so that it propagates in a more favourable orientation.

Elastic mismatch

Elastic mismatch is a mechanism whereby a hydraulic fracture becomes arrested due to the contrast in Young's modulus of two materials either side of an interface, but also contrast in the critical energy release rate (G_c) between the interface and the layer the other side of the interface from the propagating fracture. In the case that a hydraulic fracture meets an interface with a higher G_c than the layer on the other side, it is more likely that the fracture propagates across that interface rather than deflecting into it. In contrast, if the G_c of the interface is significantly lower than the layer on the other side it becomes increasingly more likely that the fracture deflects in to the interface, as long as the stress conditions are favourable for it to do so.

In terms of the contrast in Young's modulus this is expressed by the use of the Dundurs parameter α:

$$\alpha = \frac{E_1^* - E_2^*}{E_1^* + E_2^*} \tag{1}$$

where E^* is the plane-strain Young's modulus and equal to:

$$E^* = \frac{E}{1-\nu^2}$$

Where E is plane-stress Young's modulus and v is Poisson's ratio.

He et al (1994)[4] demonstrates how a fracture may propagate across an interface or deflect along it based on α and the ratio of G_c of the interface (G_d) and the layer across the interface (G_p) – Supplementary figure 1.

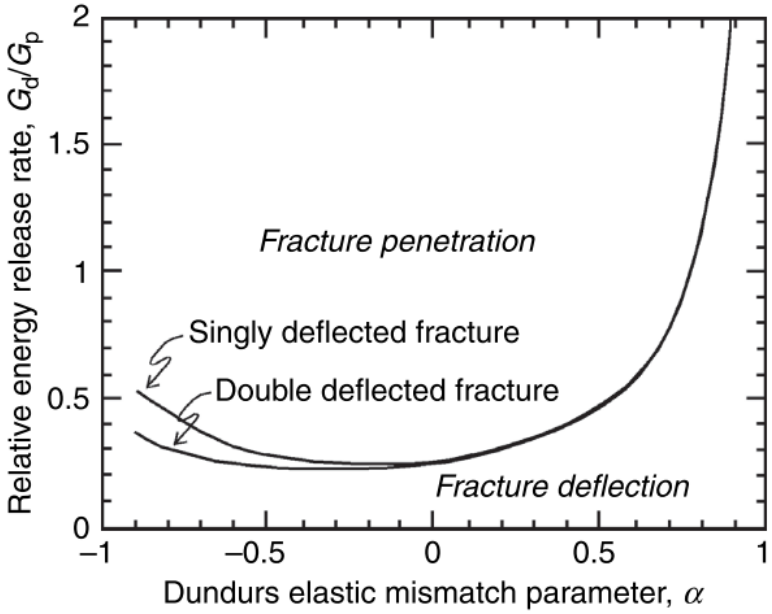

Supplementary figure 1: The conditions required for fracture propagation across and interface or deflection along an interface for the elastic mismatch mechanism. Here a single deflected fracture means that the fracture will continue to propagate along the interface in one direction, whereas a double deflected fracture means that the fracture will deflect along the interface in both directions. Figure modified after [4].

Supplementary material references

1. Gudmundsson, A. *Rock Fractures in Geological Processes*. (Cambridge University Press, 2011).

2. Barnett, Z. a. & Gudmundsson, A. Numerical modelling of dykes deflected into sills to form a magma chamber. *J. Volcanol. Geotherm. Res.* **281,** 1–11 (2014).

3. Cook, J. & Gordon, J. E. A mechanism for the control of crack propagation in all-brittle systems. *Proc. ofthe R. Soc. London* 508–520 (1964).

4. He, M. Y., Evans, A. G. & Hutchinson, J. W. Crack deflection at an interface between dissimilar elastic materials: Role of residual stresses. *Int. J. Solids Struct.* **31,** 3443–3455 (1994).

5. Gudmundsson, A. Mechanical aspects of postglacial volcanism and tectonics of the Reykjanes Peninsula, SW Iceland. *J. Geophys. Res.* **91,** 12,711-12,721 (1986).

6. Gudmundsson, A. Postglacial crustal doming, stresses and fracture formation with application to Norway. *Tectonophysics* **307,** 407–419 (1999).

6 Discussion and critical evaluation

6.1 Critical evaluation of methodology

The following section provides a critical evaluation of the different techniques and methods used throughout this study, and discussed in detail in Chapter 2. These include field work, laboratory experiments and numerical models, each of which will now be discussed in terms of their merits but also limitation in this study and other potential future work.

6.1.2 Field data and sample collection

The outcrop at Nash Point is heavily jointed, and so it was determined that the easiest way in which to collect samples would be to lever out blocks of material by use of a crowbar forced into the joints. It was relatively easy to lever out whole blocks of limestone as it is very competent. By contrast, collecting shale samples was much more problematic. As is discussed in Chapter 2, Nash Point shale contains bedding plane fractures which are laterally extensive. In the field it is almost impossible to detect these fractures until a block has been levered out, at which point the block would sometimes fall apart along these planes of weakness. Hence, most material was collected from the more competent sections and may not always be fully representative of the shale sequence as a whole. This is a common occurrence, as is also reported in other studies (Chandler 2014; Lee 2015).

Furthermore, while sampling from only one shale bed and one limestone bed meant that there was a consistency in material between the different tests, it also meant that heterogeneity between beds was not measured. Although the interbedded nature of Nash Point shale and limestone is both laterally and vertically extensive, there are likely to be some variations in properties between the beds. As is discussed in Chapter 4 some of the limestone beds at Nash Point (and indeed along much of the Bristol Channel (Afşar *et al.*

2014)) are nodular in nature while others are tabular. The limestone bed from which samples were taken for this study was tabular.

Afşar *et al*. (2014) measured a suite of petrophysical properties from both a well-bedded and a semi-nodular limestone from the Liassic portion of the Bristol Channel, including porosity, tensile strength and Young's modulus. It is not clear if their results are from, or include, samples taken from Nash Point. However, it is known that the authors did conduct field work at Nash Point as part of their study, along with field work at Kilve and Lilstock, both of which contain the same Liassic interbedded sequence found at Nash Point but are located on the opposite side of the Bristol Channel, on the Somerset coast. They found that the well-bedded limestone was both more competent (had a higher Young's modulus, 48 GPa) and stronger (tensile strength of 11 MPa) than the semi-nodular limestone which had a Young's modulus of 38 GPa, and tensile strength of 9 MPa. The Young's modulus values presented by Afşar *et al*. (2014) are higher than those measured in this study (26.3 GPa on cores loaded parallel to bedding, and 28.5 GPa on cores loaded normal to bedding) but the tensile strength values are lower than those measured in this study (12.70 MPa in the Divider orientation, 13.49 MPa in the Arrester orientation, and 14.68 MPa in the Short-transverse orientation). Theoretically the tensile strength of any specific material is related to its Young's modulus but also the size and distribution of flaws existing within the material (Griffith 1920; Orowan 1949), and that for a given flaw size and distribution a materials strength will be proportional to its Young's modulus. Therefore, given that samples tested by Afşar *et al*. (2014) have a higher Young's modulus to those in this study it would be expected that the tensile strength of their samples would also be higher, but they are not. Therefore it is likely that these values represent the degree of mechanical heterogeneity present in limestones from the Liassic portion of the Bristol Channel.

It is suggested that further work be carried out to quantify the degree of mechanical heterogeneity between different beds of shale and limestone outcropping at Nash Point and compare these to the results of this study. Consequently this will aid in determining if heterogeneity between beds of the same rock type would significantly affect the conclusions of this study. Although a full characterisation of the rocks would be preferred (i.e. measure the Young's modulus, Poisson's ratio, tensile strength, fracture toughness etc.), as a first pass it is suggested that measuring the ultrasonic wave velocities would provide a good indication as to the heterogeneity present between different beds. This would much easier and simpler than a full characterisation, and could be done on relatively small samples compared to some of the other methods used during this project.

6.1.2 Experimental methods

Preparing samples of Nash Point limestone for mechanical testing was relatively straightforward due to the limestone's competent nature. In contrast, preparing samples of Nash Point shale was problematic for the same reason that it was difficult to retrieve blocks of material from the field, namely that the samples would sometimes break apart along pre-existing weaknesses. Methods to address this problem have already been discussed in Chapter 2 and will not be repeated here. However, despite my best efforts many samples broke apart during preparation, and therefore samples were made from the more competent sections, and may not always be fully representative of the shale sequence as a whole. Furthermore, due to this issue several trips to the outcrop were required to obtain material, and consequently the experimental part of this PhD project took considerably more time than originally anticipated. Despite this, I was able to produce a lot of data, particularly in orientations other than those normal and parallel to bedding, which will hopefully be useful to others working on similar projects.

Each of the methods are now evaluated individually.

6.1.2.1 UCS tests

The main purpose of conducting UCS tests was to measure the static Young's modulus and Poisson's ratio of both Nash Point shale and limestone. Unfortunately, I did not have access to a diametral strain transducer, but only a circumferential strain transducer (Figure 10 in Chapter 2). For an isotropic material both the circumferential and diametral strain should be the same (ISRM 1970), and while this may be true of Nash Point limestone, it certainly isn't of Nash Point shale.

Being transversely isotropic, circumferential strain and diametral strain should be equal when loading a Nash Point shale core normal to bedding (Figure 31A). However, when loading a core parallel to bedding the diametral strain will vary depending on (as a function of) the angle to bedding (Figure 31B). When loading a core parallel to bedding, diametral strain will be greatest in the bedding normal orientation (ε_1 in Figure 31B) and lowest in the bedding parallel orientation (ε_3 in Figure 31B). This difference is due to the laminations in the shale, which are parallel to bedding, being forced apart during loading along bedding plane fractures and weak interfaces between laminations. A similar observation was made by Heap & Faulkner (2008) whereby Young's modulus and Poisson's ratio were measured on samples of Westerly granite that were cyclically loaded to introduce micro-fractures in the samples. They found that as micro-fracture damage accumulated in the samples the micro-fractures were predominantly orientated parallel to the core axis and that this ultimately increased the circumferential strain recorded in subsequent loading cycles. The micro-fractures orientated parallel to the core axis (and therefore loading direction) in Heap & Faulkner (2008) are thought to act in a similar way to the bedding plane fractures and weak interfaces in Nash Point shale during loading.

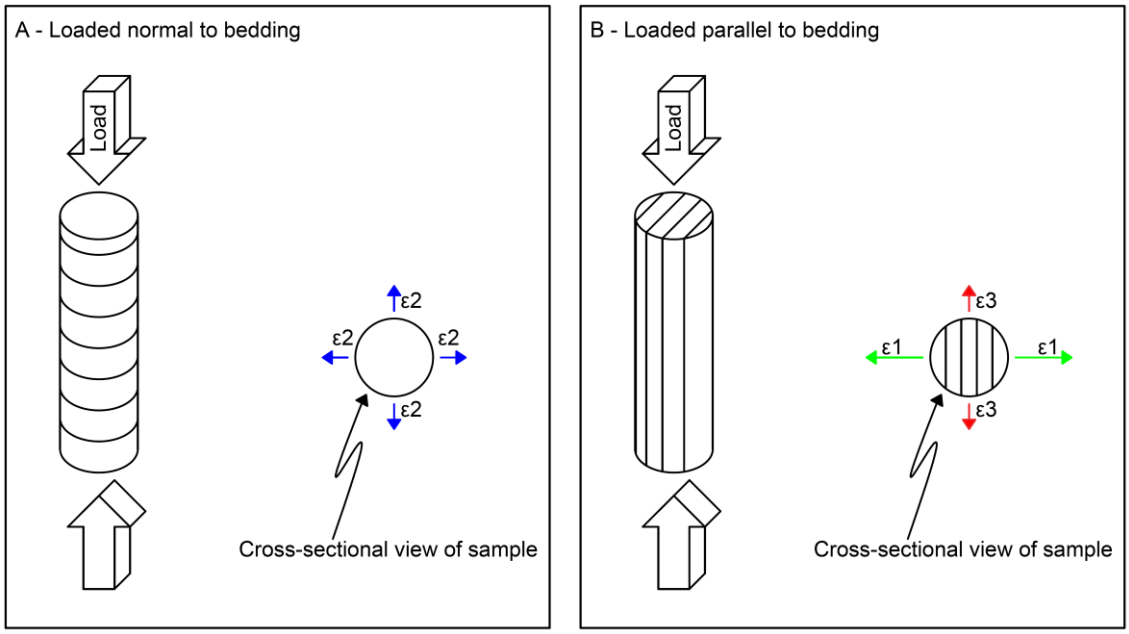

Figure 31: Schematic illustration of UCS samples being loaded (A) normal to bedding and (B) parallel to bedding. The black lines on the sample depict the bedding plane. Principal strain directions with respect to bedding are displayed in the cross-sectional view of the sample.

It follows that the value of Poisson's ratio for Nash Point cores loaded normal to bedding (0.39, as presented in the Supporting information of Chapter 3) should be used with caution as the circumferential strain used to calculate the value is likely to be a value between diametral strains in the bedding normal and bedding parallel orientations. However, where Poisson's ratio is used in Chapters 3 and 4 to calculate G_c, the dependence on Poisson's ratio is low and any variation in G_c due to a variation in Poisson's ratio will be very small, as discussed in the Supporting Information of Chapter 3. Poisson's ratio is also used in numerical models presented in Chapters 5 and 6 of this thesis. However, sensitivity analysis carried out by Le Corvec *et al.* (2018), who also used COMSOL to model crustal deformation, found that varying Poisson's ratio had a negligible effect on their model solutions. Similar sensitivity analysis was carried out for the numerical modelling in Chapter 5, and again it was found that varying Poisson's ratio had a negligible effect on the model solutions.

During UCS testing the axial strain transducer is situated in the middle of the sample, but necessarily the circumferential strain transducer is situated off centre. Initially cores of lengths 62.5 – 70 mm (which meets the suggested length : diameter ratio as set out by ISRM (1970)) were used, however it was found that the position of the circumferential strain gauge was too close to the ends of the sample. This resulted in circumferential strains that were anomalously high, and consequently Poisson's ratio values which were erroneously high (>0.5). I then manufactured samples that were 75 mm long, and found that the values were more in keeping with those of other crustal materials (Heap & Faulkner 2008; Heap *et al.* 2009; Gudmundsson 2011; Sayers 2013). The Poisson's ratio values in this study are derived only from the tests where samples were 75 mm long, whereas Young's modulus values are derived from all the samples (62.5 – 75 mm long), as there were no effects on the axial strain transducer.

Thin (<1 mm aperture) calcite veins are common in both Nash point shale and limestone and are mostly orientated at high angles to bedding (60-90° - see Chapter 3). As such it was difficult to manufacture UCS samples of sufficient length without intersecting a vein. During testing, some of the samples that contained veins would fail along the vein(s), which acted as a plane of weakness, at stresses lower than samples without veins. However, upon inspection of the quasilinear portion of the stress-strain curves used to calculate the moduli, there is no discernible difference between the samples that fail along veins and those that do not. Consequently, there is no discernible difference in the elastic moduli between samples that fail along veins and those that do not.

6.1.2.2 Brazil disk tests

Brazil disk tests were used to measure the indirect tensile strength of both Nash Point limestone and shale in a variety of orientations, as described in Chapters 2-4. Testing of limestone samples was straightforward due to its isotropic nature. In contrast, for samples of Nash Point shale tested oblique to bedding and in the Arrester orientation, the fracture

would seldom pass through the centre of the sample or was straight and parallel to the loading direction. Both of which are requirements for the test to be considered valid (Figure 32). This problem has already been discussed in Chapter 3 and so I will not discuss it any further here except to reiterate that in such cases we could not be confident that the failure loads in the tests correspond to the true tensile strength of the material in that respective orientation. Fracture toughness is then considered a better measure of a materials resistance to fracture propagation.

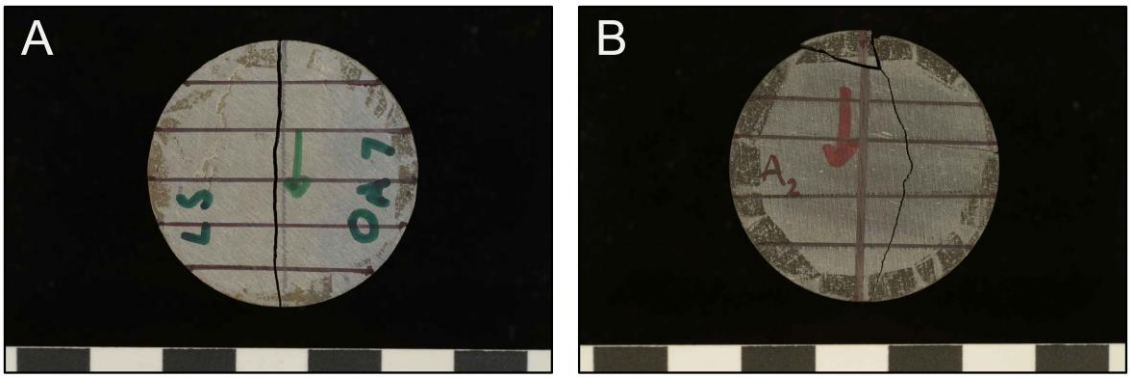

Figure 32: Brazil disk samples of Nash Point limestone (A) and shale (B) tested in the Arrester orientation. The fracture in the limestone pass through the centre and are straight and parallel to the loading direction (indicated by the arrows on the samples). By contrast, the fracture in the shale does not pass through the centre and is curved and thus not parallel to the loading direction.

6.1.2.3 SCB tests

The SCB method was used to measure the mode-I fracture toughness, K_{Ic}, of both Nash Point shale and limestone in a variety of orientations. Again the testing of limestone samples was straightforward due to its isotropic nature, whereby, like in the Brazil disk tests, fractures were straight and parallel to the loading direction. By contrast, for samples of Nash Point shale tested oblique to bedding and in the Arrester orientation, fractures would often deflect away from the intended direction (i.e. parallel to the loading direction) towards the weaker Short-transverse orientation (Figure 33). For such fracture deflections

a mode-II component exists and is accounted for using the method described in Chapter 3.

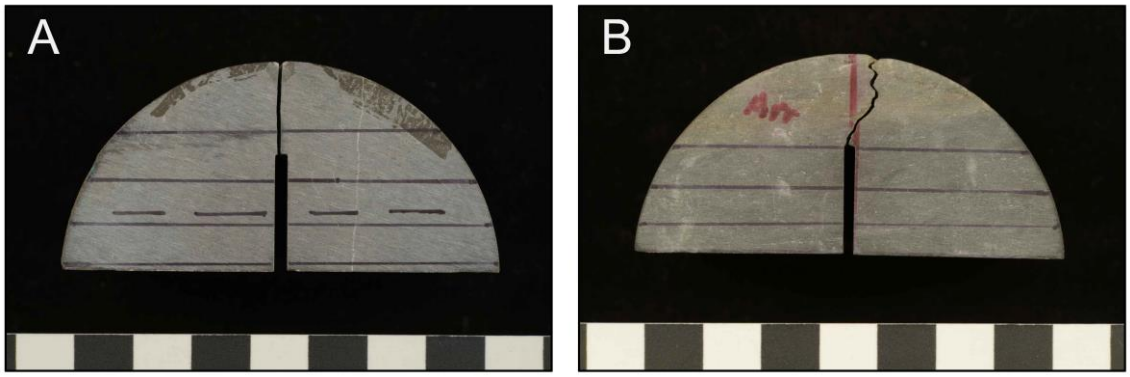

Figure 33: SCB samples of Nash Point limestone (A) and shale (B) tested in the Arrester orientation. The fracture in the limestone is straight and parallel to the loading direction whereas the fracture in the shale is tortuous and deviates away from the intended direction (i.e. parallel to the loading direction).

As well as there being fracture deflection from the intended direction, there was also observed occasional fracture deflection (twisting) from the intended plane across the sample thickness. The latter implies a mode-III shear component to the fracture propagation. However, such twisting always occurred at some distance from the point of fracture initiation.

For the sample geometry and notch depth used for this study, fracture propagation is inherently unstable so that the peak load is recorded at the onset of fracture propagation, and the fracture toughness is evaluated at this point. Hence, if a fracture deflects from the intended direction, or twists away from the intended plane, after some increment of fracture growth in the correct orientation and plane, the evaluation of K_{Ic} remains valid.

As such, the twisting of fractures witnessed in this study does not need to be corrected for. However, for a different sample geometry and/or material this may be an issue that needs to be considered.

Another problem that was encountered in some SCB tests was premature failure along samples which contained veins, similar to what was described in the critical evaluation of the UCS testing. When calculating Young's modulus, it is the gradient of the stress-strain curves from a UCS test which is used. By contrast, when calculating K_{Ic} from SCB tests, it is the peak load which is used. Lee *et al.* (2015) examined how the presence of calcite veins affect fracture propagation in samples of Marcellus shale using the SCB method. They found that the propagating fracture would commonly deflect into a vein upon meeting it. However, they also observed that the propagating fracture would also deflect prior to meeting the vein so that they met at 90°. This also occurred in my samples where veins were present.

It is known that in layered media where the layers have contrasting mechanical properties (particularly Young's modulus) a rotation of up to 90° of the principal stresses may occur (Gudmundsson & Philipp 2006; Barnett & Gudmundsson 2014). The fracture propagating in a SCB sample is ideally mode-I, and it will be in the case of undeflected factures, however as is shown in Chapter 3 deflecting fractures contain a mode-II (and possibly and mode-III) component. However, propagation is still governed by the principal stress orientations within the material, along with any mechanical anisotropy (hence the stepping nature of the fractures described in Chapter 3). It is likely that the calcite vein will have a different Young's modulus to that of the host rock. Lee *et al.* (2015) originally considered the calcite veins in their study to have a Young's modulus of 84.3 GPa, based on the work by Carmichael (1989). However, this value is based on a single calcite crystal and therefore a vein, which contains discontinuities, is likely to be somewhat lower, as discussed by Lee *et al.* (2015). Nevertheless, the difference in Young's modulus is likely to cause a rotation in the principal stress directions and this may explain why fractures deflect so as to meet the vein at 90°. Unfortunately, Lee *et al.* (2015) do not quote either the peak load or K_{Ic} for samples where fractures deflected into

a vein. Therefore a full comparison with the values presented in this study is not possible. However, it is clear from our analysis, both in terms of UCS and SCB samples failing at a lower peak stresses when failure occurs within or deflects along a calcite vein, that calcite veins act as a plane of weakness in both Nash Point shale and limestone. It follows, as was stated in Chapter 3, SCB samples which failed prematurely along calcite veins were not considered for further analysis as this fell outside of the scope of this project.

6.1.2.4 SR testing

In this study SR testing was used as a means to compare (and validate) to the values obtained using the SCB method as it had not been used in the laboratories at UCL before. Testing of Nash Point limestone samples was again straightforward, and the results were consistent with other results in that Nash Point limestone is essentially isotropic. However, the results are slightly higher than those obtained using the SCB method. This is discussed in Chapter 4 and therefore will not be discussed further here.

The practical problems associated with the sample preparation and testing of shale using the SR method are well known (Chandler 2014; Chandler *et al.* 2016), I therefore followed the protocol of Chandler (2014). This involved using steel loading plates bonded to the sample ends to prevent failure and cracking at the loading points. This method enabled me to perform successful experiments in the Short-transverse and Divider orientations. The results show that the SR and the SCB are comparable and consistent as in Table 1 in Chapter 3. However, it was not possible to make measurements in the Arrester orientation as the fracture would deflect into the Short-transverse orientation before reaching the point at which K_{Ic} is evaluated. Again, this has been documented by others testing transversely isotropic materials (Ingraffea *et al.* 1984; Chandler 2014; Chandler *et al.* 2016). Ingraffea *et al*. (1984) propose a method whereby an axial pressure is applied along the length of the SR sample during testing so as to promote continued fracture growth in the Arrester orientation. The axial pressure is applied by using a plate

on each end of the sample, connected by two lengths of studding and a set of nuts which are tightened with a torque wrench. Axial pressure was then calculated from the amount of torque applied. Ingraffea *et al.* (1984) used this method to test samples of Westerly granite and Indiana limestone and found that K_{Ic} decreased by approximately 5% when an axial pressure of 8% of the compressive strength of the respective rock type was applied. By contrast, Chandler (2014) found that when testing samples of Darley Dale sandstone using the same method, K_{Ic} decreased by aprroximately 20% when an axial pressure of approximately 6% of the material compressive strength was applied. From the UCS tests conducted as part of this study the compressive strength of Nash Point shale was measured to be ~57 MPa. It was found that even when applying an axial pressure in excess of 10% of the compressive strength it was not possible to propagate a fracture successfully in the Arrester orientation. Therefore, as it is likely that applying a greater axial pressure to the samples would significantly affect the K_{Ic} results, it was decided not to pursue trying to measure K_{Ic} in the Arrester orientation using the SR method.

6.1.3 Critical evaluation of numerical modelling

6.1.3.1 Limitation of FEM

One limitation in using FEM software such as COMSOL is that it is not possible to break the elements apart and simulate fracture propagation directly. More specifically, the software can only be used to provide a static solution. It follows that once a model run has been interpreted, the model parameters must be changed (e.g. a fracture is increased in length to simulate fracture growth) and the model re-run.

It is possible to dynamically propagate a fracture using the Discrete Element Method (DEM) as this relies on particle elements, commonly circles or spheres, which are bonded together with adjacent elements. Bonds are assigned a certain strength (shear, tensile and compressive) and during a model run if the strength of the bond is overcome it breaks and

the elements are separated. However, there are some limitations with this type of modelling. For example, macroscopic mechanical properties (e.g. Young's modulus, Poisson's ratio etc.) cannot be prescribed in the model directly but must rather be determined by the packing and sorting of the elements. Furthermore, a packing of spherical elements may not be the best representation of crustal materials at depth and is similar to analogue models which use sand grains as the crustal material. In the case of using sand grains in analogue models, when up-scaled the individual grains are often much larger than most fractures that are expected to exist at depth. In DEM models a similar issue often exists unless the elements are scaled appropriately to the process being modelled, however this then requires significant computational power to run the model.

Hydraulic fractures propagate in a step-like manner, whereby a fracture tip will propagate for a certain length (step) once the tensile strength and σ_3 are overcome. When the fracture propagates, however, its volume increases. As the volume increases the internal fluid pressure decreases and therefore the stress at the fracture tip also decreases. Eventually fracture propagation stops once the tensile stress drops below the combination of the tensile strength of the rock and σ_3. If fluid continues to be injected into the fracture the process will start again and continue in this step like way. It follows that although there are limitations of using FEM, its use is well suited to this project especially considering that the way in which we model fracture propagation in FEM is similar to how hydraulic fractures propagate in the crust.

6.1.3.2 2D vs 3D modelling

Hydraulic fractures are commonly considered to be ellipsoids or penny-shaped in nature (Kavanagh *et al.* 2006, 2015; Gudmundsson 2011), whereby the height (dip length) and width (strike length) are much larger than the aperture, and in many cases are similar in length. As the fluid pressure within the fracture increases stress will concentrate along the tip line (i.e. at the edge of the fracture). Furthermore, if the height and width of the fracture

are similar, so that it is circular (penny-shaped), the tensile stress at the tip should be reasonably uniform along the whole circumferential tip (the tip line), because the stress intensity is directly proportional to the length of the fracture (Griffith 1920; Orowan 1949). To demonstrate this I have run a 3D model whereby a penny-shaped fracture is fully contained with an isotropic and homogeneous body (Figure 34). The corners of the model are fixed, and the only loading condition is fluid overpressure within the fracture.

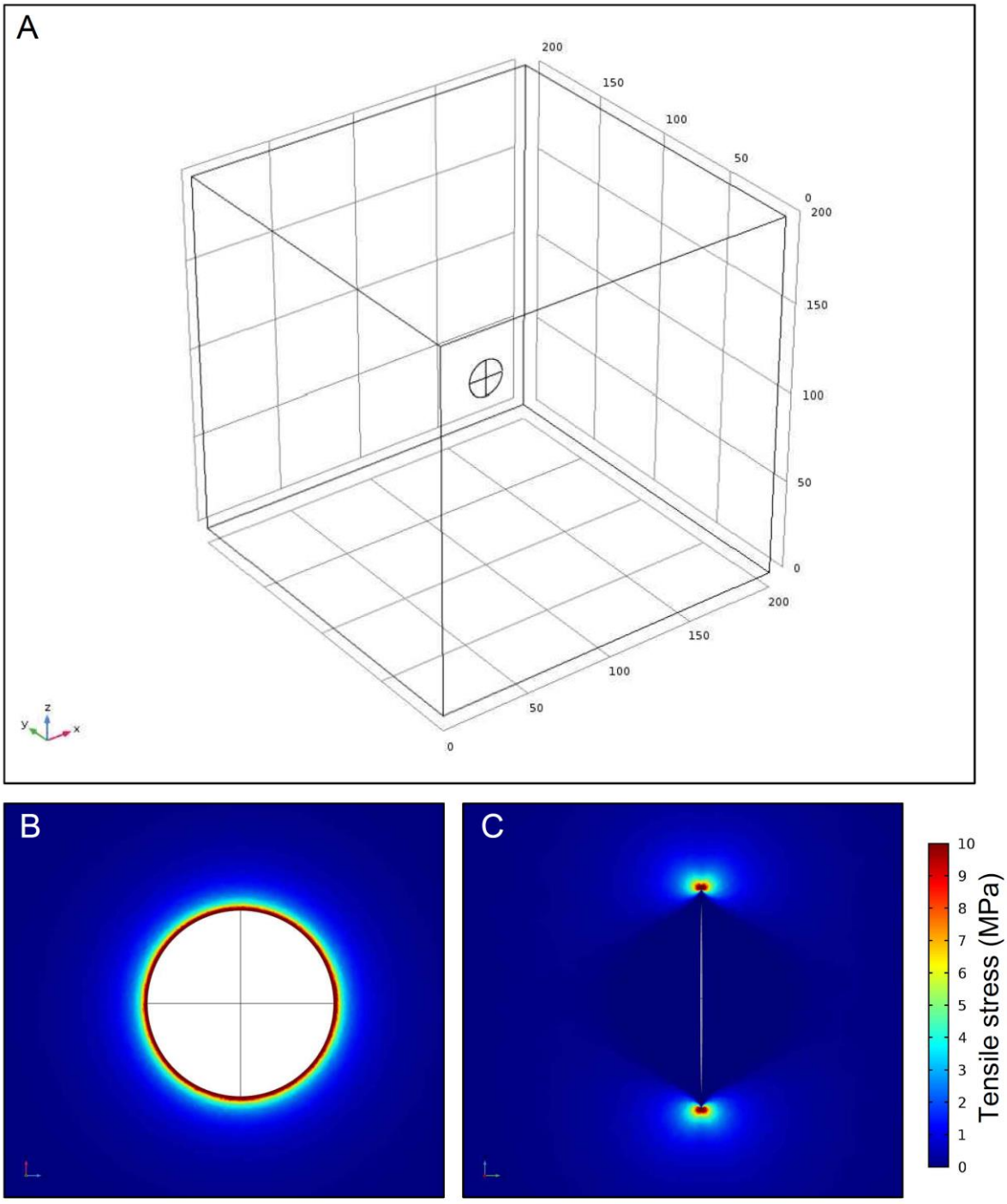

Figure 34: (A) Model set up for a penny-shaped fracture with a height and width (strike and dip dimension) of 10 m and maximum aperture of 0.1 m. The fracture is enclosed within an isotropic and homogeneous model of 200 x 200 x 200 m, which has a Young's modulus of 10 GPa, Poisson's ratio of 0.25 and a density of 2600 $kg.m^{-3}$. Here the fracture contains a fluid overpressure of 5 MPa. (B) 2D slice demonstrating the tensile stress concentrations (MPa) through the centre (a slice through the centre) of the fracture in its plane. (C) 2D slice demonstrating the tensile stress concentrations (MPa) through the centre of the fracture in the fracture plane.

Plotted in Figure 34 are two orthogonal 2D slices of tensile stress where the slices correspond to the height-width plane (B) and height-aperture plane (C), respectively. The results of (C) compare well with a similar model run in 2D where a 2D slice of the same fracture in the height-aperture plane is modelled (Figure 35). Although the absolute values of tensile stress differ between the 3D and 2D models, in this case using a 2D model to determine changes in tensile stress at a fracture tip seems reasonable.

Ideally, all the models run as part of this project would be 3D, however due to the significant computational power required to run even a simple 3D model (for example these simple models described here took several hours to build, mesh and run) this was not possible.

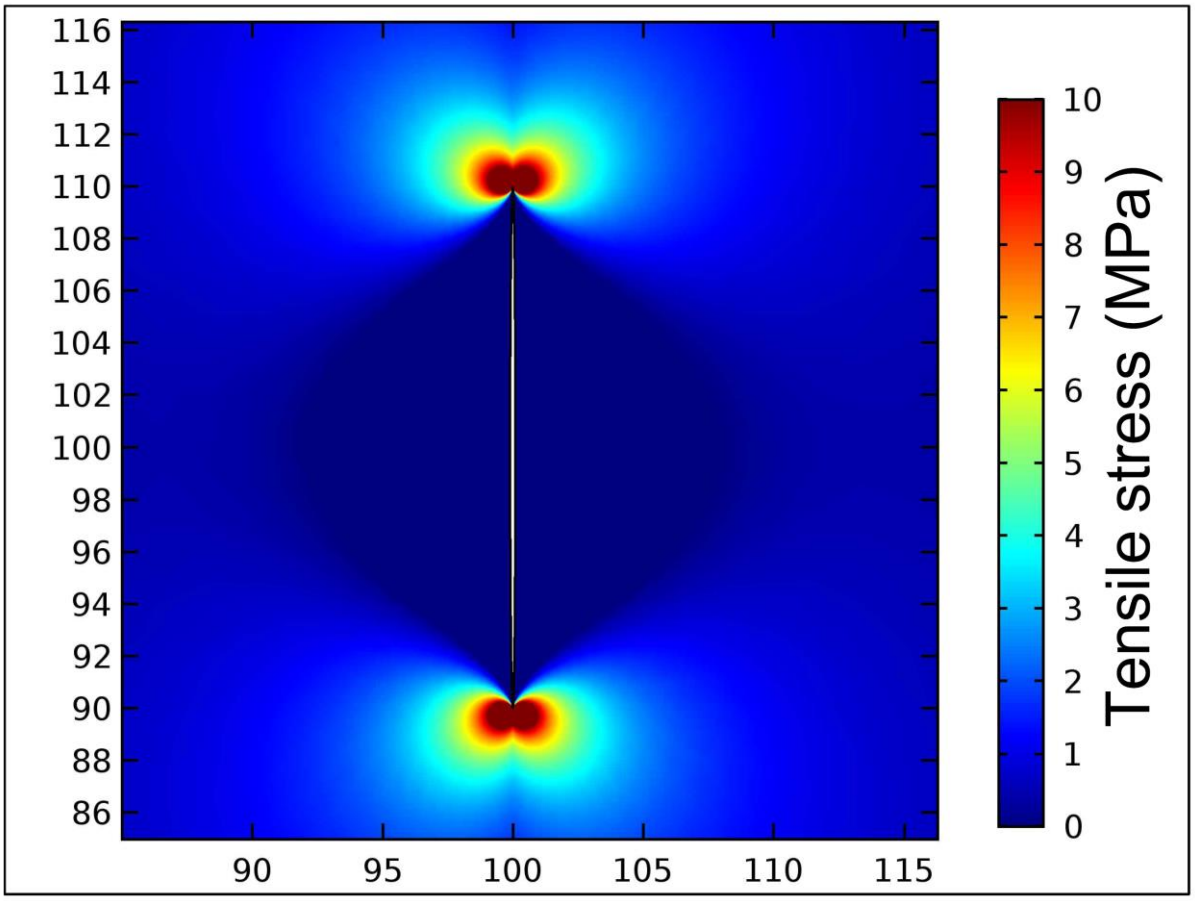

Figure 35: Tensile stress concentrations around a fracture modelled as a 2D ellipse for comparison with Figure 34. The fracture has a height of 10 m and an aperture of 0.1 m, and is enclosed in a 200 x 200 m model which is isotropic and homogeneous. Here the fracture is subject to fluid overpressure of 5 MPa.

The model set up from Figure 34 was then modified so that the height was twice as long as the width, but all other parameters remained the same. These results are presented in Figure 36. In Figure 36B the tensile stress is greater at the tips of the short axis (width) than at the tip of the long axis (height). As the fracture grows it will grow along the short axis faster than along the long axis until the fracture nears or becomes circular. Therefore, again, as a first pass it is considered that using a 2D approach is reasonable.

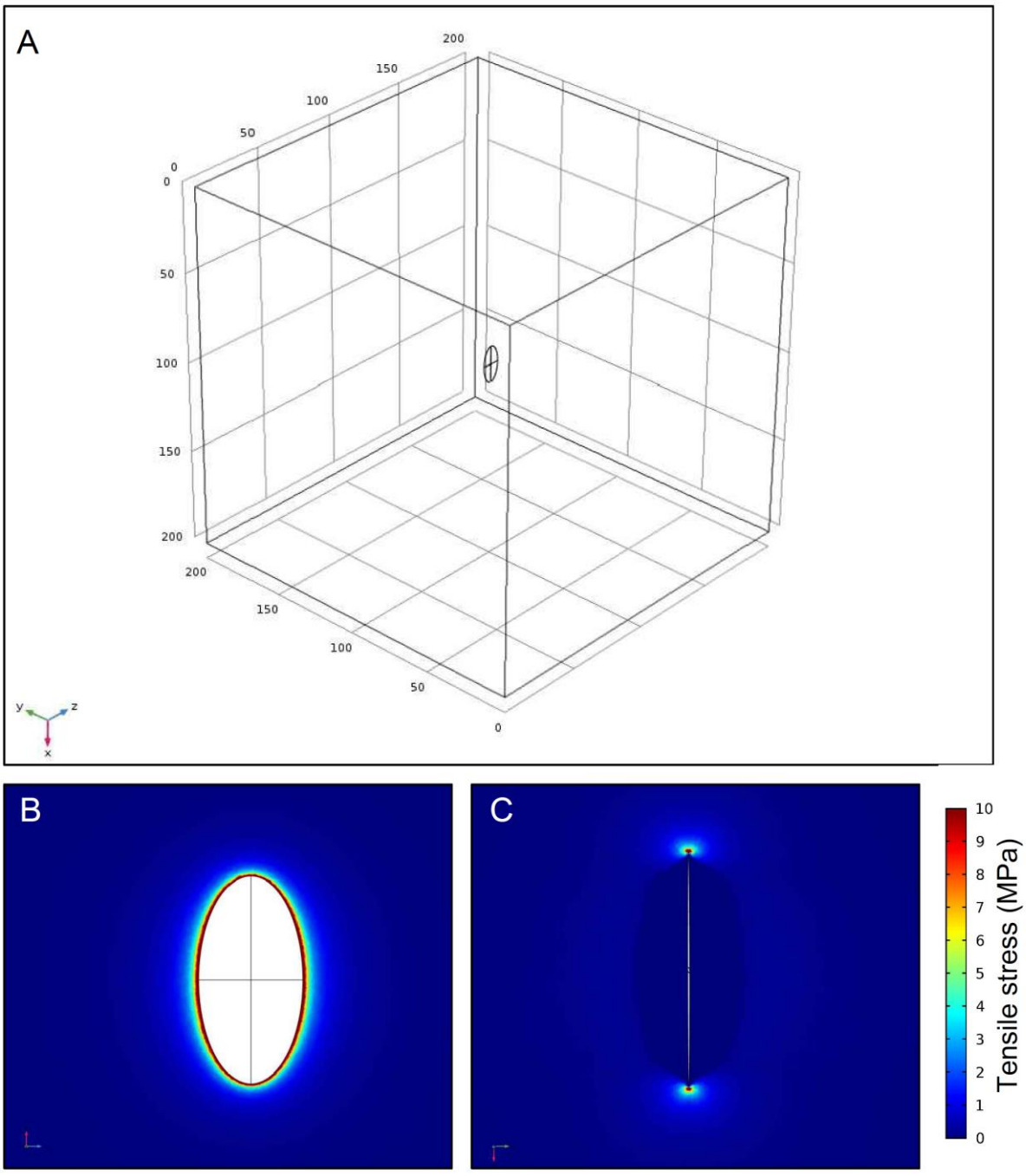

Figure 36: (A) Model set up for an ellipsoid shaped fracture with a height of 10 m, width of 5 m and maximum aperture of 0.1 m. The fracture is enclosed in an isotropic and homogeneous model of 200 x 200 x 200 m, which has a Young's modulus of 10 GPa, Poisson's ratio of 0.25 and a density of 2600 $kg.m^{-3}$. Here the fracture contains a fluid overpressure of 5 MPa. (B) 2D slice demonstrating the tensile stress concentrations (MPa) through the centre of the fracture in the height-width plane. (C) 2D slice demonstrating the tensile stress concentrations (MPa) through the centre of the fracture in the height-aperture plane.

6.1.3.3 Gravity

Some authors consider that it is necessary to apply a gravity load to FEM models analysing hydraulic fractures (e.g. Grosfils 2007). However, as fluid overpressure or excess pressure rather than total fluid pressure is used in the models presented in this thesis, any effect from gravity is automatically taken into account at a local scale i.e. close vicinity of the fracture. However, it is known that the effects from a pressurised fracture decrease rapidly with distance from the fracture tip (Gudmundsson 2011). This assumption may therefore not be as valid when considering far field stresses in models that only consider fluid overpressure as the only loading condition (i.e. no other tectonic forces such as extension). However, this thesis only considers local affects in hydraulic fracture propagation (usually within one fracture length), and any further study of far field stresses falls outside of the scope of the project.

Furthermore, complications arise when applying a gravity load to models as they inevitably become 'crushed' due to the conflict between the gravity load and the fixing of the model to avoid rigid body rotation or translation and because the gravity load is normally so large. Consequently, stress concentrates mainly around the fixed corners of the model, and the magnitude of the stress is so large that it completely masks any effect from the fluid overpressure within the fracture.

These problems have been encountered in other studies that use COMSOL to model hydraulic fractures in crustal segments (Barnett 2014; Browning 2015), and consequently they deemed that by using a fluid overpressure rather than a total fluid pressure there was no need to apply a gravity load to their models. For the same reasons, gravity was not applied to any of the models run as part of this thesis.

6.2 Discussion

6.2.1 Tortuosity of fractures

As is described in Chapter 3, the geometry of fractures produced in the SCB tests of Nash Point shale samples vary significantly. By contrast, fractures produced in Nash Point limestone samples were straight and vertical in all tests, and displayed little to no variability. This is similar to what is observed in the field with regards to the joints which propagate through the sequence at Nash Point (Chapter 5 - Figure 1B and D), whereby fractures in the shale beds are often inclined and sometimes become arrested within the bed, but fractures in the limestone beds are often through going and are vertical.

This could have significant implications with regards to hydrocarbon production from unconventional reservoirs. For example, rough fractures by their nature are harder to close as asperities along the fracture surfaces continue to prop the fracture open after the fluid pressure within the fracture drops (Fredd *et al.* 2000; Wang & Sharma 2018). As such, a fracture network containing many rough fractures may be beneficial in maintaining connectivity between the fractures and the wellbore.

Furthermore, in addition to increasing permeability in tight unconventional reservoirs, the introduction of fractures also increases the surface area of hydrocarbon bearing rock and its connectivity to the well bore (Roshan *et al.* 2016). The true length of a fracture (i.e. taking into account roughness and tortuosity) may be several times larger than the apparent linear length. Therefore, the amount of hydrocarbon bearing rock which is ultimately connected to the wellbore will also be greater, which may therefore aid production. By contrast, there may also be a negative impact on fluid flow through a more tortuous fracture, for example through an increase in turbulent flow (Chapman 1981; Javadi *et al.* 2014). All of these are complex issues outside the current scope of the project, but warrant further study to quantify these qualitative observations.

6.2.2 Fracture propagation across the Nash Point sequence

6.2.2.1 Material inelasticity

In order to understand how fractures may cross the sequence at Nash Point it is important to compare the fracture properties of both rocks. Both the tensile strength and K_{Ic} of the Nash Point limestone are greater than those of the Nash Point shale in all tested orientations. This would suggest that the limestone is both stronger and more resistive to fracture propagation. Consequently, a greater tensile stress is required for a fracture to propagate through the limestone than the shale. However, as the limestone is stiffer (has a higher Young's modulus) it will also concentrate more stress than the shale under the same loading conditions, and so there will likely be a trade-off between the strength of the material and its ability to concentrate stress.

Within the shale this trade-off is likely to be a significant factor in fracture deflection towards the Short-transverse orientation as the shale is weakest in this orientation but also stiffer (The Young's modulus is much higher parallel to bedding than it is normal to bedding) therefore the stress concentration along this orientation will be higher. Conversely, fracture growth in the Arrester orientation will be inhibited by the combined effect of the shale being both stronger and more compliant in this orientation. This is demonstrated in Figure 37 which shows numerical simulations of SCB tests of Nash Point shale tested in the Short-transverse (A) and Arrester (B) orientations. COMSOL allows for different mechanical properties to be prescribed in the orthogonal orientations, therefore it is possible to include elastic anisotropy into the models (i.e. Young's modulus and Poisson's ratio in both bedding normal and bedding parallel orientations). In both (A) and (B) tensile stress concentrates at the tip of the notch as expected. However, tensile stress in the Short-transverse model (A) concentrates more vertically than in the Arrester model (B), whereby stress concentrates horizontally. This is due to the Young's modulus being higher in the bedding-parallel orientation, and therefore tensile stress concentrating

more in this orientation. Both a gradual decrease in strength and a gradual increase in Young's modulus was measured between the Arrester and Short-transverse orientations, which would suggest that fractures should deflect towards the Short-transverse orientation (which is observed in the BD, SCB and SR tests) and at reservoir conditions it is largely the in-situ stresses that force a fracture to grow in the Arrester orientation. Analysis of the G_c data presented in Chapter 3 suggests that the vertical stress during the formation of the natural fractures at Nash Point must have been much greater than any horizontal stress, as the energy required to propagate a fracture in Nash Point shale in the Arrester orientation is almost two orders of magnitude higher than in the Short-transverse orientation.

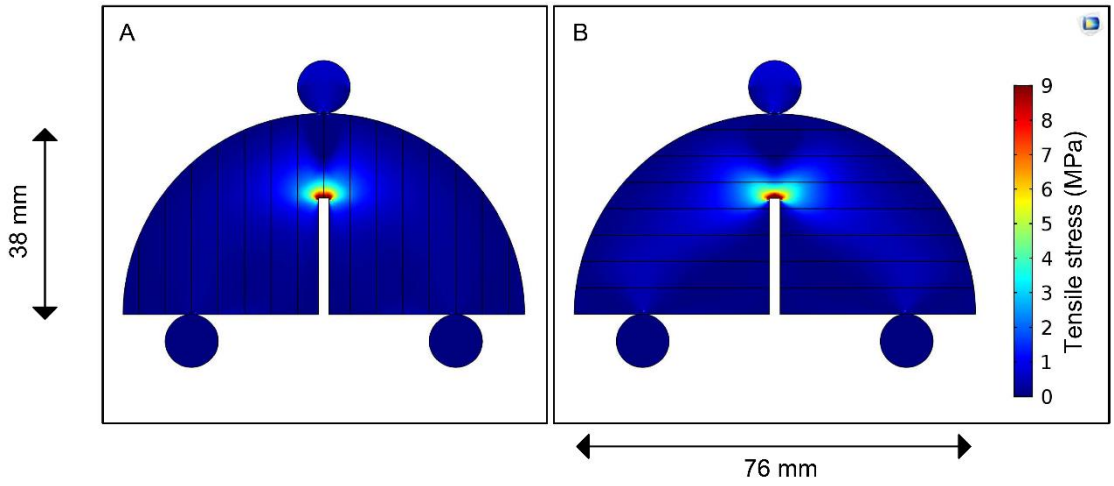

Figure 37: Numerical simulation of SCB tests of Nash Point shale in the Short-transverse (A) and Arrester (B) orientation. Here the bedding plane is depicted by the black lines on the sample.

By using the method described in chapter 3 to calculate G_c, I calculate G_c of Nash Point limestone to be 25.0 ± 3.9 J.m^{-2} (mean ± one standard deviation) for samples tested in the Short-transverse orientation and 27.6 ± 2.4 J.m^{-2} (mean ± one standard deviation) for samples tested in the Arrester orientation. Therefore the energy required to propagate a fracture in the limestone in any orientation (~26 J m^2) is much lower than that required to

propagate a fracture in the shale in the Arrester orientation (~177 J.m^2). However, both the tensile strength and K_{Ic} in the limestone are higher. This would suggest that for a fracture propagating vertically across the sequence, more energy is required for it to propagate through the low-toughness shale than the high-toughness limestone layers, which seems counterintuitive at first. But the definition of K_{Ic} is based on the concept of linear elastic fracture mechanics. The assumption of linear elasticity may be more, or less, valid for many hard rocks but is certainly less valid for soft or compliant rocks. Unfortunately, the SCB method to measure K_{Ic} does not allow us to take account of any non-linear elastic behaviour of the material. However, this can be accounted for using an adaptation of the SR method in which samples are cyclically loaded and unloaded up to failure (ISRM 1988). The cyclic loading and unloading method cannot measure the inelasticity directly, but is able to measure the effect of inelasticity on the value of K_{Ic} determined from the linear elastic fracture mechanics (LEFM) analysis. This enables the determination of a so-called *ductility* correction factor, *m*. The true, inelasticity corrected fracture toughness, K_{Ic}^{c} (superscript c is to denote that the value has been corrected for inelastic deformation), is then simply K_{Ic} multiplied by *m*. In this analysis a perfectly linear elastic material would have an *m* value of 1 and materials with larger values of *m* would have an increasing amount of inelastic content. No values exist for Nash Point limestone or shale, but there are values in the literature for comparable materials, i.e. 'shelly' limestone (Meredith 1989) and Mancos shale (Chandler *et al.* 2016).

Meredith (1989) found the *m* value of a 'shelly' limestone to be 1.02, i.e. near linear elastic. Although not much detail is provided by Meredith (1989) with regards to the origin or make up of the 'shelly' limestone tested, it is stated that it does contain large shell fragments of 0.25 – 3 mm in length. This is not dissimilar from that of the Nash Point limestone, where the rock is predominately made up of shell fragments up to 3 mm in length. As such, as an approximation and using the *m* value of 1.02 as measured from

the 'shelly' limestone, K_{Ic}^{c} of Nash Point limestone is calculated to be 0.84 MPa.m$^{1/2}$ and 0.91 MPa.m$^{1/2}$ in the Short-transverse and Arrester orientations, respectively.

Chandler *et al* (2016) found that the *m* values for Mancos shale were 1.83 in the Short-transverse orientation and 1.49 in the Arrester orientation, which therefore suggests that Mancos shale is far from linear elastic. Using these values, K_{Ic}^{c} of Nash Point shale is calculated to be 0.44 MPa.m$^{1/2}$ in the Short-transverse orientation and 1.10 MPa.m$^{1/2}$ in the Arrester orientation.

Interestingly, in comparing these approximate K_{Ic}^{c} values for Nash Point shale and limestone, the limestone has a lower K_{Ic}^{c} value than the shale in the Arrester orientation but a higher K_{Ic}^{c} value in the Short-transverse orientation. This is consistent with the G_c analysis, in that for a fracture propagating vertically across the sequence more energy is require for it to propagate across the shale layers than the limestone layers.

These values of K_{Ic}^{c} are only a first pass approximation. However, it suggests that if a significant amount of inelastic deformation occurs during fracture propagation in Nash Point shale, but not in Nash Point limestone, the fracture toughness of Nash Point shale may be significantly higher, and higher than that of Nash Point limestone. Furthermore, if Nash Point limestone is considered near linear elastic, and to have an *m* value of 1.02, then an *m* value of > 1.23 is required for the K_{Ic}^{c} of Nash Point shale to be higher than Nash Point limestone in the Arrester orientation. This *m* value is considerably lower than that of the Mancos shale as measured by Chandler *et al*. (2016) but also of other rocks measured by Chandler *et al*. (2016).

6.2.2.2 The effect of layering on fracture propagation

There are very few experimental studies that measure the mechanical properties of, or analyse fracture propagation in, layered rock samples. Kavanagh & Pavier (2014) used

core samples which contained a sharp contact between a siltstone and sandstone to measure the K_{Ic} of both rocks, but also the contact between them. Interestingly they found that the K_{Ic} of the contact (0.45 MPa.m$^{1/2}$) to have a value between the sandstone (0.42 MPa.m$^{1/2}$) and the siltstone (0.56 MPa.m$^{1/2}$). However, the way in which the experiments were set up meant that the induced fracture would propagate along the contact rather than across it. Therefore the results are not really applicable to this study.

Teufel & Clark (1984) manufactured layered samples by stacking three individual layers that had been polished, and applying a load normal to the layering in order to keep them together. They then simulated a hydraulic fracturing operation in a vertical well by injecting fluid into a predrilled hole through the layers, where the fracture would initiate in the middle layer and propagate in a vertical plane away from the hole and towards the interfaces with the layers above and below (Figure 38).

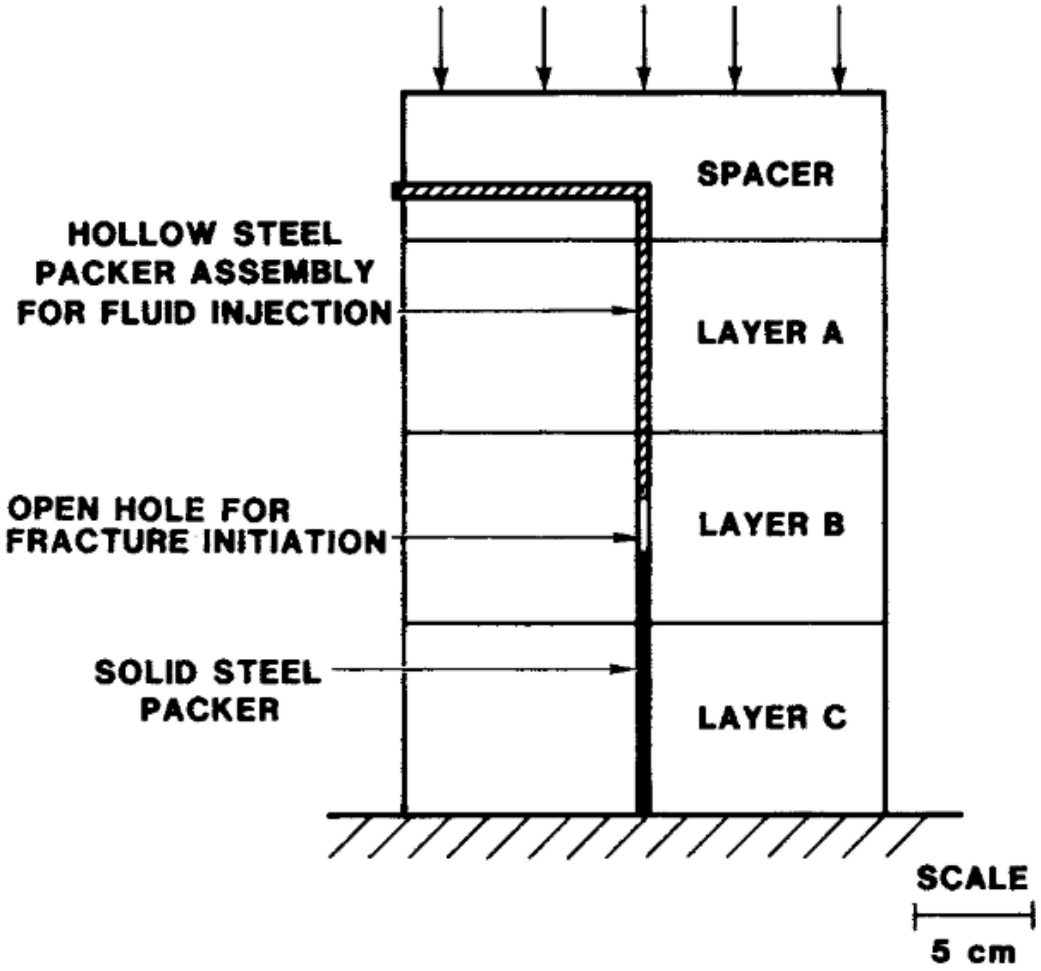

Figure 38: Experimental set up from Teufel & Clark (1984), where layers A, B and C are individual rock layers that have been stacked on top of each other. The vertical arrows above the space indicate a compressive load which is used to apply a normal stress to the layered sample. Figure taken directly from Teufel & Clark (1984).

Their study had two main conclusions. Firstly, when all three layers were the same rock type the induced fracture would only cross the interface between the layers if the normal stress was higher than tensile strength of the rock. This is due to the Cook-Gordon delamination mechanism (see Supplementary Information in Chapter 5) where the tensile stress at the fracture tip is high enough to delaminate the two layers. Secondly, when conducting tests whereby the middle layer was a different rock type to the layer above and below (which were both the same), differential horizontal stresses were induced across the interfaces, which were dependent on both the normal stress and the contrast in

elastic properties of the individual layers. Compliant layers would concentrate compressive horizontal stress, whereas competent layers would concentrate a tensional horizontal stress. As the normal stress was increased the differential stress between the layers would also increase. They found that for fractures propagating from a compliant layer towards a competent layer the differential stress had little effect on fracture propagation as the horizontal stress was tensional, which would promote vertical fracture growth. By contrast, when a fracture was propagating from a competent layer to a compliant layer the fracture would become arrested at the interface at both low normal stresses (because of delamination) and higher normal stresses (because of increased compressive horizontal stress in the compliant layer). However, for intermediate normal stresses the fracture would propagate across the interface. Fracture arrest due to increased compressive horizontal stresses in the compliant layer is synonymous with the stress barrier mechanism (see Supplementary Material in Chapter 5). As the layered samples were manufactured and only 'bonded' together by a normal stress, caution must be exercised when applying the results to natural sequences where the interface may have residual strength (i.e. the layers above and below are bonded). Therefore, if possible it is usually preferable to test samples that contain natural contacts or interfaces.

During one of the field campaigns I tried, unsuccessfully, to obtain a sample which contained both shale and limestone to be able to test the contact properties between the two, and analyse how fracture propagation may be affected by the layering directly.

As I was unable to do this I have run two numerical models to understand what affect the layering at Nash Point may have on fracture propagation across the sequence. Both models consider a 30 x 30 m model with alternating beds of limestone and shale, each of 1 m thickness, and a hydraulic fracture 2 m in length located at the centre of the model. In Figure 39 the model is set up so that the fracture tip is located in the middle of a shale layer, while the model illustrated in Figure 40 is set up so that the fracture tip is located

in the middle of a limestone layer. The mechanical properties (Young's modulus, Poisson's ratio and density) of the two layers are taken directly from the measurements presented in Chapters 3 and 4. Again as COMSOL allows different mechanical properties to be prescribed in the orthogonal orientations, I am able to include elastic anisotropy into the models (i.e. Young's modulus and Poisson's ratio in both bedding normal and bedding parallel orientations). The hydraulic fracture in both models has an internal fluid overpressure of 5 MPa.

As hydraulic fractures are predominately mode-I, they will propagate in the σ_1-σ_2 plane. As such σ_1 and σ_2 are plotted and should the fracture propagate (i.e. the tensile stress at the fracture tip overcomes both the tensile strength of the rock but also σ_3 – I will refer to this as the critical condition) it will propagate crudely parallel to the cone marks. I say crudely here as it was demonstrated in Chapter 3 that mechanical anisotropy can cause fracture deflections and tortuosity. Therefore there may be some slight deviation from the σ_1- σ_2 plane on a micro scale, but on a meso or macro scale the fracture will largely propagate in the σ_1- σ_2 plane, as we see in the field.

Where the fracture tip is located in the shale layer (Figure 39), the σ_1- σ_2 plane is vertical directly ahead of the fracture until the interface between the limestone layer above and the subsequent shale layer, where the σ_1- σ_2 plane rotates by up to 90°. Therefore, as long as the critical condition is met the fracture will grow vertically until this point. Note, however, how tensile stress also concentrates at the shale-limestone interface directly ahead of the fracture. Stress concentrates here due to the Young's modulus of the limestone ahead being greater than the shale layer hosting the fracture (see Chapter 5). Should the stress concentrating at this interface be sufficient as to overcome the strength of the interface (if it is cemented for example) and the normal stress acting on the interface (which at depth is likely to be σ_1) the interface may open up which could promote fracture deflection along the interface, or fracture arrest. This is known as Cook-Gordon

delamination, and is described in the Supplementary Material of Chapter 5. For a horizontal interface this mechanism is likely to be more effective at shallow depths as the normal stress will be lower, and as Teufel & Clark (1984) demonstrate in their experimental work. Should the interface not open up, the fracture will continue to propagate vertically until the next interface which is between the limestone and the subsequent shale layer. At this point the local stress field is no longer favourable for vertical fracture growth (due to the rotation of the σ_1- σ_2 plane), and so the fracture may become arrested, or if the interface between the limestone and the shale is weak enough the fracture may become deflected in to the interface. However, again, in this case the pressure within the fracture would also need to overcome the normal stress acting on the interface, which at depth is likely to be σ_1.

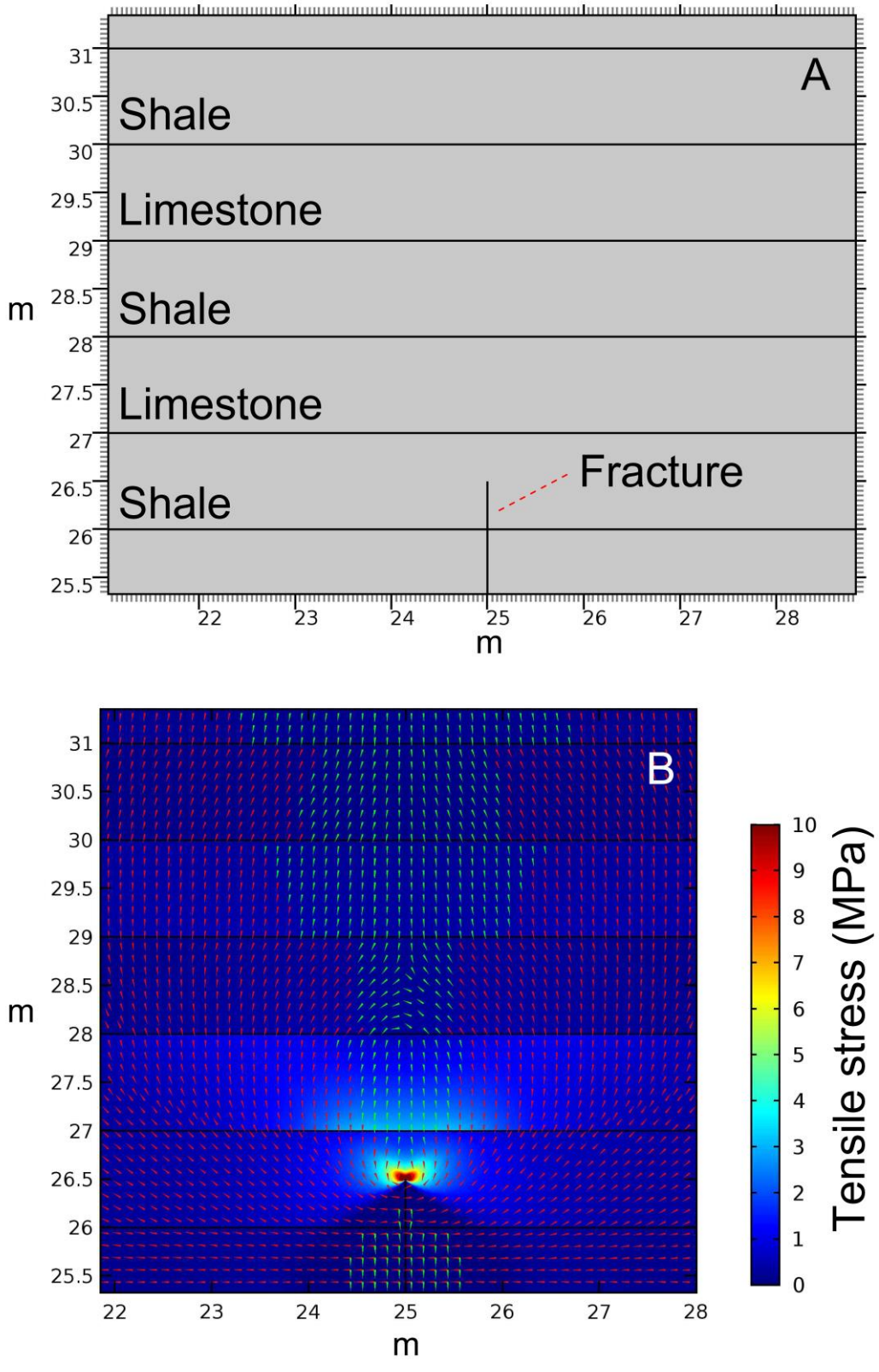

Figure 39: (A) Model set up for hydraulic fracture with tip located in shale layer (B) Plot of resultant stresses from the pressurised hydraulic fracture. Contours display the concentration of tensile stress, while the cones depict the orientation of σ_1 (red cones) and σ_2 (green cones)

Where the fracture tip is located in the middle of a limestone layer (Figure 40) there is short distance where the σ_1- σ_2 plane is vertical ahead of the fracture tip, which would therefore promote vertical fracture growth should the critical condition be met. However, the σ_1- σ_2 plane rotates at the limestone-shale interface ahead of the fracture, thereby creating a stress barrier, as described in the Supplementary Material of Chapter 5.

Therefore, it appears as though the stress barrier mechanism is more likely to occur as a fracture approaches a more compliant layer than the one hosting the tip of the fracture, again this is similar to what Teufel & Clark (1984) demonstrate in their experimental work. This is in contrast to the elastic mismatch mechanism, discussed in Chapter 5, whereby a fracture is more likely to become arrested upon approaching a more competent layer than the one hosting the fracture tip. In a layered sequence, whereby the Young's modulus between the layers is significantly different, fracture arrest may occur upon approaching a more compliant layer (through the stress barrier mechanism) or a more competent layer (through the elastic mismatch mechanism). Fracture arrest could also occur through the Cook-Gordon delamination mechanism; however, this is increasingly less likely at depth.

In Chapter 5 it was discussed how the elastic mismatch mechanism may not be as effective when the fracture length is significantly greater than the thickness of the layer ahead. By contrast, even for a fracture which is much longer than the thickness of the individual layers, there still appears to be a significant rotation of the σ_1- σ_2 plane at the interface between a competent layer hosting the fracture tip and a more compliant layer ahead of the fracture, as illustrated in Figure 41. Here the fracture is 10 m long (dip length) but all other parameters are the same as in the setup in Figure 40. Note how the tensile stress concentrations are much greater throughout the model, which is due to the longer fracture length.

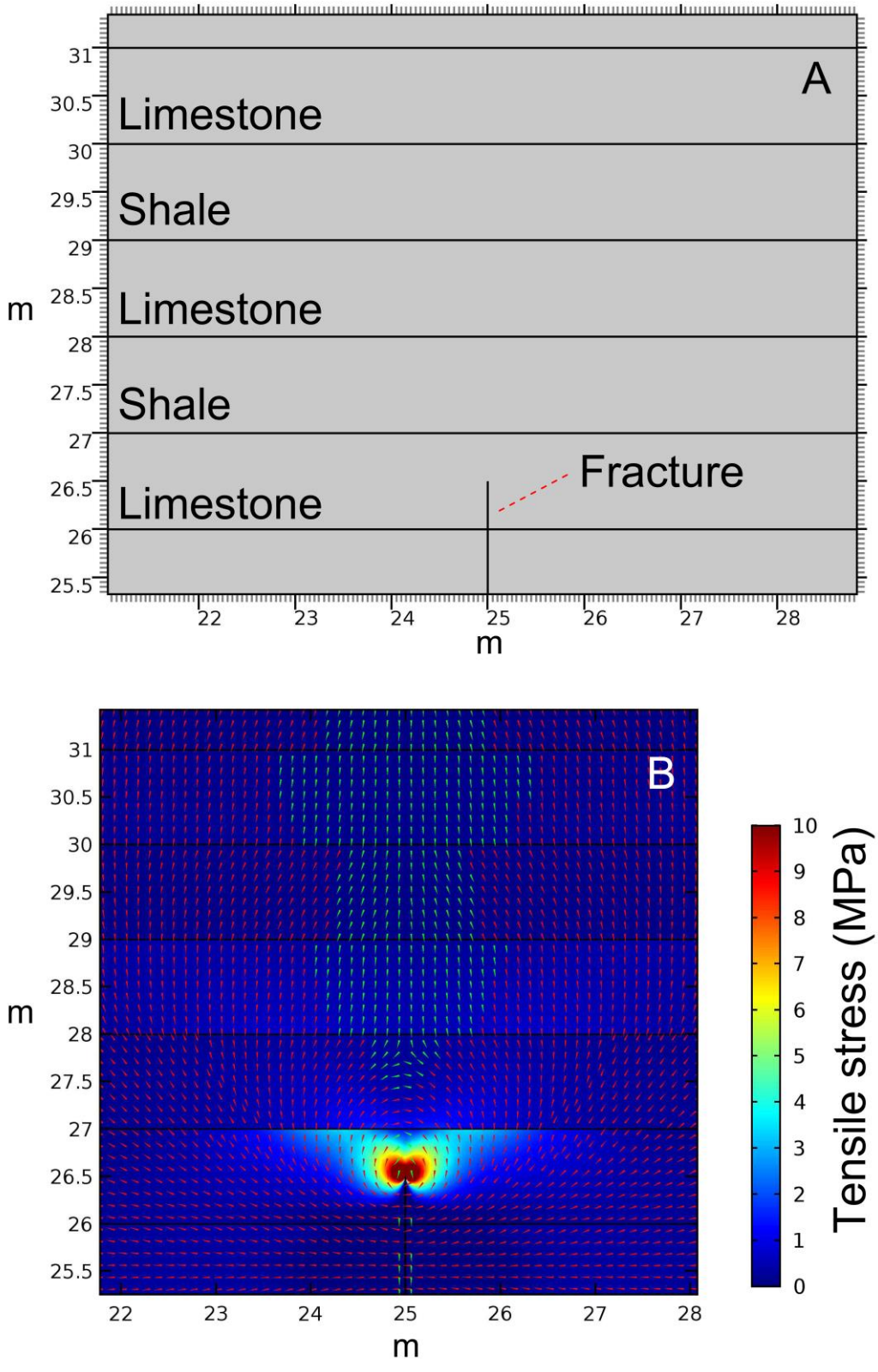

Figure 40: (A) Model set up for hydraulic fracture with tip located in limestone layer. (B) Plot of resultant stresses from the pressurised hydraulic fracture. Contours display the concentration of tensile stress, while the cones depict the orientation of σ_1 (red cones) and σ_2 (green cones)

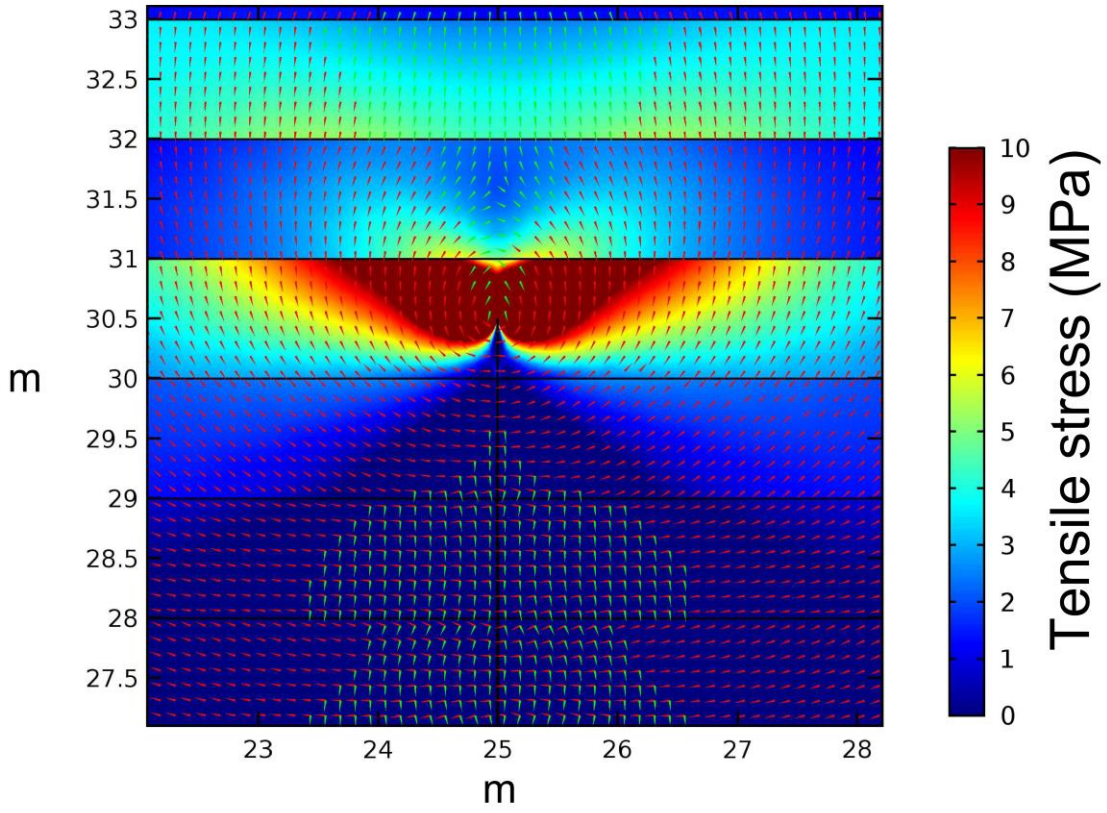

Figure 41: Results of the same model set up as Figure 40. However, here the fracture length is 10 m. Contours display the concentration of tensile stress, while the cones depict the orientation of σ_1 (red cones) and σ_2 (green cones)

What has not been discussed here is what affect the presence of natural fractures would have on hydraulic fracture propagation. It is likely that the presence of fractures would perturb the induced stress field demonstrated in Figures 34 to 36, and this could lead to fracture linkage between the hydraulic fracture and any existing fractures. Although further analysis falls outside the scope of this project I would refer the reader to the following literature, and references therein, for a more detailed discussion on this topic (Häring *et al.* 2008; Dorbath *et al.* 2010; Larsen & Gudmundsson 2010; de Pater & Baisch 2011; Jinzhou *et al.* 2014; Lee 2015; Lee *et al.* 2015).

6.2.3 Mechanical properties at depth

All the experiments conducted as part of this study were carried out at ambient pressure and temperature conditions. It is noted, however, that the mechanical properties of rocks are likely to be different at reservoir conditions (where temperature and pressure will be higher). Many, if not most, unconventional reservoirs are at less than 5 km deep (Fisher & Warpinski 2012). For an average geothermal gradient of 25°C.km^{-1} (Gudmundsson 2011) this would mean a temperature of approximately 140°C at this maximum depth (taking ambient temperature to be 15°C). Within this temperature range temperatures it has been shown that the Young's modulus (Sygała *et al.* 2013), tensile strength (Lü *et al.* 2017) and fracture toughness (Chandler *et al.* 2017) of crustal materials does not vary significantly. By contrast, for the same depth range, it is generally accepted that the Young's modulus of crustal materials will increase with depth (Jaeger & Cook 1979; Gudmundsson 2011; Browning *et al.* 2015), which is largely a result of the increased pressures at depth closing up pores and existing fractures in the rock.

In transversely isotropic rocks, where there is likely a strong alignment of pores and micro-fractures in a particular direction, the relationship with depth is a little more complex. For example, Ong *et al*. (2016) measured the Young's modulus dependence on confining pressure for a series of calcareous shales from Duvernay reservoir in Alberta, Canada, by subjecting samples to confining pressure of up to 90 MPa. Using an average pressure gradient of 25 MPa.km^{-1} (Gudmundsson 2011) the corresponding depth would be 3.6 km at the maximum confining pressure tested. They found that although the Young's modulus increased in the bedding normal orientation with increased confining pressure there was no discernible variation of the Young's modulus in the bedding parallel orientation with increased confining pressure. Similar to Nash Point shale, the pores and micro-fractures within the shales tested by Ong *et al.* (2016) were strongly aligned to the bedding plane. Therefore it may be expected that the Young's modulus of Nash Point

shale would vary in a similar way. By contrast, as Nash Point limestone is essentially isotropic, this directional dependence on Young's modulus with increasing pressure should not exist.

The effect of confining pressure on fracture toughness is not as well constrained. Several authors have attempted to measure the fracture toughness of rocks by simply applying a confining pressure to the notched samples used to measure fracture toughness (Schmidt & Huddle 1977; Chandler 2014; Kataoka *et al.* 2017), and have reported that fracture toughness increases with increasing confining pressure, and therefore depth. In order to accurately measure the fracture toughness at elevated confining pressures the sample must be jacketed or sealed using an impermeable coating, so as to stop the infiltration of the confining fluid in to the material. However, pressure must also be applied within the notch, but not within the propagating fracture (Schmidt & Huddle 1977). This therefore becomes problematic if using a coating or epoxy resin to seal the sample as the formation of the fracture at the tip of the notch will breach the seal, therefore allowing fluid to enter the fracture. The problem may be overcome if the sample is jacketed properly, but due to the complex geometry of the notched sample, it is incredibly difficult to manufacture and apply a jacket that allows the confining fluid to enter the notch properly. As such, direct measurements of fracture toughness at elevated confining pressures must therefore be used with caution, unless the proper sealing of the notched is ensured.

Alternatively, it may be possible to measure the fracture toughness indirectly from thick walled cylinder tests also known as burst tests (Stoeckhert *et al.* 2016; Gehne 2018; Vinciguerra *et al.* 2004; Clifton *et al.* 1976; Abou-Sayed 1978). This test involves manufacturing a cylindrical core of testing material, with a through-going hole bored out of the centre of the sample axially. The sample is then jacketed and a confining fluid pressure applied to the outside of the sample, and an axial load applied to the top of the sample to keep the sample in place. Fluid is then injected into the central bore. An

example of the experimental set up is presented in Figure 42, and is taken directly from Vinciguerra *et al*. (2004). In the case of a permeable material it may also be necessary to line the inner bore with an impermeable jacket to stop fluid permeating into the sample from the central bore (Vinciguerra *et al.* 2004). However, shales are known to have very low permeability, and as such this inner jacket may not be required (Gehne 2018).

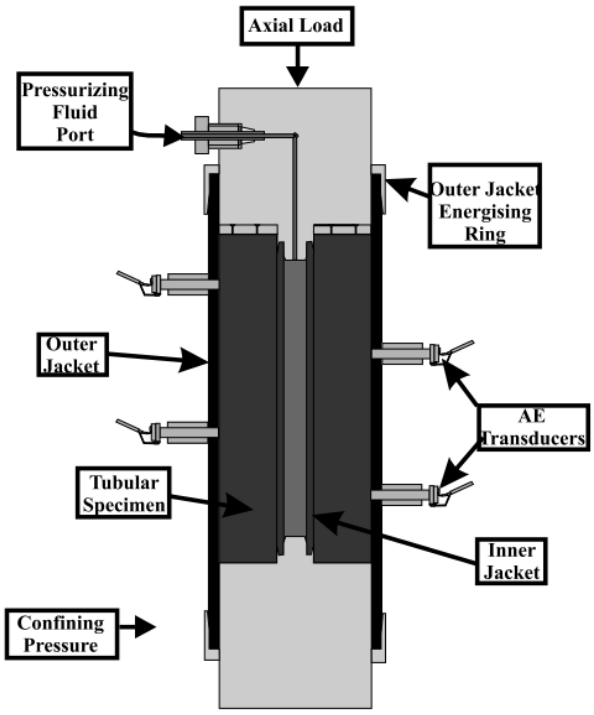

Figure 42: Example of the set-up for a thick walled cylinder test. Figure taken directly from Vinciguerra *et al*. (2004). For experiments on very low permeability rocks, such as shale, the inner jacket may not be required. Here AE stands for Acoustic Emission.

At a critical internal (within the bore) fluid pressure a fracture will propagate from the central bore towards the out wall of the sample. Using a combination of Acoustic Emission (AE) transducers and monitoring any drop in fluid pressure within the central bore it is possible to deduce when and at what internal fluid pressure the fracture begins to propagate. This critical pressure is called the breakdown pressure.

The breakdown pressure and fracture toughness are inevitably related and Abou-Sayed (1978) suggest the following relationship:

$$P_b = P_c + \frac{K_{Ic}}{1.2 \times \sqrt{\pi a_0}} \tag{14}$$

where P_b is the breakdown pressure, P_c is the confining pressure and a_0 is the critical flaw size of the material. The critical flaw size of the material relates to the length of the largest flaw in the material that is able to concentrate stress. By conducting a test at ambient conditions (i.e. $P_c = 0$) and using the K_{Ic} at ambient conditions (from Chapters 3 and 4) it is possible to solve equation (14) for a_0. However, as has already been discussed, existing fractures and flaws within a material close up as the confining pressure increases, therefore it is possible that a_0 will reduce with increasing confining pressures. This will therefore mean that there are two unknowns in equation (14) when $P_c > 0$ (i.e. K_{Ic} and a_0). However, as the fracture grows in increments (Vinciguerra *et al.* 2004; Gehne 2018) it may be possible to deduce the length of the fracture after a certain growth increment by measuring the pressure drop within the internal bore along with AE caused during fracture propagation. If so this would allow for a_0 to be determined at different fracture growth increments, and using equation (14), the K_{Ic} can be calculated using the pressure required to propagate the fracture to the subsequent growth increment. This work is a is currently an unsolved but key problem in crustal fracture mechanics worthy of further study.

7 Conclusions

Before going through the main conclusions of this study it is important to recall the two questions which were to be addressed and constitute the main aims of the study, namely:

1. How does mechanical anisotropy within a rock type affect fracture propagation?

2. How does large scale heterogeneity, in particular mechanical layering, affect fracture propagation?

With these questions (Q1 and Q2) in mind the main conclusions may be summarised as follows:

- Nash Point shale is highly anisotropic in terms of its mechanical properties, being more resistant to fracture propagation, and thus stronger, in the Arrester and the Divider orientations than in the Short-transverse orientation. Extensive testing found that both the apparent tensile strength and the fracture toughness, K_{Ic}, increased from the Short-transverse to the Arrester orientation. Nash Point shale also has a much higher (three times greater) Young's modulus parallel to bedding than it does normal to bedding. This mechanical anisotropy is strongly related to its structural anisotropy. **(Q1)**
- As a result of its mechanical anisotropy (of the Nash Point shale) fractures propagating between the Short-transverse and the Arrester orientation tend to deflect towards the weaker Short-transverse orientation and are tortuous. We therefore propose a method of correcting the measured apparent K_{Ic} for fractures that are deflected from the initiation point. This allows the determination of a deflection-corrected mode-I stress intensity factor, K_{Id}. However, since deflected fractures propagate in mixed mode, critical crack growth is likely controlled by some combination of K_I and K_{II}, and hence K_{Id} alone cannot be considered a critical value. Thus, we adopted a fracture energy (G_c) based approach to analyse

fracture propagation at orientations between the Short-transverse and Arrester orientations and determined the angular variation of G_c. **(Q1)**

- By contrast, Nash Point limestone is essentially isotropic in terms of its mechanical properties. The isotropy is, again, largely down to the rock structure. As a result all fractures produced from during Brazil disk, SCB and SR tests showed little or no tortuosity. **(Q1)**
- Although Nash Point limestone had a higher K_{Ic} than Nash Point shale in all orientations, the G_c of Nash Point shale in the Arrester orientation was an order of magnitude higher than that of Nash Point limestone. This discrepancy is presumably because K_{Ic} measurements assume that the material is linear elastic, and if corrected for inelastic behaviour during fracture propagation it is likely that the K_{Ic}^{c} (superscript c is to denote that the value has been corrected for inelastic deformation) of Nash Point shale would be higher than Nash Point limestone. **(Q2)**
- Numerical modelling demonstrates that for a hydraulic fracture propagating through a layered sequence, the contrast in Young's moduli between the individual layers has significant effect on whether the fracture becomes arrested. Other factors that affect the likelihood of fracture arrest are the thickness of the individual layers and the proximity of the fracture tip to an interface between different layers. For a vertical fracture propagating through a horizontally layered sequence we observe as follows:
    - Tensile stress at fracture tips increases as the tip approaches an interface if the layer ahead (above the interface) is more compliant than the layer hosting the fracture tip, but decreases when the layer ahead is stiffer than the hosting layer. **(Q2)**

- The contrast in Young's modulus between the layers has a larger effect on the fracture-tip tensile stress as the layer ahead of the propagating fracture increases in thickness and as the proximity of the fracture tip to the interface decreases. **(Q2)**
- Fracture arrest is most likely to occur exactly at the interface when the layer ahead is more compliant than the host layer (through either the Cook-Gordon delamination or the stress barrier mechanism). By contrast, when the layer ahead is stiffer than the host layer fracture arrest can occur either at the interface, or at some distance within the host layer before the interface is reached (through the elastic mismatch mechanism). **(Q2)**

It is clear from the results presented in the thesis that both rock heterogeneity and anisotropy can have a significant effect on hydraulic fractures propagating in an unconventional reservoir (be it gas shales or carbonate reservoirs), with several mechanisms by which a fracture may become arrested or deflected. Therefore, both heterogeneity and anisotropy within a reservoir must be understood before any reliable forecast of fracture propagation can be made.

7.1 Further work

Although I have been able to address the questions set out in the aims of this project, some unknown factors still remain as regards to our present understanding of how heterogeneity and anisotropy may affect fracture propagation. The further work, proposed below, is meant to address some of the unknowns:

- Measure the mechanical properties of different beds from the Nash Point sequence to quantify what heterogeneity exists between different beds across the sequence and analyse if this heterogeneity affects the conclusions of this study.

- Measure the amount of inelastic deformation during fracture propagation of Nash Point shale and limestone by using an adaptation of the SR method. Use this to calculate the inelasticity corrected fracture toughness, K_{Ic}^{c}.
- Measure the fracture toughness of Nash Point shale and limestone at confining pressures (indirectly) using the thick walled cylinder tests to understand how fracture toughness may vary at depth.
- Incorporate further heterogeneities such as existing fractures in the numerical models.

8 References

Abou-Sayed, A.S. 1978. Experimental technique for measuring the fracture toughness of rocks under downhole stress conditions. *VDI Ber*, 819–824.

Afşar, F., Westphal, H. & Philipp, S.L. 2014. How facies and diagenesis affect fracturing of limestone beds and reservoir permeability in limestone-marl alternations. *Marine and Petroleum Geology*, **57**, 418–432, https://doi.org/10.1016/j.marpetgeo.2014.05.024.

Al-Harthi, A.A., Al-Amri, R.M. & Shehata, W.M. 1999. The porosity and engineering properties of vesicular basalt in Saudi Arabia. *Engineering Geology*, **54**, 313–320, https://doi.org/10.1016/S0013-7952(99)00050-2.

Aliha, M.R.M., Sistaninia, M., Smith, D.J., Pavier, M.J. & Ayatollahi, M.R. 2012. Geometry effects and statistical analysis of mode I fracture in guiting limestone. *International Journal of Rock Mechanics and Mining Sciences*, **51**, 128–135, https://doi.org/10.1016/j.ijrmms.2012.01.017.

Arzani, N. 2004. Diagenetic Evolution of Mudstones: Black Shales to Laminated Limestones, an Example from the Lower Jurassic of SW Britain. *Journal of Sciences Islamic Republic of Iran*, **15**, 257–267.

Atkinson, B.K. 1987. *Fracture Mechanics of Rock*. London, https://doi.org/10.1007/978-94-007-2595-9.

Barnett, Z.A. 2014. *Emplacement and Evolution of Sills into Shallow Magma Chambers and Hydrocarbon Reservoirs*. Royal Holloway, University of London.

Barnett, Z.A. & Gudmundsson, A. 2014. Numerical modelling of dykes deflected into

sills to form a magma chamber. *Journal of Volcanology and Geothermal Research*, **281**, 1–11, https://doi.org/10.1016/j.jvolgeores.2014.05.018.

BGS. 2013. *The Carboniferous Bowland Shale Gas Study : Geology and Resource Estimation*.

Bieniawski, Z.T. & Bernede, M.J. 1979. Suggested methods for determining the uniaxial compressive strength and deformability of rock materials. *International Journal of Rock Mechanics and Mining Sciences & Geomechanics Abstracts*, **16**, 138–140, https://doi.org/10.1016/0148-9062(79)91451-7.

Boyer, C., Lewis, R., Miller, C.K. & Clark, B. 2011. Shale Gas : A Global Resource. *Oilfield Review*, **23**, 28–39.

Brenne, S. 2015. *Hydraulic Fracturing and Flow Experiments on Anisotropic and Pre-Fractured Rocks*. Ruhr-University Bochum.

Browning, J. 2015. *Thermo-Mechanical Effects of Magma Chambers and Caldera Faults*. Royal Holloway, University of London.

Browning, J. & Gudmundsson, A. 2015. Caldera faults capture and deflect inclined sheets: an alternative mechanism of ring dike formation. *Bulletin of Volcanology*, **77**, https://doi.org/10.1007/s00445-014-0889-4.

Browning, J., Drymoni, K. & Gudmundsson, A. 2015. Forecasting magma-chamber rupture at Santorini volcano, Greece. *Scientific reports*, **5**, 15785, https://doi.org/10.1038/srep15785.

Bubeck, A., Healy, D., Walker, R.J., Holwell, D.A. & Dobbs, M. 2016. Pore geometry as a control on rock strength. *Earth and Planetary Science Letters*, **457**, 38–48, https://doi.org/10.1016/j.epsl.2016.09.050.

Burberry, C.M. & Peppers, M.H. 2017. Fracture characterization in tight carbonates: An example from the Ozark Plateau, Arkansas. *AAPG Bulletin*, **101**, 1675–1696, https://doi.org/10.1306/01251715242.

Carmichael, R.S. 1989. *Practical Handbook of Physical Properties of Rocks and Minerals*. Carmichael, R. S. (ed.). Boca Raton.

Chalmers, G.R.L. & Bustin, R.M. 2017. A multidisciplinary approach in determining the maceral (kerogen type) and mineralogical composition of Upper Cretaceous Eagle Ford Formation: Impact on pore development and pore size distribution. *International Journal of Coal Geology*, **171**, 93–110, https://doi.org/10.1016/j.coal.2017.01.004.

Chandler, M.R. 2014. *A Fracture Mechanics Study of an Anisotropic Shale*. PhD, Univeristy College London.

Chandler, M.R., Meredith, P.G., Brantut, N. & Crawford, B.R. 2016. Fracture toughness anisotropy in shale. *Journal of Geophysical Research : Solid Earth*, **121**, 1–24, https://doi.org/10.1002/2015JB012756.

Chandler, M.R., Meredith, P.G., Brantut, N. & Crawford, B.R. 2017. Effect of temperature on the fracture toughness of anisotropic shale and other rocks. *Geological Society, London, Special Publications*, SP454.6, https://doi.org/10.1144/SP454.6.

Chapman, R.E. 1981. *Geology and Water*, 1st ed. Nijhoff, M. (ed.). Dordrecht, Dr. W. Junk Publishers.

Chong, K.P., Kuruppu, M.D. & Kuszmaul, J.S. 1987. Fracture toughness determination of layered materials. *Engineering Fracture Mechanics*, **28**, 43–54,

https://doi.org/http://dx.doi.org/10.1016/0013-7944(87)90118-4.

Cicero, S., García, T., Castro, J., Madrazo, V. & Andrés, D. 2014. Analysis of notch effect on the fracture behaviour of granite and limestone: An approach from the Theory of Critical Distances. *Engineering Geology*, **177**, 1–9, https://doi.org/10.1016/j.enggeo.2014.05.004.

Clark, J. 1949. Hydrafrac process for well treatment. *Division of Production, American Petroleum Institute*.

Clifton, R.J., Simonson, E.R., Jones, A.H. & Green, S.J. 1976. Determination of the critical-stress-intensity factor KIc from internally pressurized thick-walled vessels - The critical-stress-intensity factor of thick-walled rock specimens is determined from the pressure at failure. *Experimental Mechanics*, **16**, 233–238, https://doi.org/10.1007/BF02329274.

Cooke, M.L. & Underwood, C.A. 2001. Fracture termination and step-over at bedding interfaces due to frictional slip and interface opening. *Journal of Structural Geology*, **23**, 223–238, https://doi.org/10.1016/S0191-8141(00)00092-4.

Cornford, C. 1986. The Bristol Channel Graben: Organic geochemical limits on subsidence and speculation on the origin of inversion. *Geoscience in South-West England*, **6**, 360–367.

Cuervo, S., Lombardo, E., Vallejo, D., Crousse, L. & Mosse, L. 2016. Towards a Simplified Petrophysical Model for the Vaca Muerta Formation. **2**.

Dai, F., Wei, M.D., Xu, N.W., Zhao, T. & Xu, Y. 2015. Numerical investigation of the progressive fracture mechanisms of four ISRM-suggested specimens for determining the mode I fracture toughness of rocks. *Computers and Geotechnics*,

69, 424–441, https://doi.org/10.1016/j.compgeo.2015.06.011.

Dashti, R., Rahimpour-Bonab, H. & Zeinali, M. 2018. Fracture and mechanical stratigraphy in naturally fractured carbonate reservoirs-A case study from Zagros region. *Marine and Petroleum Geology*, **97**, 466–479, https://doi.org/10.1016/j.marpetgeo.2018.06.027.

de Pater, C.J. & Baisch, S. 2011. *Geomechanical Study of Bowland Shale Seismicity*.

Dibb, T.E., Hughes, D.W. & Poole, A.B. 1983. The identification of critical factors affecting rock durability in marine environments. *Quarterly Journal of Engineering Geology and Hydrogeology*, **16**, 149–161, https://doi.org/10.1144/gsl.qjeg.1983.016.02.08.

Dorbath, L., Evans, K., Cuenot, N., Valley, B., Charléty, J. & Frogneux, M. 2010. The stress field at Soultz-sous-Forêts from focal mechanisms of induced seismic events: Cases of the wells GPK2 and GPK3. *Comptes Rendus Geoscience*, **342**, 600–606, https://doi.org/10.1016/j.crte.2009.12.003.

Elston, H.W. 2014. *Mineralogical and Geochemical Assessment of the Eagle Ford Shale*. Ohio State University.

F. Stoeckhert, Brenne, S., Molenda, M. & Alber, M. 2016. Mode I fracture toughness of rock under confining pressure. *Eurock2016*.

Fantín, M.A., Crousse, L.C., Cuervo, S., Vallejo, D., González Tomassini, F., Reijenstein, H.M. & Christopher, L. 2014. Vaca Muerta stratigraphy in central neuqúen basin: Impact on unconventional project development. *Society of petroleum engineers*, 11, https://doi.org/10.15530/urtec-2014-1923793.

Ferrill, D.A., McGinnis, R.N., et al. 2014. Control of mechanical stratigraphy on bed-

restricted jointing and normal faulting: Eagle Ford Formation, south-central Texas. *AAPG Bulletin*, **98**, 2477–2506, https://doi.org/10.1306/08191414053.

Fisher, K. & Warpinski, N. 2012. Hydraulic-fracture-height growth : Real data. *Society of petroleum engineers*, https://doi.org/10.2118/145949-PA.

Forbes Inskip, N.D., Meredith, P.G., Chandler, M.R. & Gudmundsson, A. 2018. Fracture properties of Nash Point shale as a function of orientation to bedding. *Journal of Geophysical Research: Solid Earth*, 1–17, https://doi.org/10.1029/2018JB015943.

Fredd, C.N., McConnell, S.B., Boney, C.L. & England, K.W. 2000. Experimental Study of Hydraulic Fracture Conductivity Demonstrates the Benefits of Using Proppants. *SPE Rocky Mountain Regional/Low-Permeability Reservoirs Symposium and Exhibition*, 14, https://doi.org/10.2118/60326-MS.

Galvis, H., Becerra, D. & Slatt, R. 2017. Lithofacies and stratigraphy of a complete Woodford Shale outcrop section in South Central Oklahoma: Geologic considerations for the evaluation of unconventional shale reservoirs. *Interpretation*, **6**, SC15–SC27, https://doi.org/10.1190/int-2017-0074.1.

Gehne, S. 2018. *A Laboratory Study of Fluid-Driven Tensile Fracturing in Anisotropic Rocks*. University of Portsmouth.

Gentzis, T. 2013. A review of the thermal maturity and hydrocarbon potential of the mancos and lewis shales in parts of New Mexico, USA. *International Journal of Coal Geology*, **113**, 64–75, https://doi.org/10.1016/j.coal.2012.09.006.

Griffith, A.A. 1920. The Phenomena of Rupture and Flow in Solids. *Royal Soc. Phil. Series A*.

Grosfils, E.B. 2007. Magma reservoir failure on the terrestrial planets: Assessing the

importance of gravitational loading in simple elastic models. *Journal of Volcanology and Geothermal Research*, **166**, 47–75, https://doi.org/10.1016/j.jvolgeores.2007.06.007.

Gudmundsson, A. 2011. *Rock Fractures in Geological Processes*. Cambridge, Cambridge University Press.

Gudmundsson, A. 2016. The mechanics of large volcanic eruptions. *Earth-Science Reviews*, **163**, 72–93, https://doi.org/10.1016/j.earscirev.2016.10.003.

Gudmundsson, A. & Lotveit, I.F. 2012. Sills as fractured hydrocarbon reservoirs: examples and models. *Geological Society, London, Special Publications*, **374**, 251–271, https://doi.org/10.1144/SP374.5.

Gudmundsson, A. & Philipp, S.L. 2006. How local stress fields prevent volcanic eruptions. *Journal of Volcanology and Geothermal Research*, **158**, 257–268, https://doi.org/10.1016/j.jvolgeores.2006.06.005.

Gunsallus, K.L. & Kulhawy, F.H. 1984. A comparative evaluation of rock strength measures. *International Journal of Rock Mechanics and Mining Sciences and Geomechanics*, **21**, 233–248, https://doi.org/10.1016/0148-9062(84)92680-9.

Guo, H., Aziz, N.I. & Schmidt, L.C. 1993. Rock fracture-toughness determination by the Brazilian test. *Engineering Geology*, **33**, 177–188, https://doi.org/10.1016/0013-7952(93)90056-I.

Haines, T.J., Michie, E.A.H., Neilson, J.E. & Healy, D. 2016. Permeability evolution across carbonate hosted normal fault zones. *Marine and Petroleum Geology*, **72**, 62–82, https://doi.org/10.1016/j.marpetgeo.2016.01.008.

Häring, M.O., Schanz, U., Ladner, F. & Dyer, B.C. 2008. Characterisation of the Basel 1

enhanced geothermal system. *Geothermics*, **37**, 469–495, https://doi.org/10.1016/j.geothermics.2008.06.002.

Heap, M. 2009. Creep: Time-dependent brittle deformation in rocks. 399.

Heap, M.J. & Faulkner, D.R. 2008. Quantifying the evolution of static elastic properties as crystalline rock approaches failure. *International Journal of Rock Mechanics and Mining Sciences*, **45**, 564–573, https://doi.org/10.1016/j.ijrmms.2007.07.018.

Heap, M.J., Vinciguerra, S. & Meredith, P.G. 2009. The evolution of elastic moduli with increasing crack damage during cyclic stressing of a basalt from Mt. Etna volcano. *Tectonophysics*, **471**, 153–160, https://doi.org/10.1016/j.tecto.2008.10.004.

Heap, M.J., Xu, T. & Chen, C. feng. 2014. The influence of porosity and vesicle size on the brittle strength of volcanic rocks and magma. *Bulletin of Volcanology*, **76**, 1–15, https://doi.org/10.1007/s00445-014-0856-0.

Heller, R., Vermylen, J. & Zoback, M. 2014. Experimental investigation of matrix permeability of gas shales. *AAPG Bulletin*, **98**, 975–995, https://doi.org/10.1306/09231313023.

Helmer, G., Sulem, J., Ghabezloo, S., Rohmer, J. & Hild, F. 2014. Experimental evaluation of the fracture toughness on a limestone. *Rock Engineering and Rock Mechanics: Structures in and on Rock Masses*, 217–221, https://doi.org/10.1201/b16955-34.

Herrmann, J., Rybacki, E., Sone, H. & Dresen, G. 2018. Deformation Experiments on Bowland and Posidonia Shale—Part I: Strength and Young's Modulus at Ambient and In Situ p c–T Conditions. *Rock Mechanics and Rock Engineering*, **51**, 3645–3666, https://doi.org/10.1007/s00603-018-1572-4.

Hickey, J. & Gottsmann, J. 2014. Benchmarking and developing numerical Finite Element models of volcanic deformation. *Journal of Volcanology and Geothermal Research*, **280**, 126–130, https://doi.org/10.1016/j.jvolgeores.2014.05.011.

Hosseini, M., Tavakoli, V. & Nazemi, M. 2018. The effect of heterogeneity on NMR derived capillary pressure curves, case study of Dariyan tight carbonate reservoir in the central Persian Gulf. *Journal of Petroleum Science and Engineering*, **171**, 1113–1122, https://doi.org/10.1016/j.petrol.2018.08.054.

Houben, M.E., Barnhoorn, A., Lie-A-Fat, J., Ravestein, T., Peach, C.J. & Drury, M.R. 2016. Microstructural characteristics of the Whitby Mudstone Formation (UK). *Marine and Petroleum Geology*, **70**, 185–200, https://doi.org/10.1016/j.marpetgeo.2015.11.011.

Inglis, C.E. 1913. Stresses in Plates Due to the Presence of Cracks and Sharp Corners. *Transactions of the Institute of Naval Architects*, **55**, 219–241.

Ingraffea, A., Gunsallus, K., Beech, J. & Nelson, P. 1984. A Short-rod based system for fracture toughness testing of rock. *In*: Underwood, J. H., Freiman, S. W. & Baratta, F. I. (eds) *Chevron-Notched Specimens - Testing and Stress Analysis*. Philadelphia, ASTM, 152–166.

Islam, M.A. & Skalle, P. 2013. An Experimental Investigation of Shale Mechanical Properties Through Drained and Undrained Test Mechanisms. *Rock Mechanics and Rock Engineering*, **46**, 1391–1413, https://doi.org/10.1007/s00603-013-0377-8.

ISRM. 1970. Suggested method for determining deformability of rock materials in uniaxial compression. 138–140.

ISRM. 1978. Suggested Methods For Determining Tensile Strength of Rock Materials.

International Journal of Rock Mechanics and Mining Sciences and Geomechanics, **15**, 99–103, https://doi.org/10.1016/0148-9062(78)90003-7.

ISRM. 1988. Suggested methods for determining the fracture toughness of rock. *International Journal of Rock Mechanics and Mining Sciences & Geomechanics Abstracts*, **25**, 71–96, https://doi.org/10.1016/S0148-9062(96)00015-0.

Jaeger, J.C. & Cook, N.G.W. 1979. *Fundamentals of Rock Mechanics*, 3rd ed. London, Meuthan.

Javadi, M., Sharifzadeh, M., Shahriar, K. & Mitani, Y. 2014. Critical Reynolds number for nonlinear flow through rough-walled fractures: The role of shear processes. *Water Resources Research*, 1003, https://doi.org/10.1002/2013WR014610.

Jinzhou, Z., Yongming, L., Song, W., Youshi, J. & Liehui, Z. 2014. Simulation of complex fracture networks influenced by natural fractures in shale gas reservoir. *Natural Gas Industry B*, **1**, 89–95, https://doi.org/10.1016/j.ngib.2014.10.012.

Kabir, P., Ulm, F.-J. & Akono, A.-T. 2017. Rate-independent fracture toughness of gray and black kerogen-rich shales. *Acta Geotechnica*, https://doi.org/10.1007/s11440-017-0562-0.

Kataoka, M., Mahdavi, E., Funatsu, T., Takehara, T., Obara, Y., Fukui, K. & Hashiba, K. 2017. Estimation of Mode i Fracture Toughness of Rock by Semi-Circular Bend Test under Confining Pressure Condition. *Procedia Engineering*, **191**, 886–893, https://doi.org/10.1016/j.proeng.2017.05.258.

Kavanagh, J.L. & Pavier, M.J. 2014. Rock interface strength influences fluid- filled fracture propagation pathways in the crust. *Journal of Structural Geology*, **63**.

Kavanagh, J.L., Menand, T. & Sparks, R.S.J. 2006. An experimental investigation of sill

formation and propagation in layered elastic media. *Earth and Planetary Science Letters*, **245**, 799–813, https://doi.org/10.1016/j.epsl.2006.03.025.

Kavanagh, J.L., Boutelier, D. & Cruden, A.R. 2015. The mechanics of sill inception , propagation and growth : Experimental evidence for rapid reduction in magmatic overpressure. *Earth and Planetary Science Letters*, **1**, 1–12, https://doi.org/10.1016/j.epsl.2015.03.038.

Khan, K. & Al-Shayea, N.A. 2000. Effect of specimen geometry and testing method on mixed Mode I-II fracture toughness of a limestone rock from Saudi Arabia. *Rock Mechanics and Rock Engineering*, **33**, 179–206, https://doi.org/10.1007/s006030070006.

Klaver, J., Desbois, G., Urai, J.L. & Littke, R. 2012. BIB-SEM study of the pore space morphology in early mature Posidonia Shale from the Hils area, Germany. *International Journal of Coal Geology*, **103**, 12–25, https://doi.org/10.1016/j.coal.2012.06.012.

Knorr, A.F. 2016. *The Effect of Rock Properties on Fracture Conductivity in the Eagle Ford*. Texas A&M University., https://doi.org/10.2118/181867-MS.

Kuruppu, M.D., Obara, Y., Ayatollahi, M.R., Chong, K.P. & Funatsu, T. 2014. ISRM-Suggested method for Determining the Mode I static fracture toughness using Semi-circular Bend specimen. *In*: Ulusay, R. (ed.) *The ISRM Suggested Methods for Rock Characterization, Testing and Monitoring 2007-2014*. Springer, 107–114.

Lamarche, J., Lavenu, A.P.C., Gauthier, B.D.M., Guglielmi, Y. & Jayet, O. 2012. Relationships between fracture patterns, geodynamics and mechanical stratigraphy in Carbonates (South-East Basin, France). *Tectonophysics*, **581**, 231–245, https://doi.org/10.1016/j.tecto.2012.06.042.

Larsen, B. & Gudmundsson, A. 2010. Linking of fractures in layered rocks: Implications for permeability. *Tectonophysics*, **492**, 108–120, https://doi.org/10.1016/j.tecto.2010.05.022.

Lawn, B. 1993. *Fracture of Brittle Solids - Second Edition*, Second. Davis, E. A. & Ward, I. M. (eds). Cambridge, Cambridge University Press, https://doi.org/10.1017/CBO9780511623127.

Le Corvec, N., Muirhead, J.D. & White, J.D.L. 2018. Shallow magma diversions during explosive diatreme-forming eruptions. *Nature Communications*, **9**, 1459, https://doi.org/10.1038/s41467-018-03865-x.

Lee, H.P. 2015. *Fracture Propagation in Naturally Fractured Reservoirs*. The University of Texas at Austin.

Lee, H.P., Olson, J.E., Holder, J., Gale, J.F.W. & Myers, R.D. 2015. The interaction of propagating opening mode fractures with preexisting discontinuities in shale. *Journal of Geophysical Research : Solid Earth*, **120**, 169–181, https://doi.org/10.1002/2014JB011358.

Levine, J.S., Fukai, I., et al. 2016. U.S. DOE NETL methodology for estimating the prospective CO2 storage resource of shales at the national and regional scale. *International Journal of Greenhouse Gas Control*, **51**, 81–94, https://doi.org/10.1016/j.ijggc.2016.04.028.

Li, B., Shen, H., Qu, S., Wang, D. & Liu, C. 2018. Tight carbonate reservoir characterization based on the modified rock physics model. *Journal of Applied Geophysics*, **159**, 374–385, https://doi.org/10.1016/j.jappgeo.2018.09.012.

Lian, C., Zhuge, Y. & Beecham, S. 2011. The relationship between porosity and strength

for porous concrete. *Construction and Building Materials*, **25**, 4294–4298, https://doi.org/10.1016/j.conbuildmat.2011.05.005.

Lü, C., Sun, Q., Zhang, W., Geng, J., Qi, Y. & Lu, L. 2017. The effect of high temperature on tensile strength of sandstone. *Applied Thermal Engineering*, **111**, 573–579, https://doi.org/10.1016/j.applthermaleng.2016.09.151.

Meille, S., Lombardi, M., Chevalier, J. & Montanaro, L. 2012. Mechanical properties of porous ceramics in compression: On the transition between elastic, brittle, and cellular behavior. *Journal of the European Ceramic Society*, **32**, 3959–3967, https://doi.org/10.1016/j.jeurceramsoc.2012.05.006.

Meredith, P.G. 1989. Comparative fracture toughness testing of rocks. *In*: Mihashi, H., Takahashi, H. & Wittman, F. H. (eds) *Fracture Toughness and Fracture Energy: Test Methods for Concrete and Rock*. Rotterdam, Brookfield, 265–278.

Milliken, K.L., Ergene, S.M. & Ozkan, A. 2016. Quartz types, authigenic and detrital, in the Upper Cretaceous Eagle Ford Formation, South Texas, USA. *Sedimentary Geology*, **339**, 273–288, https://doi.org/10.1016/j.sedgeo.2016.03.012.

Modi, C., Kumari, P. & Sharma, V.K. 2016. Reflection/refraction of qP/qSV wave in layered self-reinforced media. *Applied Mathematical Modelling*, https://doi.org/10.1016/j.apm.2016.05.015.

Mokhtari, M. 2015. *Characterization of Anisotropy in Organic-Rich Sahles: Shear and Tensile Failure, Wave Velocity, Matrix and Fracture Permeability*. Colorado School of Mines.

Mullen, J., Lowry, J.C. & Nwabuoku, K.C. 2010. Lessons Learned Developing the Eagle Ford Shale. *In*: *SPE Tight Gas Completions Conference*. 2–3.,

https://doi.org/10.2118/138446-MS.

Na, S.H., Sun, W.C., Ingraham, M.D. & Yoon, H. 2017. Effects of spatial heterogeneity and material anisotropy on the fracture pattern and macroscopic effective toughness of Mancos Shale in Brazilian tests. *Journal of Geophysical Research: Solid Earth*, **122**, 6202–6230, https://doi.org/10.1002/2016JB013374.

Nath Singh, R. & Sun, G. 1990. A numerical and experimental investigation for determining fracture toughness of Welsh limestone. *Mining Science and Technology*, **10**, 61–70, https://doi.org/10.1016/0167-9031(90)90850-R.

Ong, O.N., Schmitt, D.R., Kofman, R.S. & Haug, K. 2016. Static and dynamic pressure sensitivity anisotropy of a calcareous shale. *Geophysical Prospecting*, **64**, 875–897, https://doi.org/10.1111/1365-2478.12403.

Orowan, E. 1949. Reports on Progress in Physics: Fracture and strength of solids. *Rep. Prog. Phys.*, **12**, 185, https://doi.org/10.1088/0034-4885/12/1/309.

Palchik, V. & Hatzor, Y.H. 2004. The Influence of Porosity on Tensile and Compressive Strength of Porous Chalks. *Rock Mechanics and Rock Engineering*, **37**, 331–341, https://doi.org/10.1007/s00603-003-0020-1.

Perras, M.A. & Diederichs, M.S. 2014. A Review of the Tensile Strength of Rock: Concepts and Testing. *Geotechnical and Geological Engineering*, **32**, 525–546, https://doi.org/10.1007/s10706-014-9732-0.

Radi, Z., Yelles-Chaouche, A. & Bokelmann, G. 2015. Seismic anisotropy of northeastern Algeria from shear-wave splitting analysis. *Physics of the Earth and Planetary Interiors*, **248**, 73–82, https://doi.org/10.1016/j.pepi.2015.08.002.

Rashid, F., Glover, P.W.J., Lorinczi, P., Hussein, D. & Lawrence, J.A. 2017.

Microstructural controls on reservoir quality in tight oil carbonate reservoir rocks. *Journal of Petroleum Science and Engineering*, **156**, 814–826, https://doi.org/10.1016/j.petrol.2017.06.056.

Roshan, H., Sarmadivaleh, M. & Iglauer, S. 2016. Shale fracture surface area measured by tracking exchangeable cations. *Journal of Petroleum Science and Engineering*, **138**, 97–103, https://doi.org/10.1016/j.petrol.2015.12.005.

Sabatakakis, N., Koukis, G., Tsiambaos, G. & Papanakli, S. 2008. Index properties and strength variation controlled by microstructure for sedimentary rocks. *Engineering Geology*, **97**, 80–90, https://doi.org/10.1016/j.enggeo.2007.12.004.

Sayers, C.M. 2013. The effect of anisotropy on the Young's moduli and Poisson's ratios of shales. *Geophysical Prospecting*, **61**, 416–426, https://doi.org/10.1111/j.1365-2478.2012.01130.x.

Schaefer, L.N., Kendrick, J.E., Oommen, T., Lavallee, Y. & Chigna, G. 2015. Geomechanical rock properties of a basaltic volcano. *Frontiers in Earth Science*, **3**, 1–15, https://doi.org/10.3389/feart.2015.00029.

Schmidt, R.A. 1977. Fracture Mechanics Of Oil Shale - Unconfined Fracture Toughness, Stress Corrosion Cracking, And Tension Test Results. *In*: *The 18th U.S. Symposium on Rock Mechanics (USRMS)*. American Rock Mechanics Association.

Schmidt, R.A. & Huddle, C.W. 1977. Effect of confining pressure on fracture toughness of Indiana limestone. *International Journal of Rock Mechanics and Mining Sciences and*, **14**, 289–293, https://doi.org/10.1016/0148-9062(77)90740-9.

Secor, D.T. 1965. Role of fluid pressure in jointing. *American Journal of Science*, **263**, 633–646, https://doi.org/10.2475/ajs.263.8.633.

Shueili, A.M. Al, Manji, A. Al & Rylance, M. 2016. Khazzan : Making the Most of the Fracturing Sweet-Spot Between Verticals.

Sosa, A., Espinoza, D.N., Frydman, M., Barredo, S. & Cuervo, S. 2017. Analyzing a suitable elastic geomechanical model for Vaca Muerta Formation. *Journal of South American Earth Sciences*, **79**, 472–488, https://doi.org/10.1016/J.JSAMES.2017.09.011.

Stoeckhert, F., Molenda, M., Brenne, S. & Alber, M. 2015. Fracture propagation in sandstone and slate - Laboratory experiments, acoustic emissions and fracture mechanics. *Journal of Rock Mechanics and Geotechnical Engineering*, **7**, 237–249, https://doi.org/10.1016/j.jrmge.2015.03.011.

Sygała, A., Bukowska, M. & Janoszek, T. 2013. High Temperature Versus Geomechanical Parameters of Selected Rocks – The Present State of Research. *Journal of Sustainable Mining*, **12**, 45–51, https://doi.org/10.7424/jsm130407.

Tavallali, A. & Vervoort, A. 2013. Behaviour of layered sandstone under Brazilian test conditions: Layer orientation and shape effects. *Journal of Rock Mechanics and Geotechnical Engineering*, **5**, 366–377, https://doi.org/10.1016/j.jrmge.2013.01.004.

Teufel, L. & Clark, J. 1984. Hydraulic Fracture Propagation in Layered Rock: Experimental Studies of Fracture Containment. *Society of Petroleum Engineers Journal*, **24**, 19–32, https://doi.org/10.2118/9878-PA.

Tucker, M. & Wright, V. 2009. *Carbonate Sedimentology*, https://doi.org/10.1002/9781444314175.

Tucker, M.E. 2001. Sedimentary Petrology: An introduction to the Origin of Sedimnetary

Rocks.

Ulusay, R. 2014. *The ISRM Suggested Methods for Rock Characterization , Testing and Monitoring :* Ulusay, R. (ed.). Springer.

Vinciguerra, S., Meredith, P.G. & Hazzard, J. 2004. Experimental and modeling study of fluid pressure-driven fractures in Darley Dale sandstone. *Geophysical Research Letters*, **31**, 1–4, https://doi.org/10.1029/2004GL019638.

Vinciguerra, S., Trovato, C., Meredith, P.G. & Benson, P.M. 2005. Relating seismic velocities, thermal cracking and permeability in Mt. Etna and Iceland basalts. *International Journal of Rock Mechanics and Mining Sciences*, **42**, 900–910, https://doi.org/10.1016/j.ijrmms.2005.05.022.

Wang, H. & Sharma, M.M. 2018. Estimating Un-propped Fracture Conductivity and Fracture Compliance from Diagnostic Fracture Injection Tests. *Society of Petroleum Engineers Journal*, https://doi.org/10.2118/189844-PA.

Wei, M.D., Dai, F., Xu, N.W., Liu, Y. & Zhao, T. 2018. A novel chevron notched short rod bend method for measuring the mode I fracture toughness of rocks. *Engineering Fracture Mechanics*, **190**, 1–15, https://doi.org/10.1016/j.engfracmech.2017.11.041.

Yao, Y. 2012. Linear elastic and cohesive fracture analysis to model hydraulic fracture in brittle and ductile rocks. *Rock Mechanics and Rock Engineering*, **45**, 375–387, https://doi.org/10.1007/s00603-011-0211-0.

9 Appendix

The following tables are the data for each of the model runs in Chapter 5.

They are segmented into the following:

1. Changing Young's modulus of the layer ahead

2. Changing the distance between the fracture tip and the layer ahead

3. Changing the thickness of the layer ahead

4. Changing all three parameters simultaneously

Changing Young's modulus						
Model run	Young's modulus of host layer (GPa)	Young's modulus of layer ahead (GPa)	Young's modulus ratio	Distance to Layer ahead (m)	Thickness (m)	Tensile stress at fracture tip (MPa)
1	10	1.25	0.125	10	10	4.15
2	10	2.5	0.25	10	10	4.04
3	10	5	0.5	10	10	3.94
4	10	10	1	10	10	3.84
5	10	20	2	10	10	3.75
6	10	40	4	10	10	3.67
7	10	80	8	10	10	3.60

Changing distance to the layer ahead							
Model run	Young's modulus of host layer (GPa)	Young's modulus of layer ahead (GPa)	Young's modulus ratio	Distance to Layer ahead (m)	Thickness (m)	Tensile stress at fracture tip (MPa)	Normalised Tensile stress at fraccture tip (MPa)
1	10	5	0.5	0.125	10	5.32	5.33
2	10	5	0.5	0.25	10	5.05	5.06
3	10	5	0.5	0.5	10	4.81	4.81
4	10	5	0.5	1	10	4.55	4.56
5	10	5	0.5	2	10	4.31	4.32
6	10	5	0.5	4	10	4.11	4.12
7	10	5	0.5	8	10	3.97	3.98
8	10	5	0.5	16	10	3.89	3.90
9	10	5	0.5	32	10	3.85	3.86
10	10	5	0.5	64	10	3.83	3.84
11	10	20	2	0.125	10	2.83	2.85
12	10	20	2	0.25	10	2.97	2.98
13	10	20	2	0.5	10	3.12	3.14
14	10	20	2	1	10	3.28	3.30
15	10	20	2	2	10	3.45	3.46
16	10	20	2	4	10	3.60	3.61
17	10	20	2	8	10	3.72	3.74
18	10	20	2	16	10	3.79	3.81
19	10	20	2	32	10	3.82	3.84
20	10	20	2	64	10	3.83	3.84

Changing the thickness of the layer ahead						
Model run	Young's modulus of host layer (GPa)	Young's modulus of layer ahead (GPa)	Young's modulus ratio	Distance to Layer ahead (m)	Thickness (m)	Tensile stress at fracture tip (MPa)
1	10	5	0.5	10	2	3.87
2	10	5	0.5	10	5	3.91
3	10	5	0.5	10	10	3.94
4	10	5	0.5	10	20	3.97
5	10	5	0.5	10	40	4.00
6	10	5	0.5	10	80	4.01
7	10	20	2	10	2	3.81
8	10	20	2	10	5	3.78
9	10	20	2	10	10	3.75
10	10	20	2	10	20	3.72
11	10	20	2	10	40	3.70
12	10	20	2	10	80	3.70

Changing all three parameters at once							
Model run	Young's modulus of host layer (GPa)	Young's modulus of layer ahead (GPa)	Young's modulus ratio	Distance to Layer ahead (m)	Thickness (m)	Tensile stress at fracture tip (MPa)	Normalised Tensile stress at fraccture tip (MPa)
1	10	1.25	0.125	0.125	1	6.37	6.36
2	10	1.25	0.125	0.125	2	7.30	7.31
3	10	1.25	0.125	0.125	5	8.57	8.64
4	10	1.25	0.125	0.125	10	9.80	9.80
5	10	1.25	0.125	0.125	20	10.72	10.72
6	10	1.25	0.125	0.125	40	11.46	11.46
7	10	1.25	0.125	0.125	80	11.58	11.67
8	10	1.25	0.125	0.25	1	5.67	5.67
9	10	1.25	0.125	0.25	2	6.44	6.44
10	10	1.25	0.125	0.25	5	7.59	7.58
11	10	1.25	0.125	0.25	10	8.42	8.42
12	10	1.25	0.125	0.25	20	9.17	9.16
13	10	1.25	0.125	0.25	40	9.74	9.74
14	10	1.25	0.125	0.25	80	10.12	10.11
15	10	1.25	0.125	0.5	1	5.12	5.12
16	10	1.25	0.125	0.5	2	5.66	5.69
17	10	1.25	0.125	0.5	5	6.59	6.58
18	10	1.25	0.125	0.5	10	7.25	7.24
19	10	1.25	0.125	0.5	20	7.79	7.79
20	10	1.25	0.125	0.5	40	8.22	8.22
21	10	1.25	0.125	0.5	80	8.45	8.47
22	10	1.25	0.125	1	1	4.67	4.68
23	10	1.25	0.125	1	2	5.10	5.09
24	10	1.25	0.125	1	5	5.72	5.73
25	10	1.25	0.125	1	10	6.21	6.21
26	10	1.25	0.125	1	20	6.61	6.61
27	10	1.25	0.125	1	40	6.92	6.92
28	10	1.25	0.125	1	80	7.07	7.09
29	10	1.25	0.125	2	1	4.34	4.34
30	10	1.25	0.125	2	2	5.05	4.69
31	10	1.25	0.125	2	5	5.03	5.03
32	10	1.25	0.125	2	10	5.36	5.35
33	10	1.25	0.125	2	20	5.63	5.63
34	10	1.25	0.125	2	40	5.85	5.84
35	10	1.25	0.125	2	80	5.97	5.97
36	10	1.25	0.125	4	1	4.10	4.10
37	10	1.25	0.125	4	2	4.24	4.25
38	10	1.25	0.125	4	5	4.50	4.50
39	10	1.25	0.125	4	10	4.69	4.69
40	10	1.25	0.125	4	20	4.87	4.87
41	10	1.25	0.125	4	40	5.01	5.00
42	10	1.25	0.125	4	80	5.07	5.07
43	10	1.25	0.125	8	1	3.95	3.95
44	10	1.25	0.125	8	2	3.97	4.02
45	10	1.25	0.125	8	5	4.15	4.14
46	10	1.25	0.125	8	10	4.25	4.25
47	10	1.25	0.125	8	20	4.33	4.34
48	10	1.25	0.125	8	40	4.41	4.41
49	10	1.25	0.125	8	80	4.45	4.45

50	10	1.25	0.125	16	1	3.88	3.88
51	10	1.25	0.125	16	2	3.90	3.90
52	10	1.25	0.125	16	5	3.95	3.95
53	10	1.25	0.125	16	10	4.00	4.00
54	10	1.25	0.125	16	20	4.04	4.04
55	10	1.25	0.125	16	40	4.07	4.08
56	10	1.25	0.125	16	80	4.10	4.10
57	10	1.25	0.125	32	1	3.85	3.85
58	10	1.25	0.125	32	2	3.86	3.86
59	10	1.25	0.125	32	5	3.87	3.87
60	10	1.25	0.125	32	10	3.89	3.89
61	10	1.25	0.125	32	20	3.70	3.90
62	10	1.25	0.125	32	40	3.91	3.92
63	10	1.25	0.125	32	80	3.93	3.92
64	10	1.25	0.125	40	1	3.84	3.85
65	10	1.25	0.125	40	2	3.85	3.85
66	10	1.25	0.125	40	5	3.86	3.86
67	10	1.25	0.125	40	10	3.75	3.87
68	10	1.25	0.125	40	20	3.88	3.88
69	10	1.25	0.125	40	40	3.89	3.89
70	10	1.25	0.125	40	80	3.90	3.89
71	10	2.5	0.25	0.125	1	5.34	5.34
72	10	2.5	0.25	0.125	2	5.89	5.90
73	10	2.5	0.25	0.125	5	6.60	6.68
74	10	2.5	0.25	0.125	10	7.32	7.32
75	10	2.5	0.25	0.125	20	7.78	7.78
76	10	2.5	0.25	0.125	40	8.11	8.11
77	10	2.5	0.25	0.125	80	8.06	8.16
78	10	2.5	0.25	0.25	1	4.93	4.93
79	10	2.5	0.25	0.25	2	5.41	5.41
80	10	2.5	0.25	0.25	5	6.11	6.11
81	10	2.5	0.25	0.25	10	6.60	6.60
82	10	2.5	0.25	0.25	20	7.01	7.00
83	10	2.5	0.25	0.25	40	7.28	7.28
84	10	2.5	0.25	0.25	80	7.45	7.44
85	10	2.5	0.25	0.5	1	4.60	4.60
86	10	2.5	0.25	0.5	2	4.93	4.96
87	10	2.5	0.25	0.5	5	5.55	5.54
88	10	2.5	0.25	0.5	10	5.96	5.95
89	10	2.5	0.25	0.5	20	6.27	6.27
90	10	2.5	0.25	0.5	40	6.50	6.50
91	10	2.5	0.25	0.5	80	6.60	6.62
92	10	2.5	0.25	1	1	4.32	4.33
93	10	2.5	0.25	1	2	4.60	4.60
94	10	2.5	0.25	1	5	5.02	5.03
95	10	2.5	0.25	1	10	5.36	5.35
96	10	2.5	0.25	1	20	5.60	5.60
97	10	2.5	0.25	1	40	5.79	5.79
98	10	2.5	0.25	1	80	5.86	5.88
99	10	2.5	0.25	2	1	4.13	4.12
100	10	2.5	0.25	2	2	4.71	4.34

101	10	2.5	0.25	2	5	4.59	4.60
102	10	2.5	0.25	2	10	4.83	4.83
103	10	2.5	0.25	2	20	5.01	5.02
104	10	2.5	0.25	2	40	5.16	5.15
105	10	2.5	0.25	2	80	5.24	5.23
106	10	2.5	0.25	4	1	3.98	3.98
107	10	2.5	0.25	4	2	4.08	4.08
108	10	2.5	0.25	4	5	4.26	4.26
109	10	2.5	0.25	4	10	4.40	4.40
110	10	2.5	0.25	4	20	4.54	4.53
111	10	2.5	0.25	4	40	4.63	4.63
112	10	2.5	0.25	4	80	4.67	4.68
113	10	2.5	0.25	8	1	3.90	3.90
114	10	2.5	0.25	8	2	3.89	3.94
115	10	2.5	0.25	8	5	4.04	4.03
116	10	2.5	0.25	8	10	4.11	4.11
117	10	2.5	0.25	8	20	4.17	4.18
118	10	2.5	0.25	8	40	4.24	4.24
119	10	2.5	0.25	8	80	4.27	4.27
120	10	2.5	0.25	16	1	3.87	3.86
121	10	2.5	0.25	16	2	3.88	3.87
122	10	2.5	0.25	16	5	3.90	3.91
123	10	2.5	0.25	16	10	3.94	3.94
124	10	2.5	0.25	16	20	3.98	3.98
125	10	2.5	0.25	16	40	4.00	4.01
126	10	2.5	0.25	16	80	4.03	4.03
127	10	2.5	0.25	32	1	3.84	3.84
128	10	2.5	0.25	32	2	3.85	3.85
129	10	2.5	0.25	32	5	3.86	3.86
130	10	2.5	0.25	32	10	3.87	3.87
131	10	2.5	0.25	32	20	3.69	3.88
132	10	2.5	0.25	32	40	3.89	3.90
133	10	2.5	0.25	32	80	3.91	3.90
134	10	2.5	0.25	40	1	3.84	3.84
135	10	2.5	0.25	40	2	3.85	3.85
136	10	2.5	0.25	40	5	3.85	3.85
137	10	2.5	0.25	40	10	3.74	3.86
138	10	2.5	0.25	40	20	3.87	3.87
139	10	2.5	0.25	40	40	3.88	3.88
140	10	2.5	0.25	40	80	3.88	3.88
141	10	5	0.5	0.125	1	4.53	4.53
142	10	5	0.5	0.125	2	4.75	4.77
143	10	5	0.5	0.125	5	5.00	5.08
144	10	5	0.5	0.125	10	5.32	5.32
145	10	5	0.5	0.125	20	5.48	5.47
146	10	5	0.5	0.125	40	5.57	5.57
147	10	5	0.5	0.125	80	5.46	5.56
148	10	5	0.5	0.25	1	4.34	4.34
149	10	5	0.5	0.25	2	4.56	4.56
150	10	5	0.5	0.25	5	4.86	4.86
151	10	5	0.5	0.25	10	5.05	5.05

152	10	5	0.5	0.25	20	5.21	5.20
153	10	5	0.5	0.25	40	5.28	5.28
154	10	5	0.5	0.25	80	5.34	5.33
155	10	5	0.5	0.5	1	4.19	4.19
156	10	5	0.5	0.5	2	4.33	4.36
157	10	5	0.5	0.5	5	4.63	4.62
158	10	5	0.5	0.5	10	4.81	4.80
159	10	5	0.5	0.5	20	4.92	4.92
160	10	5	0.5	0.5	40	4.99	5.00
161	10	5	0.5	0.5	80	5.01	5.03
162	10	5	0.5	1	1	4.06	4.06
163	10	5	0.5	1	2	4.20	4.19
164	10	5	0.5	1	5	4.39	4.40
165	10	5	0.5	1	10	4.55	4.54
166	10	5	0.5	1	20	4.65	4.65
167	10	5	0.5	1	40	4.72	4.72
168	10	5	0.5	1	80	4.73	4.75
169	10	5	0.5	2	1	3.97	3.97
170	10	5	0.5	2	2	4.44	4.07
171	10	5	0.5	2	5	4.20	4.20
172	10	5	0.5	2	10	4.31	4.31
173	10	5	0.5	2	20	4.40	4.40
174	10	5	0.5	2	40	4.46	4.46
175	10	5	0.5	2	80	4.49	4.49
176	10	5	0.5	4	1	3.90	3.90
177	10	5	0.5	4	2	3.94	3.95
178	10	5	0.5	4	5	4.04	4.04
179	10	5	0.5	4	10	4.11	4.11
180	10	5	0.5	4	20	4.19	4.18
181	10	5	0.5	4	40	4.23	4.22
182	10	5	0.5	4	80	4.24	4.24
183	10	5	0.5	8	1	3.87	3.86
184	10	5	0.5	8	2	3.84	3.88
185	10	5	0.5	8	5	3.94	3.93
186	10	5	0.5	8	10	3.97	3.97
187	10	5	0.5	8	20	4.00	4.01
188	10	5	0.5	8	40	4.04	4.04
189	10	5	0.5	8	80	4.05	4.06
190	10	5	0.5	16	1	3.85	3.85
191	10	5	0.5	16	2	3.86	3.85
192	10	5	0.5	16	5	3.87	3.87
193	10	5	0.5	16	10	3.89	3.89
194	10	5	0.5	16	20	3.91	3.91
195	10	5	0.5	16	40	3.92	3.93
196	10	5	0.5	16	80	3.94	3.94
197	10	5	0.5	32	1	3.84	3.84
198	10	5	0.5	32	2	3.85	3.84
199	10	5	0.5	32	5	3.85	3.85
200	10	5	0.5	32	10	3.85	3.85
201	10	5	0.5	32	20	3.66	3.86
202	10	5	0.5	32	40	3.87	3.87

203	10	5	0.5	32	80	3.88	3.87
204	10	5	0.5	40	1	3.84	3.84
205	10	5	0.5	40	2	3.84	3.84
206	10	5	0.5	40	5	3.85	3.85
207	10	5	0.5	40	10	3.73	3.85
208	10	5	0.5	40	20	3.85	3.85
209	10	5	0.5	40	40	3.86	3.86
210	10	5	0.5	40	80	3.86	3.86
211	10	10	1	0.125	1	3.84	3.84
212	10	10	1	0.125	2	3.83	3.84
213	10	10	1	0.125	5	3.77	3.84
214	10	10	1	0.125	10	3.84	3.84
215	10	10	1	0.125	20	3.84	3.84
216	10	10	1	0.125	40	3.84	3.84
217	10	10	1	0.125	80	3.74	3.84
218	10	10	1	0.25	1	3.84	3.84
219	10	10	1	0.25	2	3.84	3.84
220	10	10	1	0.25	5	3.84	3.84
221	10	10	1	0.25	10	3.84	3.84
222	10	10	1	0.25	20	3.85	3.84
223	10	10	1	0.25	40	3.84	3.84
224	10	10	1	0.25	80	3.85	3.84
225	10	10	1	0.5	1	3.84	3.84
226	10	10	1	0.5	2	3.81	3.84
227	10	10	1	0.5	5	3.85	3.84
228	10	10	1	0.5	10	3.85	3.84
229	10	10	1	0.5	20	3.84	3.84
230	10	10	1	0.5	40	3.84	3.84
231	10	10	1	0.5	80	3.82	3.84
232	10	10	1	1	1	3.84	3.84
233	10	10	1	1	2	3.85	3.84
234	10	10	1	1	5	3.84	3.84
235	10	10	1	1	10	3.85	3.84
236	10	10	1	1	20	3.84	3.84
237	10	10	1	1	40	3.84	3.84
238	10	10	1	1	80	3.82	3.84
239	10	10	1	2	1	3.84	3.84
240	10	10	1	2	2	4.21	3.84
241	10	10	1	2	5	3.84	3.84
242	10	10	1	2	10	3.84	3.84
243	10	10	1	2	20	3.84	3.84
244	10	10	1	2	40	3.84	3.84
245	10	10	1	2	80	3.85	3.84
246	10	10	1	4	1	3.84	3.84
247	10	10	1	4	2	3.84	3.84
248	10	10	1	4	5	3.84	3.84
249	10	10	1	4	10	3.84	3.84
250	10	10	1	4	20	3.85	3.84
251	10	10	1	4	40	3.85	3.84
252	10	10	1	4	80	3.84	3.84
253	10	10	1	8	1	3.85	3.84

254	10	10	1	8	2	3.79	3.84
255	10	10	1	8	5	3.85	3.84
256	10	10	1	8	10	3.84	3.84
257	10	10	1	8	20	3.83	3.84
258	10	10	1	8	40	3.84	3.84
259	10	10	1	8	80	3.84	3.84
260	10	10	1	16	1	3.85	3.84
261	10	10	1	16	2	3.84	3.84
262	10	10	1	16	5	3.84	3.84
263	10	10	1	16	10	3.84	3.84
264	10	10	1	16	20	3.84	3.84
265	10	10	1	16	40	3.83	3.84
266	10	10	1	16	80	3.84	3.84
267	10	10	1	32	1	3.84	3.84
268	10	10	1	32	2	3.84	3.84
269	10	10	1	32	5	3.84	3.84
270	10	10	1	32	10	3.84	3.84
271	10	10	1	32	20	3.64	3.84
272	10	10	1	32	40	3.84	3.84
273	10	10	1	32	80	3.85	3.84
274	10	10	1	40	1	3.83	3.84
275	10	10	1	40	2	3.84	3.84
276	10	10	1	40	5	3.84	3.84
277	10	10	1	40	10	3.72	3.84
278	10	10	1	40	20	3.84	3.84
279	10	10	1	40	40	3.84	3.84
280	10	10	1	40	80	3.84	3.84
281	10	20	2	0.125	1	3.24	3.23
282	10	20	2	0.125	2	3.08	3.09
283	10	20	2	0.125	5	2.87	2.94
284	10	20	2	0.125	10	2.83	2.83
285	10	20	2	0.125	20	2.78	2.78
286	10	20	2	0.125	40	2.76	2.76
287	10	20	2	0.125	80	2.68	2.78
288	10	20	2	0.25	1	3.37	3.37
289	10	20	2	0.25	2	3.23	3.23
290	10	20	2	0.25	5	3.06	3.06
291	10	20	2	0.25	10	2.97	2.97
292	10	20	2	0.25	20	2.92	2.91
293	10	20	2	0.25	40	2.89	2.89
294	10	20	2	0.25	80	2.89	2.88
295	10	20	2	0.5	1	3.50	3.50
296	10	20	2	0.5	2	3.35	3.37
297	10	20	2	0.5	5	3.21	3.21
298	10	20	2	0.5	10	3.12	3.11
299	10	20	2	0.5	20	3.06	3.06
300	10	20	2	0.5	40	3.03	3.04
301	10	20	2	0.5	80	3.01	3.03
302	10	20	2	1	1	3.62	3.62
303	10	20	2	1	2	3.52	3.51
304	10	20	2	1	5	3.36	3.37

305	10	20	2	1	10	3.28	3.28
306	10	20	2	1	20	3.22	3.22
307	10	20	2	1	40	3.19	3.20
308	10	20	2	1	80	3.17	3.19
309	10	20	2	2	1	3.72	3.71
310	10	20	2	2	2	3.99	3.62
311	10	20	2	2	5	3.52	3.52
312	10	20	2	2	10	3.45	3.44
313	10	20	2	2	20	3.39	3.39
314	10	20	2	2	40	3.37	3.36
315	10	20	2	2	80	3.36	3.35
316	10	20	2	4	1	3.78	3.78
317	10	20	2	4	2	3.73	3.74
318	10	20	2	4	5	3.66	3.66
319	10	20	2	4	10	3.60	3.60
320	10	20	2	4	20	3.56	3.55
321	10	20	2	4	40	3.54	3.53
322	10	20	2	4	80	3.52	3.52
323	10	20	2	8	1	3.82	3.82
324	10	20	2	8	2	3.75	3.80
325	10	20	2	8	5	3.77	3.76
326	10	20	2	8	10	3.72	3.72
327	10	20	2	8	20	3.68	3.69
328	10	20	2	8	40	3.67	3.67
329	10	20	2	8	80	3.66	3.66
330	10	20	2	16	1	3.84	3.83
331	10	20	2	16	2	3.83	3.83
332	10	20	2	16	5	3.81	3.81
333	10	20	2	16	10	3.79	3.79
334	10	20	2	16	20	3.78	3.78
335	10	20	2	16	40	3.76	3.76
336	10	20	2	16	80	3.76	3.76
337	10	20	2	32	1	3.84	3.84
338	10	20	2	32	2	3.84	3.84
339	10	20	2	32	5	3.83	3.83
340	10	20	2	32	10	3.82	3.83
341	10	20	2	32	20	3.62	3.82
342	10	20	2	32	40	3.81	3.81
343	10	20	2	32	80	3.82	3.81
344	10	20	2	40	1	3.83	3.84
345	10	20	2	40	2	3.84	3.84
346	10	20	2	40	5	3.84	3.83
347	10	20	2	40	10	3.71	3.83
348	10	20	2	40	20	3.82	3.83
349	10	20	2	40	40	3.82	3.82
350	10	20	2	40	80	3.82	3.82
351	10	40	4	0.125	1	2.71	2.71
352	10	40	4	0.125	2	2.49	2.51
353	10	40	4	0.125	5	2.25	2.33
354	10	40	4	0.125	10	2.20	2.19
355	10	40	4	0.125	20	2.14	2.14

356	10	40	4	0.125	40	2.12	2.12
357	10	40	4	0.125	80	2.06	2.16
358	10	40	4	0.25	1	2.93	2.93
359	10	40	4	0.25	2	2.72	2.72
360	10	40	4	0.25	5	2.50	2.50
361	10	40	4	0.25	10	2.39	2.39
362	10	40	4	0.25	20	2.34	2.33
363	10	40	4	0.25	40	2.31	2.31
364	10	40	4	0.25	80	2.31	2.29
365	10	40	4	0.5	1	3.16	3.16
366	10	40	4	0.5	2	2.94	2.96
367	10	40	4	0.5	5	2.74	2.73
368	10	40	4	0.5	10	2.62	2.61
369	10	40	4	0.5	20	2.55	2.55
370	10	40	4	0.5	40	2.52	2.53
371	10	40	4	0.5	80	2.51	2.52
372	10	40	4	1	1	3.38	3.38
373	10	40	4	1	2	3.21	3.20
374	10	40	4	1	5	2.98	2.99
375	10	40	4	1	10	2.87	2.87
376	10	40	4	1	20	2.80	2.80
377	10	40	4	1	40	2.77	2.77
378	10	40	4	1	80	2.75	2.77
379	10	40	4	2	1	3.57	3.57
380	10	40	4	2	2	3.76	3.39
381	10	40	4	2	5	3.25	3.25
382	10	40	4	2	10	3.14	3.14
383	10	40	4	2	20	3.07	3.07
384	10	40	4	2	40	3.04	3.04
385	10	40	4	2	80	3.03	3.03
386	10	40	4	4	1	3.71	3.70
387	10	40	4	4	2	3.62	3.62
388	10	40	4	4	5	3.49	3.49
389	10	40	4	4	10	3.40	3.40
390	10	40	4	4	20	3.35	3.34
391	10	40	4	4	40	3.31	3.31
392	10	40	4	4	80	3.29	3.29
393	10	40	4	8	1	3.79	3.79
394	10	40	4	8	2	3.70	3.75
395	10	40	4	8	5	3.68	3.67
396	10	40	4	8	10	3.62	3.62
397	10	40	4	8	20	3.56	3.57
398	10	40	4	8	40	3.54	3.54
399	10	40	4	8	80	3.52	3.53
400	10	40	4	16	1	3.83	3.82
401	10	40	4	16	2	3.81	3.81
402	10	40	4	16	5	3.78	3.78
403	10	40	4	16	10	3.75	3.75
404	10	40	4	16	20	3.72	3.72
405	10	40	4	16	40	3.70	3.70
406	10	40	4	16	80	3.69	3.69

407	10	40	4	32	1	3.83	3.84
408	10	40	4	32	2	3.83	3.83
409	10	40	4	32	5	3.82	3.82
410	10	40	4	32	10	3.81	3.81
411	10	40	4	32	20	3.60	3.80
412	10	40	4	32	40	3.79	3.79
413	10	40	4	32	80	3.79	3.78
414	10	40	4	40	1	3.83	3.84
415	10	40	4	40	2	3.84	3.83
416	10	40	4	40	5	3.83	3.83
417	10	40	4	40	10	3.70	3.82
418	10	40	4	40	20	3.81	3.81
419	10	40	4	40	40	3.81	3.80
420	10	40	4	40	80	3.81	3.80
421	10	80	8	0.125	1	2.28	2.28
422	10	80	8	0.125	2	2.08	2.09
423	10	80	8	0.125	5	1.87	1.94
424	10	80	8	0.125	10	1.82	1.82
425	10	80	8	0.125	20	1.78	1.78
426	10	80	8	0.125	40	1.76	1.76
427	10	80	8	0.125	80	1.72	1.81
428	10	80	8	0.25	1	2.54	2.54
429	10	80	8	0.25	2	2.33	2.33
430	10	80	8	0.25	5	2.13	2.13
431	10	80	8	0.25	10	2.04	2.04
432	10	80	8	0.25	20	2.00	1.99
433	10	80	8	0.25	40	1.97	1.97
434	10	80	8	0.25	80	1.97	1.96
435	10	80	8	0.5	1	2.83	2.83
436	10	80	8	0.5	2	2.60	2.62
437	10	80	8	0.5	5	2.41	2.40
438	10	80	8	0.5	10	2.31	2.30
439	10	80	8	0.5	20	2.25	2.25
440	10	80	8	0.5	40	2.22	2.23
441	10	80	8	0.5	80	2.21	2.23
442	10	80	8	1	1	3.12	3.13
443	10	80	8	1	2	2.93	2.92
444	10	80	8	1	5	2.70	2.71
445	10	80	8	1	10	2.60	2.60
446	10	80	8	1	20	2.54	2.54
447	10	80	8	1	40	2.52	2.52
448	10	80	8	1	80	2.49	2.52
449	10	80	8	2	1	3.40	3.40
450	10	80	8	2	2	3.54	3.17
451	10	80	8	2	5	3.03	3.04
452	10	80	8	2	10	2.93	2.93
453	10	80	8	2	20	2.87	2.87
454	10	80	8	2	40	2.84	2.84
455	10	80	8	2	80	2.83	2.83
456	10	80	8	4	1	3.61	3.61
457	10	80	8	4	2	3.49	3.50

458	10	80	8	4	5	3.35	3.35
459	10	80	8	4	10	3.25	3.26
460	10	80	8	4	20	3.20	3.19
461	10	80	8	4	40	3.17	3.16
462	10	80	8	4	80	3.15	3.15
463	10	80	8	8	1	3.75	3.74
464	10	80	8	8	2	3.64	3.69
465	10	80	8	8	5	3.60	3.59
466	10	80	8	8	10	3.53	3.53
467	10	80	8	8	20	3.47	3.48
468	10	80	8	8	40	3.45	3.45
469	10	80	8	8	80	3.44	3.44
470	10	80	8	16	1	3.81	3.81
471	10	80	8	16	2	3.79	3.78
472	10	80	8	16	5	3.74	3.74
473	10	80	8	16	10	3.71	3.71
474	10	80	8	16	20	3.68	3.68
475	10	80	8	16	40	3.65	3.66
476	10	80	8	16	80	3.65	3.65
477	10	80	8	32	1	3.83	3.83
478	10	80	8	32	2	3.83	3.82
479	10	80	8	32	5	3.81	3.81
480	10	80	8	32	10	3.79	3.79
481	10	80	8	32	20	3.59	3.78
482	10	80	8	32	40	3.77	3.77
483	10	80	8	32	80	3.77	3.77
484	10	80	8	40	1	3.83	3.83
485	10	80	8	40	2	3.83	3.83
486	10	80	8	40	5	3.82	3.82
487	10	80	8	40	10	3.69	3.81
488	10	80	8	40	20	3.80	3.80
489	10	80	8	40	40	3.79	3.79
490	10	80	8	40	80	3.79	3.79